

STRUCTURE AND KINETICS OF TWIN BOUNDARIES IN SHAPE MEMORY
ALLOYS

by

Bibek Jung Karki



A dissertation

submitted in partial fulfillment

of the requirements for the degree of

Doctor of Philosophy in Materials Science and Engineering

Boise State University

December 2021

© 2021

Bibek Jung Karki

ALL RIGHTS RESERVED

BOISE STATE UNIVERSITY GRADUATE COLLEGE

DEFENSE COMMITTEE AND FINAL READING APPROVALS

of the dissertation submitted by

Bibek Jung Karki

Dissertation Title: Structure and Kinetics of Twin Boundaries in Shape Memory Alloys

Date of Final Oral Examination: 01 November 2021

The following individuals read and discussed the dissertation submitted by student Bibek Jung Karki, and they evaluated the student's presentation and response to questions during the final oral examination. They found that the student passed the final oral examination.

Peter Müllner, Ph.D. Chair, Supervisory Committee

Rick Ubic, Ph.D. Member, Supervisory Committee

Robert Pond, Ph.D. External Committee Member

Doron Shilo, Ph.D. External Committee Member

The final reading approval of the dissertation was granted by Peter Müllner, Ph.D., Chair of the Supervisory Committee. The dissertation was approved by the Graduate College.

DEDICATION

I dedicate this dissertation to my late mother, Kushma Giri Karki.

Thank you to everyone who believed in me and gave me the courage and strength to persevere and complete this work.

ACKNOWLEDGMENTS

I am grateful to everyone who was instrumental in the completion of my degree. I apologize for I might have missed listing all involved in this path.

I would like to thank my advisor, Dr. Peter Müllner, for his pivotal role in developing me as a researcher. I was fortunate to have him as my mentor, and I learned much from him inside and outside the classroom. I am most thankful to Dr. Robert Pond, Dr. Doron Shilo, and Dr. Eilon Faran for their help, guidance, insight, and contribution to my work.

I want to thank all my lab mates, and everyone involved in the path since I joined the lab in July 2017. In particular, I thank Dr. Amy Moll, Dr. Paul Lindquist, Dr. Andrew Armstrong, Dr. Medha Veligatla, and Ali Mustafa for assistance and guidance throughout my studies.

I thank the National Science Foundation (NSF), United States - Israel Binational Science Foundation (BSF), and Micron School of Materials Science and Engineering for funding my studies.

I thank my friends and family; I owe them a lot.

ABSTRACT

Shape memory alloys (SMAs) are functional materials that recover from large strains without permanent deformation. In magnetic shape memory alloys (MSMAs), the reversible deformation is driven either magnetically or mechanically. Two underlying phenomena are responsible for the shape memory effect: (a) a diffusionless, martensitic transformation and (b) twinning in the martensite phase.

In MSMAs, the reversible plastic deformation occurs via twinning in the martensite phase, particularly via the movement of twinning disconnections (TDs) along the twin boundaries (TBs). A geometric algorithm called the classical model (CM) of deformation twinning describes operative twinning modes of a given crystal system. There are four types of twins - compound, non-conventional (NC), type I, and type II, which are distinguished based on the crystal's orientation relationship (OR) across the TB. Recently, Pond, Hirth, and coworkers developed a dislocation model of twinning called the topological model (TM) to describe the formation and growth of twins. We apply the TM to characterize the defect structure of junction lines and TBs. We show that the relaxed structure of type II TBs differs distinctly from those of type I and compound TBs. Furthermore, depending on the crystal, the type II interface can either relax into a coherently faceted structure (e.g., NiTi) or remain inherently irrational (e.g., 10M Ni-Mn-Ga (NMG)).

One of the characteristic features of type II twins is that chains of quadruple junction lines (QJLs) appear in the vicinity of the TB. Our analysis shows that QJLs have

no long-range stress field. Triple junction lines (TJLs), on the other hand, contain a rotational displacement field, i.e., a disclination. A stable chain of TJLs requires a local minimum of the strain energy associated with the disclinations. A disclination quadrupole approximation shows that the system's total energy scales with the distance of the defects. So, as we approach larger defect spacing, two TJLs may coalesce to form a QJL, thus minimizing the system's energy.

A complete description of twinning includes the kinetic relation, i.e., the relationship between the driving force acting on the TB and the resulting velocity of TB motion. In 2014, Faran and Shilo presented an analytic kinetic relation for TB motion, a general kinetic law typical of viscous interface motion in a periodic potential. We refine the model by incorporating the structural differences between type I and type II twins in the kinetic relation. We establish the structure of type II TBs in various alloys and correlate their kinetic properties with the interface's structure.

Our work helps establish the kinetic relation for type II twins. Our model predicts the mechanism responsible for the high mobility and temperature insensitivity of type II TBs. Furthermore, we correctly predict the twinning stress of an alloy for compound and type I twins. Our investigation and discovery help enhance the understanding of the dynamic behavior of SMAs.

TABLE OF CONTENTS

DEDICATION.....	iv
ACKNOWLEDGMENTS.....	v
ABSTRACT	vi
LIST OF TABLES.....	xiii
LIST OF FIGURES	xiv
LIST OF ABBREVIATIONS.....	xxi
CHAPTER ONE: INTRODUCTION.....	1
CHAPTER TWO: SCIENTIFIC BACKGROUND	4
2.1 Shape Memory Alloys	4
2.1.1 Thermal Shape Memory Alloys.....	4
2.1.2 Magnetic Shape Memory Alloys	5
2.2 Deformation Twinning.....	5
2.3 Classical Model of Twinning	8
2.4 Topological Model of Twinning	10
2.5 Kinetics of Twin Boundary Motion.....	13
2.5.1 Analytical Model for Kinetics of TB Motion	16
CHAPTER THREE: MOTIVATION AND CONTRIBUTIONS.....	21
CHAPTER FOUR: TOPOLOGICAL MODEL OF TYPE II DEFORMATION	
TWINNING IN 10M NI-MN-GA	24
Abstract.....	25

1. Introduction.....	25
2. Crystallography of Ni-Mn-Ga	27
2.1 Austenite Crystal Structure and Symmetry.....	27
2.2 Modulated Martensite Structure and Symmetry	28
2.3 Approximated Monoclinic Structure and Symmetry.....	28
3. Theories of Deformation Twinning	30
3.1 Classical Model	30
3.2 Topological Model	32
4. Structural Models of Type II Twins in NMG.....	38
4.1 Previous Investigations	38
4.2 Crystallography of Twins in NMG.....	39
4.3 Interface Models	44
5. Discussion.....	47
5.1 Properties of Type I and Type II Twins.....	47
5.2 Mobility of Type I Twins.....	50
5.3 Mobility of Type II Twins	52
6. Conclusion	55
Acknowledgement	56
References	57
Appendices	66
Appendix A: Transformation Matrices.....	66
Appendix B: Bevis & Crocker Ttttheory.....	67
Appendix C: Coherently Faceted Approximant to Type II Interface.....	69

CHAPTER FIVE: TWIN BOUNDARY JUNCTIONS IN 10M NI-MN-GA	73
Abstract.....	74
1. Introduction.....	74
2. Crystallography of 10M Ni-Mn-Ga.....	76
3. Non-Conventional Twins.....	78
3.1 Crystallography.....	79
3.2 Orientation Relationship.....	81
4. Junction Lines.....	82
4.1 Quadruple Junction Lines.....	83
4.2 Quadruple Junction Line Formation Energetics	85
4.3 Walls of Triple Junction Lines.....	90
5. Discussion	92
6. Conclusion.....	94
Acknowledgement.....	95
References.....	96
Appendices.....	101
Dissymmetrisation Stages	102
Twinning Orientation Relationship.....	103
CHAPTER SIX: A SIMPLE METHOD TO CHARACTERIZE HIGH RATE TWIN BOUNDARY KINETICS IN NI-MN-GA	104
Abstract.....	105
1. Introduction.....	105
2. Experimental Setup and Test Procedure.....	110

3. Image Analysis.....	114
4. Results	117
5. Discussion.....	124
6. Summary.....	129
Acknowledgement	130
References	130
CHAPTER SEVEN: TWIN BOUNDARY STRUCTURE AND MOBILITY	133
Abstract	134
1. Introduction.....	135
2. Definitions and Basic Concepts	140
3. Topological Models for Twin Interfaces.....	143
4. Lattice Barriers for Twin Boundary Motion and Classifications of Different Regimes	146
5. Activation Energies for Nucleation Process.....	153
5.1 Homogeneous Nucleation of Kink Pairs on Disconnection Lines	154
5.2 Thermally Activated Homogeneous Nucleation of Disconnection Loops	156
5.3 Athermal Heterogeneous Nucleation of Disconnections at the Surface	159
6. Kinetic relations for TB Motion, Rate-Limiting Processes and Twinning Stress	169
6.1 Kinetic Relations	169

6.2 Motion of Compound and Type I Twins in the Low Driving Force Range.....	171
6.3 Motion of Type II Twins in the Low Driving Force Range	173
7. Comparison of Model Predictions to Experimental Results.....	175
7.1 Differences in Twinning Stress between Twin Types	176
7.2 Twinning Stress of Compound and Type I Twins	177
7.3 Twinning Stress of Type II Twins	182
8. Summary	184
Acknowledgement.....	185
References.....	185
CHAPTER EIGHT: SUMMARY OF WORK AND CONTRIBUTIONS.....	199
8.1 Summary of Work	199
8.2 Outstanding Questions	204
8.3 Future Work	206
REFERENCES	208

LIST OF TABLES

Table 4.1	Crystallographic parameters of twinning modes in NMG expressed in the approximated martensite framework. The shear values, s , and non-integer coefficients q and r are obtained using the lattice parameters determined by Sozinov et al. [15].....	41
Table 4.2	Topological parameters used to characterize the disconnections in compound, type I and type II interfaces. In the formulation of Burgers vectors, the twin (λ) is assumed to be above the matrix (μ), and the result is expressed in the matrix coordinate frame.	42
Table 4.B3	Correspondence matrices formulated as 2' symmetry operations that are suppressed in the martensite phase compared to its austenite parent phase.	69
Table 5.1	Crystallographic parameters of non-conventional (NC) twin mode in NMG expressed in the approximate martensite framework. The shear value, s , and the non-integer coefficients q and r are obtained using the lattice parameters as determined by Sozinov et al. [24]	80
Table 7.1	Sub-processes in the various ranges of the driving force (g) and TB velocity (v_{TB}). The different ranges of the driving force are defined based on the magnitudes of the lattice barriers Γ_D , γ_{TB}	149
Table 7.2	Typical material parameters for type II twins in 10M Ni-Mn-Ga and Ni-Ti.	168
Table 7.3	Material properties and measured data used for plotting (in Figure 7.6) the room temperature twinning stress of type I and compound twins in several materials.....	180

LIST OF FIGURES

Figure 1.1	Stress-strain curve of 10M Ni-Mn-Ga (NMG) under compressive loading at room temperature for type I (red) and type II (blue) TBs. The twinning stress for type II twins is about 0.1 MPa, and for type I twins is about 1 MPa. Reprinted from <i>Experimental Techniques</i> , 40 (2016), Faran and Shilo, Ferromagnetic shape memory alloys—challenges, applications, and experimental characterization, 1005-1031, with permission from Springer Nature.....	2
Figure 2.1	(a) A volume-conserving plane-strain deformation shows a circle deformed to an ellipse. As we see, two undistorted planes k_1 and k_2 are rotated in the deformed medium (k_1' and k_2'). A further rotation of the ellipse by $\pm\alpha$ results in a simple shear of twinning. (b) An illustration of twinning parameters K and η : the inset table shows a degenerate solution for a given twin mode.	7
Figure 2.2	Schematic illustration of a disconnection in compound and type I twins, with $K_1 = k_1$ in both cases.....	11
Figure 2.3	Schematic illustration of type II twin interface formed after the partitioning of displacement and rotational field of the tilt-wall. Tilt-wall forms when disconnections in the k_1 plane accumulate in a planar boundary and lose their step character.....	13
Figure 2.4	Twinning process showing (a) nucleation, (b) forward growth, and (c) sideways thickening of the twin variant. Figure reprinted from <i>Experimental Techniques</i> , 40 (2016), Faran and Shilo, Ferromagnetic shape memory alloys—challenges, applications, and experimental characterization, 1005-1031, with permission from Springer Nature.....	15
Figure 2.5	Experimental result of kinetic relation for type I (red) and type II (blue) twin boundaries (TBs) in NMG. The line is fitted to the boxed data points, representing the maximal velocity for a given driving force. Figure reprinted from <i>J. Mech. Phys. Solids</i> , 61 (2013), Faran and Shilo, The kinetic relation for twin wall motion in Ni-Mn-Ga—part 2, 726-741, with permission from Elsevier.....	16
Figure 2.6	A summary of mechanisms for TB motion are presented in (a), (c), and (e). The corresponding two-dimensional and one-dimensional lattice	

potentials are shown in (b) and (d). v_{TB} , v_d , and v_k are velocities of the TB, twinning disconnections (TDs), and disconnection kink, respectively. Figure reprinted from Materials Science and Technology, 30 (2014), Faran and Shilo, Dynamics of twin boundaries in ferromagnetic shape memory alloys, 1545-1558, with permission from Taylor & Francis.....20

- Figure 4.1 (a) Austenite crystal structure of stoichiometric Ni_2MnGa viewed along one of its axes. Red is Gallium (circle), green is Manganese (square), and blue is Nickel (triangle). (b) The crystal structure of 10M Ni-Mn-Ga (NMG) viewed along its unique axis $[010]_{10M}$ shows the modulated assembly of the crystal; a periodic simple shear along $\{220\}_c$ planes achieve modulation during the martensitic transformation. The monoclinic angle, β_{10M} , is exaggerated in the current illustration. (c) Experimentally observed diffraction pattern of NMG that corresponds to the schematic illustration in (b): the superlattice reflections correspond to the periodic offset of the $\{220\}_c$ planes. (d) Approximated NMG crystal lattice using only the fundamental reflections in (c) and derived from the parent cubic axes through a monoclinic distortion.30
- Figure 4.2 (a) A volume conserving plane-strain deformation shows two undistorted planes k_1 and k_2 that are simply rotated in the deformed medium (k_1' and k_2'). (b) The k_1 plane becomes the invariant plane of twinning when the deformed medium in (a) is further rotated by $+\alpha$ about n_s (c) An illustration of experimentally observed twinning parameters K and η : the inset table shows their relationship with twinning elements described in the text. The table also shows the conjugate relation between type I and type II twins.32
- Figure 4.3 Schematic illustration of the formation and growth of (a) $(011)_m$ and (b) $(011)_m$ type I twins in NMG under compressive load. The disconnections (b , h) nucleate near the corner of a parallelepiped specimen and propagate into the bulk by gliding along k_1 planes. The disconnection line sense $\xi \parallel n_s$ points out of the page.....34
- Figure 4.4 Schematic illustration of the formation of $(q_111)_m$ type II twins in NMG. (a) Initially, nascent $(011)_m$ type I disconnections nucleate at the surface source in response to a local compressive stress. (b) The notional intermediate stage in an inhomogeneous stress field due to specimen bending: here the disconnections begin to accumulate and form a tilt wall perpendicular to the glide plane k_1 . (c) Finally, a $(q_111)_m$ type II conjugate is formed after symmetrical partitioning of the rotational distortions across the tilt wall. (d) The exploded view of the sharp type II interface in (c), showing the character of the defects in the array: $b^s = b \cos\alpha$ is the resultant Burgers vector of each grain boundary dislocation. (e) The stress distribution in a bent parallelepiped specimen showing the stress reversal across the neutral plane, which promotes tip blunting.37

Figure 4.5	Schematic illustration of a disconnection in (a) $(011)_m$ type I twin interface, and (b) $(q_111)_m$ type II twin interface.	44
Figure 4.6	(a) Schematic illustration of defect kinking along low energy Peierls valleys in a $(q_111)_m$ type II twin. Here, $\xi \parallel n_s = [1 \ q_1/2 \ -q_1/2]_m \approx 10[100]_m + \frac{1}{2}[011]_m$. (b) An orderly array of aligned kinked defects. (c) A disorderly array of non-aligned kinked defects.	46
Figure 4.7	Schematic illustration of the common $(011)_m$ planes (a) before and (b) after they are sheared into 2-D coherency. In (a), the angle between $[100]^\mu_m$ and $[100]^\lambda_m$ (in reality only 0.52°) is exaggerated. The partitioning of coherency strain between the μ and λ crystals results in $[100]_m$ and $[011]_m$ becoming orthogonal.	47
Figure 4.8	Schematic illustration of (a) $(011)_m$ type I twin boundary (TB) and (b) $(q_111)_m$ type II TB in the reference location. The k_1, γ_1 in (a) and k_2, γ_2 in (b) are not a conjugate pair.	50
Figure 4.9	Schematic illustration of misfit accommodation at a coherently faceted approximant structure. The line direction of RH coherency dislocations, $\xi^{\mathcal{C}}$, points out of the page, parallel to $[011]_m$. The angle between $(011)_m$ and $(q_111)_m$ is 4.12° . The LH screw misfit disconnections have b^m anti-parallel to $\xi^{\mathcal{C}}$ and a negative sense of steps. The direction n_s is the average line direction of the twinning disconnections in the $(q_111)_m$ twin plane.	72
Figure 5.1	(a) Austenite crystal structure of stoichiometric Ni_2MnGa viewed along one of its axes. Circles (red), squares (green), and triangles (blue) represent Gallium, Manganese, and Nickel atoms. (b) Approximated 10M Ni-Mn-Ga (NMG) lattice viewed along its unique axis, $[001]_m$; the crystal lattice is derived from the parent cubic axes through a monoclinic distortion. (c) Electron diffraction pattern of NMG with the electron beam along $[001]_m$. The superlattice reflections correspond to the modulation event, and by only considering the fundamental reflection, we obtain the averaged unit cell (b).....	77
Figure 5.2	Schematic illustration of $(1r0)/(1q0)$ NC twinning in NMG. The subscript μ and λ denote the matrix and the twin, respectively. The conjugate relationship of the twinning elements is expressed in NC TBs because the TB is k_1 for the matrix, but k_2 for the twin.	81
Figure 5.3	Experimentally observed junction lines in NMG. (a) Scanning Electron Microscopy (SEM) image showing a periodic array of quadruple junction lines (QJLs) in the vicinity of type II twin boundaries (TBs). (b) Transmission Electron Microscopy (TEM) image of a chain of triple junction lines (TJLs) formed at the interface between $(110)_m$ TB laminate and a homogeneous region. Reprinted from Scripta Materialia, 162 (2019),	

	Seiner <i>et al.</i> [19], NC twins in five-layered modulated Ni-Mn-Ga martensite, 497-502, with permission from Elsevier. We follow the notation of Straka <i>et al.</i> [17] for the designation of variants.83
Figure 5.4	a) Schematic illustration of austenite single crystal viewed along one of the principal axes; the colors define the four variants that form after the phase transformation. The dotted lines represent point symmetry operations – 2100, 2010, 2110, and 2110 – that get suppressed in the martensite phase. Phase transformation breaks the symmetry, and these operations, along with 4001+ and 4001-, become correspondence matrices, which define the twinning relation at QJLs. (b) The orientation of TBs around a QJL in NMG, which is obtained by a systematic operation of OR across the TB in the QJL arrangement. The associated correspondence matrices, in order, is 2110, 4001+, 2110, and 4001-.....85
Figure 5.5	Schematic illustration of TJLs forming a disclination quadrupole system to accommodate four martensite variants: the four distinct disclination strengths are obtained by systematically studying the OR of variants across the junction's TBs.89
Figure 5.6	a) Equilibrium energy (U_{eq}) of disclination quadrupole approximation as a function of L_1 and R_1 , both ranging from 0 to 20 nm. $\alpha = \omega_2 / \omega_1 \approx 2$ in the present case. (b) For a fixed R_1 , U_{eq} as a function of L_1 is a logarithmic plot. (c) For a fixed L_1 , U_{eq} as a function of R_1 is a polynomial plot of an order of about 2.5. Thus, the energy of the disclination quadrupole is sensitive to the size of the dipole arm length.90
Figure 5.7	The orientation of TBs around a TJL in NMG, as shown in (a), is reproduced crystallographically in (b). The arrangement is deduced by a taking a systematic operation of OR across the TB in the TJL arrangement. Figure (a) is adapted from Scripta Materialia, 162 (2019), Seiner <i>et al.</i> [19], NC twins in five-layered modulated Ni-Mn-Ga martensite, 497-502, with permission from Elsevier. We follow the notation of Straka <i>et al.</i> [17] for the designation of variants.91
Figure 5.8	An intermediate stage in the pairwise coalescence of TJLs into QJLs, with disclination quadrupole approximation, as in Figure 5.5, as a starting reference.....93
Figure 6.1	(a) Overall image of the base frame and setup for the experiments. The 30 cm ruler serves as a scale bar for the setup. (b) Zoom in on the region of interest that shows setup of sample, force sensor and optical displacement sensor. The solenoid's push rod provides mechanical load, and the attached extension eliminates its magnetic effect on the MSM element. The rigid spacer is required because of the MSM sample dimension. (c) Further zoom in on the solenoid region for detailed optical displacement

	sensor setup. The reflecting surface is attached to improve the optical signal.	114
Figure 6.2	Calculating twin boundary displacement from microscope images. (a), (b) A typical pair of consecutive images, showing an individual twin boundary propagating along the sample. (c) The absolute grayscale difference between images (b) and (a). (d) A binary image map obtained from image (c) by setting a threshold value $\alpha = 50$ on the absolute difference. (e) Filtered binary image after noise reduction. The twin boundary displacement is calculated by averaging the number of white pixels in the filtered image (see text for details). The intensity scale bar displays the 256 greyscale levels in images (a), (b), (c).	116
Figure 6.3	Measured profiles of the force (a), sample displacement (b), and twin boundary displacement (c), taken from a pulsed loading test on the sample shown in Figure 6.2. The numbered labels mark the same time points on all charts (see text for details).....	122
Figure 6.4	(a) Calculated velocities of the sample (blue) and the twin boundary (green), overlaid on the measured force profile (red). (b) Stress-strain curves obtained from the two displacement-force measurements. The numbered labels mark the same time points shown in Figure 6.3.....	123
Figure 6.5	Dynamic behavior of Ni-Mn-Ga single crystal obtained from two different experiments conducted on the same sample. Experiment 1: (a), (b), (c). Experiment 2: (d), (e), (f). The visible twin boundary in each experiment is shown in (a) and (d). Stress-strain curves ((b), (e)) are calculated independently for the sample and for the twin boundary from the entire measured data. Kinetic relations ((c), (f)) are calculated independently for the sample and for the twin boundary, and include data recorded up to the stress peak in the stress-strain curves. The shaded area in light green represents the estimated measurement error in twin boundary velocity.	129
Figure 7.1	Schematic illustration of a coherently faceted type II TB, showing the low index plane facets separated by an array of screw disconnections. b is the Burgers vector of a disconnection, ζ is the disconnection line direction and is (anti) parallel to the shear direction η_1 . The disconnections are equally spaced at a distance l_o , such that the average interface plane coincides with the irrational K_1 twinning plane.....	146
Figure 7.2	Schematic description of the different lattice barriers for TB motion. The illustrations depict a TB with a rational twinning plane K_1 , as in compound and type I twins. (a) The lattice barrier for the motion of the TB as a flat plane along z direction. The barrier is characterized by an amplitude γ_{TB} (energy/ area) and periodicity d_{TB} . The TB can also propagate via the glide of twinning disconnections on the rational twinning plane K_1 , along x	

direction. b , ζ are the Burgers vector and line direction of the disconnection, and η_1 is the shear direction. (b) Peierls barrier for the glide of a disconnection. The barrier is characterized by an amplitude Γ_D (energy/length) and periodicity d_D . A kink-pair (KP) mechanism allows disconnection motion at driving force values that are smaller than the Peierls barrier. 148

Figure 7.3 Energy profile of a twin boundary U_{TB} (energy/area, Equation (4)) or twinning disconnection u_D (energy / length, Equation (5)), for the case that the driving force g (energy/volume) is larger than the lattice barrier. The dashed green line represents the work associated with the motion of the TB ($-g z$ in Equation (4)) or the disconnection ($-g h x$ in Equation (5)). The normalized coordinates z/d_{TB} , x/d_D represent the directions normal to the TB plane and TD line, respectively (as in Figure 7.2)..... 152

Figure 7.4 Energy profile of a twin boundary U_{TB} (energy/area, Equation (4)) or twinning disconnection u_D (energy / length, Equation (5)), for the case that the driving force g (energy/volume) is smaller than the lattice barrier. The dashed green line represents the work associated with the motion of the TB ($-g z$ in Equation (4)) or the disconnection ($-g h x$ in Equation (5)). The normalized coordinates z/d_{TB} , x/d_D represent the directions normal to the TB plane and TD line, respectively (as in Figure 7.2). The magnitude of the barrier for TB or disconnection motion associated with the lattice potential is marked as U_{TBbar} and u_{Dbar} , respectively. The energy gained due to the local advancement of the TB or the disconnection is labeled as U_{TBgain} and u_{Dgain} , respectively (see discussion on the different energy terms in Section 5.1 and 5.2)..... 153

Figure 7.5 Schematic description of the equilibrium coherently faceted type II interface (inset (a)), that contains an array of left-handed screw disconnections, which are marked with an inverted ‘S’. L marks the width of the crystal. Under an applied driving force, the disconnections move to the right (green arrows), transforming material from the top variant to the bottom (the green area in inset (b)), leading to the advancement of the TB downwards (direction marked by the vertical black arrow). The collective motion of the disconnection array creates a “depleted” region of length x_o close to the left surface (inset (b)). To maintain the coherently faceted structure, disconnections nucleate at the left surface and propagate to the right (inset (c)). The position x_D marks the location of a newly nucleated disconnection relative to the left surface. (d) A schematic illustration of the depleted region x_o close to the surface with a representation of the disconnections (large S with Burgers vector b) and coherency dislocations (small s with Burgers vector db_{mis}). Image defects maintain zero stresses on the free surface (the vertical black line)..... 162

Figure 7.6	<p>Twinning stress at room temperature versus the product $\mu^2 s^3$ for compound and type I twins in several SMA systems, presented on logarithm scales. Data for different alloys were taken from Table 7.3. The dashed grey line is a linear fit to the experimental data, exhibiting $R^2 > 0.99$. The solid black line represents the calculated relation given by Equation (42).</p>	181
Figure 7.7	<p>Temperature variation of the twinning stress of type I twin in 10M Ni-Mn-Ga. Experimental data is taken from Refs. [32, 34]. The dashed blue line represents the $1/T$ dependence obtained from Equation (42), using the room temperature values of μ and s listed in Table 7.3.</p>	181
Figure 7.8	<p>Temperature variation of the twinning stress of type II twins in 10M Ni-Mn-Ga. Experimental data is taken from Refs. [30, 32]. The temperature dependence is substantially weaker than that of the conjugate type I twins (Figure 7.7).</p>	184

LIST OF ABBREVIATIONS

BSU	Boise State University
GC	Graduate College
TDC	Thesis and Dissertation Coordinator
TDs	Twinning Disconnections
SMA _s	Shape Memory Alloys
MSMA _s	Magnetic Shape Memory Alloys
MSM	Magnetic Shape Memory
TBs	Twin Boundaries
CM	Classical Model (of Twinning)
TM	Topological Model (of Twinning)
NMG	10M Ni-Mn-Ga
NC	Non-conventional

CHAPTER ONE: INTRODUCTION

Active materials act as transducers, i.e., convert energy from one form to another. Examples include shape memory alloys (SMAs), ferroelectric materials, piezoelectrics, topological insulators, and energy storage devices. In SMAs, a material can attain a significant (3-12%) reversible plastic deformation by converting thermal energy into mechanical energy and vice-versa [1–3]. Magnetic shape memory alloys (MSMAs) allow the transformation of mechanical and magnetic energy and have potential applications as actuators, sensors, energy harvesters, and micropumps [4–10].

The underlying phenomena responsible for the shape memory effect in SMAs are a diffusionless, martensitic phase transformation and deformation twinning in the martensite phase [2, 11, 12]. The martensitic phase transformation is a shear-like interface-mediated lattice distortion [12, 13]. Several symmetry-equivalent variants arise during the phase change, allowing the transformation with little to no change in volume. The straining of SMA samples occurs in the martensite phase via deformation twinning, which is a crystallographic reorientation mechanism [12, 14–19]. At the atomistic scale, twinning occurs via the formation and growth of twinning disconnections (TDs) along twin boundaries (TBs) [18, 20–22]. Four types of twins are distinguished based on the type of orientation relationship (OR) of martensite variants across the TB: compound, non-conventional (NC), type I, and type II.

Type I and type II twins are of particular interest because they are geometrically related and attain the same overall strain [14–18, 23–25] but have distinctly contrasting

properties. For instance, in 10M Ni-Mn-Ga (NMG), the twinning stress – the stress at which the material deforms via twinning – at room temperature is about 1 MPa for type I twins and only about 0.1 MPa for type II twins [23, 24, 26–28], as shown in Figure 1.1. The difference in twinning stress is an order of magnitude within the same material for about 6% strain. Furthermore, experiments have shown that type II twins are highly mobile [23, 24, 26, 27, 29], and their twinning stress is a weak function of temperature [5, 23, 30–32]; In NMG, the type II twinning stress at 1.7 K is less than 0.3 MPa [33].

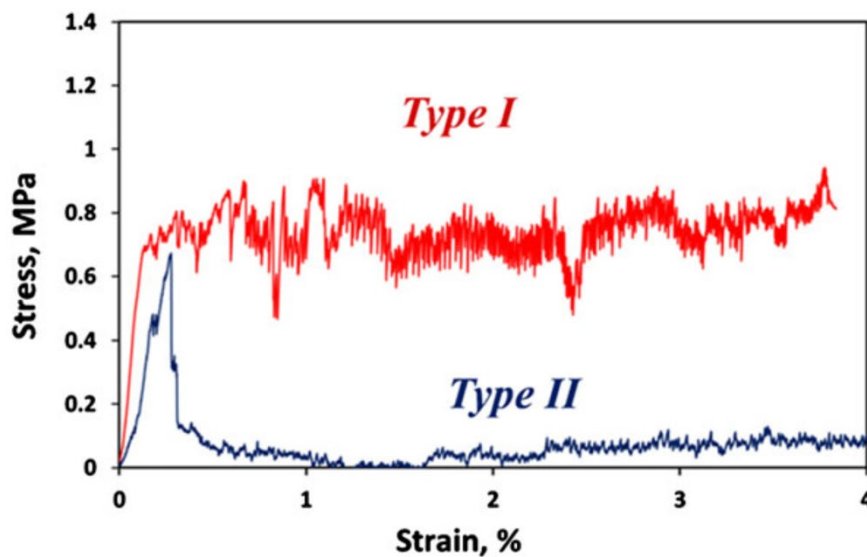


Figure 1.1 Stress-strain curve of 10M Ni-Mn-Ga (NMG) under compressive loading at room temperature for type I (red) and type II (blue) TBs. The twinning stress for type II twins is about 0.1 MPa, and for type I twins is about 1 MPa. Reprinted from *Experimental Techniques*, 40 (2016), Faran and Shilo, *Ferromagnetic shape memory alloys—challenges, applications, and experimental characterization*, 1005-1031, with permission from Springer Nature.

The properties of type II twins have puzzled the scientific community, which has yet to find agreement on type II twins' formation and growth mechanism and their interfacial structure [18, 34–42]. The habit plane of type II twins is crystallographically irrational and the only differentiating geometric parameter from type I twins. Some

scientists argue that the low twinning stress of type II twins are related to the inherently irrational nature of the habit plane. By contrast, others suggest a coherently faceted terrace-ledge structure forms the irrational TB, and the interface's defect-interactions may explain type II twins' low twinning stress.

This study aims to characterize the structure of type II TBs and defect junctions in various SMAs extensively using the topological model (TM) of interfacial defects [20, 22, 43–45]. Characterization of the defect structure of the interface enables us to analyze the potential barriers to the motion of TDs. The analysis of barriers for the motion of disconnections helps us understand the kinetic relation of TBs, i.e., explain the relationship between the velocity of a TB and the driving force that acts on it. The overall result of this study will help understand and optimize the dynamic behavior of SMAs and MSMAAs.

CHAPTER TWO: SCIENTIFIC BACKGROUND

2.1 Shape Memory Alloys

Shape memory alloys are a class of functional materials that can undergo large reversible plastic deformation [1, 2, 11]. The underlying mechanism responsible for this shape memory effect is a diffusionless martensitic phase transformation and deformation twinning in the martensite phase [2, 11, 12]. Twinning and the martensitic phase transformation in these materials serve as a basis for converting mechanical energy into other forms of energy (thermal, electrical, magnetic, etc.) and vice-versa [3–10, 23].

2.1.1 Thermal Shape Memory Alloys

In thermally activated shape memory alloys like NiTi, a strain of up to 12% is recoverable by providing thermal energy [1, 2]. The strain recovery requires activating both the martensitic transformation and deformation twinning mechanism. A NiTi sample at room temperature is in a low symmetry martensite phase, with a phase transition temperature of about 75 °C [1, 46]. The phase transformation from the high symmetry austenite phase to the low symmetry martensite phase occurs by the martensitic transformation which distorts the lattice about an invariant plane [2, 12]. Based on the reduction in the symmetry, several martensite variants form [18, 47], which fit together by twinning with little or no volume change of the material after the phase transformation. The material is strained in the martensite phase, and the primary deformation mechanism is (deformation) twinning due to a limited number of independent slip systems and low shear modulus [12, 18, 23]. Now, when the strained

material is heated, it gains thermal energy which serves as the driving force to reverse the twinning deformation (de-twinning), ultimately transforming into the austenite and recovering the strain caused in the martensite phase.

2.1.2 Magnetic Shape Memory Alloys

Magnetic shape memory alloys have a distinguishing feature where a macroscopic shape change occurs when the material is exposed to a magnetic field. In these materials, shape change occurs via reorientation of martensite variants rather than the phase transformation [12, 18, 23]. The reorientation occurs via twinning. The magnetocrystalline anisotropy, i.e., the difference in magnetic susceptibility in different crystal directions, drives the reorientation process [23]. A variant with the preferred orientation of the magnetization axis grows at the expense of the other. The maximum driving force, akin to mechanical stress, is given by the ratio of the anisotropy energy and the twinning strain and is called magnetostress [23]. In NMG alloys, the maximum available magnetostress is about 3MPa, which is higher than the twinning stress of about 0.1 MPa or 1 MPa (degenerate cases). So, the magnetostress is sufficient to drive the twinning reorientation process in NMG alloys and cause a maximum strain of about 6% [23, 25, 26, 28, 48].

2.2 Deformation Twinning

Twins are two misoriented crystals related by some symmetry operation: rotation, reflection, inversion, or rotoinversion. They can form during growth, transformation, and deformation. Based on the classical model (CM) of deformation twinning, twin *lattices* are related by a homogeneous simple shear, s , about an invariant plane.

A complete description of twinning requires four crystallographic elements, \mathbf{k}_1 , \mathbf{k}_2 , γ_1 , and γ_2 , collectively defined as a twin mode [16–19]. \mathbf{k}_1 and \mathbf{k}_2 , inclined by an angle 2φ , are the two mutually conjugate planes that remain undistorted when a medium undergoes volume-conserving plane strain shear transformation, as illustrated in Figure 2.1(a). We designate the plane of shear \mathbf{P}_s and its normal \mathbf{n}_s . Suppose we further rotate the deformed medium in Figure 2.1(a) by an angle $\alpha = \pm(\pi/2 - 2\varphi)$ about \mathbf{n}_s . In that case, one of the conjugate planes coincides with its orientation before deformation, thereby becoming the invariant plane of twinning. In either case, i.e., whether \mathbf{k}_1 or \mathbf{k}_2 is the invariant plane of twinning, the overall deformation is a simple shear. The directions parallel to \mathbf{k}_1 and \mathbf{k}_2 , which also lie in \mathbf{P}_s , are designated γ_1 and γ_2 , respectively. The magnitude of shear is $s = 2 \cot 2\varphi$, parallel to either γ_1 or γ_2 . Frank [14] suggested that a twinning mode be characterized by parameters \mathbf{K} , $\boldsymbol{\eta}$, as shown in Figure 2.1(b).

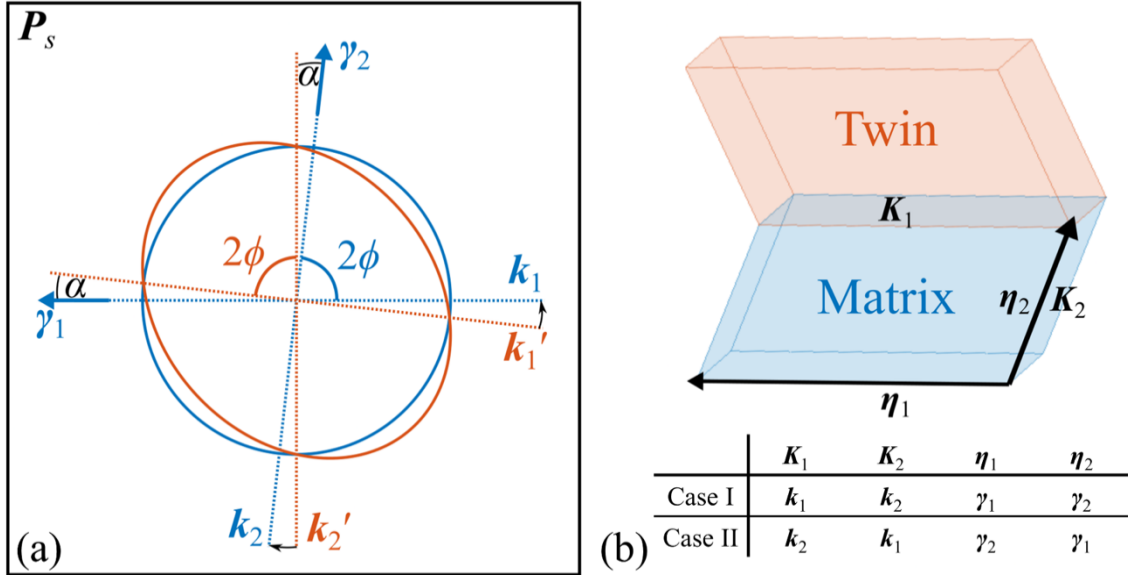


Figure 2.1 (a) A volume-conserving plane-strain deformation shows a circle deformed to an ellipse. As we see, two undistorted planes k_1 and k_2 are rotated in the deformed medium (k_1' and k_2'). A further rotation of the ellipse by $\pm\alpha$ results in a simple shear of twinning. (b) An illustration of twinning parameters K and η : the inset table shows a degenerate solution for a given twin mode.

When the plane of shear, P_s , is irrational, one of the two undistorted planes has irrational Miller indices. We define the rational plane as k_1 and the irrational plane as k_2 . With this definition, γ_1 is irrational, and γ_2 is rational. If the invariant plane of twinning is rational, the twins are designated as type I. Conversely, if the invariant plane of twinning is irrational, the twins are defined as type II. Compound and NC twins arise when the plane of shear, P_s , is rational. All the twinning elements are rational for compound twins, whereas all the twinning elements are irrational for NC twins.

The orientation relationship between the matrix and the twin *lattice* for type I twins is mirror reflection across k_1 and denoted by m' , where the prime indicates a “color-reversing” symmetry operation. The type II twins, i.e., the conjugate of type I, have k_2 as the invariant plane, and the operation interrelating the crystals is $2'$ about γ_2 . Compound twins satisfy both m' across $K_1 = k_1$ or k_2 (TB), and $2'$ about $\eta_1 = \gamma_1$ or γ_2 (shear

direction). The orientation relationship between the NC twins was not established before the work presented here.

2.3 Classical Model of Twinning

The CM of deformation twinning is a geometric algorithm to predict the operative twinning modes for a given crystal structure. A comprehensive review of the CM of deformation twinning has been presented by Christian and Mahajan [18]. We implement the general theory of twinning in lattices, formulated by Bevis & Crocker [17, 19], to predict the possible twinning modes. The theory utilizes the restrictive properties of the unimodular correspondence matrix, \mathbf{C} , to predict the twinning shear, invariant plane, and shear direction. The correspondence matrix defines the relation of coordinate axes between a pair of variants and satisfies the twinning restrictions.

An affine transformation represents a homogeneous simple shear as:

$$\mathbf{v} = \mathbf{S} \mathbf{u} \quad (1)$$

where \mathbf{u} and \mathbf{v} are lattice vectors of the parent and twin lattice vectors, respectively, and \mathbf{S} is a second rank tensor defining the shear transformation.

In some general coordinate system, A , Equation (1) is written using the Einstein summation convention as:

$${}^A v^i = {}^A S_j^i {}^A u^j \quad (2)$$

where i and j are summing indices. The superscript A denotes the crystal coordinate system. The summing indices are in superscript form for real vectors and subscript form for reciprocal space vectors.

In a general coordinate system, A , S_j^i has the form:

$${}^A S_j^i = \delta_j^i + s {}^A l^i {}^A m_j \quad (3)$$

where δ_j^i is the Kronecker delta, \mathbf{l} is the unit vector parallel to the shear direction, \mathbf{m} is the unit vector normal to the invariant plane, and s is the twinning shear.

In general, Equation (3) yields irrational components for ${}^A\mathbf{v}$. However, \mathbf{v} is a lattice vector of the twin in a new coordinate system B , where the system B is related to A by rotation, reflection, or inversion, and designated L . So, we have,

$${}^B\mathbf{v} = L {}^A\mathbf{S} {}^A\mathbf{u} = \mathbf{C} {}^A\mathbf{u} \quad (4)$$

where \mathbf{C} is the unimodular correspondence matrix. Once the correspondence matrix, \mathbf{C} , is specified, Bevis and Crocker showed that we can utilize its restrictive properties to calculate s , \mathbf{l} , and \mathbf{m} .

Implementing matrix notation, the solutions for s , \mathbf{l} , and \mathbf{m} are found as follows:

$$s^2 = \text{trace}(\mathbf{C}' \mathbf{G} \mathbf{C} \mathbf{G}^{-1}) - 3 \quad (5)$$

where, $G_{ij} = \mathbf{a}_i \cdot \mathbf{a}_j$ is the metric tensor, and \mathbf{a}_i are the basis vectors. Using, $\mathbf{Y} = \mathbf{G} - \mathbf{C}' \mathbf{G} \mathbf{C}$, we obtain three quadratic equations, defined by the equation:

$$Y_{ii} m_j^2 - 2 Y_{ij} m_i m_j + Y_{jj} m_i^2 = 0 \quad (6)$$

where $i \neq j$, and $i, j = 1, 2, 3$. Equation (6) yields two possible solutions for \mathbf{m} : the undistorted conjugate planes \mathbf{k}_1 and \mathbf{k}_2 . The unit vector \mathbf{l} can then be obtained directly from Equation (3) or derived from \mathbf{Y}^{-1} using three quadratic equations of the kind of Equation (6). Yet again, we obtain two solutions for \mathbf{l} : the conjugate shear directions γ_1 and γ_2 .

In the case of twinning, Equation (4) shows that the correspondence matrix represents point symmetry operations of the higher symmetry phase, which gets suppressed in the lower symmetry phase.

2.4 Topological Model of Twinning

The CM is a geometric model that can correctly predict the operative twinning mode. However, it fails to describe the twin formation and growth mechanisms. Pond, Hirth, and co-workers [20–22, 43, 49] extensively studied interfaces and presented a TM that rigorously characterizes the defect structure of an interface. Twinning defects possess dual topological character, namely the Burgers vector, \mathbf{b} , and the step height, h , and are referred to as disconnections [20]. These defects accommodate the misfit between the two adjoining crystals across the twinned interface. The twinning interface, called TBs, moves due to the movement of disconnections: the Burgers vector quantifies the lattice displacement accompanying the interface motion, and the step height quantifies the displacement of the interface.

The symmetry requirement of twinning imposes rather strict rules for the structure and orientation of the interface, thus restricting the admissible defect structure. In the literature, there are many accounts of disconnections in compound twins [50–55]. In compound and type I twins, the invariant plane is rational, $\mathbf{K}_1 = \mathbf{k}_1$. The formation and motion of disconnections on these rational planes, \mathbf{k}_1 , produces an engineering shear strain, $\gamma_e = |\mathbf{b}|/2h$, which has half the magnitude as the true shear strain, s , and is parallel to the classical shear direction, $\boldsymbol{\eta}_1 = \boldsymbol{\gamma}_1$. The step height, h , is equal to the integral spacing of the \mathbf{k}_1 planes, and the Burgers vector, \mathbf{b} , of the disconnection correspond to differences between the shortest translation vectors connecting the adjacent crystals: thus \mathbf{b} , expressed in the parent coordinate frame, are given by:

$$\mathbf{b} = \mathbf{P}^{-1} \mathbf{t}(\lambda) - \mathbf{t}(\mu) \quad (7)$$

where $\mathbf{t}(\mu)$ and $\mathbf{t}(\lambda)$ are translation vectors of the steps of the parent (lower) and twin (upper) crystal, respectively, as in Figure 2.2, and \mathbf{P} is the coordinate transformation from μ to λ frame. While both the translation vectors are rational, their difference is generally irrational because of the coordinate transformation, as seen in type I twins with $\mathbf{b} \parallel \pm\gamma_1$. So, compound twins represent a unique case where \mathbf{b} is rational. The nucleation and growth of type I and compound twins in terms of disconnection and motion have been modeled consistently with experimental observations [56–58]. For instance, Pond et al. [50] implemented TM to characterize the defect structure of compound twins in non-modulated Ni-Mn-Ga martensite as $\mathbf{k}_1 = (202)_T$, i.e., $h = d_{k_1}$, and $\mathbf{b} = 1/12 [10\bar{1}]_T$, where T implies face-centered tetragonal unit cell.

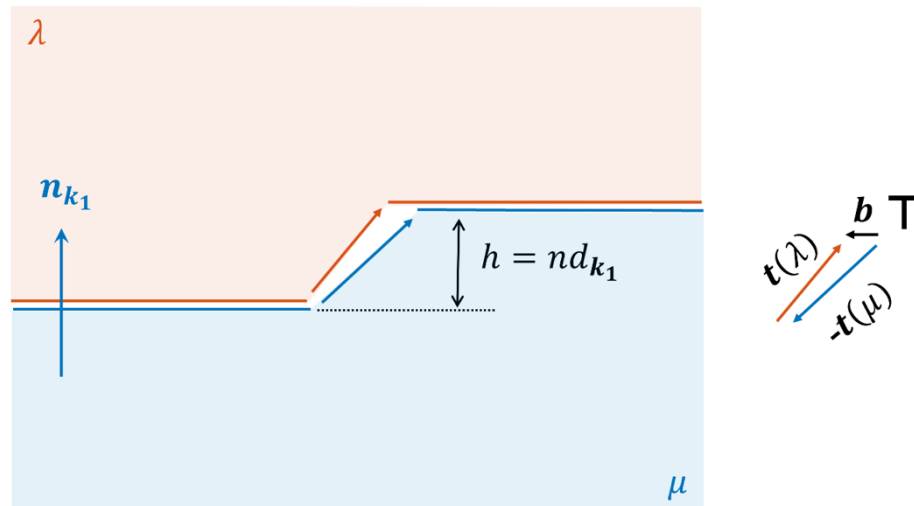


Figure 2.2 Schematic illustration of a disconnection in compound and type I twins, with $\mathbf{K}_1 = \mathbf{k}_1$ in both cases

In contrast, our knowledge of the formation and growth of type II twins is less developed. Until recently, the defect structure, formation, and growth mechanism of disconnections were unknown due to the irrational invariant plane, $\mathbf{K}_1 = \mathbf{k}_2$. In 2018, Pond

and Hirth [44, 45] presented the TM of the formation of type II twins, where the twinning shear, s , is obtained by a dual process of shear strain and rotational distortion. Based on the model, the nucleation of disconnections still occurs in the rational conjugate plane, \mathbf{k}_1 , like type I twins. However, if the leading disconnections begin to accumulate on the plane perpendicular to \mathbf{k}_1 , they would gradually form a planar boundary in which the step character of the component defects is lost. Each defect in the array undergoes accommodation relaxation to create a symmetric tilt boundary. The tilt boundary is symmetrical because of the partitioning of shear and rotation across the TB, but it must be understood in an averaged sense; the dislocation arrays can kink to lie along with the low-energy rational Peierls potential to show an overall mixed character. As the configuration relaxes, the strain field parallel to the final interface vanishes at a long range. At the same time, the rotation field, which sums to produce a rotation of 2α about \mathbf{n}_s , partitions symmetrically between the adjacent crystals. At equilibrium, the interface plane rotates relative to the fixed matrix crystal by α about \mathbf{n}_s and hence becomes parallel to \mathbf{k}_2 , i.e., the type II conjugate forms with interface $\mathbf{K}_1 = \mathbf{k}_2$, as shown in Figure 2.3.

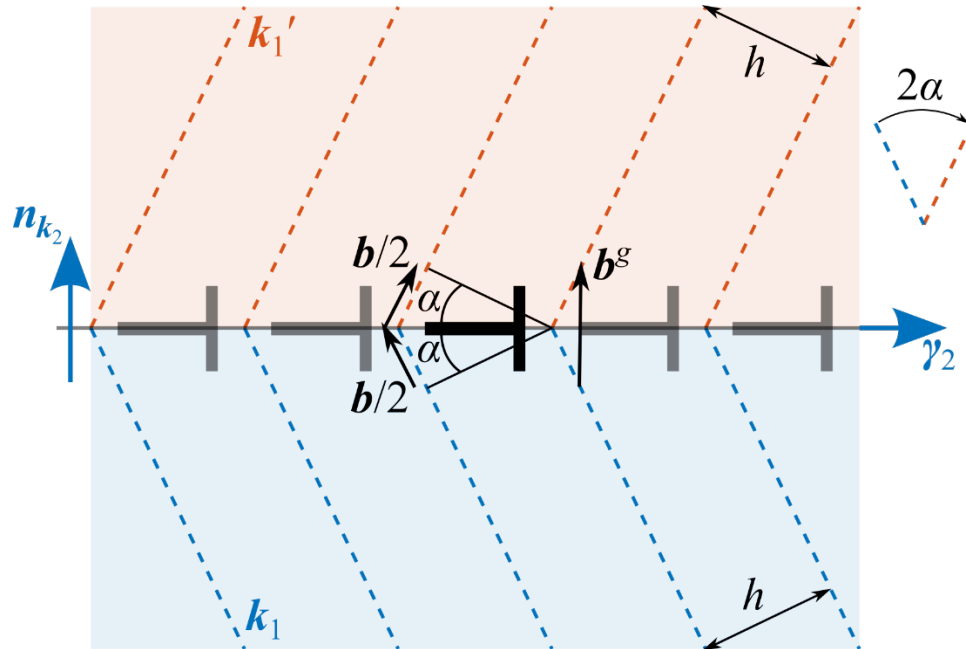


Figure 2.3 Schematic illustration of type II twin interface formed after the partitioning of displacement and rotational field of the tilt-wall. Tilt-wall forms when disconnections in the k_1 plane accumulate in a planar boundary and lose their step character.

Since the disconnection glide plane remains k_1 for type II twins, $|b|/h$ still defines the twinning shear, s , as predicted by the CM. However, based on the mechanical differences, a type II twin can be interpreted as the sum of a shear tensor of magnitude $s/2$ and a tensor rotation $\omega = \tan^{-1}\alpha$, where $\alpha = \tan^{-1}(|b|/2h)$. The overall superimposed result is a boundary with a misorientation of $n_s/2\alpha$ or equivalently $\gamma_2/2\pi$ across the boundary. Pond and Hirth showed that the TM of formation of type II twins in Ni-Ti and α -Uranium is consistent with experimental observations [44, 45].

2.5 Kinetics of Twin Boundary Motion

The mobility of TBs plays a vital role in the functionality of shape memory alloys. Knowledge of the interrelationship between TB mobility and fundamental material properties allows systematic reproduction of the shape memory effect and

engineering new materials with specific mobility. Faran and Shilo [24, 25, 27, 28] developed a microstructure-based kinetic model that can be applied to different materials systems to understand the relationship between fundamental materials properties and TB mobility. The kinetic relation serves as an input to model the dynamic evolution of TBs in a system and measure the overall state of a sample possessing many TBs.

In the kinetic model, we study the discrete TB dynamics, i.e., we measure the velocity of a single TB, v_{TB} , as a function of a thermodynamic driving force, g , i.e., $v_{TB}(g)$. The driving force represents the change in free energy as the twin grows at the parent's expense. Specifically, the driving force is the rate of change of TB energy per unit area, U_{TB} , with respect to the normal propagation direction, z :

$$g = - \frac{\partial}{\partial z}(U_{TB}) \quad (8)$$

U_{TB} includes several contributions, like mechanical, electric, thermal, and magnetic energies. Under mechanical loading, however, U_{TB} only has a mechanical contribution and is given by $U_{TB}^{mech} = - z \sigma \varepsilon_s$, where z is the normal propagation distance, σ is the applied stress, and ε_s is the twinning strain.

Deformation twinning starts with the nucleation of TDs in the glide plane of the parent lattice; the twin nucleus form lens-shaped lamellae to minimize the interfacial energy, as shown in Figure 2.4 (a). Under sustained external load, the twin nucleus grows forward, i.e., the twin tip moves, as shown in Figure 2.4 (b). The forward growth occurs at high velocities on the order of the material shear wave speed [59]. Once the tip of the twin reaches the physical boundary, the twin domain grows sideways, perpendicular to the TB, as shown in Figure 2.4 (c). The sideways growth of the twin is often the rate-limiting process, and thus it determines the rate of boundary propagation.

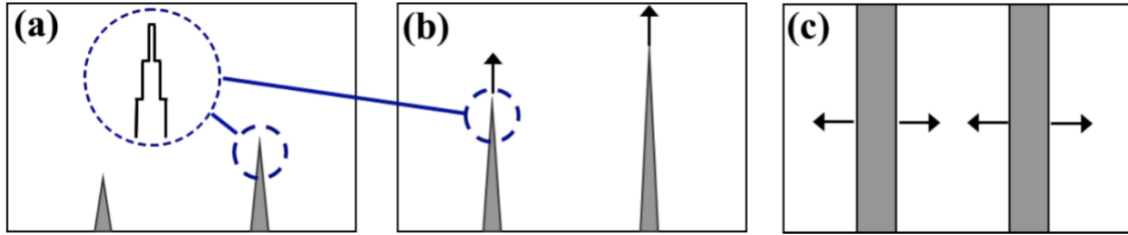


Figure 2.4 Twinning process showing (a) nucleation, (b) forward growth, and (c) sideways thickening of the twin variant. Figure reprinted from *Experimental Techniques*, 40 (2016), Faran and Shilo, *Ferromagnetic shape memory alloys—challenges, applications, and experimental characterization*, 1005-1031, with permission from Springer Nature.

Experimental studies of the TB kinetic relation for sideways growth of TBs, as in Figure 2.4 (c), are scarce. Nonetheless, Faran and Shilo [24] designed an experiment to directly measure the TB velocity as a function of a magnetically induced driving force in NMG alloy. The researchers performed a kinetic experiment on a sample containing only a single TB. They placed the sample in a magnetic driver that produced a short (μs) pulse (up to 2.5 T). For an applied magnetic driving force, the average TB velocity was measured optically by tracking the position of the TB before and after the test. By repeated testing and capturing TB velocities ranging three orders in magnitude, the researchers were able to capture the full kinetic relation, as seen in Figure 2.5.

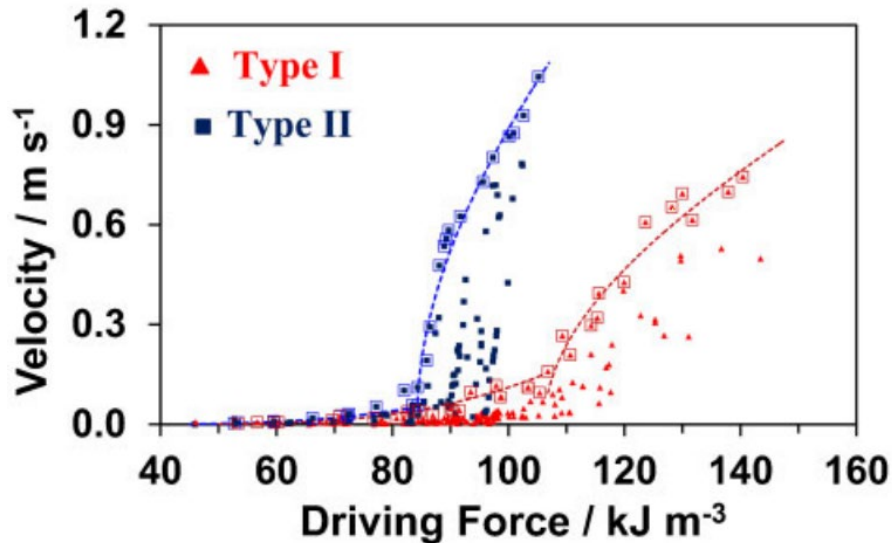


Figure 2.5 Experimental result of kinetic relation for type I (red) and type II (blue) twin boundaries (TBs) in NMG. The line is fitted to the boxed data points, representing the maximal velocity for a given driving force. Figure reprinted from *J. Mech. Phys. Solids*, 61 (2013), Faran and Shilo, The kinetic relation for twin wall motion in Ni-Mn-Ga—part 2, 726-741, with permission from Elsevier.

Experimental results of the kinetic relation in NMG show a transition in the data trend. The researchers proposed that the kinetic relation corresponds to a thermally activated process at low driving force and an athermal process at high driving force. Furthermore, they also developed an analytical kinetic model for both cases.

2.5.1 Analytical Model for Kinetics of TB Motion

Based on the experimental results for the TB relation, as shown in Figure 2.5, Faran and Shilo proposed different mechanisms for twin growth. They developed an analytical kinetic relation for both cases, i.e., thermally activated slow kinetics at small driving force and athermal fast kinetics at large driving force [24, 25, 28, 60].

Assuming the case as in Figure 2.4 (c), the TB propagates sideways if the driving force exceeds some threshold value. The change in TB interfacial energy (per unit area), as a function of the position, is represented by a periodic lattice potential. This

assumption is undoubtedly valid for compound and type I twins. The amplitude of the periodic potential is designated γ_o , and it is the activation energy per unit area required to overcome the lattice potential. If d is the lattice periodicity typical to the TB, and x is the distance the TB traveled, the change in free energy (per unit area), ΔU , for a constant driving force, g , is given by:

$$\Delta U_{TB} = -g x + \gamma_o \sin^2\left(\frac{\pi x}{d}\right) \quad (9)$$

Two different mechanisms for TB motion exist based on the sign of ΔU . The sign of ΔU depends on the value of a unitless parameter, $g \cdot d / \gamma_o$. If $g \cdot d / \gamma_o > \pi$, ΔU is a monotonically decreasing function; otherwise, positive values exist for ΔU , and thus TB motion requires thermal activation.

2.5.1.1 Athermal Kinetics

If $g \cdot d / \gamma_o > \pi$, then $\Delta U < 0$ for all values of x . So, when the driving force is higher than the critical driving force, $g_o = \gamma_o \cdot \pi / d$, the TB overcomes the two-dimensional lattice potential and moves as a flat plane with a uniform velocity. The athermal kinetics of the TB motion is modeled using the Landau-Khalatnikov equation to obtain an explicit solution for the TB velocity as [61, 62]:

$$v_{TB}(g) = \mu \sqrt{g^2 - g_o^2} \quad (10)$$

where v_{TB} is the average velocity of the TB, μ is the mobility coefficient, and g_o is the critical driving force.

2.5.1.2 Thermally Activated Kinetics

In contrast, if $g \cdot d / \gamma_o < \pi$, the TB encounters a positive Peierls barrier. As such, the TB cannot move as a flat plane (or nucleate homogeneously); its motion requires thermally activated nucleation of TDs in the glide plane of the TB. Again, similar to the

two-dimensional lattice potential for TBs, there exists a one-dimensional lattice potential for TDs. As the step edge of the TDs move, the change in TD energy (per unit length) as a function of position (parallel to the twin plane) is a periodic potential with amplitude E_p , called the Peierls energy of disconnections.

Suppose the driving force in the thermally activated regime is higher than the one-dimensional Peierls barrier. In that case, the TDs can move athermally, and the rate-limiting step is the nucleation rate of disconnections. A typical form of the kinetic relation for the current scenario, obtained using standard treatment of transformation kinetics for a two-dimensional case, is [27, 63]:

$$v_{TB}(g) = v_o \exp\left(\frac{-Q(g)}{3 k_B T}\right) \quad (11)$$

where Q is the activation energy for step nucleation, v_o is the pre-exponential term, T is the absolute temperature, and k_B is the Boltzmann constant. To formulate an explicit solution for the thermally activated process, one must identify the driving force dependency in v_o and Q . In their review of the dynamics of TB in MSMA elements, Faran and Shilo [24, 25, 28, 60] derived an explicit solution for thermally activated kinetics. For athermal kinetics of TD motion, v_o has minor dependence on g [64]. Based on the step height of the TDs and its critical nucleation size, the activation energy, Q , for the formation of a disconnection loop was derived as:

$$Q = \frac{3 \pi \Gamma^2}{2 g_o h} \left[\frac{g_o}{g} - \frac{2}{3} \left(\frac{g_o}{g} \right)^2 \right] \quad (12)$$

where Γ is the line energy of TDs, h is the step height of the TD, and g_o is the critical driving force.

The kinetic relation was established on the assumption that the nucleation of TDs is the rate-limiting process. Nonetheless, TD motion is the rate-limiting process if the

change in free energy is less than the Peierls barrier, E_p . In this case, the disconnection nucleation rate is fast enough to provide an equilibrium number of TDs. In their review, Faran and Shilo treated such a case as well, but the fit of the analytical solution to the experimental results was better when nucleation of TD was taken as the rate-limiting step.

Figure 2.6 represents a summary of the thermal and athermal TB motion. In the athermal regime, the TB overcomes the periodic potential and moves as a flat plane. In the thermally activated regime, the TB moves by the accumulated movement of TDs along the TB plane. If these TDs cannot overcome the Peierls barrier, E_p , they kink and grow along a different direction in the TB plane.

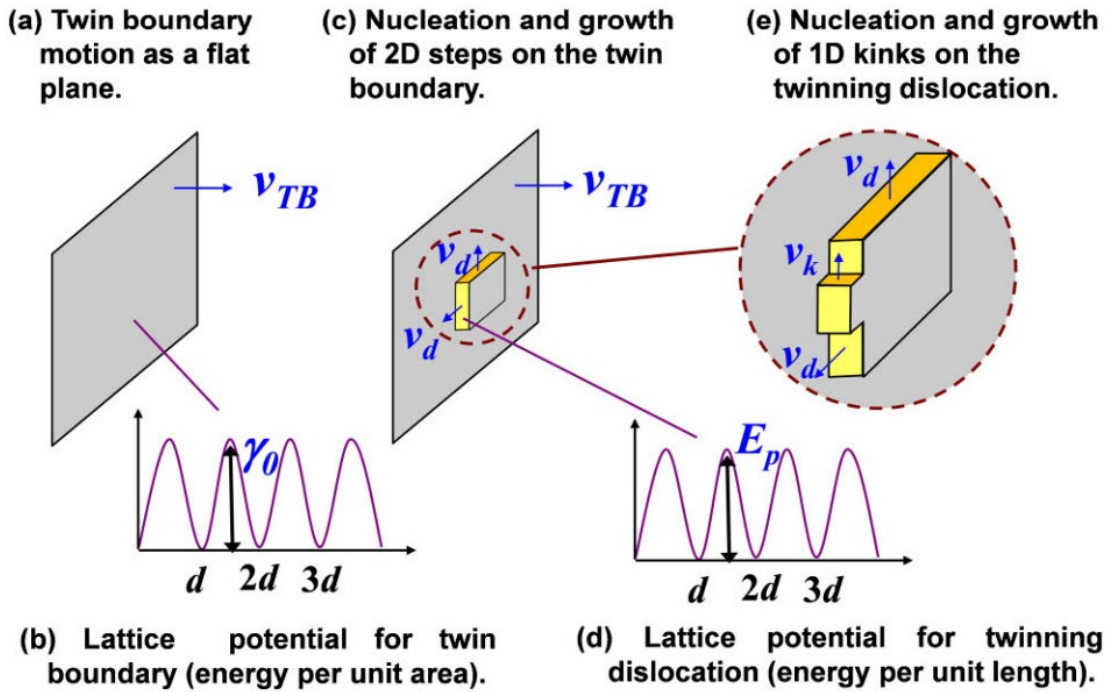


Figure 2.6 A summary of mechanisms for TB motion are presented in (a), (c), and (e). The corresponding two-dimensional and one-dimensional lattice potentials are shown in (b) and (d). v_{TB} , v_d , and v_k are velocities of the TB, twinning disconnections (TDs), and disconnection kink, respectively. Figure reprinted from Materials Science and Technology, 30 (2014), Faran and Shilo, Dynamics of twin boundaries in ferromagnetic shape memory alloys, 1545-1558, with permission from Taylor & Francis.

CHAPTER THREE: MOTIVATION AND CONTRIBUTIONS

Type II TBs are highly mobile and have significantly lower twinning stress than type I TBs [25, 26, 28]. The difference in the yield stress and kinetics of these twin modes, which are conjugate modes and carry the same overall strain, motivates this dissertation. We characterize the structure of type I and type II TBs for various shape memory alloys and discuss the impact of structural dissimilarity on energy barriers for the motion of TBs. My contributions to four journal manuscripts constitute this dissertation. Some of the results were presented at the *International Conference on Ferromagnetic Shape Memory Alloys 2019* and at the conference *Shape Memory and Elasticity 2020*.

Chapter 4 - Topological model of type II deformation twinning in 10M Ni-Mn-Ga (published October 2020 in *Acta Materialia*): We analyze the structure of type I and type II interfaces based on the TM of extended defects. My contribution to the study was establishing the defect structure of these conjugate TBs. Analysis of the structure helps understand the interface evolution mechanism and the properties materials exhibit. I performed part of this research at the University of Exeter under the supervision of Dr. Robert Pond. I wrote the manuscript as the first author.

Chapter 5 – Twin Boundary Junctions in 10M Ni-Mn-Ga (in preparation for submission to *Acta Materialia* in December 2021): We investigate the interaction of various TBs and analyze the defect structure of junctions where two or more TBs meet. We report the crystallography of NC twins in NMG and establish the equilibrium

structure of a chain of rotational defects. My contribution is in establishing the structure of defect junctions in NMG and in writing the manuscript as the first author.

Chapter 6 - *A simple method to characterize high rate twin boundary kinetics in Ni-Mn-Ga* (published October 2019 in Review of Scientific Instruments): We present a simple method to identify the transitional stress at which the TB attains high-speed kinetics in type I and type II twins. My contribution to the study is conducting the experiments, data acquisition, data evaluation, and image analysis of optical results obtained with an in-house built solenoid-based mechanical testing device. I went to Technion - Israel Institute of Technology for the experiment. I wrote the manuscript as the first author.

Chapter 7 - *Twin boundary structure and mobility* (published September 2021 for an Invited Feature Article in Acta Materialia): We evaluate energy barriers for the motion of TBs based on the interface's structure. Here we establish the kinetics of TB motion for type I and type II twins. My contribution to the project is distinguishing two possible relaxed structures of type II TBs: for example, the structures of type II TBs in NiTi vs. NMG. A coherently faceted type II TBs, for instance, in NiTi alloy, follows an athermal mechanism for the nucleation and motion of interfacial defects. The mechanism helps explain the low yield stress, low-temperature sensitivity, and high mobility of type II TBs. I wrote section 3 of the manuscript.

In Chapter 8, we discuss the contribution of each manuscript towards a consistent understanding of the unique properties of type II TBs in SMAs. We establish the structure of twin interface and defect junctions and the difference in TB evolution mechanism between type I and type II TBs. We also present a simple method to identify

the stress (driving force) at which the TB kinetics transitions from a thermally activated mechanism to athermal evolution. The structure of relaxed type II TBs enforces athermal nucleation and propagation of defects, which helps explain the low-temperature sensitivity, low yield stress, and high mobility of type II TBs.

CHAPTER FOUR: TOPOLOGICAL MODEL OF TYPE II DEFORMATION
TWINNING IN 10M NI-MN-GA

Bibek J. Karki¹,

Peter Müllner¹,

Robert C. Pond²

¹ Micron School of Materials Science and Engineering, Boise State University,
Boise, ID, 83725, USA

² College of Engineering, Mathematics, and Physical Sciences, University of
Exeter, EX4 4PY, UK

Published in Acta Materialia: B.J. Karki, P. Müllner, R.C. Pond, Topological
model of type II deformation twinning in 10M Ni-Mn-Ga, Acta Materialia 201 (2020)

604-616

Abstract

The structure of type II twins in 10M Ni-Mn-Ga is modeled using the topological method. This method predicts the same twinning parameters as the kinematic model of Bevis and Crocker. Furthermore, topological modeling provides mechanistic insight into boundary migration rates, the twinning stresses and their temperature dependence. A type II twin is envisaged to form from a precursor, which is its type I conjugate.

Disconnections on the precursor k_1 plane align into a tilt wall, which, after the relaxation of the rotational distortions, forms the type II boundary parallel on average to the k_2 plane. The component defects may align into a sharp wall or relax by kinking into a less orderly configuration. Both interfaces can host additional glissile disconnections whose motion along a boundary produces combined migration and shear. The ease of motion of these defects increases with their core width, and this, in turn, decreases with increasing sharpness of the boundary. Some experimental evidence in other materials suggests that type II twins can reduce their interfacial energy by adopting a configuration of low-index facets, which reduces twin boundary mobility. Topological modeling suggests that such a coherently faceted structure is unlikely in 10M Ni-Mn-Ga, in agreement with the high mobility of type II twin boundaries.

1. Introduction

10M Ni-Mn-Ga (hereafter NMG) is a ferromagnetic shape memory alloy which produces force and deformation in response to an applied magnetic field [1–3]. An applied field reorients martensitic variants within the material through the motion of twin boundaries (TBs), causing transformation strains of about 6% with sub-millisecond response times [4–6]. Potential applications include actuation, energy harvesting,

vibration damping, and sensing [6–11]. NMG is monoclinic and exhibits compound, type I, and type II twins [12–16]. Extensive experimental work has established that type II TBs have particularly high mobility and low twinning stress, so these twins are especially suitable for the manufacture of high-performance devices [15, 16]. Several phenomenological models have been proposed to discuss the difference in boundary mobility of type I and type II twins [17–21]. The objective of the present work is to elucidate the structure of type II TB, and hence provide some understanding of their exceptional properties.

Twinning has been studied for many decades [22–29], and a theory for predicting the associated crystallographic forms was developed by Bevis and Crocker [22]; we refer to this kinematic treatment as the Classical Model (CM). Further insight into the atomic structure of compound and type I twins was accumulated over many years because they are amenable to experimental investigations using techniques such as transmission electron microscopy (TEM) [30–33] and X-ray diffraction [13, 15, 34]. Boundary planes are rational for compound and type I twins, while the twinning direction is rational for the former but irrational for the latter. Of particular relevance to the present discussion, the mechanism of boundary migration for these twins was established to be through the motion of twinning dislocations along a boundary [35]. In a later theory of interfacial defects, called the topological theory [36], these defects were re-named “disconnections” to emphasize that they exhibit both dislocation and step character.

By comparison with compound and type I twins, much less is known about type II twins [27, 30, 37]: this is mainly because type II TB planes are irrational, which makes TEM and atomic-scale simulations problematic. However, a theoretical model for the

formation of type II twins was suggested recently [38, 39] and shown to be consistent with experimental observations in α -U and NiTi. Disconnection motion and assembly into arrays are central in this model, which we refer to as the Topological Model (TM) [36]. Thus, the principal aims of the present work are to analyze the structure of type II twins in NMG using the TM and to investigate boundary migration by disconnection motion. The relative ease with which disconnections move pertains not only to boundary migration rates but also to the magnitude and temperature dependence of twinning stress.

Section 2 is a review of the crystal structure of NMG. It is important to demonstrate that the crystallographic twinning parameters for NMG predicted by the TM are the same as those obtained by the CM. In Section 3, we apply the original CM formulation to find all possible conventional twins in NMG. The type II TB structure, according to the TM, is described in Section 4. Three alternative boundary structures are proposed, and their differing migration rates and twinning stresses are discussed in Section 5. Section 6 is a summary of our conclusions.

2. Crystallography of Ni-Mn-Ga

In our analysis, we refer to the axis systems with subscript c, 10M, and m, for the cubic austenite structure, the modulated monoclinic martensite structure, and the approximated monoclinic martensite structure, respectively.

2.1 Austenite Crystal Structure and Symmetry

Above the martensitic transformation temperature, stoichiometric Ni_2MnGa is a $L2_1$ -ordered Heusler alloy exhibiting symmetry of space group $Fm\bar{3}m$ [40]. The atomic motif is Ga at 0,0,0, Mn at 0,0.5,0, and Ni at 0.25,0.25,0.25 and 0.25,0.25,0.75 at each lattice point, as illustrated in Figure 4.1 (a). The near-stoichiometry alloy with nominal

composition $Ni_{50}Mn_{25+x}Ga_{25-x}$, with x often between 2 and 4, exhibits the modulated martensite structure with highly mobile TBs [13, 41]. In the present work, we refer specifically to the alloy $Ni_{50.2}Mn_{28.3}Ga_{21.5}$, with the lattice parameter $a_c = 0.5832$ nm and martensite transformation temperature $M_s = 323$ K [13].

2.2 Modulated Martensite Structure and Symmetry

Following a martensitic transformation, the symmetry of the alloy reduces to monoclinic (space group $I2/m$ [42]). A schematic illustration of the martensite viewed along its unique axis $[010]_{10M}$ is shown in Figure 4.1 (b), including an outline of the unit cell with lattice parameters a_{10M} , b_{10M} , c_{10M} , and β_{10M} . In this diagram, we see the modulated structure of the crystal, designated $10M$, where these modulations have formed by a simple shear along $\{220\}_c$ planes of the parent FCC unit cell. The repeating sequence of shears between adjacent planes is three leftwards followed by two rightwards, and they are characterized as $(\bar{3}2)_2$ to emphasize the ten-layer sequence. An electron diffraction pattern obtained with the beam direction $[010]_{10M}$ (i.e., parallel to the $\{220\}_c$ planes, Figure 4.1 (c)) exhibits fundamental and superlattice reflections. Atomic positions in the actual martensite structure may not correspond exactly to the configuration in Figure 4.1 (b), and alternative atomic displacements parallel to these $\{220\}_c$ are discussed elsewhere [12, 43, 44].

2.3 Approximated Monoclinic Structure and Symmetry

To assist the crystallographic analysis of twinning in NMG, we adopt the suggestions of Sozinov et al. [13, 15] whereby a non-conventional monoclinic unit cell is established by suppressing the modulation evident in Figure 4.1 (c) and considering only the fundamental reflections. This unit cell is derived from the cubic form in Figure 4.1 (a)

by a monoclinic distortion with lattice parameters a_m , b_m , c_m and γ_m . The systematic offsets of $\{220\}_c$ planes in the modulated martensite are averaged in this visualization: the 10M sequence now is $(1)_{10}$ rather than $(\bar{3}2)_2$.

The point symmetry of this non-conventional face-centered monoclinic unit cell is $2/m$ as illustrated in projection along its unique axis, $[001]_m$, in Figure 4.1 (d). Using X-ray diffraction, Sozinov et al. [15] determined the lattice parameters for $Ni_{50}Mn_{28.5}Ga_{21.5}$ (± 0.2 at.%) as $a_m = 0.5974$ nm, $b_m = 0.5947$ nm, $c_m = 0.5581$ nm and $\gamma_m = 90.36^\circ$. Transformation matrices interrelating planes and directions in 10M and m crystals are set out in Appendix A.

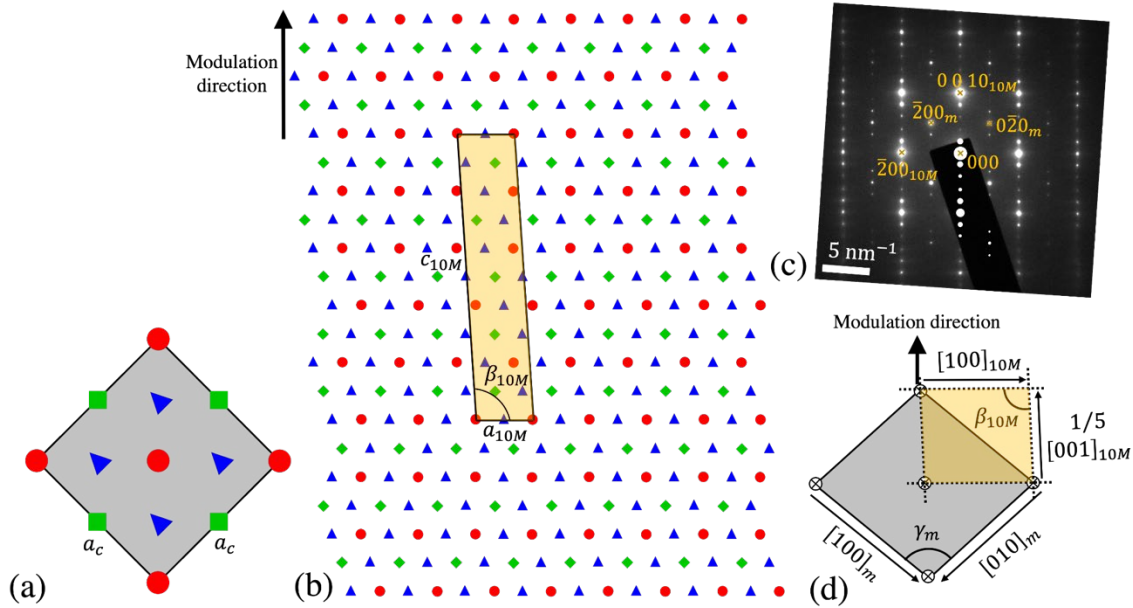


Figure 4.1 (a) Austenite crystal structure of stoichiometric Ni_2MnGa viewed along one of its axes. Red is Gallium (circle), green is Manganese (square), and blue is Nickel (triangle). (b) The crystal structure of $10M$ Ni-Mn-Ga (NMG) viewed along its unique axis $[010]_{10M}$ shows the modulated assembly; a periodic simple shear along $\{220\}_c$ planes achieve modulation during the martensitic transformation. The monoclinic angle, β_{10M} , is exaggerated in the current illustration. (c) Experimentally observed diffraction pattern of NMG that corresponds to the schematic illustration in (b): the superlattice reflections correspond to the periodic offset of the $\{220\}_c$ planes. (d) Approximated NMG crystal lattice using only the fundamental reflections in (c) and derived from the parent cubic axes through a monoclinic distortion.

3. Theories of Deformation Twinning

3.1 Classical Model

A comprehensive review of the CM of deformation twinning has been presented by Christian and Mahajan [27] and is briefly summarized here. When a medium is deformed by a volume conserving homogeneous plane strain shear, two mutually conjugate planes k_1 and k_2 , inclined by an angle 2ϕ , remain undistorted, as illustrated in Figure 4.2 (a). The plane of shear is designated P_s , and its normal is n_s . When the plane of shear is irrational, one of the undistorted planes is rational (defined as k_1), and the

other is irrational (defined as k_2) [23, 24]. If the deformed crystal is further rotated by an angle $\alpha = \pm(\pi/2-2\phi)$ about n_s , one of the conjugate planes comes into coincidence with its orientation before deformation, thereby becoming the invariant plane of twinning. If k_1 is brought into coincidence by rotation, the invariant plane is rational, as illustrated in Figure 4.2 (b); conversely, if k_2 is brought into coincidence, the invariant plane is irrational.

In both cases, the overall deformation is a simple shear. The directions parallel to k_1 and k_2 , which also lie in P_s , are designated γ_1 and γ_2 respectively. The magnitude of shear is $s = 2 \cot 2\phi$, parallel to either γ_1 or γ_2 . When the invariant plane is rational, the twins are designated type I, and the orientation relationship between the matrix and twin crystal is mirror reflection across k_1 , denoted by m' , where the prime indicates a “color-reversing” symmetry operation [45, 46]. The conjugate of a type I twin, i.e., where the invariant plane is parallel to k_2 , is called type II, and the operation interrelating the crystals is $2'$ about γ_2 . In centrosymmetric crystals such as NMG, the interrelationship for type I twins can be equivalently described as $2'$ about the vector normal to k_1 , and for type II twins as m' across the plane normal to γ_2 . A third kind of twin called compound arises when all the twinning elements – P_s , n_s , k_1 , k_2 , γ_1 and γ_2 – are rational. There is a fourth kind of twin called non-conventional where P_s and n_s are rational, but k_1 , k_2 , γ_1 and γ_2 are irrational. Such twins have been observed in composite arrangements of compound twins [47] but are not pertinent to the present study. Frank [24] suggested that an experimentally observed twinning mode be characterized by parameters K , η , as shown in Figure 4.2 (c).

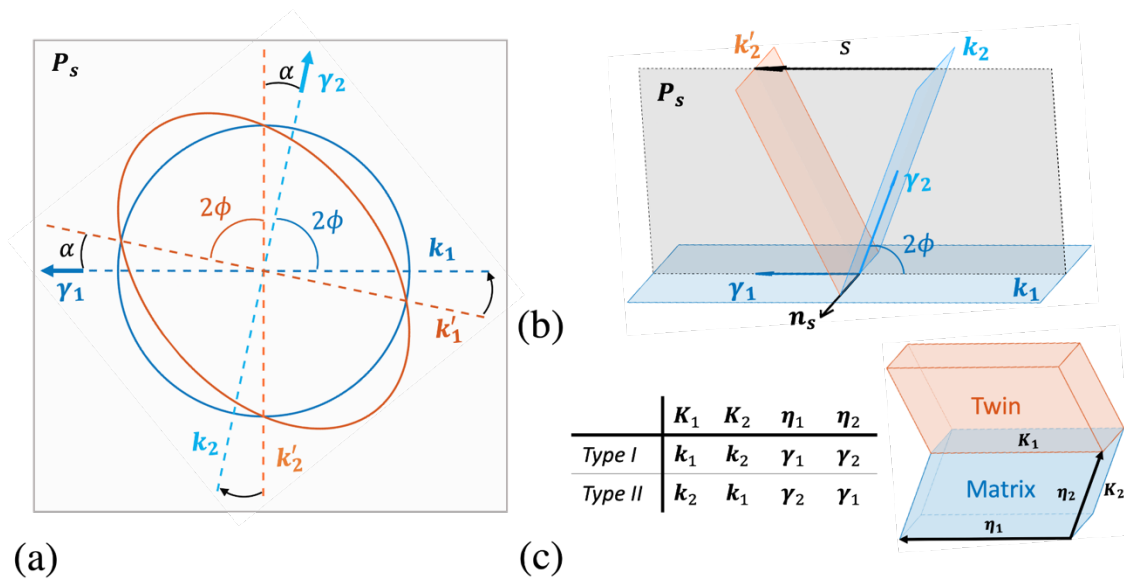


Figure 4.2 (a) A volume conserving plane-strain deformation shows two undistorted planes k_1 and k_2 that are simply rotated in the deformed medium (k_1' and k_2'). (b) The k_1 plane becomes the invariant plane of twinning when the deformed medium in (a) is further rotated by $+\alpha$ about n_s (c) An illustration of experimentally observed twinning parameters K and η : the inset table shows their relationship with twinning elements described in the text. The table also shows the conjugate relation between type I and type II twins.

The geometrical parameters and shear magnitudes for conjugate twinning modes can be predicted theoretically [22, 25–27, 29]. In the present work, we use the approach developed by Bilby and Crocker [26] and Bevis and Crocker [22, 29], where the parameters are deduced from the elements of correspondence matrices. In the present case, where the monoclinic unit cell is obtained by a small distortion of the cubic cell, correspondence matrices conform to cubic symmetry operations that are suppressed by this distortion.

3.2 Topological Model

While the CM evaluates the geometrical parameters defining a twinning mode, it fails to provide insight into the mechanism of formation and growth of twins. The study of twinning dislocations has led to a better understanding of the twinning mechanism

[27]. Pond, Hirth, and co-workers [35, 36, 45, 46] extensively studied the character of interfacial defects and presented a TM, which rigorously characterizes the dislocation and step character of twinning defects. Because of this dual topological character, twinning defects are referred to as disconnections, exhibiting both Burgers vector, \mathbf{b} , and step height, h . In the literature, there are many accounts of disconnections in compound twins [35, 48–52]. In compound and type I twins, the motion of a disconnection along the $\mathbf{K}_1 = \mathbf{k}_1$ plane produces an engineering shear, $\gamma_e = b/h$, which has the same magnitude as the classical value, s , and is parallel to the classical shear direction, $\boldsymbol{\eta}_1 = \boldsymbol{\gamma}_1$. In addition, the nucleation and growth of type I and compound twins in terms of disconnection generation and motion have been modeled consistently with experimental observations [52–54]. Figure 4.3 is a schematic illustration of type I twins nucleated at a crystal surface source and growing into the bulk during compressive loading of NMG. The Burgers vector \mathbf{b} is shown for the line sense $\boldsymbol{\zeta} \parallel \mathbf{n}_s$ pointing out of the page.

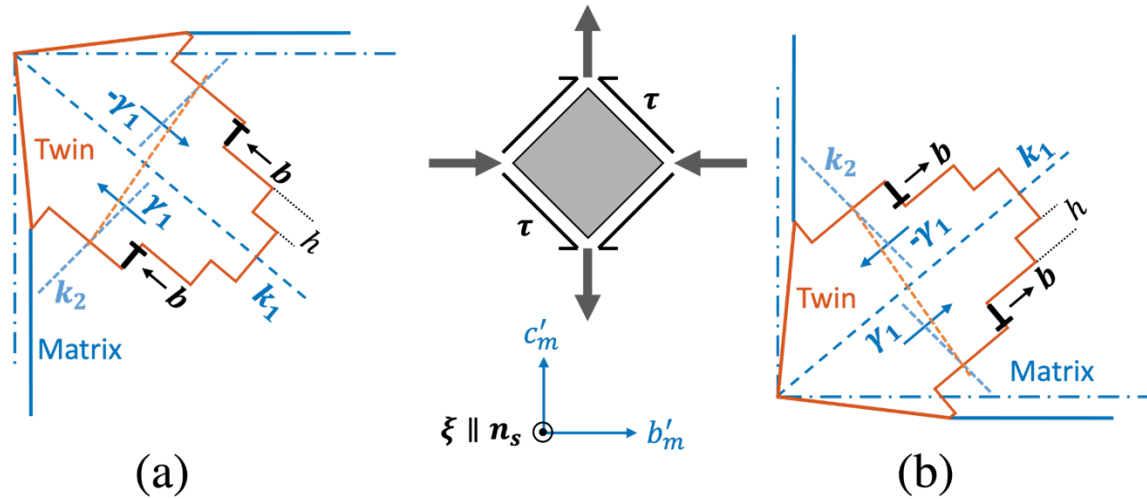


Figure 4.3 Schematic illustration of the formation and growth of (a) $(011)_m$ and (b) $(0\bar{1}1)_m$ type I twins in NMG under compressive load. The disconnections (b, h) nucleate near the corner of a parallelepiped specimen and propagate into the bulk by gliding along k_1 planes. The disconnection line sense $\xi \parallel n_s$ points out of the page.

In contrast, our knowledge of the formation and growth of type II twins is less developed. Recently, Pond and Hirth [38] presented a model in the framework of the TM that provides insight into the formation of type II twins; we apply this model to the case of NMG. Figure 4.4 is a schematic depiction of the formation of the type II twin during compressive loading of NMG. The $(q_1\bar{1}1)_m$ type II twin shown in Figure 4.4 is the conjugate of the $(011)_m$ type I twin shown in Figure 4.3 (a). Initially the disconnections (b, h) are generated at a surface source and propagate into the bulk by gliding along the k_1 planes (Figure 4.4 (a)), tending to form a lenticular twin tip. However, if the leading disconnections begin to accumulate on the plane perpendicular to k_1 , Figure 4.4 (b), they would gradually form a planar boundary in which the step character of the component defects has been lost. Each defect in this array produces a displacement field comprising both strain and rotational distortions. As the configuration relaxes, the strain field parallel to the final interface, Figure 4.4 (c), vanishes at long range. At the same time, the rotation

field, which sums to produce a rotation of 2α about \mathbf{n}_s , partitions symmetrically between the adjacent crystals: the rotation of the twin crystal is unconstrained because of the free surfaces. At equilibrium, the interface plane rotates relative to the fixed matrix crystal about \mathbf{n}_s and hence becomes parallel to \mathbf{k}_2 , i.e. the type II conjugate has formed with interface $\mathbf{K}_1 = \mathbf{k}_2$, as shown in Figure 4.4 (c).

We propose that the tip blunting of the initial type I twin occurs because of the stress-state imposed to induce twinning in single crystal specimens: for example, one method involves bending the specimen [90]. This would produce an inhomogeneous stress field: compressive in the upper region of the specimen but tensile in the lower part, as indicated schematically by the stress figures in Figure 4.4 (e). Thus, the leading disconnections would experience a diminishing driving force as they approach the neutral plane, and an opposing force thereafter. Furthermore, it is known that in a homogeneous stress field, the force necessary for an additional dislocation to join a tilt wall diminishes as the wall lengthens [55, 56]. We emphasize that specimen bending induces twin nucleation and formation of a type II twin: once the type II twin has been introduced in this manner, its dynamic properties are studied by the application of a homogeneous compressive or tensile stress to the specimen.

The defect structure of a sharp type II interface viewed along the direction $\xi \parallel \mathbf{n}_s$ is schematically illustrated in Figure 4.4 (d). The step character of individual defects is lost, and there is no residual component of \mathbf{b} along \mathbf{k}_2 . Thus, the tilt array can be envisaged as a wall of grain boundary dislocations with Burgers vector $\mathbf{b}^g = \mathbf{b} \cos\alpha$ and spacing $h/\cos\alpha$. Hence from the geometry of Figure 4.4 (d) we see that $\alpha = \tan^{-1}(b/2h)$: using the magnitudes for $|\mathbf{b}|$ and h listed in Section 4.2, we find $\alpha = 3.64^\circ$, which is the

same as the value obtained from the CM. Thus, the total misorientation across the boundary is the combination of the type I misorientation, \mathbf{n}_{k1}/π , with the supplementary tilt, $\mathbf{n}_s/2\alpha$. This combination brings the $[011]_m$ directions of the two crystals into coincidence, thereby forming the $\boldsymbol{\eta}_1 = \boldsymbol{\gamma}_2$ direction. Thus, the final misorientation can be expressed as $\boldsymbol{\gamma}_2/\pi$, or as a $\mathbf{2}'$ axis along this direction interrelating the two crystals. While the long-range strain field of the sharp interface vanishes, we presume that its core energy may be substantial because the component defects in Figure 4.4 (c) lie on adjacent \mathbf{k}_1 planes. Atomic scale simulations are required to determine such energies, but this is beyond the scope of the present work. Some authors [27, 30, 57–60] have suggested the twin interface may reconfigure into rational facets lying in the $\boldsymbol{\eta}_1 = \boldsymbol{\gamma}_2$ zone: this possibility is investigated further in Appendix C. Pond and Hirth [38] suggested another relaxation mechanism where the core energy of the defects diminishes by kinking into rational segments while retaining the average line direction, $\boldsymbol{\xi} \parallel \mathbf{n}_s$. Since the kinked defects retain the overall average line direction, they do not produce a long-range strain field; nonetheless, a strain field arises near the interface extending to a distance on the order of the kink length. Such a kinked configuration might also affect the mechanism and kinetics of interface migration in response to an applied driving force, as is explored later.

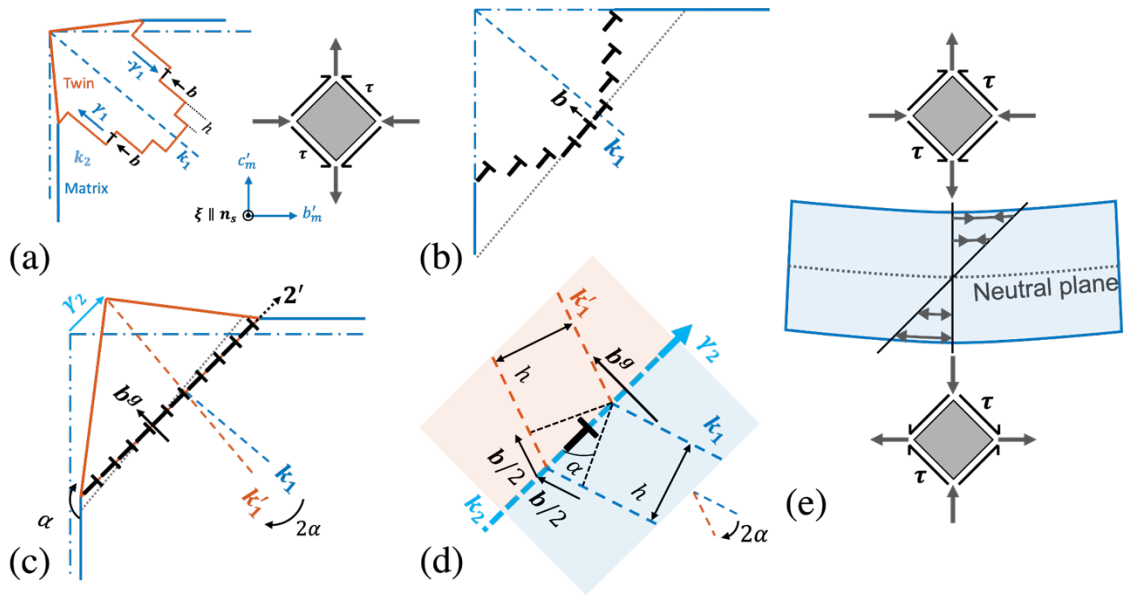


Figure 4.4 Schematic illustration of the formation of $(q_1\bar{1}1)_m$ type II twins in NMG. (a) Initially, nascent $(011)_m$ type I disconnections nucleate at the surface source in response to a local compressive stress. (b) The notional intermediate stage in an inhomogeneous stress field due to specimen bending: here the disconnections begin to accumulate and form a tilt wall perpendicular to the glide plane k_1 . (c) Finally, a $(q_1\bar{1}1)_m$ type II conjugate is formed after symmetrical partitioning of the rotational distortions across the tilt wall. (d) The exploded view of the sharp type II interface in (c), showing the character of the defects in the array: $b^g = b \cos\alpha$ is the resultant Burgers vector of each grain boundary dislocation. (e) The stress distribution in a bent parallelepiped specimen showing the stress reversal across the neutral plane, which promotes tip blunting.

When twin nucleation occurs in the bulk, it has been suggested [38] that whether the type I or the type II conjugate forms is the outcome of a competitive process. The model is consistent with experimental findings where predominantly either a type I or a type II twin forms [38, 39]. However, experimental observations of NMG [19, 61, 62] show that non-conjugate type I and type II pairs of twins are sometimes observed following surface nucleation, implying that the activation energy of both processes may be similar. In the present article, our focus is the difference in mobility between type I and type II twins.

4. Structural Models of Type II Twins in NMG

4.1 Previous Investigations

Researchers have investigated the structure of type II twins in NMG using a variety of experimental techniques. While observations using optical microscopy [13, 63], X-ray diffraction [13, 15, 64, 65], and electron diffraction [14, 16, 66] are consistent with the twinning parameters predicted by the CM, the atomic structure of type II twins is not yet established. Based on high-resolution transmission electron microscopy (HRTEM) observations, there are two opposing conjectures:

The TB is inherently irrational, and thus we find randomly curved strain contrast along the boundary in HRTEM images [31, 37, 66, 67].

The TB consists of terraces of a nearest low-index rational plane with periodic step-like features. The overall boundary is close to the predicted irrational plane [27, 30, 57–60].

Matsuda et al. [66] employed HRTEM to study various twins including the type II twinning mode in NMG with $\eta_1 = \langle \bar{5}\bar{5}1 \rangle_{10M} = \langle \bar{1}0\bar{1} \rangle_m$. Although the authors were able to simultaneously resolve lattice fringes of the adjacent crystals, the boundary was not oriented edge-on to the beam, and thus image interpretation was difficult. Moreover, no step-like line-defects were discerned.

Müllner [68] adopted the TM of type II boundaries and showed that disconnection loops can be formally defined on the irrational boundary based on the elastic properties of crystals. Moreover, using this formalism, Müllner described the difference in twinning stress and the impact of temperature on the twinning stress of type I and type II boundaries.

Knowles and Smith [69] investigated [011] type II TBs in a monoclinic NiTi using TEM, and noted that the common $(11\bar{1})$ planes are inclined at $10 \pm 2^\circ$ to $\mathbf{K}_1 = \mathbf{k}_2$. Later, using HRTEM, Knowles [30] proposed that these TBs may be composed of a combination of $(11\bar{1})$ and $(01\bar{1})$ facets. Further investigation by Liu and Xie [57, 58] using HRTEM combined with image simulation reached similar conclusions.

4.2 Crystallography of Twins in NMG

The crystallographic parameters predicted by the CM of twinning in NMG are set out in Appendix B. The point symmetry of monoclinic NMG martensite and of the cubic parent phase are $2/m$ (order 4) and $m\bar{3}m$ (order 48). Therefore, we obtain twelve monoclinic variants interrelated by the symmetry operations of the parent group, which are suppressed by the monoclinic deformation. These operations define correspondence matrices, \mathbf{C}_i , from which the twinning parameters are deduced. The predicted twinning modes are presented in Table 4.1.

Using the lattice parameters of Sozinov et al. [15], as listed in Section 2, the values of the irrational indices are $q_1 = 0.1058$, $q_2 = 0.0983$, $r_1 = 0.0924$ and $r_2 = 0.0866$.

The Burgers vector and step height, (\mathbf{b}, h) , of defects separating energetically degenerate regions of an interface (designated admissible defects) are obtained using the topological theory of interfacial defects [45, 46], which is based on the fundamental principles of symmetry breaking. It is found that the Burgers vector of admissible disconnections corresponds to differences between translation vectors in the adjacent crystals: thus, Burgers vectors, expressed in the parent coordinate frame, are given by:

$$\mathbf{b} = \mathbf{P}^{-1} \mathbf{t}(\lambda) - \mathbf{t}(\mu) \quad (1)$$

where $\mathbf{t}(\lambda)$ and $\mathbf{t}(\mu)$ are translation vectors of the upper (twin) and the lower (matrix) crystal, as in Figure 4.5, and \mathbf{P} represents the coordinate transformation from the μ to λ frame. In the present case, we take \mathbf{P} to correspond to an operation of the form $\mathbf{2}'$, as defined in Section 3: thus, for type I boundaries, $\mathbf{P}(I)$ corresponds to \mathbf{n}_{k_1}/π , and for type II, $\mathbf{P}(II)$ corresponds to γ_2/π . The Burgers vector of perfect interfacial defects are independent of the relative position of the adjacent crystals, designated \mathbf{p} in the formal theory [45, 46]. However, the magnitudes of atomic shuffles accompanying disconnection motion do depend on \mathbf{p} , as described elsewhere [52, 54]. The step height of a glissile twinning disconnection, h , is given by,

$$h = \mathbf{n} \cdot \mathbf{P}^{-1} \mathbf{t}(\lambda) = \mathbf{n} \cdot \mathbf{t}(\mu) \quad (2)$$

where \mathbf{n} represents the unit vector normal to the twin interface. For disconnections in type I boundaries, h also corresponds to an integral number of lattice plane spacings parallel to the interface, i.e., $h = n d_{k_1}$, where n is an integer, and d_{k_1} is the interplanar spacing of the \mathbf{k}_1 lattice planes, as illustrated schematically in Figure 4.5 (a).

Equations (1) and (2) are derived from fundamental principles of symmetry breaking [45, 46] so are also valid for disconnections in irrational type II boundaries. Admissible defects now separate energetically degenerate regions which are locally isomorphic. Table 4.2 lists the smallest magnitude values of (\mathbf{b}, h) for disconnections in selected examples of all three types of TBs specified in Table 4.1. The corresponding engineering shear values, γ_e , are the same as the values from the CM, and we note that the magnitudes of γ_e for disconnections in conjugate interfaces are equal. Moreover, the Burgers vectors are parallel to the relevant $\boldsymbol{\eta}_1$. The disconnection depicted in Figure 4.5 (b) exhibits the topological properties, (\mathbf{b}, h) , listed in Table 4.2, where h is understood as

the offset in a type II boundary. Motion of this glissile disconnection along a k_2 boundary would produce coupled shear and migration, manifested macroscopically as the engineering shear, γ_e . If in reality a defect is less localized, its topological properties remain unchanged overall. More complex perturbations of a type II boundary can be envisioned, and can be modeled for example in terms of disconnection dipoles [70, 71].

Table 4.1 Crystallographic parameters of twinning modes in NMG expressed in the approximated martensite framework. The shear values, s , and non-integer coefficients q and r are obtained using the lattice parameters determined by Sozinov et al. [15].

Twin type	k_1	k_2	γ_1	γ_2	s
Compound	$(110)_m$	$(\bar{1}10)_m$	$[\bar{1}10]_m$	$[110]_m$	0.0091
	$(010)_m$	$(100)_m$	$[100]_m$	$[010]_m$	0.0126
type I & type II	$(011)_m$	$(q_1\bar{1}1)_m$	$[r_1\bar{1}1]_m$	$[011]_m$	0.1274
	$(0\bar{1}1)_m$	$(\bar{q}_111)_m$	$[\bar{r}_111]_m$	$[0\bar{1}1]_m$	0.1274
type II	$(101)_m$	$(\bar{1}q_21)_m$	$[\bar{1}r_21]_m$	$[101]_m$	0.1365
	$(\bar{1}01)_m$	$(1\bar{q}_21)_m$	$[1\bar{r}_21]_m$	$[\bar{1}01]_m$	0.1365
$q_1 = (2 a_m b_m \cos \gamma_m) / (c_m^2 - b_m^2)$			$r_1 = (2 b_m c_m^2 \cos \gamma_m) / a_m(c_m^2 - b_m^2 \sin^2 \gamma_m)$		
$q_2 = (2 a_m b_m \cos \gamma_m) / (c_m^2 - a_m^2)$			$r_2 = (2 a_m c_m^2 \cos \gamma_m) / b_m(c_m^2 - a_m^2 \sin^2 \gamma_m)$		

Table 4.2 Topological parameters used to characterize the disconnections in compound, type I and type II interfaces. In the formulation of Burgers vectors, the twin (λ) is assumed to be above the matrix (μ), and the result is expressed in the matrix coordinate frame.

Twin type	K_1	η_1	$\mathbf{t}(\mu)$	$\mathbf{t}(\lambda)$	\mathbf{b}	$ \mathbf{b} $ (nm)	h (nm)	γ_e
Compound	$(110)_m$	$[\bar{1}10]_m$	$\frac{1}{2}[101]_m$	$\frac{1}{2}[01\bar{1}]_m$	$\begin{bmatrix} 0.0023 \\ 0.0023 \\ 0 \end{bmatrix}_m$	0.0019	0.2101	0.0091
	$(010)_m$	$[100]_m$	$\frac{1}{2}[011]_m$	$\frac{1}{2}[01\bar{1}]_m$	$\begin{bmatrix} 0.0063 \\ 0 \\ 0 \end{bmatrix}_m$	0.0037	0.2973	0.0126
type I	$(011)_m$	$[r_1\bar{1}1]_m$	$\frac{1}{2}[110]_m$	$\frac{1}{2}[\bar{1}01]_m$	$\begin{bmatrix} 0.0029 \\ 0.0317 \\ 0.0317 \end{bmatrix}_m$	0.0259	0.2035	0.1274
	$(101)_m$	$[\bar{1}r_21]_m$	$\frac{1}{2}[110]_m$	$\frac{1}{2}[0\bar{1}1]_m$	$\begin{bmatrix} 0.0340 \\ 0.0029 \\ 0.0340 \end{bmatrix}_m$	0.0278	0.2039	0.1365

Twin type	K_1	η_1	$\mathbf{t}(\mu)$	$\mathbf{t}(\lambda)$	\mathbf{b}	$ b $ (nm)	h (nm)	γ_e
type II	$(q_1\bar{1}1)_m$	$[011]_m$	$\frac{1}{2}[\bar{1}01]_m$	$\frac{1}{2}[110]_m$	$\begin{bmatrix} 0 \\ 0.0284 \\ 0.0284 \end{bmatrix}_m$	0.0231	0.1815	0.1274
type II	$(\bar{1}q_21)_m$	$[101]_m$	$\frac{1}{2}[0\bar{1}1]_m$	$\frac{1}{2}[110]_m$	$\begin{bmatrix} 0.0306 \\ 0 \\ 0.0306 \end{bmatrix}_m$	0.0250	0.1835	0.1365

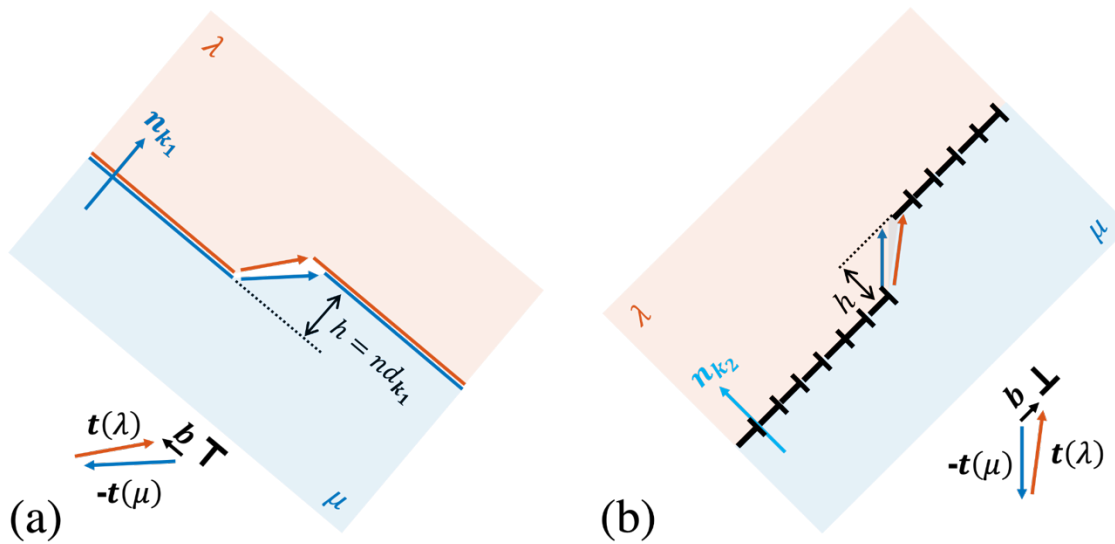


Figure 4.5 Schematic illustration of a disconnection in (a) $(011)_m$ type I twin interface, and (b) $(q_1\bar{1}1)_m$ type II twin interface.

4.3 Interface Models

The sharp interface model of type II boundaries is illustrated in Figure 4.4 (d). Here, the defects have irrational line direction, $\xi \parallel \mathbf{n}_s$, and are spaced $h/\cos\alpha$ apart. In a possible relaxed structure, the disconnections in the glide plane \mathbf{k}_1 are kinked into rational segments to minimize their line energy [38] (Figure 4.6). In the present case, where $\mathbf{k}_1 = (011)_m$ and $\mathbf{k}_2 = (q_1\bar{1}1)_m$, the average line sense, $\xi \parallel [1 \ q_1/2 \ \bar{q}_1/2]_m$ can be approximated as $\approx 10[100]_m + \frac{1}{2}[01\bar{1}]_m$. These two line segments lie in the $(0\bar{1}1)_m$ and $(\bar{1}00)_m$ planes respectively, which are common to both the twin and matrix as they belong to the $\boldsymbol{\eta}_1 = [011]_m$ zone. Since the \mathbf{k}_1 planes are misaligned by 2α about \mathbf{n}_s , the $[100]_m^\mu$ and $[\bar{1}00]_m^\lambda$ directions are not parallel, and neither are $[01\bar{1}]_m^\mu$ and $[0\bar{1}1]_m^\lambda$, as illustrated in Figure 4.6 (a). In the case of ordered line segments, as illustrated in Figure 4.6 (b), where one segment is aligned with those above and below it in the array, the boundary is wider than the sharp $\mathbf{k}_2 = (q_1\bar{1}1)_m$ form because $[100]_m^\mu$ is inclined by 4.13° to \mathbf{n}_s . The kinked

configuration does not exhibit a long-range displacement field, although short-range stresses arise. One can imagine less ordered defect configurations where the component line segments are of different lengths and not completely aligned in the array, as shown in Figure 4.6 (c). Also, in this situation, no long-range displacement field arises, but short-range stresses appear depending on the degree of disorder. We refer to such relaxed structures as ragged type II boundaries (Figure 4.6) in contrast to the sharp interface depicted in Figure 4.4 (c) and (d).

All planes in the η_1 zone are common to the parent and twin crystals: thus, a diffraction pattern taken with the beam along η_1 resembles one of a single crystal [31, 37, 66, 69]. However, these common planes are rationally commensurate only in the η_1 direction [27]: an example is illustrated in Figure 4.7 (a) for the common $(0\bar{1}1)_m$ planes. An engineering coherency shear strain of magnitude 0.0092 parallel to η_1 would bring $[100]^\mu_m$ and $[\bar{1}00]^\lambda_m$ into parallelism, thereby creating fully coherent $(0\bar{1}1)_m$ planes, as seen in Figure 4.7 (b). These planes are inclined by only 4.12° to the k_2 planes and may exhibit relatively modest interfacial energy. The coherency strain produces a long-range displacement field unless an interfacial defect array compensates this field. We refer to such an interface structure as being a (misfit-relieved) coherent (low-index) approximant. The immediate vicinity of such a faceted boundary resembles a compound twin with a coherent rational interface and a rational twinning direction. In the published HRTEM images of type II boundaries in NMG [66], step-like defects were not discernible due to the local strain field, so direct experimental observation of the approximant structure is not available. In Appendix C, we show that in NMG the coherency strain can be accommodated by an array of admissible screw disconnections with $\mathbf{b} \parallel [0\bar{1}\bar{1}]_m$. However,

the sign of the steps associated with these disconnections causes the average orientation of the faceted configuration to rotate away from k_2 rather than towards it.

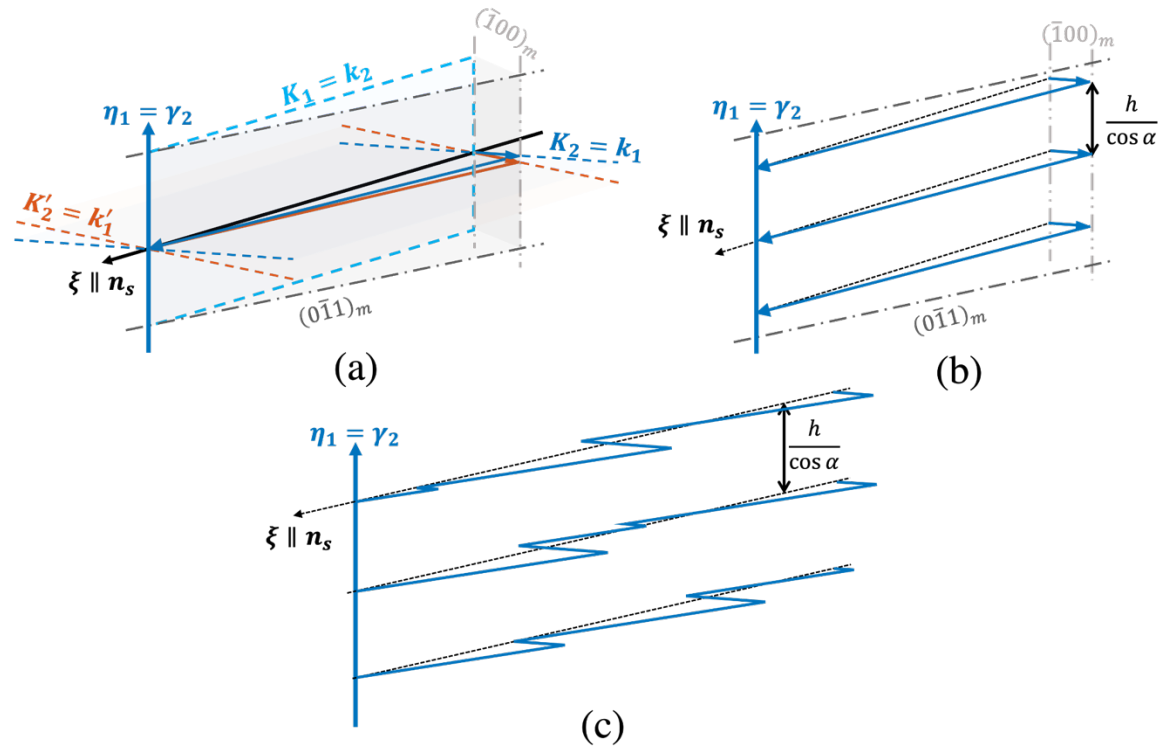


Figure 4.6 (a) Schematic illustration of defect kinking along low energy Peierls valleys in a $(q_1\bar{1}1)_m$ type II twin. Here, $\xi \parallel n_s = [1 \ q_1/2 \ \bar{q}_1/2]_m \approx 10[100]_m + \frac{1}{2}[0\bar{1}\bar{1}]_m$. (b) An orderly array of aligned kinked defects. (c) A disorderly array of non-aligned kinked defects.

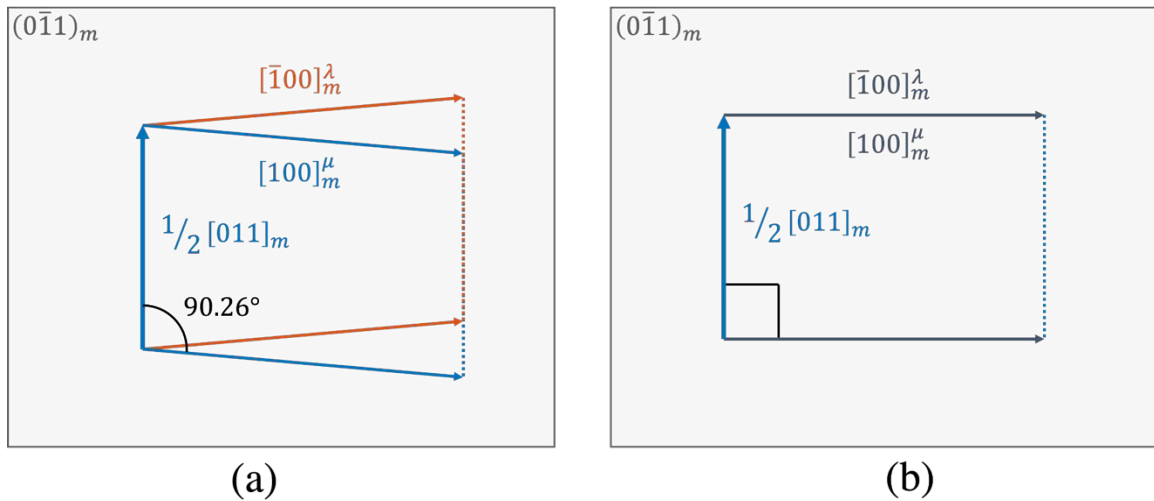


Figure 4.7 Schematic illustration of the common $(0\bar{1}1)_m$ planes (a) before and (b) after they are sheared into 2-D coherency. In (a), the angle between $[100]_m^\mu$ and $[100]_m^\lambda$ (in reality only 0.52°) is exaggerated. The partitioning of coherency strain between the μ and λ crystals results in $[100]_m$ and $[011]_m$ becoming orthogonal.

5. Discussion

5.1 Properties of Type I and Type II Twins

Experimental observations indicate that the physical properties of type I and type II twins differ, notably in NMG [3, 61, 65, 72]. Earlier works have developed phenomenological descriptions of the observed kinetic behavior of twins: for example, Faran and Shilo [73] found experimentally that the behavior is bimodal, and formulated an expression relating the velocity of a propagating boundary to the thermodynamic driving force. At driving forces below a threshold value, g_o , they propose that motion is governed by thermally activated motion of disconnections, and invoke a mobility coefficient. Above g_o , disconnection motion is modeled as athermal. In later experiments by Saren and colleagues [74, 75], bimodal kinetic behavior was not observed, and the authors pointed out the importance of avoiding any mechanical constraints in the experimental apparatus, and also taking the inertia of the growing twin into account when

modeling. On this basis, they derived a differential equation relating velocity to magnetic driving force, while incorporating the material's density and specimen geometry.

Here, building on these empirical studies, we outline aspects of disconnection motion in type I and type II twins which are relevant to the development of a mechanistic understanding of boundary kinetics. In particular, we consider the twinning stress for type I and type II twins and their dependence on temperature, $\sigma_I'(T)$ and $\sigma_{II}'(T)$, respectively. Twinning stress is the stress required to sustain TB motion [76]. In the case of type I TBs, the basic mechanism of twinning is the motion of glissile disconnections along low-energy, sharp interfaces [52–54]. Here, we explore the possibility that a similar mechanism operates for type II twins, considering that a twin interface may be (a) a relatively high-energy, sharp interface, (b) a disordered arrangement of kinked disconnections, or (c) a coherently faceted interface. Extrinsic microstructural features such as magnetic domain interactions [77] and junctions between compatible twins influence disconnection motion [34, 78]. For simplicity, we neglect such extrinsic effects here, and consider only effects on the disconnection mobility intrinsic to the interface structure.

The two primary features governing TB mobility are the nucleation rate, \dot{N} , of glissile disconnections at a given applied stress and the twin growth rate, \dot{G} , perpendicular to the boundary. For homogenous nucleation of disconnection loops, the activation energy at a fixed stress is approximately proportional to the magnitude of $|\mathbf{b}|^2$. As such, thermal activation contributes significantly to \dot{N} at modest stresses because of the small magnitude of Burgers vectors of twinning disconnections [79]. \dot{G} is expected to be dominated by the disconnection mobility. The Peierls stress necessary to move a

straight edge dislocation has the form $\tau_p = 2G_m/(1-\nu) \exp(-2\pi w/b)$, where G_m is the shear modulus, ν is the Poisson's ratio, and w is the defect core width. Thus, wide core width and small magnitude of Burgers vector lead to mobile defects. Attendant shuffling reduces the disconnection mobility [27]: shuffling is defined here as any additional atomic displacements necessary to restore perfect twin crystal structure beyond the displacement of each atom by \mathbf{b} when a disconnection moves along the boundary [54]. Since small step height, h , is thought to promote both wide cores and simple shuffles [27, 80], it is used here as a guide to mobility.

To illustrate the comparison of type I and type II twins in NMG, we choose a non-conjugate pair of incompatible twins which has been observed in several experimental investigations [19, 61, 62]. The \mathbf{K}_1 planes of these two twins, $(0\bar{1}1)_m$ and $(q_1\bar{1}1)_m$, have very similar orientations, as depicted schematically in Figure 4.8: thus their traces on a $(100)_m$ surface differ by only about 6° [19, 61, 62]. Inspection of Table 4.1 and Figure 4.3 shows that a $(0\bar{1}1)_m$ twin is related to the conjugate of the $(q_1\bar{1}1)_m$ twin, i.e. the $(011)_m$ twin, by the $(001)_m$ crystal mirror plane. The early stage of growth of the $(0\bar{1}1)_m$ twin is depicted schematically in Figure 4.3 (b), and formation of the $(q_1\bar{1}1)_m$ twin from its $(011)_m$ precursor is shown in Figure 4.4. As the twin grows, the area of the TB increases until the twin transects the entire specimen: we refer to this position, where the area of TB has reached maximum, as the reference location, as shown in Figure 4.8 for type I (a) and type II (b) twins.

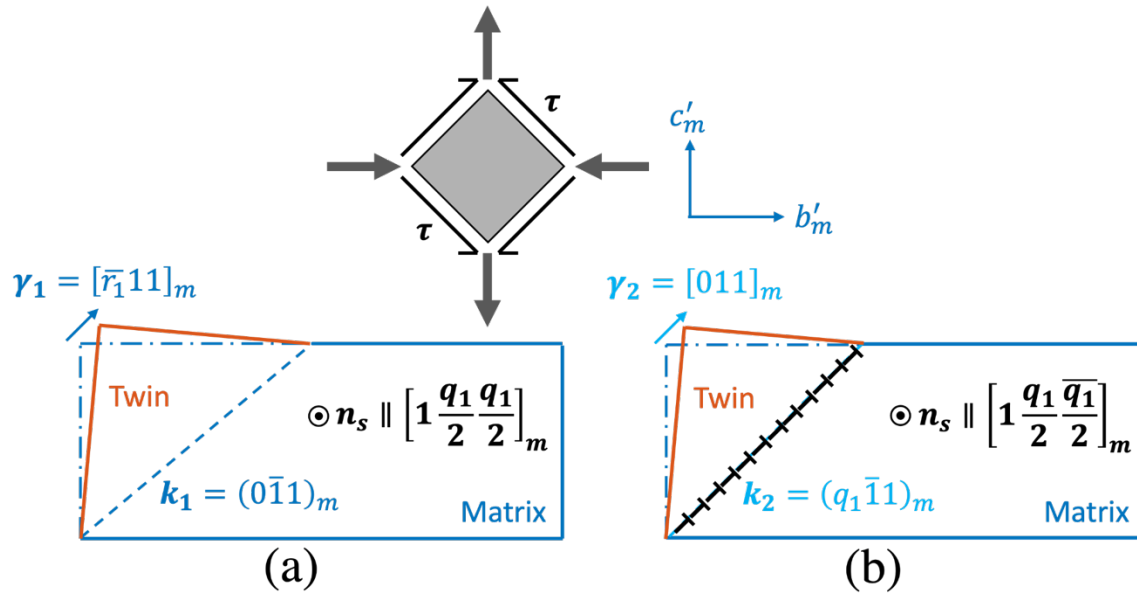


Figure 4.8 Schematic illustration of (a) $(0\bar{1}1)_m$ type I twin boundary (TB) and (b) $(q_1\bar{1}1)_m$ type II TB in the reference location. The k_1, γ_1 in (a) and k_2, γ_2 in (b) are not a conjugate pair.

5.2 Mobility of Type I Twins

In a $(0\bar{1}1)_m$ type I twin, glissile disconnections with smallest magnitude Burgers vector have $|\mathbf{b}|=0.0259$ nm with a corresponding high \dot{N} at ambient temperature. At equilibrium, the type I TB at the reference location is flat with no disconnections present: it is anticipated that the interface structure is sharp and of relatively low energy. In response to a driving force, nucleation and propagation of disconnections along the rational TB produce the engineering shear $\gamma_e = |\mathbf{b}|/h = 0.1274$, where $h = d_{(0\bar{2}2)_m} = 0.2035$ nm. Since \mathbf{b} is parallel to $\boldsymbol{\eta}_1 = [\bar{r}_1 11]_m$, these defects have pure edge character if their line direction, $\boldsymbol{\xi}$, is parallel to $\mathbf{n}_s = [1 \ q_1/2 \ q_1/2]_m$. Since the line direction is irrational, these defects may lie predominantly along $[100]_m$ Peierls valleys for minimum energy, with kinks spaced approximately every $10a_m$, as discussed in Section 4.3. The core width, w , is best investigated using computer simulations, but limited results have been published for

defects in NMG. Nonetheless, simulations of disconnections for compound twins in hcp metals indicate that the cores of disconnections with small h can be relatively wide [81–83].

The disconnection motion described above is conservative, i.e. no climb is involved, because \mathbf{b} is parallel to the $(0\bar{1}1)_m$ twin plane. Moreover, shuffling accompanying the defect motion is expected to be small: in austenitic NMG, all four atoms in the basis lie in the $(0\bar{1}1)_c$ plane, and since the martensite is a slight monoclinic distortion of the cubic phase, all four atoms in the basis are expected to remain close to the $(0\bar{1}1)_m$ plane. Thus, all atoms are displaced by \mathbf{b} as a disconnection sweeps along the boundary, and minimal additional shuffles are anticipated.

Taking all the factors mentioned above into account, we anticipate relatively easy motion of disconnections in type I twins because \dot{N} and \dot{G} are significant. For modest driving forces, kink motion along the disconnections, rather than rigid disconnection motion, may be the elemental mechanism of twin growth: quantitative assessment of the energy barrier opposing the motion is beyond the scope of the paper. Furthermore, we surmise that TB mobility is temperature dependent because the activation energy for disconnection motion in a periodic rational interface, either by rigid disconnection motion or kink motion, is assisted by thermal energy.

It has also been reported that the twinning stress is a function of imposed strain rate [72, 84, 85], and this has been ascribed to increased viscous drag at higher velocities. This behavior may arise in part from increased damping at higher disconnection velocities, analogous to that of dislocation velocity as a function of applied stress in single crystals [79], but additional dissipative mechanisms, such as magnetization

rotation and domain wall motion, are also likely to be active in NMG, and are not considered further here.

5.3 Mobility of Type II Twins

The formation of a $(q_1\bar{1}1)_m$ type II TB according to the TM, is depicted schematically in Figure 4.4. Disconnection half-loops with \mathbf{b} parallel to $[r_1\bar{1}1]_m$ are initially nucleated at the surface source and glide on the $(011)_m$ plane forming a nascent type I twin. However, their progress is impeded, as described in Section 3.2, so they accumulate into a wall of edge defects approximately perpendicular to $(011)_m$. The displacement field of these defects, with line direction ζ parallel to $\mathbf{n}_s = [1\ q_1/2\ \bar{q}_1/2]_m$, exhibits both strain and rotational distortion. The latter sums to a rigid body rotation equal to $2\alpha = 7.29^\circ$ between the matrix and twin. This rotational relaxation is unconstrained in the present case since the twin crystal has free surfaces.

5.3.1 Sharp $(q_1\bar{1}1)_m$ Type II Twins

Figure 4.8 (b) schematically illustrates the structure of this sharp $(q_1\bar{1}1)_m$ type II twin in the reference location when viewed along \mathbf{n}_s . Disconnections can be introduced into this boundary, as outlined in Section 4.2 and illustrated schematically in Figure 4.5 (b): those with the smallest Burgers vector and step height are formed using $\mathbf{t}(\lambda) = \frac{1}{2}[110]_m$ and $\mathbf{t}(\mu) = \frac{1}{2}[\bar{1}01]_m$ in Equations (1) and (2), and $\mathbf{P}(\text{II})$ corresponds to the $\mathbf{2}'$ axis parallel to $\boldsymbol{\eta}_1 = [011]_m$. The resulting \mathbf{b} is parallel to $\boldsymbol{\eta}_1$ with magnitude 0.0231 nm, and $h = 0.1815$ nm. The result is consistent with previous modeling in terms of an offset tilt wall [70], as illustrated schematically in Figure 4.5 (b), and $\gamma_e = 0.1274$, identical to that of the type I conjugate twin. Thus, glissile disconnections could either be nucleated as

half-loops at the surface or homogeneously on the boundary as complete loops. In either case, \dot{N} , is expected to be similar to that of type I twins at ambient temperature.

As depicted in Figure 4.4, the defects in the type II TB can be regarded either as disconnections with characteristic topological parameters (\mathbf{b}, h) or as offsets in the tilt wall [70]. In the latter visualization, type I disconnections initially glide on the $(011)_m$ planes and form tilt walls in the manner described by Read and Shockley [86]. In this configuration, the disconnections lose their step character, becoming grain boundary dislocations with residual Burgers vector, \mathbf{b}^g , perpendicular to the interface. Thus, lateral motion of type II disconnections, (\mathbf{b}, h) , can alternatively be regarded as motion of the grain boundary dislocations in the direction normal to the interface. Dynamic simulations are needed to elucidate the extent of shuffling in the present case. Nonetheless, as has been described in Section 5.2, shuffling is thought to be minimal for such motion.

Unlike type I boundaries considered previously, these type II disconnections are superimposed on a high energy TB, with only one rational direction, $\boldsymbol{\eta}_1$, in the twin plane. Therefore, deep Peierls valleys can only be envisaged lying along this direction. Thus, disconnections with line direction other than $\boldsymbol{\eta}_1$ are likely to have delocalized cores. Consequently, we expect $\sigma_{II'}(T)$ to be lower than $\sigma_I'(T)$. Moreover, if the activation energy for disconnection motion is comparable to thermal energy, $\sigma_{II'}(T)$ would be effectively temperature independent, as is observed experimentally [61, 87].

5.3.2 Ragged $(q_1\bar{1}1)_m$ Type II Twins

In this model, the type I disconnections that accumulate in the tilt wall are kinked on their rational $(011)_m$ glide planes. The line direction, $\boldsymbol{\xi} \parallel [1\ 0.0529\ \overline{0.0529}]_m$ in the sharp interface can be approximated as $\approx 10[100]_m + \frac{1}{2}[01\bar{1}]_m$. In other words, a

disconnection lies along a $[100]_m$ Peierls valley with kinks spaced about every $10a_m$, as depicted schematically in Figure 4.6. In the most orderly arrangement, the kinks on the successive $(011)_m$ planes are vertically aligned (Figure 4.6 (b)), and increasingly disordered configurations can be imagined (Figure 4.6 (c)).

As discussed in Section 5.3.1, the migration of ragged type II TBs can be regarded either in terms of type II disconnections (\mathbf{b}, h) , or forward motion of the now kinked grain boundary dislocations in offset tilt walls. One consequence of the boundary becoming less sharp is that the effective width, w , of type II disconnections increases, thereby tending to lower $\sigma_{II}(T)$ and reducing the activation barrier for defect motion.

5.3.3 Coherently Faceted Type II Twin Approximants

In Section 4.2 the concept of a (misfit-relieved) coherent (low-index) approximant to a type II twin was introduced. In this relaxation mechanism, the sharp type II TB maximizes the extent of coherent $(0\bar{1}1)_m$ interface. In the reference location, this interface structure would differ from that of the $(0\bar{1}1)_m$ type I twin discussed in Section 5.2. While the latter is flat with no disconnections present, the former is reticulated by an array of screw disconnections to accommodate the shear coherency strain. We assume that the coherency strain appears spontaneously, and that the screw disconnections with $\mathbf{b}^m \parallel [0\bar{1}\bar{1}]_m$ are nucleated at the surface sources. As shown in Appendix C, the final interface orientation of the coherent approximant TB rotates away from $(q_1\bar{1}1)_m$. Under the influence of a driving force, the disconnections in the array move synchronously perpendicular to their line direction thereby producing an engineering shear. Since the overall orientation relationship between the crystals has not changed, the smallest magnitude Burgers vector, given in Table 4.2 for the $(q_1\bar{1}1)_m$ twin, is enhanced by the

coherency strain, giving $|b^m| = 0.0233$ nm. Similarly, $h = d_{(0\bar{2}2)_m} = 0.2035$ nm, resulting in $\gamma_e = 0.1147$. If the coherency strain is assumed to be partitioned equally between the crystals, the rational vectors $[100]_m$ and $[01\bar{1}]_m$ in the $(0\bar{1}1)_m$ interface become orthogonal, thus resembling a compound twin structure near the interface. Defect motion would therefore need to be activated thermally to surmount the Peierls barriers. Consequently, we expect $\sigma_{II}'(T)$ to be higher than for the ragged structure. Further, $\sigma_{II}'(T)$ of the coherent approximant would be temperature dependent.

6. Conclusion

The objective of the present work is to elucidate the exceptional mobility of type II twins in NMG. Their structure has been investigated through the TM [38], with particular emphasis on the role of disconnections in determining the twinning stress and its temperature dependence, $\sigma_{II}'(T)$. Our principal conclusions are as follows.

A type II twin can form by surface nucleation of a precursor twin, which is its type I conjugate, as in the model of Pond and Hirth [38]. An applied stress leads to nucleation of disconnections in the precursor k_1 plane, which due to lack of mobility, accumulate and form a tilt wall; after symmetric partitioning of the rotational distortions, the boundary exhibits the crystallography of the k_2 twin predicted by the CM [22, 27]. The defects forming this wall may form (i) a “sharp” array of aligned edge dislocations, or (ii) a more “ragged” configuration by virtue of individual defects becoming kinked in their k_1 plane, and/or progressive misalignment of defects within the array, or (iii) a misfit-relieved coherently faceted interface.

Sharp type II twins can host glissile disconnections with high mobility, leading to fast interface migration. It is suggested that this arises because such disconnections have

wider cores than their counterparts in type I twins, combined with simple shuffles accompanying their motion. Ancillary consequences are that the magnitude and temperature dependence of $\sigma_{II}'(T)$ for type II twins are expected to be lower than those quantities for type I twins, $\sigma_I'(T)$. For ragged type II twins, we anticipate this trend to be more pronounced because of the increase in effective core width.

Previous authors have suggested that a type II twin may lower its interfacial energy by reconfiguring into a misfit-relieved assembly of coherent low-index facets [30, 57–60]. Here, we considered such a mechanism for $(q_1\bar{1}1)_m$ type II twins by formation of $(0\bar{1}1)_m$ facets. We assume the $(0\bar{1}1)_m$ facets spontaneously adopt a 2-D periodic structure through a coherency strain of less than 1%, and this displacement field is accommodated by an array of superimposed screw disconnections. However, according to the TM, the step sense of disconnections with the appropriate sense of Burgers vector leads to the misfit-relieved interface that rotates away from $(q_1\bar{1}1)_m$ rather than towards it, contrary to experimental observations. Thus, we find that surface nucleated $(q_1\bar{1}1)_m$ type II twins in NMG are unlikely to adopt a faceted configuration. This conclusion is consistent with the expectation that such structures would exhibit higher magnitudes of $\sigma_{II}'(T)$ and lower mobilities because the admissible disconnections would have relatively narrower cores.

Acknowledgement

This research was funded in part by the National Science Foundation through Grant No. NSF-DMR-1710640.

References

- [1] S.J. Murray, M. Marioni, S.M. Allen, R.C. O’Handley, T.A. Lograsso, 6% magnetic-field-induced strain by twin-boundary motion in ferromagnetic Ni–Mn–Ga, *Appl. Phys. Lett.* 77 (2000) 886–888. <https://doi.org/10.1063/1.1306635>.
- [2] A. Sozinov, A.A. Likhachev, K. Ullakko, Crystal structures and magnetic anisotropy properties of Ni–Mn–Ga martensitic phases with giant magnetic-field-induced strain, *IEEE Trans. Magn.* 38 (2002) 2814–2816. <https://doi.org/10.1109/tmag.2002.803567>.
- [3] D. Kellis, A. Smith, K. Ullakko, P. Müllner, Oriented single crystals of Ni–Mn–Ga with very low switching field, *J. Cryst. Growth.* 359 (2012) 64–68. <https://doi.org/10.1016/j.jcrysgro.2012.08.014>.
- [4] M.A. Marioni, R.C. O’Handley, S.M. Allen, Pulsed magnetic field-induced actuation of Ni–Mn–Ga single crystals, *Appl. Phys. Lett.* 83 (2003) 3966–3968. <https://doi.org/10.1063/1.1626021>.
- [5] I. Suorsa, E. Pagounis, K. Ullakko, Magnetic shape memory actuator performance, *J. Magn. Magn. Mater.* 272–276 (2004) 2029–2030. <https://doi.org/10.1016/j.jmmm.2003.12.1026>.
- [6] A.R. Smith, J. Tellinen, K. Ullakko, Rapid actuation and response of Ni–Mn–Ga to magnetic-field-induced stress, *Acta Mater.* 80 (2014) 373–379. <https://doi.org/10.1016/j.actamat.2014.06.054>.
- [7] S.A. Wilson, R.P.J. Jourdain, Q. Zhang, R.A. Dorey, C.R. Bowen, M. Willander, Q.U. Wahab, M. Willander, S.M. Al-Hilli, O. Nur, E. Quandt, C. Johansson, E. Pagounis, M. Kohl, J. Matovic, B. Samel, W. Van Der Wijngaart, E.W.H. Jager, D. Carlsson, Z. DjinoVIC, M. Wegener, C. Moldovan, R. Iosub, E. Abad, M. Wendlandt, C. Rusu, K. Persson, New materials for micro-scale sensors and actuators, *Mater. Sci. Eng. R Rep.* 56 (2007) 1–129. <https://doi.org/10.1016/j.mser.2007.03.001>.

- [8] P. Lindquist, T. Hobza, C. Patrick, P. Müllner, Efficiency of Energy Harvesting in Ni–Mn–Ga Shape Memory Alloys, *Shape Mem. Superelasticity*. 4 (2018) 93–101. <https://doi.org/10.1007/s40830-018-0158-z>.
- [9] S. Barker, E. Rhoads, P. Lindquist, M. Vreugdenhil, P. Müllner, Magnetic Shape Memory Micropump for Submicroliter Intracranial Drug Delivery in Rats, *J. Med. Devices*. 10 (2016) 041009. <https://doi.org/10.1115/1.4034576>.
- [10] K. Ullakko, L. Wendell, A. Smith, P. Müllner, G. Hampikian, A magnetic shape memory micropump: contact-free, and compatible with PCR and human DNA profiling, *Smart Mater. Struct.* 21 (2012) 115020. <https://doi.org/10.1088/0964-1726/21/11/115020>.
- [11] I. Aaltio, K.P. Mohanchandra, O. Heczko, M. Lahelin, Y. Ge, G.P. Carman, O. Söderberg, B. Löfgren, J. Seppälä, S.-P. Hannula, Temperature dependence of mechanical damping in Ni–Mn–Ga austenite and non-modulated martensite, *Scr. Mater.* 59 (2008) 550–553. <https://doi.org/10.1016/j.scriptamat.2008.05.005>.
- [12] J. Pons, R. Santamarta, V.A. Chernenko, E. Cesari, Structure of the layered martensitic phases of Ni–Mn–Ga alloys, *Mater. Sci. Eng. A*. 438–440 (2006) 931–934. <https://doi.org/10.1016/j.msea.2006.02.179>.
- [13] L. Straka, O. Heczko, H. Seiner, N. Lanska, J. Drahokoupil, A. Soroka, S. Fähler, H. Hänninen, A. Sozinov, Highly mobile twinned interface in 10M modulated Ni–Mn–Ga martensite: analysis beyond the tetragonal approximation of lattice, *Acta Mater.* 59 (2011) 7450–7463. <https://doi.org/10.1016/j.actamat.2011.09.020>.
- [14] R. Chulist, E. Pagounis, A. Böhm, C.-G. Oertel, W. Skrotzki, Twin boundaries in trained 10M Ni–Mn–Ga single crystals, *Scr. Mater.* 67 (2012) 364–367. <https://doi.org/10.1016/j.scriptamat.2012.05.026>.
- [15] A. Sozinov, N. Lanska, A. Soroka, L. Straka, Highly mobile type II twin boundary in Ni–Mn–Ga five-layered martensite, *Appl. Phys. Lett.* 99 (2011) 124103. <https://doi.org/10.1063/1.3640489>.

- [16] R. Chulist, L. Straka, N. Lanska, A. Soroka, A. Sozinov, W. Skrotzki, Characterization of mobile type I and type II twin boundaries in 10M modulated Ni–Mn–Ga martensite by electron backscatter diffraction, *Acta Mater.* 61 (2013) 1913–1920. <https://doi.org/10.1016/j.actamat.2012.12.012>.
- [17] R. Abeyaratne, S. Vedantam, A lattice-based model of the kinetics of twin boundary motion, *J. Mech. Phys. Solids.* 51 (2003) 1675–1700. [https://doi.org/10.1016/s0022-5096\(03\)00069-3](https://doi.org/10.1016/s0022-5096(03)00069-3).
- [18] E. Faran, D. Shilo, The kinetic relation for twin wall motion in Ni-Mn-Ga, *J. Mech. Phys. Solids.* 59 (2011) 975–987. <https://doi.org/10.1016/j.jmps.2011.02.009>.
- [19] E. Faran, D. Shilo, The kinetic relation for twin wall motion in Ni-Mn-Ga—part 2, *J. Mech. Phys. Solids.* 61 (2013) 726–741. <https://doi.org/10.1016/j.jmps.2012.11.004>.
- [20] H. Seiner, L. Straka, O. Heczko, A microstructural model of motion of macro-twin interfaces in Ni–Mn–Ga 10M martensite, *J. Mech. Phys. Solids.* 64 (2014) 198–211. <https://doi.org/10.1016/j.jmps.2013.11.004>.
- [21] J. Wang, P. Du, Theoretical study and numerical simulations on the stress-induced twin interface nucleation in single-crystalline Ni-Mn-Ga alloys, *J. Appl. Phys.* 126 (2019) 115101. <https://doi.org/10.1063/1.5115486>.
- [22] M. Bevis, A.G. Crocker, Twinning shears in lattices, *Proc. R. Soc. Lond. Ser. Math. Phys. Sci.* 304 (1968) 123–134. <https://doi.org/10.1098/rspa.1968.0077>.
- [23] R.W. Cahn, Plastic deformation of alpha-uranium; twinning and slip, *Acta Metall.* 1 (1953) 49–70. [https://doi.org/10.1016/0001-6160\(53\)90009-1](https://doi.org/10.1016/0001-6160(53)90009-1).
- [24] F.C. Frank, A note on twinning in alpha-uranium, *Acta Metall.* 1 (1953) 71–74. [https://doi.org/10.1016/0001-6160\(53\)90010-8](https://doi.org/10.1016/0001-6160(53)90010-8).
- [25] M.A. Jaswon, D.B. Dove, The crystallography of deformation twinning, *Acta Crystallogr.* 13 (1960) 232–240. <https://doi.org/10.1107/S0365110X60000534>.

- [26] B.A. Bilby, A.G. Crocker, The theory of the crystallography of deformation twinning, *Proc. R. Soc. Lond. Ser. Math. Phys. Sci.* 288 (1965) 240–255. <https://doi.org/10.1098/rspa.1965.0216>.
- [27] J.W. Christian, S. Mahajan, Deformation twinning, *Prog. Mater. Sci.* 39 (1995) 1–157.
- [28] K. Bhattacharya, Theory of Martensitic Microstructure and the Shape-Memory Effect, in: *Microstruct. Martensite*, 2004: p. 87.
- [29] M. Bevis, A.G. Crocker, Twinning modes in lattices, *Proc. R. Soc. Math. Phys. Eng. Sci.* 313 (1969) 21. <https://doi.org/10.1098/rspa.1969.0208>.
- [30] K.M. Knowles, A high-resolution electron microscope study of nickel-titanium martensite, *Philos. Mag. A.* 45 (1982) 357–370. <https://doi.org/10.1080/01418618208236176>.
- [31] M. Nishida, K. Yamauchi, I. Itai, H. Ohgi, A. Chiba, High resolution electron microscopy studies of twin boundary structures in B19' martensite in the Ti-Ni shape memory alloy, *Acta Metall. Mater.* 43 (1995) 1229–1234. [https://doi.org/10.1016/0956-7151\(94\)00328-f](https://doi.org/10.1016/0956-7151(94)00328-f).
- [32] R.C. Pond, S. Celotto, Special interfaces: military transformations, *Int. Mater. Rev.* 48 (2003) 225–245. <https://doi.org/10.1179/095066003225010245>.
- [33] P. Komninou, E. Polychroniadis, J.G. Antonopoulos, T. Karakostas, P. Delavignette, A DISLOCATION MECHANISM FOR THE GROWTH OF TWINS IN DEFORMED HCP METALS, *J. Phys. Colloq.* 51 (1990) C1-C1-219. <https://doi.org/10.1051/jphyscol:1990133>.
- [34] S. Kustov, A. Saren, A. Sozinov, V. Kaminskii, K. Ullakko, Ultrahigh damping and Young's modulus softening due to a/b twins in 10M Ni-Mn-Ga martensite, *Scr. Mater.* 178 (2020) 483–488. <https://doi.org/10.1016/j.scriptamat.2019.12.024>.
- [35] R.C. Pond, D.J. Bacon, A. Serra, A.P. Sutton, The crystallography and atomic structure of line defects in twin boundaries in hexagonal-close-packed metals, *Metall. Trans. A.* 22 (1991) 1185–1196. <https://doi.org/10.1007/BF02660650>.

- [36] J.P. Hirth, R.C. Pond, Steps, dislocations and disconnections as interface defects relating to structure and phase transformations, *Acta Mater.* 44 (1996) 4749–4763. [https://doi.org/10.1016/S1359-6454\(96\)00132-2](https://doi.org/10.1016/S1359-6454(96)00132-2).
- [37] M. Nishida, T. Hara, M. Matsuda, S. Ii, Crystallography and morphology of various interfaces in Ti–Ni, Ti–Pd and Ni–Mn–Ga shape memory alloys, *Mater. Sci. Eng. A.* 481–482 (2008) 18–27. <https://doi.org/10.1016/j.msea.2007.01.179>.
- [38] R.C. Pond, J.P. Hirth, Topological model of type II deformation twinning, *Acta Mater.* 151 (2018) 229–242. <https://doi.org/10.1016/j.actamat.2018.03.014>.
- [39] R.C. Pond, J.P. Hirth, K.M. Knowles, Topological model of type II deformation twinning in Ni–Ti martensite, *Philos. Mag.* 99 (2019) 1619–1632. <https://doi.org/10.1080/14786435.2019.1587185>.
- [40] P.J. Webster, K.R.A. Ziebeck, S.L. Town, M.S. Peak, Magnetic order and phase transformation in Ni₂MnGa, *Philos. Mag. B.* 49 (1984) 295–310. <https://doi.org/10.1080/13642817408246515>.
- [41] C. Jiang, Y. Muhammad, L. Deng, W. Wu, H. Xu, Composition dependence on the martensitic structures of the Mn-rich NiMnGa alloys, *Acta Mater.* 52 (2004) 2779–2785. <https://doi.org/10.1016/j.actamat.2004.02.024>.
- [42] G. Mogylnyy, I. Glavatskyy, N. Glavatska, O. Söderberg, Y. Ge, V.K. Lindroos, Crystal structure and twinning in martensite of Ni_{1.96}Mn_{1.18}Ga_{0.86} magnetic shape memory alloy, *Scr. Mater.* 48 (2003) 1427–1432. [https://doi.org/10.1016/S1359-6462\(03\)00108-8](https://doi.org/10.1016/S1359-6462(03)00108-8).
- [43] L. Righi, F. Albertini, L. Pareti, A. Paoluzi, G. Calestani, Commensurate and incommensurate “5M” modulated crystal structures in Ni–Mn–Ga martensitic phases, *Acta Mater.* 55 (2007) 5237–5245. <https://doi.org/10.1016/j.actamat.2007.05.040>.
- [44] J. Pons, R. Santamarta, V.A. Chernenko, E. Cesari, Long-period martensitic structures of Ni–Mn–Ga alloys studied by high-resolution transmission electron microscopy, *J. Appl. Phys.* 97 (2005) 083516. <https://doi.org/10.1063/1.1861137>.

- [45] R.C. Pond, J.P. Hirth, Defects at Surfaces and Interfaces, in: Solid State Phys., Elsevier, 1994: pp. 287–365. [https://doi.org/10.1016/S0081-1947\(08\)60641-4](https://doi.org/10.1016/S0081-1947(08)60641-4).
- [46] R.C. Pond, Line defects in interfaces, in: Dislocations Solids, Elsevier Science Publishers, Amsterdam, 1988: pp. 1–66.
- [47] H. Seiner, R. Chulist, W. Maziarz, A. Sozinov, O. Heczko, L. Straka, Non-conventional twins in five-layer modulated Ni-Mn-Ga martensite, *Scr. Mater.* 162 (2019) 497–502. <https://doi.org/10.1016/j.scriptamat.2018.12.020>.
- [48] R.C. Pond, B. Muntifering, P. Müllner, Deformation twinning in Ni₂MnGa, *Acta Mater.* 60 (2012) 3976–3984. <https://doi.org/10.1016/j.actamat.2012.03.045>.
- [49] T. Braisaz, High-resolution electron microscopy study of the (1012) twin and defects analysis in deformed polycrystalline alpha titanium, *Philos. Mag. Lett.* 74 (1996) 331–338. <https://doi.org/10.1080/095008396180056>.
- [50] T. Braisaz, P. Ruterana, G. Nouet, R.C. Pond, Investigation of {1012} twins in Zn using high-resolution electron microscopy: Interfacial defects and interactions, *Philos. Mag. A.* 75 (1997) 1075–1095. <https://doi.org/10.1080/01418619708214012>.
- [51] A. Ostapovets, J. Buršík, R. Gröger, Deformation due to migration of faceted {101⁻2} twin boundaries in magnesium and cobalt, *Philos. Mag.* 95 (2015) 4106–4117. <https://doi.org/10.1080/14786435.2015.1115134>.
- [52] H.A. Khater, A. Serra, R.C. Pond, Atomic shearing and shuffling accompanying the motion of twinning disconnections in Zirconium, *Philos. Mag.* 93 (2013) 1279–1298. <https://doi.org/10.1080/14786435.2013.769071>.
- [53] J. Wang, S.K. Yadav, J.P. Hirth, C.N. Tomé, I.J. Beyerlein, Pure-Shuffle Nucleation of Deformation Twins in Hexagonal-Close-Packed Metals, *Mater. Res. Lett.* 1 (2013) 126–132. <https://doi.org/10.1080/21663831.2013.792019>.
- [54] R.C. Pond, J.P. Hirth, A. Serra, D.J. Bacon, Atomic displacements accompanying deformation twinning: shears and shuffles, *Mater. Res. Lett.* 4 (2016) 185–190. <https://doi.org/10.1080/21663831.2016.1165298>.

- [55] P. Müllner, C. Solenthaler, The shape of a blocked deformation twin, *Philos. Mag. Lett.* 69 (1994) 171–175. <https://doi.org/10.1080/09500839408241588>.
- [56] S.V. Kamat, J.P. Hirth, P. Müllner, The effect of stress on the shape of a blocked deformation twin, *Philos. Mag. A.* 73 (1996) 669–680. <https://doi.org/10.1080/01418619608242989>.
- [57] Y. Liu, Z.L. Xie, Twinning and detwinning of $\langle 011 \rangle$ type II twin in shape memory alloy, *Acta Mater.* 51 (2003) 5529–5543. [https://doi.org/10.1016/S1359-6454\(03\)00417-8](https://doi.org/10.1016/S1359-6454(03)00417-8).
- [58] Y. Liu, Z.L. Xie, The rational nature of type II twin in Ni-Ti shape memory alloy, *J. Intell. Mater. Syst. Struct.* 17 (2006) 1083–1090. <https://doi.org/10.1177/1045389X06064887>.
- [59] H. Yan, C. Zhang, Y. Zhang, X. Wang, C. Esling, X. Zhao, L. Zuo, Crystallographic insights into Ni–Co–Mn–In metamagnetic shape memory alloys, *J. Appl. Crystallogr.* 49 (2016) 1585–1592. <https://doi.org/10.1107/S1600576716012140>.
- [60] A.S.K. Mohammed, H. Sehitoglu, Modeling the interface structure of type II twin boundary in B19' Ni-Ti from an atomistic and topological standpoint, *Acta Mater.* 183 (2020) 93–109. <https://doi.org/10.1016/j.actamat.2019.10.048>.
- [61] L. Straka, A. Soroka, H. Seiner, H. Hänninen, A. Sozinov, Temperature dependence of twinning stress of type I and type II twins in 10M modulated Ni–Mn–Ga martensite, *Scr. Mater.* 67 (2012) 25–28. <https://doi.org/10.1016/j.scriptamat.2012.03.012>.
- [62] O. Heczko, L. Straka, H. Seiner, Different microstructures of mobile twin boundaries in 10M modulated Ni–Mn–Ga martensite, *Acta Mater.* 61 (2013) 622–631. <https://doi.org/10.1016/j.actamat.2012.10.007>.
- [63] L. Straka, N. Lanska, K. Ullakko, A. Sozinov, Twin microstructure dependent mechanical response in Ni–Mn–Ga single crystals, *Appl. Phys. Lett.* 96 (2010) 131903. <https://doi.org/10.1063/1.3373608>.

- [64] Y. Ge, O. Söderberg, N. Lanska, A. Sozinov, K. Ullakko, V.K. Lindroos, Crystal structure of three Ni-Mn-Ga alloys in powder and bulk materials, *J. Phys. IV Proc.* 112 (2003) 921–924. <https://doi.org/10.1051/jp4:20031031>.
- [65] O. Heczko, Magnetic shape memory effect and highly mobile twin boundaries, *Mater. Sci. Technol.* 30 (2014) 1559–1578. <https://doi.org/10.1179/1743284714Y.0000000599>.
- [66] M. Matsuda, Y. Yasumoto, K. Hashimoto, T. Hara, M. Nishida, Transmission electron microscopy of twins in 10M martensite in Ni-Mn-Ga ferromagnetic shape memory alloy, *Mater. Trans.* 53 (2012) 902–906. <https://doi.org/10.2320/matertrans.M2012002>.
- [67] T. Onda, Y. Bando, T. Ohba, K. Otsuka, Electron Microscopy Study of Twins in Martensite in a Ti-50.0 at%Ni Alloy, *Mater. Trans. JIM.* 33 (1992) 354–359. <https://doi.org/10.2320/matertrans1989.33.354>.
- [68] P. Müllner, Twinning stress of type I and type II deformation twins, *Acta Mater.* 176 (2019) 211–219. <https://doi.org/10.1016/j.actamat.2019.07.004>.
- [69] K.M. Knowles, D.A. Smith, The crystallography of the martensitic transformation in equiatomic nickel-titanium, *Acta Metall.* 29 (1981) 101–110. [https://doi.org/10.1016/0001-6160\(81\)90091-2](https://doi.org/10.1016/0001-6160(81)90091-2).
- [70] J.P. Hirth, R.C. Pond, J. Lothe, Disconnections in tilt walls, *Acta Mater.* 54 (2006) 4237–4245. <https://doi.org/10.1016/j.actamat.2006.05.017>.
- [71] J.P. Hirth, R.C. Pond, J. Lothe, Spacing defects and disconnections in grain boundaries, *Acta Mater.* 55 (2007) 5428–5437. <https://doi.org/10.1016/j.actamat.2007.06.004>.
- [72] E. Faran, D. Shilo, Dynamics of twin boundaries in ferromagnetic shape memory alloys, *Mater. Sci. Technol.* 30 (2014) 1545–1558. <https://doi.org/10.1179/1743284714Y.0000000570>.
- [73] E. Faran, D. Shilo, Ferromagnetic shape memory alloys—challenges, applications, and experimental characterization, *Exp. Tech.* 40 (2016) 1005–1031. <https://doi.org/10.1007/s40799-016-0098-5>.

- [74] A. Saren, T. Nicholls, J. Tellinen, K. Ullakko, Direct observation of fast-moving twin boundaries in magnetic shape memory alloy Ni–Mn–Ga 5M martensite, *Scr. Mater.* 123 (2016) 9–12. <https://doi.org/10.1016/j.scriptamat.2016.04.004>.
- [75] A. Saren, K. Ullakko, Dynamic twinning stress and viscous-like damping of twin boundary motion in magnetic shape memory alloy Ni-Mn-Ga, *Scr. Mater.* 139 (2017) 126–129. <https://doi.org/10.1016/j.scriptamat.2017.06.010>.
- [76] A.A. Likhachev, K. Ullakko, Magnetic-field-controlled twin boundaries motion and giant magneto-mechanical effects in Ni–Mn–Ga shape memory alloy, *Phys. Lett. A.* 275 (2000) 142–151. [https://doi.org/10.1016/s0375-9601\(00\)00561-2](https://doi.org/10.1016/s0375-9601(00)00561-2).
- [77] M. Veligatla, C.J. Garcia-Cervera, P. Müllner, Magnetic domain-twin boundary interactions in Ni–Mn–Ga, *Acta Mater.* 193 (2020) 221–228. <https://doi.org/10.1016/j.actamat.2020.03.045>.
- [78] A. Saren, A. Sozinov, S. Kustov, K. Ullakko, Stress-induced a/b compound twins redistribution in 10M Ni-Mn-Ga martensite, *Scr. Mater.* 175 (2020) 11–15. <https://doi.org/10.1016/j.scriptamat.2019.09.001>.
- [79] P.M. Anderson, J.P. Hirth, J. Lothe, *Theory of dislocations*, Cambridge University Press, 2017.
- [80] R.C. Pond, A. Serra, D.J. Bacon, Dislocations in interfaces in the h.c.p. metals—II. Mechanisms of defect mobility under stress, *Acta Mater.* 47 (1999) 1441–1453. [https://doi.org/10.1016/s1359-6454\(99\)00017-8](https://doi.org/10.1016/s1359-6454(99)00017-8).
- [81] A. Serra, D.J. Bacon, A new model for 1012 twin growth in hcp metals, *Philos. Mag. A.* 73 (1996) 333–343. <https://doi.org/10.1080/01418619608244386>.
- [82] A. Serra, D.J. Bacon, A model for simulating the motion of line defects in twin boundaries in HCP metals, *Z. Für Met.* 95 (2004) 242–243. <https://doi.org/10.3139/146.017942>.
- [83] H.A. Khater, A. Serra, R.C. Pond, Atomic shearing and shuffling accompanying the motion of twinning disconnections in Zirconium, *Philos. Mag.* 93 (2013) 1279–1298. <https://doi.org/10.1080/14786435.2013.769071>.

- [84] N. Zreihan, E. Faran, D. Shilo, The effect of loading rate on characteristics of type II twin boundary motion in Ni-Mn-Ga, *Scr. Mater.* 144 (2018) 44–47. <https://doi.org/10.1016/j.scriptamat.2017.09.045>.
- [85] B.J. Karki, Y. Behar, I. Harel, E. Caplan, A. Sabbag, D. Shilo, P. Mullner, E. Faran, A simple method to characterize high rate twin boundary kinetics in Ni-Mn-Ga, *Rev. Sci. Instrum.* 90 (2019) 105107. <https://doi.org/10.1063/1.5109934>.
- [86] W.T. Read, W. Shockley, Dislocation Models of Crystal Grain Boundaries, *Phys. Rev.* 78 (1950) 275–289. <https://doi.org/10.1103/PhysRev.78.275>.
- [87] L. Straka, A. Sozinov, J. Drahokoupil, V. Kopecký, H. Hänninen, O. Heczko, Effect of intermartensite transformation on twinning stress in Ni-Mn-Ga 10M martensite, *J. Appl. Phys.* 114 (2013) 063504. <https://doi.org/10.1063/1.4817717>.
- [88] T. Hahn, *International Tables of Crystallography*, A, 854 p. D, Reidel Publishing Company, Dordrecht, 1983.
- [89] J.P. Hirth, R.C. Pond, R.G. Hoagland, X.-Y. Liu, J. Wang, Interface defects, reference spaces and the Frank–Bilby equation, *Prog. Mater. Sci.* 58 (2013) 749–823. <https://doi.org/10.1016/j.pmatsci.2012.10.002>.
- [90] A. Armstrong, A. Saren, Private communication.

Appendices

Appendix A: Transformation Matrices

Let α and β designate alternative unit cell representations of the same crystal.

Then reciprocal space vectors transform co-variantly and real space vectors transform contra-variantly [88]:

$$(h \ k \ l)_\alpha = (h \ k \ l)_\beta \mathbf{P}_\alpha \quad (\text{A1})$$

$$\begin{pmatrix} u \\ v \\ w \end{pmatrix}_\alpha = {}_\alpha \mathbf{P}_\beta \begin{pmatrix} u' \\ v' \\ w' \end{pmatrix}_\beta \quad (\text{A2})$$

where, ${}_\alpha \mathbf{P}_\beta = {}_\beta \mathbf{P}_\alpha^{-1}$

From the electron diffraction pattern shown in Figure 4.1 (c), we observe, $(0\ 0\ 10)_{10M} \rightarrow (\bar{2}\bar{2}0)_m$, $(\bar{2}00)_{10M} \rightarrow (\bar{2}20)_m$ and $(020)_{10M} \rightarrow (002)_m$. Thus, we calculate the transformation matrices as follows:

$${}_{10M}\mathbf{P}_m = \frac{1}{5} \begin{pmatrix} 5 & -5 & 0 \\ 0 & 0 & 5 \\ -1 & -1 & 0 \end{pmatrix} \quad (\text{A3})$$

$${}_m\mathbf{P}_{10M} = \frac{1}{2} \begin{pmatrix} 1 & 0 & -5 \\ -1 & 0 & -5 \\ 0 & 2 & 0 \end{pmatrix} \quad (\text{A4})$$

Appendix B: Bevis & Crocker Theory

A homogeneous simple shear is represented by an affine transformation as:

$$\mathbf{v} = \mathbf{S} \mathbf{u} \quad (\text{B1})$$

where \mathbf{u} and \mathbf{v} are lattice vectors of the parent and twin respectively, and \mathbf{S} is a second rank tensor defining the shear transformation. In some general coordinate system, A , the Equation B1 can be written using the Einstein summation convention as:

$${}^A v^i = {}^A S_j^i {}^A u^j \quad (\text{B2})$$

In a general coordinate system, A , ${}^A S_j^i$ has the form:

$${}^A S_j^i = \delta_j^i + s {}^A l^i {}^A m_j \quad (\text{B3})$$

where δ_j^i is the Kronecker delta, \mathbf{l} is the unit vector parallel to the shear direction, \mathbf{m} is the unit vector normal to the invariant plane and s is the twinning shear. In general, Equation B2 yields irrational components for ${}^A v$. However, \mathbf{v} is a lattice vector of the twin in a new coordinate system B , where B is related to A by some rotation or reflection, \mathbf{L} . So,

$${}^B \mathbf{v} = \mathbf{L} {}^A \mathbf{S} {}^A \mathbf{u} = \mathbf{C} {}^A \mathbf{u} \quad (\text{B4})$$

where \mathbf{C} is the unimodular correspondence matrix.

Once the correspondence matrix, \mathbf{C} , is specified, Bevis and Crocker [22] showed that we can utilize its properties to calculate s , \mathbf{l} , and \mathbf{m} . Using matrix notation, the solutions for s , \mathbf{l} , and \mathbf{m} are found as follows:

$$s^2 = \text{trace} (\mathbf{C}' \mathbf{G} \mathbf{C} \mathbf{G}^{-1}) - 3 \quad (\text{B5})$$

where, $G_{ij} = \mathbf{a}_i \cdot \mathbf{a}_j$ is the metric tensor, and \mathbf{a}_i are the basis vectors. Using, $\mathbf{Y} = \mathbf{G} - \mathbf{C}' \mathbf{G} \mathbf{C}$, we obtain three quadratic equations, defined by the equation:

$$Y_{ii} m_j^2 - 2 Y_{ij} m_i m_j + Y_{jj} m_i^2 = 0 \quad (6)$$

where $i \neq j$, and $i, j = 1, 2, 3$. Equation B6 yields two possible solutions for \mathbf{m} , which are the conjugate undistorted planes \mathbf{k}_1 and \mathbf{k}_2 . \mathbf{l} can then be obtained directly from Equation B3 or derived from \mathbf{Y}^{-1} using three quadratic equations like B6. Yet again, we obtain two solutions for \mathbf{l} , which are the conjugate shear directions γ_1 and γ_2 .

In the case of twinning, Equation B4 shows that a correspondence matrix for a conventional twin can be formulated as a $\mathbf{2}'$ operation. Thus, the complete set of correspondence matrices for conventional twins is isomorphous with the 2-fold symmetry operations which were present in the austenite, but which are suppressed by the monoclinic distortion. There are 12 such operations in the present case, but, in the light of Equation B6 which shows that there are two solutions, \mathbf{k}_1 and \mathbf{k}_2 , for each choice of \mathbf{C} , we may select just 6 of these. Furthermore, it is helpful to subdivide these 6 into the operations which leave the $(001)_m$ crystal mirror plane invariant, i.e. $\mathbf{2}'_{[100]_c}$ and $\mathbf{2}'_{[110]_c}$, because these lead to compound twins, and the others, $\mathbf{2}'_{[101]_c}$, $\mathbf{2}'_{[\bar{1}01]_c}$, $\mathbf{2}'_{[011]_c}$ and $\mathbf{2}'_{[0\bar{1}1]_c}$, which lead to type I – type II pairs. The \mathbf{C} matrix for each of these operations is listed in Table 4.B3.

Table 4.B3 Correspondence matrices formulated as 2' symmetry operations that are suppressed in the martensite phase compared to its austenite parent phase.

Compound twins		Type I and type II twins				
$2'_{[100]_c}$	$2'_{[110]_c}$	$2'_{[011]_c}$	$2'_{[0\bar{1}1]_c}$	$2'_{[101]_c}$	$2'_{[\bar{1}01]_c}$	
\mathbf{C}	$\begin{bmatrix} 1 & 0 & 0 \\ 0 & -1 & 0 \\ 0 & 0 & -1 \end{bmatrix}$	$\begin{bmatrix} 0 & 1 & 0 \\ 1 & 0 & 0 \\ 0 & 0 & -1 \end{bmatrix}$	$\begin{bmatrix} -1 & 0 & 0 \\ 0 & 0 & 1 \\ 0 & 1 & 0 \end{bmatrix}$	$\begin{bmatrix} -1 & 0 & 0 \\ 0 & 0 & -1 \\ 0 & -1 & 0 \end{bmatrix}$	$\begin{bmatrix} 0 & 0 & 1 \\ 0 & -1 & 0 \\ 1 & 0 & 0 \end{bmatrix}$	$\begin{bmatrix} 0 & 0 & -1 \\ 0 & -1 & 0 \\ -1 & 0 & 0 \end{bmatrix}$

Appendix C: Coherently Faceted Approximant to Type II Interface

It is possible that the energy of a type II TB can be reduced by the formation of coherent facets: for example, recent work by Mohammed and Sehitoglu [60] used atomic-scale simulation to investigate a faceted approximant structure in NiTi. Since the boundary plane of a type II twin is an invariant plane, there is no long-range elastic strain field. If the boundary reconfigures to become faceted, any coherency strain at these facets (or terraces) would have to be accommodated by the introduction of an array of appropriate interfacial defects. If these defects are disconnections, their step character would cause the overall interface orientation to rotate away from the facet orientation. In an ideal approximant structure, the array of misfit-removing defects would not only fully accommodate any coherency strain but also rotate the interface orientation to that of the type II twin. Here, we consider the $(q_1\bar{1}1)_m$ type II twin in NMG.

The axis/angle pair defining the orientation relationship between the two crystals in the approximant configuration is taken to be the same as that for the type II twin, i.e. $P(II) = [011]_m/\pi$, so all planes in the $[011]_m$ zone are common to both crystals. However, these planes are not coherent in 2-D, i.e. $[011]_m$ is the only coincident rational direction in these planes. We focus on the $(0\bar{1}1)_m$ plane, which is inclined by only 4.12° to $(q_1\bar{1}1)_m$.

As illustrated in Figure 4.7, this plane becomes coherent in 2-D by the imposition of a small coherency shear strain parallel to $[011]_m$. Such a coherency strain can be accommodated by a superimposed array of screw disconnections, and, since these defects have step character, the average interface plane consequently rotates away from the $(0\bar{1}1)_m$ “terrace” orientation. We investigate whether the misfit can be fully relieved in this manner, and whether the interface structure rotates to an orientation close to the $(q_1\bar{1}1)_m$ plane. Since $(0\bar{1}1)_m$ type I TBs are observed experimentally in NMG [19, 61, 62], implying that they have low interfacial energy, this stepped configuration with $(0\bar{1}1)_m$ terraces might be energetically feasible. In the coherently strained $(0\bar{1}1)_m$ terrace illustrated in Figure 4.7 (b), the $[100]_m$ and $[011]_m$ directions become orthogonal, whereas they are not so in a $(0\bar{1}1)_m$ type I interface.

We imagine the creation of a bicrystal with a 2-D coherent $(0\bar{1}1)_m$ planar interface by the application of shear tractions to the external (top and bottom) surfaces: these tractions produce homogenous strains which are equally partitioned between the two crystals. Thus, the directions $[100]_m^\mu$ and $[\bar{1}00]_m^\lambda$, which were originally inclined by 0.53° , are brought into parallelism, and become perpendicular to the common $[011]_m$ axis. The defect content of the 2-D coherent interface can be established by applying the Frank-Bilby [89] equation. We introduce a coordinate frame where the coherent $(0\bar{1}1)_m$ terrace plane has embedded interface coordinates x, y, z with $x \parallel [011]_m$ and z parallel to the interface normal. Following Hirth et al. [89], we define the matrix, D_{ij} , which quantifies the elastic distortions required to transform the “natural” bicrystal into the “sheared-coherent” form: the only non-zero element is $D_{12} = -2 \cdot \tan(0.53^\circ/2) = -0.0092$. When this matrix operates on a probe vector, \mathbf{v} , we obtain the coherency dislocation

content, \mathbf{b}^c , necessary to sustain coherency. Using $\mathbf{v} = [0, -v_y, 0]$ (for consistency with the RH/FS convention [79]), we obtain $\mathbf{b}^c = [-D_{12} v_y, 0, 0]$. Thus, \mathbf{b}^c is parallel to x , so these dislocations have RH screw character.

To compensate for the resulting displacement field, we introduce an array of equally spaced LH screw disconnections (\mathbf{b}^m, h^m) in the interface, where $\mathbf{b}^m = \mathbf{P}(II)^{-1} \mathbf{t}^c(\lambda) - \mathbf{t}^c(\mu)$, and $h^m = \mathbf{n} \cdot \mathbf{t}^c(\mu) = \mathbf{n} \cdot \mathbf{P}(II)^{-1} \mathbf{t}^c(\lambda)$: here, $\mathbf{t}^c(\mu)$ and $\mathbf{t}^c(\lambda)$ are translation vectors in the coherent dichromatic pattern (CDP), and \mathbf{n} is the unit normal to the $(0\bar{1}1)_m$ plane (i.e. the same as \mathbf{m} in Equation B6). For the smallest magnitude $|\mathbf{b}^m|$, we use $\mathbf{t}^c(\mu) = \frac{1}{2} [10\bar{1}]_m$ and $\mathbf{t}^c(\lambda) = \frac{1}{2} [\bar{1}\bar{1}0]_m$, i.e. rational vectors with opposite sense of those shown in Table 4.2 for disconnections in the $(q_1\bar{1}1)_m$ twin. These translation vectors give us $\mathbf{b}^m \parallel [0\bar{1}\bar{1}]_m$. The coherency strain enhances the magnitude of the Burgers vector by $(1 + |D_{12}|)$ compared with the value given in Table 4.2 for the type II twin, giving $|\mathbf{b}^m| = 0.0233$ nm, and the defects' step height is $h^m = d_{(0\bar{2}2)_m} = 0.2035$ nm.

This disconnection array is shown schematically in Figure 4.C9. We define a second interfacial coordinate frame x', y', z' , inclined to the terrace by angle θ . In the terrace frame, the Burgers vector can be written as $\mathbf{b}^m = [-b_x^m, 0, 0]$, and remains the same when resolved into the inclined interface frame. The distortion matrix transformed into the inclined frame has non-zero components $D_{12}' = D_{12} \cos\theta$, and $D_{13}' = -D_{12} \sin\theta$. Thus, for misfit relief on that plane, i.e. $\mathbf{B} = -\mathbf{b}^c$, and putting $v_y = L$, where L is the disconnection spacing on this plane, we have $L D_{12} \cos\theta = b_x^m$. Since $\sin\theta = h^m/L$, we have $\tan\theta = h^m D_{12}/b_x^m$, and hence $\theta = 4.59^\circ$ in the present case. The residual strain, $D_{13}' < 0.1\%$, cannot be compensated by any regular defect array in the $x'y'$ plane. Thus, for NMG, the

partially misfit-relieved faceted coherent plane would be inclined at $4.12^\circ + 4.59^\circ = 8.71^\circ$, i.e. it rotates away from the invariant $(q_1\bar{1}1)_m$ plane, as shown in Figure 4.C9.

Referring to Figure 4.C9, we can determine whether the stress indicated in Figure 4.4 would grow or diminish the twin crystal. In the present case, the applied shear causes the disconnections in the array to move leftwards thereby promoting twin growth. The resulting engineering strain would have magnitude 0.1147.

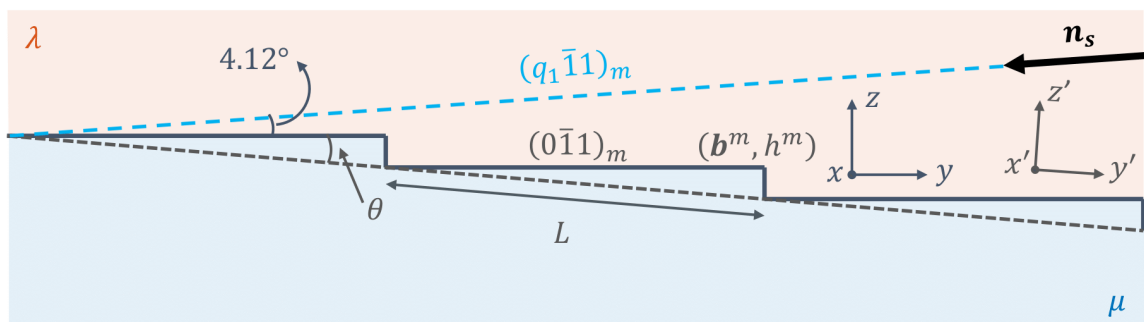


Figure 4.9 Schematic illustration of misfit accommodation at a coherently faceted approximant structure. The line direction of RH coherency dislocations, ζ^c , points out of the page, parallel to $[0\bar{1}1]_m$. The angle between $(0\bar{1}1)_m$ and $(q_1\bar{1}1)_m$ is 4.12° . The LH screw misfit disconnections have b^m anti-parallel to ζ^c and a negative sense of steps. The direction n_s is the average line direction of the twinning disconnections in the $(q_1\bar{1}1)_m$ twin plane.

CHAPTER FIVE: TWIN BOUNDARY JUNCTIONS IN 10M NI-MN-GA

Bibek J. Karki¹,

Robert C. Pond²

Peter Müllner¹

¹ Micron School of Materials Science and Engineering, Boise State University,

Boise, ID, 83725, USA

² College of Engineering, Mathematics, and Physical Sciences, University of

Exeter, EX4 4PY, UK

To be submitted to Acta Materialia

Abstract

The mobility of twin boundaries determines the performance of shape memory alloys. A martensitic transformation gives rise to a hierarchical twin microstructure with various interface and interface junction types. Using the example of the magnetic shape memory alloy Ni-Mn-Ga, this study quantifies the structure and defect contents of triple junction lines (TJLs) and quadruple junction lines (QJLs), formed by the intersection of the $(100)_m$ compound and non-conventional (NC) twin boundaries. This study implements Bevis and Crocker's kinematic model to predict the geometry of non-conventional twins and compound twins, and their arrangement at triple and quadruple junction lines. QJLs are defect-free and allow the contiguous arrangement of all four martensite variants. TJLs require rotational accommodation at the junction. Based on the three variants that TJLs accommodate, four distinct defect strengths arise. The strain energy of a chain of TJLs that fits all four variants is predicted using a disclination quadrupole approximation. The energy of the disclination quadrupole system scales as a function of the distance between defects. The strain field of the system may provide the driving force for pairwise coalescence of TJLs into QJLs at larger length scales to reduce the overall energy of the interface, in agreement with experimental findings.

1. Introduction

10M Ni-Mn-Ga (NMG) is a ferromagnetic shape memory alloy where a strain up to 6% can be induced reversibly by an external magnetic field [1–3]. The applied field induces strain via the reorientation of martensite variants. The strain rate depends on the mobility of twin boundaries (TBs), which separate the martensite variants. In NMG, TBs have low twinning stress and high mobility, attaining sub-millisecond strain response

times [4–8]. Potential device applications include actuators, sensors, energy harvesters, vibration dampeners, and micropumps [6, 9–16].

NMG is monoclinic and exhibits compound, non-conventional (NC), type I, and type II twins [17–22]. Type I and type II twins are responsible for the macroscopic 6% strain, whereas compound and NC twins help accommodate other martensite variants. Type II twins have the most suitable properties for device applications; they have extremely low twinning stress (< 0.2 MPa) and exceptionally high mobility, with TB speed reported up to 2 m/s [4, 5, 23–26]. Electron micrographs have shown that hierarchical twin microstructures appear in the vicinity of type II TBs [19]. The objective of the present work is to theoretically predict the orientation of twinned microstructure and quantify the defects that form at the junction. We evaluate the energy of these defect structures to gain insight into type II twins' exceptional properties.

Twinning is one of the primary deformation mechanisms and has been studied for decades [27–34]. Bevis and Crocker proposed a theory called the classical model of twinning to predict the operative twin modes based on the restrictive geometric properties of twinning [31, 32]. The theory predicts the existence of NC twins, but no actual examples were reported for a long time. Recent microscopy imaging revealed NC twins are present in the quadruple junction lines (QJLs) and triple junction lines (TJLs) in NMG [19]. A chain of QJLs is present in type II twins' vicinity and, based on their defect structure, may reduce, or promote the mobility of type II TBs.

In Section 2, we review the crystal structure of NMG. We outline the crystallography of NC twins and their orientation relationship (OR) in Section 3. Section 4 analyzes the orientation of TBs at QJLs and TJLs, the defect strength at each junction,

and the energetics of the interface for various junction systems. In section 5, we discuss the implication of the formation mechanism of TJLs, including NC twins, based on defect interactions and QJLs based. In section 6, we summarize our conclusion.

2. Crystallography of 10M Ni-Mn-Ga

Our analysis refers to the crystal coordinates with subscript c and m for the cubic austenite structure and the approximated monoclinic martensite structure, respectively.

In the austenite phase, stoichiometric Ni_2MnGa exhibits the space group symmetry $Fm\bar{3}m$ [35]. The basis of the face-centered cubic lattice are Ga at $0,0,0$, Mn at $0,1/2,0$, and Ni at $1/4,1/4,1/4$, and $1/4,1/4,3/4$. The 10 NMG alloys are obtained with near-stoichiometric composition $Ni_{50}Mn_{25+x}Ga_{25-x}$ (at.%), where x is between 2 and 4, and exhibit modulated martensite structure with highly mobile twin boundaries (TBs) [17, 36, 37].

Upon a martensitic transformation, the symmetry of NMG reduces to space group $I2/m$ [38]. The near-stoichiometry composition yields a modulated structure via simple shear along $\{220\}_c$ planes of the parent FCC unit cell. The shears between adjacent planes repeat in a sequence characterized as $(\bar{3}2)_2$ to underline the ten-layer series in the unit cell exhibiting the crystal's symmetry [18, 39].

We ignore the lattice modulation for the crystallographic analysis by considering a structure which gives rise to the fundamental diffraction reflections only, thus adopting an approximated monoclinic structure. A non-standard face-centered monoclinic unit cell is derived from the cubic form: The cubic lattice with parameter a_c monoclinically distorts by a small Bain strain to a lattice with parameters a_m, b_m, c_m and γ_m as shown in Figure 5.1. The point symmetry of this unit cell is $2/m$, with $[001]_m$ chosen as the unique

axis. Seiner *et al.* used X-ray diffraction to determine the lattice parameters for $Ni_{50.2}Mn_{28.3}Ga_{21.5}$ (± 0.5 at.%) as $a_m = 0.5972$ nm, $b_m = 0.5944$ nm, $c_m = 0.5584$ nm and $\gamma_m = 90.37^\circ$ [19].

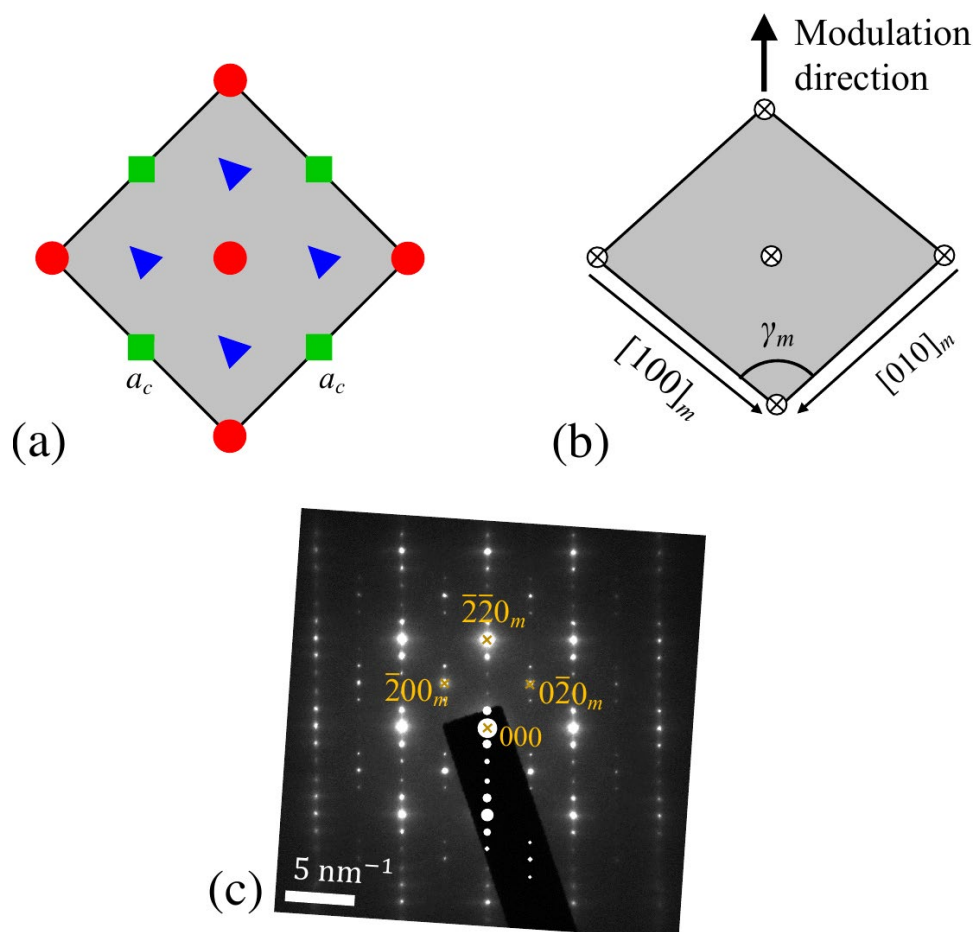


Figure 5.1 (a) Austenite crystal structure of stoichiometric Ni_2MnGa viewed along one of its axes. Circles (red), squares (green), and triangles (blue) represent Gallium, Manganese, and Nickel atoms. (b) Approximated 10M Ni-Mn-Ga (NMG) lattice viewed along its unique axis, $[001]_m$; the crystal lattice is derived from the parent cubic axes through a monoclinic distortion. (c) Electron diffraction pattern of NMG with the electron beam along $[001]_m$. The superlattice reflections correspond to the modulation event, and by only considering the fundamental reflection, we obtain the averaged unit cell (b).

3. Non-Conventional Twins

A comprehensive review of deformation twinning is presented in the works of Christian and Mahajan [33]. A complete description of deformation twinning requires four crystallographic elements: undistorted conjugate planes k_1 and k_2 , and undistorted conjugate directions γ_1 and γ_2 , collectively defined as a twin mode [27]. The overall deformation is a simple shear, s , about an invariant plane (k_1 or k_2) parallel to either γ_1 or γ_2 . The shear magnitude required to transform the matrix to the twin is given by $s = 2 \cot 2\phi$, where 2ϕ is the acute angle between k_1 and k_2 .

Based on the properties of twinning elements, deformation twinning is classified into four types: compound, type I, type II, and NC. One distinguishes the twins by identifying the invariant/habit plane and shear direction of twinning, i.e., the plane that remains unchanged during the twinning transformation and the direction in which the twin is sheared with respect to the matrix. If both the habit plane and shear direction are rational (i.e., they have integer indices), twinning is compound. If the twinning plane is rational, but the shear direction is irrational (non-integer indices), twinning is of type I. The situation is reversed for type II twinning, where the plane is irrational, but the direction is rational. Finally, both the elements are irrational in NC twinning.

The classical model of twinning predicts the twinning modes through the properties of unimodular correspondence matrices [31–33]. Correspondence matrices encode each variant's OR because they represent symmetry elements suppressed during the dissymmetrisation stages of higher symmetry precursors. The principle of symmetry compensation states that if symmetry is suppressed at one level, it manifests at another

level [40]. We explore the proposition that broken point symmetry elements, which are unimodular, are the correspondence matrices that relate the OR of twinned variants.

3.1 Crystallography

The set of proper point symmetry elements suppressed during dissymmetrisation stages of the cubic to monoclinic transition is laid out in Appendix A. The symmetry elements suppressed at each transition stage are derived by identifying the invariant subgroup of the point supergroup. In the current scenario, we only consider the tetragonal to monoclinic transition stage, allowing us to eliminate type I and type II twinning from our consideration. The proper point symmetry operations suppressed during this dissymmetrisation stages form the following unimodular correspondence matrices:

$\mathbf{2}_{[100]_c}$, $\mathbf{2}_{[010]_c}$, $\mathbf{2}_{[110]_c}$, $\mathbf{2}_{[\bar{1}10]_c}$, $\mathbf{4}_{[001]_c}^+$, $\mathbf{4}_{[\bar{0}01]_c}^-$.¹ In the current notation, the number represents n -fold symmetry, and the subscript denotes the axis of rotation. The relevant twin modes and shear magnitude are deduced from the elements of these correspondence matrices using the Bevis & Crocker method [31, 32].

Correspondence matrices appear in pairs (degenerate) and predict the same twinning mode due to its restrictive properties [31–33]. The pairs of correspondence matrices $\mathbf{2}_{[100]}$, $\mathbf{2}_{[010]}$ and $\mathbf{2}_{[110]}$, $\mathbf{2}_{[\bar{1}10]}$, predict the two compound twin modes in NMG, as shown in Ref. [22]. The remaining pair of suppressed symmetry operations, $\mathbf{4}_{[001]}^+$ and $\mathbf{4}_{[\bar{0}01]}^-$, gives rise to NC twins, and the corresponding twin mode is listed in Table 5.1. The conjugate relation between twinning elements becomes evident in NC twins: if the invariant plane is k_1 for the matrix, the same invariant plane is k_2 for the twin.

¹ We follow the notation of the International Tables for Crystallography [41].

Correspondingly γ_1 is the shear direction for the matrix, and γ_2 is the shear direction for the twin. A schematic of the NC twins predicted for NMG is shown in Figure 5.2.

Table 5.1 Crystallographic parameters of non-conventional (NC) twin mode in NMG expressed in the approximate martensite framework. The shear value, s , and the non-integer coefficients q and r are obtained using the lattice parameters as determined by Sozinov et al. [24]

k_1	k_2	γ_1	γ_2	s
$(1 \ q \ 0)_m$	$(\bar{1} \ \bar{r} \ 0)_m$	$[q \ \bar{1} \ 0]_m$	$[r \ \bar{1} \ 0]_m$	0.0159

$$q = \frac{2 a_m b_m \cos \gamma_m - \sqrt{a_m^4 + b_m^4 + 2 a_m^2 b_m^2 \cos 2\gamma_m}}{a_m^2 - b_m^2} = -3.0735$$

$$r = \frac{2 a_m b_m \cos \gamma_m + \sqrt{a_m^4 + b_m^4 + 2 a_m^2 b_m^2 \cos 2\gamma_m}}{a_m^2 - b_m^2} = 0.3254$$

$$q \cdot r = -1$$

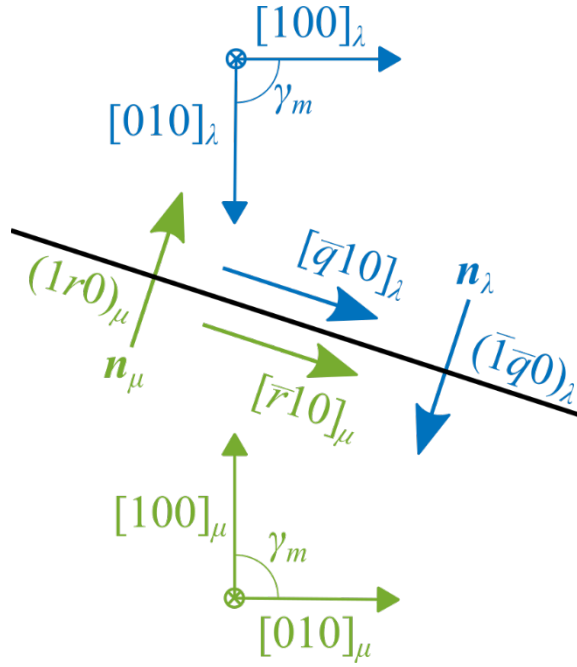


Figure 5.2 Schematic illustration of $(1r0)/(\bar{1}q0)$ NC twinning in NMG. The subscript μ and λ denote the matrix and the twin, respectively. The conjugate relationship of the twinning elements is expressed in NC TBs because the TB is k_1 for the matrix, but k_2 for the twin.

3.2 Orientation Relationship

Bevis and Crocker [31–33] showed that once the correspondence matrix, \mathbf{C} , is specified, the orientation relationship, \mathbf{L} , between the matrix and the twin is given by,

$$\mathbf{C} = \mathbf{L}^A \mathbf{S} \quad (1)$$

\mathbf{S} is the second rank tensor defining shear transformation [30–32]. The superscript A represents a crystal coordinate system. Our proposition assumes the correspondence matrix, \mathbf{C} , is the suppressed proper symmetry element. In a crystal coordinate frame A , the elements of the shear transformation, \mathbf{S} , have the form [30–33]:

$${}^A S_j^i = \delta_j^i + s {}^A l^i {}^A m_j \quad (2)$$

where δ_j^i is the Kronecker delta, \mathbf{l} is the unit vector parallel to the shear direction (γ_1 or γ_2), \mathbf{m} is the unit vector normal to the invariant plane (\mathbf{k}_1 or \mathbf{k}_2), and s is the

twinning shear. The indices i and j are superscripted for vectors and subscripted for co-vectors [41].

After determining \mathbf{C} and \mathbf{S} , we obtain the OR as:

$$\mathbf{L} = \mathbf{C}^A \mathbf{S}^{-1} \quad (3)$$

The OR, \mathbf{L} , between the two variants, if measured in the reference frame R , is given by:

$$\mathbf{L} = {}^R\mathbf{P}^A \mathbf{C}^A \mathbf{S}^{-1} ({}^R\mathbf{P}^A)^{-1} \quad (4)$$

where ${}^R\mathbf{P}^A$ is the transformation matrix relating crystal coordinate (A) to the reference (R) frame.

Using Equations (1) – (4), the OR between the NC twins in NMG with lattice parameters listed in Section 2 is equal to 89.54° rotation about the $[001]_c$ axis for $\mathbf{C} = \mathbf{4}_{[001]}^+$, or 90.46° rotation about $[00\bar{1}]_c$, for $\mathbf{C} = \mathbf{4}_{[001]}^-$.

4. Junction Lines

Seiner *et al.* [19] depicted NC twins in the hierarchical twinning microstructure of NMG using electron micrographs, which are reproduced in Figure 5.3. For a particular $[001]_m$, the symmetry compensation gives rise to four variants V_1 , V_2 , V_3 , and V_4 . NC twinning provides additional degrees of freedom for a continuum arrangement of these variants, as we discuss in Sections 4.1 and 4.2. Junction lines form where two or more TBs meet. These junction lines may either be defect-free or require elastic accommodation, depending on the twinning shear and OR of the variants. Properties of QJLs and TJLs are discussed below.

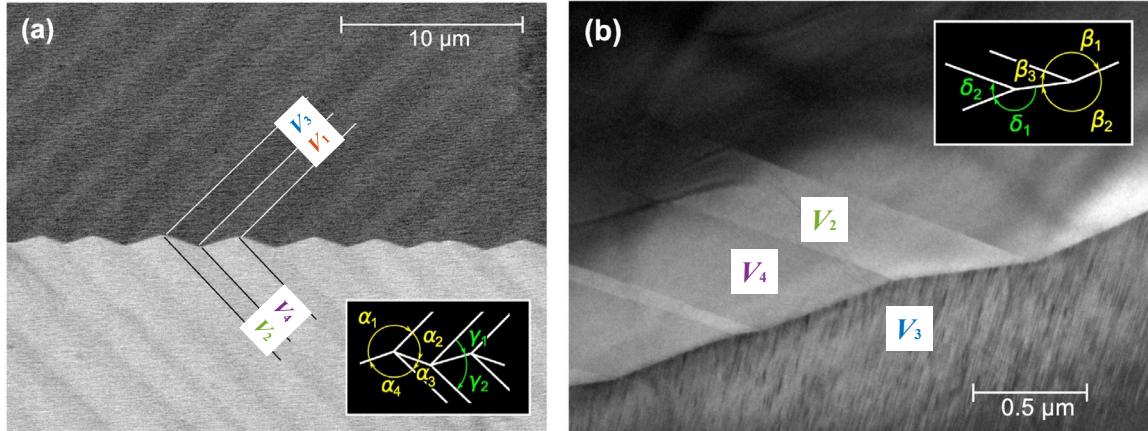


Figure 5.3 Experimentally observed junction lines in NMG. (a) Scanning Electron Microscopy (SEM) image showing a periodic array of quadruple junction lines (QJLs) in the vicinity of type II twin boundaries (TBs). (b) Transmission Electron Microscopy (TEM) image of a chain of triple junction lines (TJLs) formed at the interface between $(110)_m$ TB laminate and a homogeneous region. Reprinted from *Scripta Materialia*, 162 (2019), Seiner *et al.* [19], NC twins in five-layered modulated Ni-Mn-Ga martensite, 497-502, with permission from Elsevier. We follow the notation of Straka *et al.* [17] for the designation of variants.

4.1 Quadruple Junction Lines

Scanning electron microscopy (SEM) imaging of NMG in the micro-scale range shows an abundance of QJLs, as shown in Figure 5.3(a) [19]. We designate the variants following Straka *et al.* [17]. We implement the principle of symmetry compensation to deduce the arrangement of four variants surrounding QJLs. First, we consider lattice points of a single crystal in the cubic phase (simple cubic for simplicity) viewed along one of the principal axes, as shown in Figure 5.4 (a). Four different colors represent four regions, each for a particular variant after transformation. In Figure 5.4 (a), we also overlay the 2-fold symmetry axes – $2_{[100]}$, $2_{[010]}$, $2_{[110]}$, and $2_{[\bar{1}10]}$ – that leave the crystal unchanged after the operation (ignoring the colors), as shown by the dotted lines. These symmetry operations, as well as $4_{[001]}^+$ and $4_{[001]}^-$, get suppressed in the martensite phase, as shown in Figure 5.4 (b). The four variants that arise (as coded in colors in Figure 5.4)

after transformation can be mapped onto each other through these broken symmetry operations as correspondence matrices. Our goal is to find the sequential order of appropriate correspondence matrix operations that give rise to QJLs with the least distortion. If a systematic product of twinning OR around the QJL results in the identity, the junction is defect-free. Otherwise, a rotational misfit occurs, which is accommodated elastically by a disclination [42–45].

Seiner *et al.* [19] calculated the angles between TBs in a QJL arrangement of variants and deduced that such structures could not be obtained by a combination of $(100)_m$ and $(110)_m$ compound twins. They argued that such a QJL arrangement requires two sets of $(110)_m$ compound and $(1r0)_m$ NC twins. Figure 5.4 (b) summarizes the twinning relation around a QJL following the variant notation implemented by Straka *et al.* [17]. Starting from the top left and proceeding clockwise, the variant pairs V_3 – V_1 , V_1 – V_4 , V_4 – V_2 , and V_2 – V_3 are related by correspondence matrices $\mathbf{2}_{[\bar{1}10]}$, $\mathbf{4}_{[001]}^+$, $\mathbf{2}_{[110]}$, and $\mathbf{4}_{[001]}^-$, respectively. Thus, the required systematic operation of OR about the QJL is:

$$\mathbf{M}_{QJL} = {}^R\mathbf{L}(V_2 \rightarrow V_3) {}^R\mathbf{L}(V_4 \rightarrow V_2) {}^R\mathbf{L}(V_1 \rightarrow V_4) {}^R\mathbf{L}(V_3 \rightarrow V_1) \quad (5)$$

The overall matrix operation, \mathbf{M}_{QJL} , yields the identity or a rotation by θ about c_R , the direction normal to the plane of shear in the reference frame. If \mathbf{M}_{QJL} results in a θ rotation about c_R , the additional rotational misfit is accommodated elastically by a wedge disclination [43, 45], which is a line defect located on the junction line. The Frank vector, ω , with the magnitude $\omega = \theta$, characterizes the disclination strength. The Frank vector signifies a rotation corresponding to the rotational displacement field of the disclination.

For the current QJL, the matrix operation \mathbf{M}_{QJL} yields the identity, i.e., $\mathbf{M}_{QJL} = \mathbf{I}$. This means that QJLs do not require rotational accommodation, and the junction is

defect-free. Thus, QJLs allow for the continuous arrangement of four martensite variants without any misfits during phase transformation.

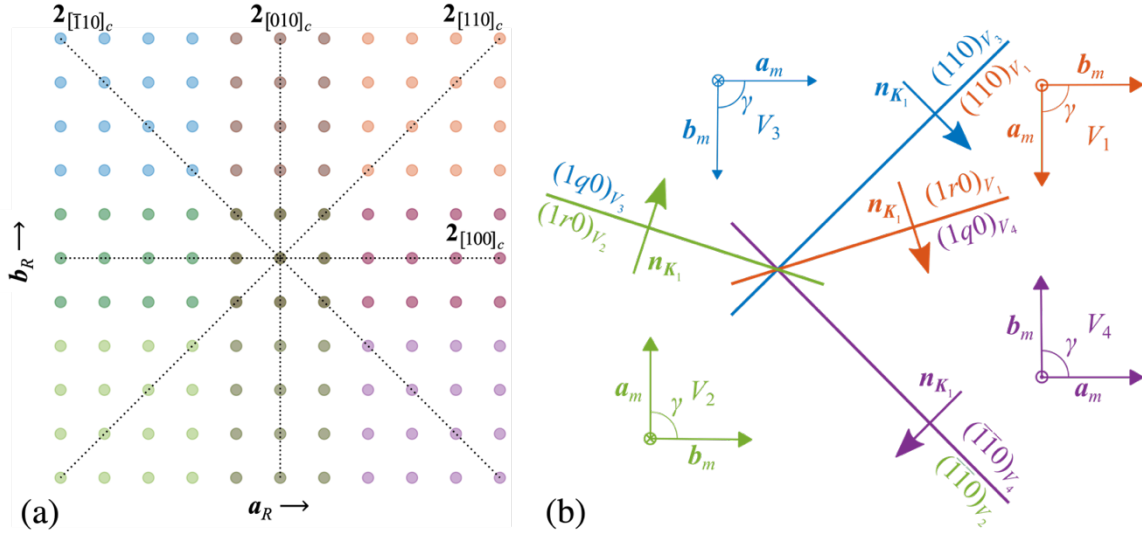


Figure 5.4 a) Schematic illustration of austenite single crystal viewed along one of the principal axes; the colors define the four variants that form after the phase transformation. The dotted lines represent point symmetry operations – $2_{[100]}$, $2_{[010]}$, $2_{[110]}$, and $2_{[\bar{1}10]}$ – that get suppressed in the martensite phase. Phase transformation breaks the symmetry, and these operations, along with $4_{[001]}^+$ and $4_{[001]}^-$, become correspondence matrices, which define the twinning relation at QJLs. (b) The orientation of TBs around a QJL in NMG, which is obtained by a systematic operation of OR across the TB in the QJL arrangement. The associated correspondence matrices, in order, is $2_{[\bar{1}10]}$, $4_{[001]}^+$, $2_{[110]}$, and $4_{[001]}^-$.

4.2 Quadruple Junction Line Formation Energetics

It is unclear how and why four TBs meet at a line to form a QJL in the vicinity of type II TBs. TJLs, on the other hand, form in the hierarchical microstructure of twins in NMG when two non-parallel TBs meet. We assume a hierarchical formation mechanism. At first, variants V_3 and V_4 form and create a $(100)_m$ TB. Second, variants V_1 and V_2 form as twins in variants V_3 and V_4 , respectively, via $(110)_m$ twinning. Third, V_1 and V_2 impinge on the $(100)_m$ TB and create TJLs as shown in Figure 5.5. In this section, we study the defect character of these TJLs and implement a disclination quadrupole

approximation [42] to quantify the energy of a system with four variants. Furthermore, we show that the strain energy vanishes if the TJLs coalesce pairwise and form QJLs.

Since we have four variants for a particular $[001]_m$, and only three variants join a TJL, four distinct TJLs emerge: $V_1-V_4-V_2$, $V_1-V_3-V_4$, $V_3-V_2-V_4$, and $V_3-V_1-V_2$. The accommodation of variants by TJLs requires an additional degree of freedom, which, for NMG, is provided by $(100)_m$ and $(010)_m$ compound twins. The TJLs are similar to QJLs in arrangement, except that the previously not joining variants in QJLs, i.e., V_1-V_2 and V_3-V_4 , are joined by $(100)_m$ and $(010)_m$ TBs, respectively. For example, in the $V_3-V_2-V_4$ TJL, V_3-V_2 are connected by $(1q0)_m$ TB, and V_2-V_4 by $(\bar{1}\bar{1}0)_m$ TB, similar to QJLs, but V_4-V_3 that were previously not joined in QJL are connected by $(0\bar{1}0)_m$ TB. Again, the sequential operation of OR around the $V_3-V_2-V_4$ TJL, with Figure 5.5 as a reference, gives the following rotational misfit:

$$\mathbf{M}_{324} = {}^R\mathbf{L}(V_4 \rightarrow V_3) {}^R\mathbf{L}(V_2 \rightarrow V_4) {}^R\mathbf{L}(V_3 \rightarrow V_2) \quad (6)$$

The resulting matrix, \mathbf{M}_{324} , represents a misorientation of -0.18° for the given TJL.

Following similar calculations, the systematic operation of OR around the TJLs for all possible combinations gives four distinct disclination strengths: $-\omega_1$, ω_1 , ω_2 , and $-\omega_2$, where the magnitudes of Frank vectors are $\omega_1 = 0.18^\circ$ and $\omega_2 = 0.36^\circ$ for NMG with lattice parameters listed in Section 2. The defect strength switches sign when we reverse the direction of sequential operation. The difference in disclination strength results because a $(100)_m$ TB connects the pair V_1-V_2 , whereas an $(010)_m$ TB connects V_3-V_4 .

We have four unique TJLs with two pairs of disclinations of equal strength but opposite signs. An isolated disclination is a high-energy defect whose strain field squares

with the screening length ($U_{self} \propto R^2$). However, these defects are screened by the presence of other disclinations; for instance, the pair $(\omega_i, -\omega_i)$ forms a disclination dipole, which effectively screens each other's diverging strain field [43, 46–48]. Disclination dipoles correspond to a superdislocation with Burgers vector, \mathbf{B}_i , whose magnitude is $B_i = \omega_i R_i$, where R_i is the dipole arm length. The energy of a disclination dipole depends logarithmically on the screening length R (as does the energy of a dislocation). The direction of \mathbf{B}_i is perpendicular to the plane containing dipole as well as the line direction of the dipoles. Two sets of nearby disclination dipoles lying in the same plane with equal but opposite Burgers vector form a disclination quadrupole. The energy of a disclination quadrupole depends only on the geometry and not on the screening radius R .

The disclination quadrupole reaches an unstable equilibrium when the superdislocations, representative of disclination dipoles, are flushed along the same plane and are equal but opposite in sign. The long-range strain fields of the four disclinations cancel if $\mathbf{B}_1 = -\mathbf{B}_2$, (implying $\omega_1 R_1 = \omega_2 R_2$). Using disclination theory (Romanov and Vladimirov [42]), we implement disclination quadrupole approximation to calculate the energy of the system. The energy of the system is the sum of self-energies and interaction-energies of disclinations [42], $U = U_{self} + U_{int}$:

$$U_{self}(\omega) = 1/8 D \omega^2 R^2 \quad (7)$$

$$U_{int}(\omega_1, \omega_2, R_2) = 1/4 D \omega_1 \omega_2 [R^2 - R_2^2 - 2 R_2^2 \ln(R/R_2)] \quad (8)$$

where $D = G / (2\pi (1 - \nu))$, with G as the shear modulus and ν as the Poisson's ratio. R is an outer cut-off radius, and R_2 is the $(\omega_2, -\omega_2)$ dipole arm length.

With the equilibrium parameter $\alpha = \omega_2 / \omega_1 = R_1 / R_2$, the disclination quadrupole approximation (U_{eq}) is a function of three parameters, α , R_1 and L_1 (defined in Figure 5.5), with the solution:

$$U_{eq} = \frac{D\omega_1^2}{2} \left[\alpha(L_1 - R_1)^2 \log\left(\frac{L_1 - R_1}{L_1 - R_1 + R_1/\alpha}\right) + \frac{(aL_1 + R_1)^2}{\alpha} \log\left(\frac{L_1 + R_1/\alpha}{L_1 - R_1 + R_1/\alpha}\right) - \alpha L_1^2 \log\left(\frac{L_1}{L_1 - R_1 + R_1/\alpha}\right) - R_1^2 \log\left(\frac{R_1^2/\alpha}{(L_1 - R_1 + R_1/\alpha)^2}\right) \right] \quad (9)$$

The solution for Equation 9 assumes that all the four disclinations lie in the same plane, which is not the case for NMG, as seen in Figure 5.5. Nonetheless, the solution is useful for understanding the trends in energy as we vary the input parameters. For NMG, $\alpha = \omega_2 / \omega_1 \approx 0.36^\circ / 0.18^\circ \approx 2$. The image plot of the energy as a function of L_1 (x -axis) and R_1 (y -axis) is shown in Figure 5.6. Since Equation (9) assumes $L_1 > R_1$, no solution exists when $R_1 > L_1$, as seen by the lack of colors in the upper left triangle of the image plot. We can discern from the image plot that energy value is more sensitive to an increase in R_1 than L_1 : the color changes faster when moving vertically than horizontally. The result becomes more apparent when we fix one of the variables (L_1 or R_1) and plot the energy as a function of the other variable, as seen in Figures 5.6 (b) and (c). Figure 5.6 (b) shows that U_{eq} vs. L_1 gives us a logarithmic curve for a fixed R_1 , whereas, in Figure 5.6 (c), we approximate U_{eq} vs. R_1 as a polynomial function of order about 2.5 for a fixed L_1 . For small values of R_1 , the energy is proportional to the square of R_1 . This result is a consequence of the linear relation between R_1 and the Burgers vector \mathbf{B} as the energy of a dislocation depends quadratically on its Burgers vector. Thus, the arm length of the disclination dipole significantly affects the energy of the quadrupole system. For narrow dipoles, the energy of the system is a logarithmic function, i.e., the energy of the system is a function of the length scale of the defects.

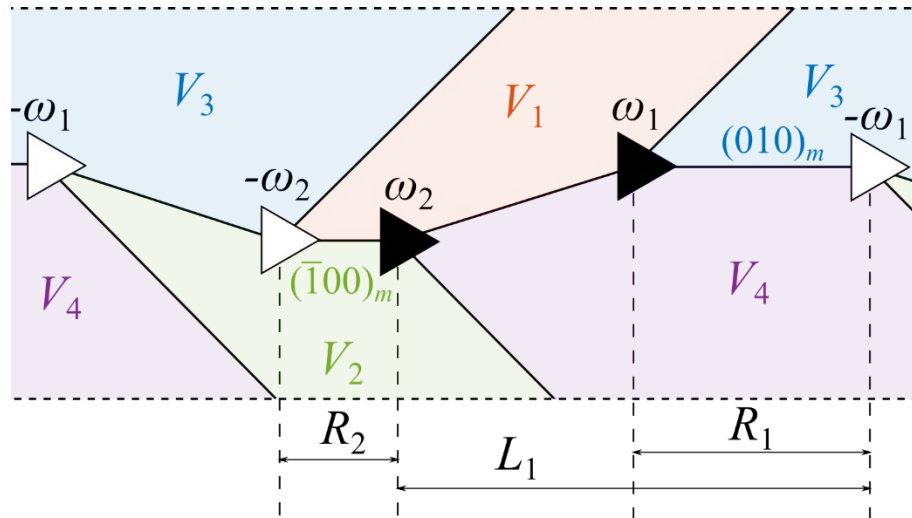


Figure 5.5 Schematic illustration of TJLs forming a disclination quadrupole system to accommodate four martensite variants: the four distinct disclination strengths are obtained by systematically studying the OR of variants across the junction's TBs.

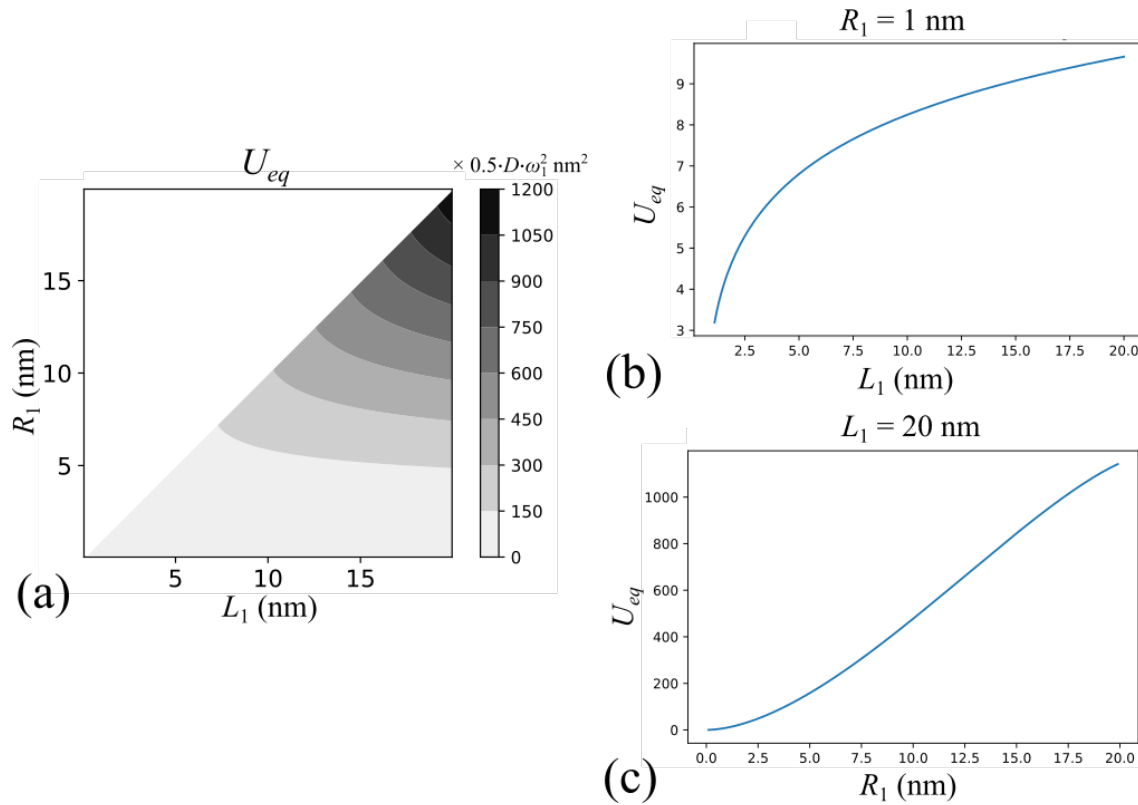


Figure 5.6 a) Equilibrium energy (U_{eq}) of disclination quadrupole approximation as a function of L_1 and R_1 , both ranging from 0 to 20 nm. $\alpha = \omega_2 / \omega_1 \approx 2$ in the present case. (b) For a fixed R_1 , U_{eq} as a function of L_1 is a logarithmic plot. (c) For a fixed L_1 , U_{eq} as a function of R_1 is a polynomial plot of an order of about 2.5. Thus, the energy of the disclination quadrupole is sensitive to the size of the dipole arm length.

4.3 Walls of Triple Junction Lines

Figure 5.3 (b) (also reproduced in Figure 5.7 (a)) shows a wall of TJLs including only three variants, V_4 , V_2 , and V_3 ; in these chains of TJLs, the defect strength at the junction alters in sign but has the same magnitude. In the $V_4 \rightarrow V_2 \rightarrow V_3 \rightarrow V_4$ transformation, we follow the OR across (110) TB, $(\bar{1}\bar{7}0)$ TB and $(0\bar{1}0)$ TB systematically and obtain a disclination strength of ω_1 , as in Section 4.2. The defect strength of the next junction in the chain is obtained by following the transformation $V_2 \rightarrow V_4 \rightarrow V_3 \rightarrow V_2$. Here, the disclination strength, given by the Frank vector, is $-\omega_1$. A schematic illustration

of orientation and crystallography of TBs around a V_4 - V_2 - V_3 TJL is shown in Figure 5.7 (b).

A wall of wedge disclination junctions with the same disclination power but alternating sign corresponds to a tilt wall [49, 50]. A tilt wall can be thought of as a wall of dislocations (represented by disclination dipoles), which relaxes by partitioning of the strain field across the interface. The overall effect is a rotation of the interface and a superimposed misorientation. The total misorientation depends on the volume fraction of V_2 in V_4 . The strain energy increases with the distance between the TJLs, since their spacing determines the magnitude of the Burgers vector. A dense chain of TJLs may appear in sub-micron length scale, as seen in Figure 5.7 (a), since, at this scale, the energy of the system due to the rotational displacement field is small.

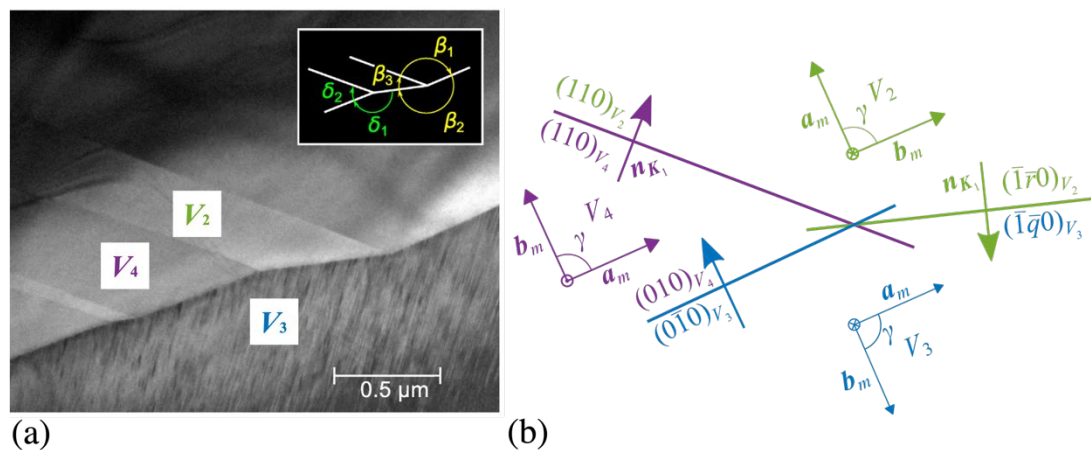


Figure 5.7 The orientation of TBs around a TJL in NMG, as shown in (a), is reproduced crystallographically in (b). The arrangement is deduced by a taking a systematic operation of OR across the TB in the TJL arrangement. Figure (a) is adapted from Scripta Materialia, 162 (2019), Seiner *et al.* [19], NC twins in five-layered modulated Ni-Mn-Ga martensite, 497-502, with permission from Elsevier. We follow the notation of Straka *et al.* [17] for the designation of variants.

5. Discussion

The phase transformation from the cubic to the monoclinic structure gives rise to twelve variants [22, 33, 40]. For a given $[001]_m$, we have four variants. QJLs accommodate four variants without additional misfits and may arise during the phase transformation. However, their formation mechanism is unclear. TJLs form readily in hierarchical twin microstructure but are accompanied by a rotational misfit. Disclinations (line-defects) accommodate the rotational misfits, and four disclination strengths appear for all possible combination of TJLs.

While the formation mechanism of QJLs is unclear, the formation of the wall of TJLs containing only three variants can be inferred topologically: Imagine regions of variants V_3 and V_4 that are separated by $(010)_m$ TB. Now, imagine V_2 nucleates and grows inside V_4 , interrelated by $(110)_m$ TB. The growth of the variant V_2 leads to the propagation of twinning disconnections towards the $(010)_m$ boundary separating V_3 . On reaching this boundary, the superposition of the disconnections would, after relaxation, form an NC TB between V_2 and V_3 and a TJL separating $V_3-V_2-V_4$. Based on the density of variant V_2 nucleation sites, a chain of TJL forms; the defect structure of the interface comprises a chain of disclination dipoles $(\omega_1, -\omega_1)$, which is equivalent to a tilt wall. The rotational displacement field of the tilt wall causes rotation of the interface. The total rotation depends on the defect strength and the density and separation distance of the dipoles [49, 50]. We see such a dipole chain in TEM images of NMG, as seen in Figure 5.3 (b). The rotation of the interface adds strain energy to the system but is small in the present case.

Accommodation of four variants with TJsLs means four distinct disclinations emerge, as discussed in Section 4.2. We implement a disclination quadrupole approximation to show a stable chain of TJsLs that accommodate four variants. The strain energy of a disclination quadrupole system is proportional to the square of R_1 at small values (Figure 5.6 (c)). This dependence provides a driving force for the pairwise coalescence of TJsLs into QJsLs. Imagine a disclination quadrupole approximation at the beginning, as shown in Figure 5.5. For TJsLs to coalesce into QJsLs, the mobility of $(110)_m$ and NC twins is critical. If the strain field at the $(010)_m/(100)_m$ interface can nucleate disconnections and move $(110)_m$ and NC TBs synchronously, the disclination dipoles can converge via the migration of $(010)_m/(100)_m$ boundary to form QJsLs. An intermediate stage of the formation of QJsLs from TJsLs via the movement of TBs is shown in Figure 5.8. Thomas *et al.* [51] suggested a similar mechanism, using molecular dynamics simulations, for forming various twin junctions in nanocrystalline nickel, including penta-twin junctions.

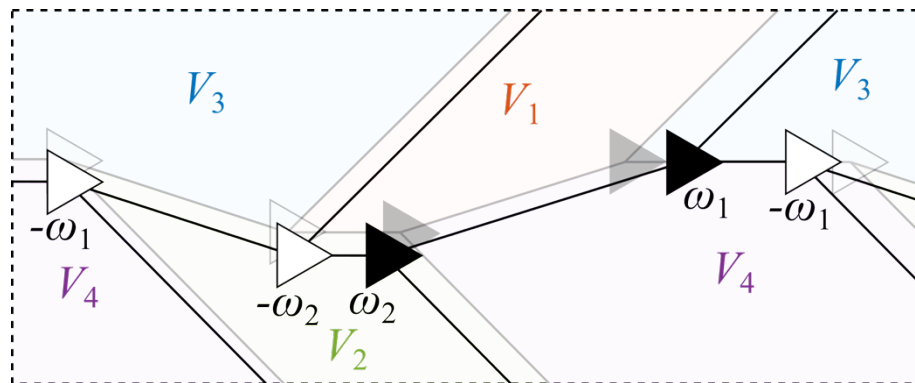


Figure 5.8 An intermediate stage in the pairwise coalescence of TJsLs into QJsLs, with disclination quadrupole approximation, as in Figure 5.5, as a starting reference.

Our QJL formation assumption is based purely on the energetics and may not represent the actual formation mechanism. The orientation of defects and their interactions play a crucial role in the mobility and synchronous motion of $(110)_m$ and NC TBs. Furthermore, we assume the disclination quadrupole as a starting point. The stress field near the interface, as the disconnections on $(110)_m$ TBs move and approach $(010)_m/(100)_m$ TB, is high and may drive the formation of QJLs rather than a chain of TJLs. Finally, our description of QJL formation does not address the question as to why a chain of QJLs forms only in the vicinity of type II twins. Type II TBs have an irrational interface and consist of an array of dislocations that form a tilt boundary [22, 52, 53]. Thus, the tilt boundary of type II twins may interact with $(100)_m$ and $(110)_m$ compound TBs and provide an additional driving force for the formation of NC twins and QJLs. Information about the orientation of the tilt-wall in type II and NC twins and their interaction with the disconnections in compound TBs is required to understand the formation mechanism of QJLs near type II TBs. However, this is outside the scope of the current work.

6. Conclusion

We study the properties of the twin boundary junctions motivated by an abundance of TJLs and QJLs in NMG. NC twins join TJLs with $(110)_m$ and $(100)_m / (010)_m$ TBs. QJLs are composed of two NC TBs and two $(110)_m$ TBs.

QJLs form, most likely during the phase transformation, because they allow for continuous arrangement of the four twin variants without any additional misfit. TJLs, on the other hand, carry a rotational misfit whose strain field diverges. When arranged in chains such that the net Burgers vectors of nearby disclination dipoles cancel,

disclinations mutually screen their diverging fields effectively. A disclination quadrupole approximation predicts a stable structural configuration involving all four variants, where the strain energy scales with the length-scale of defects, i.e., the arm of disclination dipoles.

A wall of TJLs accommodating only three variants is also found in NMG. This configuration forms due to the superposition of twinning disconnections when a $(110)_m$ TB abuts the $(100)_m$ (or $(010)_m$) boundary from one side. The overall interfacial structure corresponds to a tilt wall which causes the rotation of the interface. The rotation of the interface increases the strain field and may explain why these chains of TJLs are only observed at the sub-micron length scale.

Since the formation mechanism of a QJL is not clear, we explore the proposition that the strain field near the junction interface serves as a driving force for the migration of a $(100)_m / (010)_m$ TB, which causes synchronous motion of $(110)_m$ and NC TBs and consequently the pairwise coalescence of TJLs into QJLs. Nevertheless, the proposed QJL formation mechanism does not consider the interactions of type I and type II TBs; a chain of QJLs is present in the vicinity of type II twins, but not so at type I twins [19]. This characteristic feature implies that the interaction of the type II tilt boundary with the compound twins drives the formation of QJLs.

Acknowledgement

This research was supported by the National Science Foundation through Grant No. NSF-DMR-1710640.

References

- [1] S.J. Murray, M. Marioni, S.M. Allen, R.C. O’Handley, T.A. Lograsso, 6% magnetic-field-induced strain by twin-boundary motion in ferromagnetic Ni–Mn–Ga, *Applied Physics Letters*. 77 (2000) 886–888.
<https://doi.org/10.1063/1.1306635>.
- [2] A. Sozinov, A.A. Likhachev, K. Ullakko, Crystal structures and magnetic anisotropy properties of Ni-Mn-Ga martensitic phases with giant magnetic-field-induced strain, *IEEE Transactions on Magnetics*. 38 (2002) 2814–2816.
<https://doi.org/10.1109/tmag.2002.803567>.
- [3] D. Kellis, A. Smith, K. Ullakko, P. Müllner, Oriented single crystals of Ni–Mn–Ga with very low switching field, *Journal of Crystal Growth*. 359 (2012) 64–68.
<https://doi.org/10.1016/j.jcrysgro.2012.08.014>.
- [4] E. Faran, D. Shilo, The kinetic relation for twin wall motion in Ni-Mn-Ga, *Journal of the Mechanics and Physics of Solids*. 59 (2011) 975–987.
<https://doi.org/10.1016/j.jmps.2011.02.009>.
- [5] E. Faran, D. Shilo, The kinetic relation for twin wall motion in Ni-Mn-Ga—part 2, *Journal of the Mechanics and Physics of Solids*. 61 (2013) 726–741.
<https://doi.org/10.1016/j.jmps.2012.11.004>.
- [6] A.R. Smith, J. Tellinen, K. Ullakko, Rapid actuation and response of Ni–Mn–Ga to magnetic-field-induced stress, *Acta Materialia*. 80 (2014) 373–379.
<https://doi.org/10.1016/j.actamat.2014.06.054>.
- [7] M.A. Marioni, R.C. O’Handley, S.M. Allen, Pulsed magnetic field-induced actuation of Ni–Mn–Ga single crystals, *Appl. Phys. Lett.* 83 (2003) 3966–3968.
<https://doi.org/10.1063/1.1626021>.
- [8] I. Suorsa, E. Pagounis, K. Ullakko, Magnetic shape memory actuator performance, *Journal of Magnetism and Magnetic Materials*. 272–276 (2004) 2029–2030. <https://doi.org/10.1016/j.jmmm.2003.12.1026>.

- [9] S.A. Wilson, R.P.J. Jourdain, Q. Zhang, R.A. Dorey, C.R. Bowen, M. Willander, Q.U. Wahab, M. Willander, S.M. Al-Hilli, O. Nur, E. Quandt, C. Johansson, E. Pagounis, M. Kohl, J. Matovic, B. Samel, W. Van Der Wijngaart, E.W.H. Jager, D. Carlsson, Z. Djinovic, M. Wegener, C. Moldovan, R. Iosub, E. Abad, M. Wendlandt, C. Rusu, K. Persson, New materials for micro-scale sensors and actuators, *Materials Science and Engineering: R: Reports*. 56 (2007) 1–129. <https://doi.org/10.1016/j.mser.2007.03.001>.
- [10] P. Lindquist, T. Hobza, C. Patrick, P. Müllner, Efficiency of Energy Harvesting in Ni–Mn–Ga Shape Memory Alloys, *Shape Memory and Superelasticity*. 4 (2018) 93–101. <https://doi.org/10.1007/s40830-018-0158-z>.
- [11] S. Barker, E. Rhoads, P. Lindquist, M. Vreugdenhil, P. Müllner, Magnetic Shape Memory Micropump for Submicroliter Intracranial Drug Delivery in Rats, *Journal of Medical Devices*. 10 (2016) 041009. <https://doi.org/10.1115/1.4034576>.
- [12] I. Aaltio, K.P. Mohanchandra, O. Heczko, M. Lahelin, Y. Ge, G.P. Carman, O. Söderberg, B. Löfgren, J. Seppälä, S.-P. Hannula, Temperature dependence of mechanical damping in Ni–Mn–Ga austenite and non-modulated martensite, *Scripta Materialia*. 59 (2008) 550–553. <https://doi.org/10.1016/j.scriptamat.2008.05.005>.
- [13] K. Ullakko, L. Wendell, A. Smith, P. Müllner, G. Hampikian, A magnetic shape memory micropump: contact-free, and compatible with PCR and human DNA profiling, *Smart Mater. Struct.* 21 (2012) 115020. <https://doi.org/10.1088/0964-1726/21/11/115020>.
- [14] K. Ullakko, J.K. Huang, C. Kantner, R.C. O’Handley, V.V. Kokorin, Large magnetic-field-induced strains in Ni₂MnGa single crystals, *Appl. Phys. Lett.* 69 (1996) 1966–1968. <https://doi.org/10.1063/1.117637>.
- [15] I. Karaman, B. Basaran, H.E. Karaca, A.I. Karsilayan, Y.I. Chumlyakov, Energy harvesting using martensite variant reorientation mechanism in a NiMnGa magnetic shape memory alloy, *Appl. Phys. Lett.* 90 (2007) 172505. <https://doi.org/10.1063/1.2721143>.

- [16] P. Müllner, V.A. Chernenko, M. Wollgarten, G. Kostorz, Large cyclic deformation of a Ni-Mn-Ga shape memory alloy induced by magnetic fields, *Journal of Applied Physics*. 92 (2002) 6708–6713.
<https://doi.org/10.1063/1.1513875>.
- [17] L. Straka, O. Heczko, H. Seiner, N. Lanska, J. Drahokoupil, A. Soroka, S. Fähler, H. Hänninen, A. Sozinov, Highly mobile twinned interface in 10M modulated Ni–Mn–Ga martensite: analysis beyond the tetragonal approximation of lattice, *Acta Materialia*. 59 (2011) 7450–7463.
<https://doi.org/10.1016/j.actamat.2011.09.020>.
- [18] J. Pons, R. Santamarta, V.A. Chernenko, E. Cesari, Structure of the layered martensitic phases of Ni–Mn–Ga alloys, *Materials Science and Engineering: A*. 438–440 (2006) 931–934. <https://doi.org/10.1016/j.msea.2006.02.179>.
- [19] H. Seiner, R. Chulist, W. Maziarz, A. Sozinov, O. Heczko, L. Straka, Non-conventional twins in five-layer modulated Ni-Mn-Ga martensite, *Scripta Materialia*. 162 (2019) 497–502. <https://doi.org/10.1016/j.scriptamat.2018.12.020>.
- [20] R. Chulist, E. Pagounis, A. Böhm, C.-G. Oertel, W. Skrotzki, Twin boundaries in trained 10M Ni–Mn–Ga single crystals, *Scripta Materialia*. 67 (2012) 364–367.
<https://doi.org/10.1016/j.scriptamat.2012.05.026>.
- [21] R. Chulist, L. Straka, N. Lanska, A. Soroka, A. Sozinov, W. Skrotzki, Characterization of mobile type I and type II twin boundaries in 10M modulated Ni–Mn–Ga martensite by electron backscatter diffraction, *Acta Materialia*. 61 (2013) 1913–1920. <https://doi.org/10.1016/j.actamat.2012.12.012>.
- [22] B. Karki, P. Müllner, R. Pond, Topological model of type II deformation twinning in 10M Ni-Mn-Ga, *Acta Materialia*. 201 (2020) 604–616.
<https://doi.org/10.1016/j.actamat.2020.10.020>.
- [23] B.J. Karki, Y. Behar, I. Harel, E. Caplan, A. Sabbag, D. Shilo, P. Mullner, E. Faran, A simple method to characterize high rate twin boundary kinetics in Ni-Mn-Ga, *Review of Scientific Instruments*. 90 (2019) 105107.
<https://doi.org/10.1063/1.5109934>.

- [24] A. Sozinov, N. Lanska, A. Soroka, L. Straka, Highly mobile type II twin boundary in Ni-Mn-Ga five-layered martensite, *Appl. Phys. Lett.* 99 (2011) 124103. <https://doi.org/10.1063/1.3640489>.
- [25] A. Saren, T. Nicholls, J. Tellinen, K. Ullakko, Direct observation of fast-moving twin boundaries in magnetic shape memory alloy Ni–Mn–Ga 5M martensite, *Scripta Materialia*. 123 (2016) 9–12. <https://doi.org/10.1016/j.scriptamat.2016.04.004>.
- [26] A. Saren, K. Ullakko, Dynamic twinning stress and viscous-like damping of twin boundary motion in magnetic shape memory alloy Ni-Mn-Ga, *Scripta Materialia*. 139 (2017) 126–129. <https://doi.org/10.1016/j.scriptamat.2017.06.010>.
- [27] R.W. Cahn, Plastic deformation of alpha-uranium; twinning and slip, *Acta Metallurgica*. 1 (1953) 49–70. [https://doi.org/10.1016/0001-6160\(53\)90009-1](https://doi.org/10.1016/0001-6160(53)90009-1).
- [28] F.C. Frank, A note on twinning in alpha-uranium, *Acta Metallurgica*. 1 (1953) 71–74. [https://doi.org/10.1016/0001-6160\(53\)90010-8](https://doi.org/10.1016/0001-6160(53)90010-8).
- [29] M.A. Jaswon, D.B. Dove, The crystallography of deformation twinning, *Acta Cryst.* 13 (1960) 232–240. <https://doi.org/10.1107/S0365110X60000534>.
- [30] B.A. Bilby, A.G. Crocker, The theory of the crystallography of deformation twinning, *Proc. R. Soc. Lond. A*. 288 (1965) 240–255. <https://doi.org/10.1098/rspa.1965.0216>.
- [31] M. Bevis, A.G. Crocker, Twinning shears in lattices, *Proc. R. Soc. Lond. A*. 304 (1968) 123–134. <https://doi.org/10.1098/rspa.1968.0077>.
- [32] M. Bevis, A.G. Crocker, Twinning modes in lattices, *Proceedings of the Royal Society A: Mathematical, Physical and Engineering Sciences*. 313 (1969) 21. <https://doi.org/10.1098/rspa.1969.0208>.
- [33] J.W. Christian, S. Mahajan, Deformation twinning, *Progress in Materials Science*. 39 (1995) 1–157. [https://doi.org/10.1016/0079-6425\(94\)00007-7](https://doi.org/10.1016/0079-6425(94)00007-7).
- [34] K. Bhattacharya, Theory of Martensitic Microstructure and the Shape-Memory Effect, in: *Microstructure of Martensite, 2004*: p. 87.

- [35] P.J. Webster, K.R.A. Ziebeck, S.L. Town, M.S. Peak, Magnetic order and phase transformation in Ni_2MnGa , *Philosophical Magazine B*. 49 (1984) 295–310. <https://doi.org/10.1080/13642817408246515>.
- [36] M. Chmielus, Composition, structure and magneto-mechanical properties of Ni-Mn-Ga magnetic shape-memory alloys, (2010) 166.
- [37] C. Jiang, Y. Muhammad, L. Deng, W. Wu, H. Xu, Composition dependence on the martensitic structures of the Mn-rich NiMnGa alloys, *Acta Materialia*. 52 (2004) 2779–2785. <https://doi.org/10.1016/j.actamat.2004.02.024>.
- [38] G. Mogylnyy, I. Glavatsky, N. Glavatska, O. Söderberg, Y. Ge, V.K. Lindroos, Crystal structure and twinning in martensite of $\text{Ni}_{1.96}\text{Mn}_{1.18}\text{Ga}_{0.86}$ magnetic shape memory alloy, *Scripta Materialia*. 48 (2003) 1427–1432. [https://doi.org/10.1016/S1359-6462\(03\)00108-8](https://doi.org/10.1016/S1359-6462(03)00108-8).
- [39] R.C. Pond, B. Muntifering, P. Müllner, Deformation twinning in Ni_2MnGa , *Acta Materialia*. 60 (2012) 3976–3984. <https://doi.org/10.1016/j.actamat.2012.03.045>.
- [40] A.V. Shubnikov, V.A. Koptsik, *Symmetry in Science and Art*, Springer US, 1974. <https://www.springer.com/gp/book/9781468420692> (accessed June 9, 2020).
- [41] T. Hahn, *International Tables of Crystallography, A*, 854 p. D, Reidel Publishing Company, Dordrecht, 1983.
- [42] A.E. Romanov, V.I. Vladimirov, Disclinations in Crystalline Solids, *Dislocations in Solids*. 9 (1992). <https://ci.nii.ac.jp/naid/10029464238/> (accessed October 8, 2021).
- [43] A.E. Romanov, Screened disclinations in solids, *Materials Science and Engineering: A*. 164 (1993) 58–68.
- [44] P. Müllner, W.-M. Kuschke, Disclinations due to grain boundary relaxation in fine-grained materials and thin films, *Scripta Materialia*. 36 (1997) 1451–1455. [https://doi.org/10.1016/S1359-6462\(97\)00042-0](https://doi.org/10.1016/S1359-6462(97)00042-0).

- [45] A.E. Romanov, A.L. Kolesnikova, Application of disclination concept to solid structures, *Progress in Materials Science*. 54 (2009) 740–769.
<https://doi.org/10.1016/j.pmatsci.2009.03.002>.
- [46] P. Müllner, C. Solenthaler, A proper model of a deformation twin for twin-intersection problems, *Philosophical Magazine Letters*. 69 (1994) 111–113.
<https://doi.org/10.1080/09500839408241578>.
- [47] P. Müllner, A.E. Romanov, Internal Twinning in Deformation Twinning, *Acta Materialia*. 48 (2000) 15.
- [48] P. Müllner, A.H. King, Deformation of hierarchically twinned martensite, *Acta Materialia*. 58 (2010) 5242–5261. <https://doi.org/10.1016/j.actamat.2010.05.048>.
- [49] P.M. Anderson, J.P. Hirth, J. Lothe, *Theory of dislocations*, Cambridge University Press, 2017.
- [50] J.P. Hirth, R.C. Pond, J. Lothe, Disconnections in tilt walls, *Acta Materialia*. 54 (2006) 4237–4245. <https://doi.org/10.1016/j.actamat.2006.05.017>.
- [51] S.L. Thomas, A.H. King, D.J. Srolovitz, When twins collide: Twin junctions in nanocrystalline nickel, *Acta Materialia*. 113 (2016) 301–310.
<https://doi.org/10.1016/j.actamat.2016.04.030>.
- [52] R.C. Pond, J.P. Hirth, Topological model of type II deformation twinning, *Acta Materialia*. 151 (2018) 229–242. <https://doi.org/10.1016/j.actamat.2018.03.014>.
- [53] R.C. Pond, J.P. Hirth, K.M. Knowles, Topological model of type II deformation twinning in Ni-Ti martensite, *Philosophical Magazine*. 99 (2019) 1619–1632.
<https://doi.org/10.1080/14786435.2019.1587185>.

Appendices

We consider twinning in monoclinic Ni_2MnGa , with space group $P2/m$. We regard this monoclinic form to be derived from a higher symmetry precursor, space group $Fm\bar{3}m$, by a notional sequence of dissymmetrisation stages, whereby the point symmetry elements suppressed at each stage become potential twinning ORs.

Dissymmetrisation Stages

The maximal point supergroup of $2/m$ is $m\bar{3}m$: it is convenient to consider the dissymmetrisation sequence as:

Stage 1 – cubic, $m\bar{3}m$ to tetragonal, $4/mmm$.

Stage 2 – tetragonal, $4/mmm$ to orthorhombic, mmm ;

Stage 3 – orthorhombic, mmm to monoclinic, $2/m$.

Stage 1: $\{4/mmm\}$ is not an invariant subgroup of $\{m\bar{3}m\}$, so three conjugate subgroups are interrelated by symmetry operations:

$$\{m\bar{3}m\} = \mathbf{1} \{4/mmm\} \cup \mathbf{3}^+ \{4/mmm\} \cup \mathbf{3}^- \{4/mmm\} \quad (\text{A1})$$

Stage 2: $\{mmm\}$ is an invariant subgroup of $\{4/mmm\}$; there are two distinct subgroups which are interrelated by $[001]/45^\circ$ – i.e., not a symmetry operation.

$$\{4/mmm\} = \mathbf{1} \{mmm\} \cup \mathbf{4}_{[001]}^+ \{mmm\} \quad (\text{A2a})$$

where the mirror planes are parallel to (100), (010) and (001), and

$$\{4/mmm\} = \mathbf{1} \{mmm\} \cup \mathbf{2}_{[100]} \{mmm\} \quad (\text{A2b})$$

where the mirror planes are parallel to (110), $(1\bar{1}0)$ and (001)

Stage 3: $\{2/m\}$ is an invariant subgroup of $\{mmm\}$; there are three distinct subgroups which are not interrelated by symmetry operations.

$$\{mmm\} = \mathbf{1} \left\{ \mathbf{2}_{[001]}/m \right\} \cup \mathbf{2}_{[100]} \left\{ \mathbf{2}_{[001]}/m \right\} \quad (\text{A3a})$$

$$\{mmm\} = \mathbf{1} \left\{ \mathbf{2}_{[010]}/m \right\} \cup \mathbf{2}_{[001]} \left\{ \mathbf{2}_{[010]}/m \right\} \quad (\text{A3b})$$

$$\{mmm\} = \mathbf{1} \left\{ \mathbf{2}_{[100]}/m \right\} \cup \mathbf{2}_{[010]} \left\{ \mathbf{2}_{[100]}/m \right\} \quad (\text{A3c})$$

Twinning Orientation Relationship

We take our reference monoclinic form to be $\{2^{[001]}/m\} = \{\mathbf{1}, \mathbf{2}_{[001]}, \mathbf{m}_{(001)}, \bar{\mathbf{1}}\}$.

The possible twinning OR correspond to operations in the cosets in A1, A2a, and A3a.

We ignore the elements in A1 because they do not leave (001) invariant; the remaining elements are:

$$\mathbf{4}_{[001]}^+ \{mmm\} = (\mathbf{4}_{[001]}^+, \mathbf{4}_{[001]}^-, \mathbf{2}_{[110]}, \mathbf{2}_{[1\bar{1}0]}, \mathbf{m}_{(110)}, \mathbf{m}_{(1\bar{1}0)}, \bar{\mathbf{4}}_{[001]}^-, \bar{\mathbf{4}}_{[001]}^+) \quad (\text{A4})$$

and

$$\mathbf{2}_{[100]} \{2^{[001]}/m\} = (\mathbf{2}_{[100]}, \mathbf{2}_{[010]}, \mathbf{m}_{(010)}, \mathbf{m}_{(100)}) \quad (\text{A5})$$

Thus, the following set of proper operations are suppressed in the tetragonal to monoclinic dissymmetrisation: $(\mathbf{2}_{[100]}, \mathbf{2}_{[010]}, \mathbf{2}_{[110]}, \mathbf{2}_{[1\bar{1}0]}, \bar{\mathbf{4}}_{[001]}^+, \bar{\mathbf{4}}_{[001]}^-)$. Each of these operations can be represented by a unitary matrix and conforms to a correspondence matrix interrelating our monoclinic reference to a symmetry related variant. The correspondence matrices can be input to the Bevis & Crocker treatment for predicting twinning modes.

CHAPTER SIX: A SIMPLE METHOD TO CHARACTERIZE HIGH RATE TWIN
BOUNDARY KINETICS IN NI-MN-GA

Bibek J. Karki¹,

Yotam Behar²,

Itai Harel²,

Eitan Caplan²,

Arik Sabbag²,

Doron Shilo²,

Peter Müllner¹,

Eilon Faran²

¹ Micron School of Materials Science and Engineering, Boise State University,
Boise, ID, 83725, USA

² Technion - Israel Institute of Technology, Haifa 3200003, Israel

Published in Review of Scientific Instruments: B.J. Karki, Y. Behar, I. Harel, E. Caplan, A. Sabbag, D. Shilo, P. Müllner, E. Faran, A simple method to characterize high rate twin boundary kinetics in Ni-Mn-Ga, Review of Scientific Instruments 90, 105107 (2019)

Abstract

Experimental characterization of twin boundary kinetics is essential to systematically test and reproduce the actuation properties of magnetic shape memory (MSM) elements at high rates. Here we present a simple, non-destructive, experimental method to quantify the dynamic response of a MSM crystal and extract the major material properties that govern its kinetics. The tested sample is subjected to a mechanical pulse that is produced by a simple off-the-shelf solenoid. The mechanical pulse leads to actuation of the tested MSM Ni-Mn-Ga single crystal within 10 ms, during which the twin boundary velocity varies between zero and 2 m/s. The displacement and force in the MSM crystal are measured simultaneously using an optical sensor and a miniature force sensor, respectively. The data captured during a single loading experiment allows plotting a dynamic stress-strain curve as well as a kinetic relation that characterizes the macroscopic response of the crystal. In particular, the obtained kinetic relation enables the extraction of the transition driving force between slow (thermally activated) and fast (athermal) twin boundary motion. This transition driving force is a key material property that governs fast actuation capabilities of MSM elements. The macroscopic behavior of the sample is correlated to the motion of individual twin boundaries within the crystal by adding high speed microscopy to the experimental setup. This allows simultaneous high-rate tracking of individual twinning interfaces in Ni-Mn-Ga.

1. Introduction

Magnetic shape memory (MSM) alloys are candidate materials for fast actuation due to their ability to exhibit large and reversible displacements in the martensite phase

[1-5]. The mechanical response of MSM alloys can be driven either by a mechanical load or by a magnetic field, both of which promote the twinning reorientation process within the material. Twinning reorientation proceeds through the motion of individual twin boundaries, which are interfaces separating different martensite variants. Thus, the kinetics of individual twin boundaries under an external driving force (either mechanical, magnetic or both) directly determines the macroscopic response of a given MSM crystal [6, 7]. Because a major advantage of MSM alloys over ordinary shape memory alloys is their ability to display a high-frequency response under a cyclic magnetic field (typically in the 10-1000 Hz range), it is necessary to characterize the twin boundary motion at velocities and time scales that are relevant for MSM applications.

The most common experimental method used for evaluating the motion of twin boundaries in MSM alloys is the uniaxial loading method, in which the crystal is deformed (usually in compression) at a constant strain rate while the force is recorded. Such experiments are performed at slow strain rates, typically smaller than 0.01 s^{-1} , and provide a quasi-static stress-strain curve (see, for example, Refs. [8–11]). The resulting curve usually displays a long plateau of approximately constant stress, during which the twinning reorientation occurs. The average stress during the plateau is known as the twinning stress, which is a fundamental material property that represents the minimal stress required for twin boundary motion. For example, uniaxial loading tests revealed substantial differences between the typical values of the twinning stress of type I (0.7–1 MPa) and type II (0.05–0.2 MPa) twins in MSM Ni-MN-Ga single crystals [12–16].

While the twinning stress is an important property, it provides information only on the response of an MSM crystal at slow loading rates, which corresponds to a

complete twinning reorientation during times longer than 10 s. In addition, kinetic measurements performed under slow varying magnetic fields (see, for example, Refs. [17, 18]) provide information that is relevant at velocities that are several orders of magnitude slower than typical actuation rates. Thus, complementary experimental methods must be employed to understand and quantify the kinetics of twinning over a wide range of velocities, and in particular at velocities and time scales that match typical actuation rates, i.e., at the millisecond scale. In their recent works, Faran and Shilo measured the kinetics of individual twin boundaries in MSM Ni-Mn-Ga using pulsed magnetic field experiments [19, 20]. This method involves the exposure of an MSM crystal to short (typically microsecond scale) magnetic pulses with a nearly constant amplitude throughout the majority of the pulse duration. The position of an individual twin boundary is tracked optically before and after each pulse, which allows calculating an average velocity value during each pulse. By performing a large number of pulsed experiments at different intensities of the magnetic field, twin boundary velocities were measured in Ni-Mn-Ga over nearly three decades (in the range of 0.01 - 10 m/s) [16]. The kinetic relation for twin boundary motion was obtained by plotting the discrete velocity values as a function of the driving force.

The results obtained for Ni-Mn-Ga showed that the velocity of an individual twin boundary exhibits a sharp transition from slow (typically below 0.2 m/s) to much faster velocities at a distinct value of the driving force. A physical model was developed to explain this behavior [19, 20] and predicted that the slow velocity regime corresponds to thermally activated motion (where the velocity follows an exponential dependence on the

driving force), while the faster regime describes athermal motion, which follows a square root kinetic relation of the type:

$$v_{TB} = \mu \sqrt{g^2 - g_o^2} \quad (1)$$

Here, μ is a mobility coefficient, g is the driving force and g_o represents the transition value from one mechanism of motion to the other, which is associated with the energy required for twin boundary motion (analogous to the Peierls barrier for dislocation motion).

The value of the transition driving force g_o is 2-10 times larger than the value that corresponds to the twinning stress [6] and is of great engineering importance as it determines the magneto-mechanical response of the MSM alloy at time-scales that are relevant for practical applications. Faran and Shilo showed that the performance of MSM actuators that are operated at frequencies above 1 Hz is determined mainly by g_o , while the twinning stress plays a minor role [6, 7]. In addition, it was shown that the experimentally validated kinetic relations can be implemented in simple models that accurately predict and capture the dynamic response of an actual MSM Ni-Mn-Ga actuator [21].

The above discussion emphasizes the importance in experimentally measuring the transition driving force g_o . This information is essential during the development of improved MSM crystals as well as for quality control and regular production of existing compositions. Despite the satisfactory results obtained using the pulsed magnetic field method, it is relatively time-consuming and requires a large number of individual pulsed experiments to obtain the full kinetic behavior of a given crystal. In addition, a given set of pulsed magnetic field experiments typically provides kinetic information that

characterizes only a small fraction of the tested crystal's volume. For example, under a 100 μs long magnetic pulse, at a velocity of 1 m/s, the twin boundary propagates about 0.1 mm. For a crystal whose length is 5 mm, the volume covered by the moving twin boundary during this pulse is only about 2% of the total volume of the crystal, thus providing only local information on twinning kinetics. Moreover, applying a well-controlled magnetic pulse at the microsecond time scale requires a complex experimental magnetic assembly, which is suitable mainly for small sized samples, typically not larger than 5 mm in length (see also similar pulsed magnetic field experiments reported by Ullakko et. al., Refs. [22, 23])

In principle, uniaxial loading experiments can be used for measuring twin boundary dynamics at high rates and for identifying g_0 . Recently, Zreihan et al. performed sets of such experiments at different rates and showed that, for type II twins in monoclinic Ni-Mn-Ga, the plateau stress in the stress-strain curves increases at high rates [24]. In their fastest experiment, an almost complete twinning reorientation was obtained within 0.5 s, by going to the strain rate limit of a conventional material testing machine. Yet, the highest twin boundary velocity they obtained was 10^{-2} m/s, while the transition to the fast regime of the twin boundary motion occurs at velocities of approximately 0.2 m/s. Thus, these experiments could not reveal the value of g_0 .

In this paper, we present an experimental approach that is simple, relatively inexpensive and easy to operate, which allows extraction of the full twin boundary kinetics in a given MSM crystal from a single experiment. The tested MSM crystal is subjected to a uniaxial mechanical pulse in the ms time scale, while the displacement and force are measured simultaneously. Loading conditions are designed such that the strain

rate during the mechanical pulse varies from zero (at rest position) up to about 20 s^{-1} . Under these conditions, twin boundary velocity varies within the interesting kinetic regime, and the important kinetic parameters can be extracted. By comparing the obtained measurements with high-speed optical images that allow tracking the motion of individual twin boundaries, we conclude that the simple setup is adequate for obtaining the kinetics of an MSM single crystal. In particular, we show that this method allows the identification and extraction of the transition driving force from slow to fast twin boundary motion.

2. Experimental Setup and Test Procedure

The custom-made mechanical setup is shown in Figure 6.1. A commercial push-pull solenoid (GEEPLUS 301F) is used for applying uniaxial compression to the sample. This actuator is able to produce a mechanical load larger than 30 Newtons over a stroke of 2 mm within less than 15 ms. These capabilities are suitable for the stress and strain requirements (up to 10 MPa and 10%, respectively) of typical samples with a cross-section area below 3 mm^2 and length below 20 mm.

The tested sample is placed within a designated groove in the base frame, between the solenoid's push rod and rigid support. In order to avoid proximity of the magnetic flux lines in the ferromagnetic push rod to the tested ferromagnetic sample (which may induce an additional, undesired, magnetic driving force for twin boundary motion), a 6 mm long aluminum rod with diameter of 4 mm was firmly attached (glued) to the front end of the push rod, i.e., to the end that forms contact with the sample (Figure 6.1 (b)).

A miniature force sensor, FlexiForce, type A-201, with a thickness of 0.2 mm is placed between the sample and the base frame and measures the compressive force

developed in the sample. The force sensor has a typical response time of 5 microseconds. The system is designed to accommodate samples of up to 20 mm in length. For shorter samples, like the 5 mm long crystal reported in this work, an additional rigid steel spacer was inserted between the sample and the force sensor (Figure 6.1 (b)).

The position of the solenoid's push rod is measured continuously using an optical sensor, MTI 2100 Fotonic sensor, which tracks the back end of the push rod. The optical sensor has a resolution of about 1 μm and a frequency response of 150 kHz. A thin alumina sheet was glued to the push rod's back end to improve the reflectance of the optical signal Figure 6.1 (c)). Since the plunger is in direct contact with the sample's end, displacement measurement of the push rod provides approximate change in the length of the tested sample, which allows calculating its macroscopic strain (the total displacement error introduced by elastic deformations of the push rod, the extension aluminum rod and the steel spacer is less than 0.3 μm).

Overall, the mass of the plunger including the added parts described above is 17 g. Acceleration of this finite mass has some inertial effect, particularly during the first stages of the loading pulse. However, the force sensor measures the resultant force applied directly on the tested sample, and thus this effect is already taken into account and does not require a separate evaluation.

We measured the kinetics in a 10M $\text{Ni}_{50.0}\text{Mn}_{28.3}\text{Ga}_{21.7}$ (at %) single crystal obtained from AdaptaMat Ltd. The sample size was $2.5 \times 0.9 \times 5.3 \text{ mm}^3$ when fully elongated, and the sample faces were cut along $\{100\}$ of the parent austenite phase. Loading tests were performed along the long, 5.3 mm, axis of the crystal. All measurements were performed at room temperature, at which the crystal is fully in the

martensite phase. The transformation temperature from martensite to austenite for this composition is about 50 °C. The crystallographic structure of the martensite is monoclinic, which gives rise to the appearance of both type I and type II twinning modes. For both types of twins, the magnitude of the axial twinning strain is about 6% (Refs. [12, 25]). Thus, for a 5.3 mm long sample, a total displacement of about 0.32 mm is expected when the sample is completely switched from one twin variant to another.

Prior to each test, the sample was elongated along its 5mm axis and brought to a state of a single martensite variant. This was achieved by placing it inside a dedicated magnet assembly. The crystal was then inserted into the loading system, and the plunger position was adjusted using a precision linear stage to obtain a small preload of about 0.2 N. This preload ensured that all gaps between the plunger, sample, force sensor, and the rigid support are eliminated prior to the activation of the solenoid.

The proposed setup is positioned under an optical microscope (Olympus BX51) equipped with Nomarski interference contrast imaging and a high-speed camera (Photron's FASTCAM Mini AX200 camera). Fast imaging was performed at a rate of 20,000 frames per second, with an image size of 704 x 384 pixels, and an exposure time of 1.05 microseconds for each frame. An objective magnification of 5 resulted in a field of view of approximately 5.5 x 3.0 mm², which allowed capturing the entire surface area of the sample. Under these conditions, each pixel in the captured image corresponds to 7.9 micrometers on the sample. We emphasize that the use of an optical microscope and a high-speed camera is not an essential part of the proposed method and is employed only to evaluate and validate its performance.

Trained Ni-Mn-Ga single crystals typically contain few twin boundaries that span the entire cross section of the sample. This is characteristic to crystals produced by the former Adaptamat (which are tested in this work) as well as to crystals produced to date by other manufacturers, such as ETO magnetics (see for example Refs. [10, 26–28]). Thus, under most conditions, the number and location of twin boundaries observed at the top surface provides a reliable indication of the bulk structure (e.g., when the distance between adjacent twin boundaries as well as the distance between a twin boundary and the sample edges is larger than the sample's thickness). In addition, previous studies have shown that twin boundary motion is symmetric with respect to tension or compression, during quasi static loading as well as under high rate loading (see, for example Refs. [10, 20, 29]). This can be reasoned by the fact that in crystals that contain few twin boundaries the distance between adjacent twins is large and thus the interaction between twin boundaries is negligible.

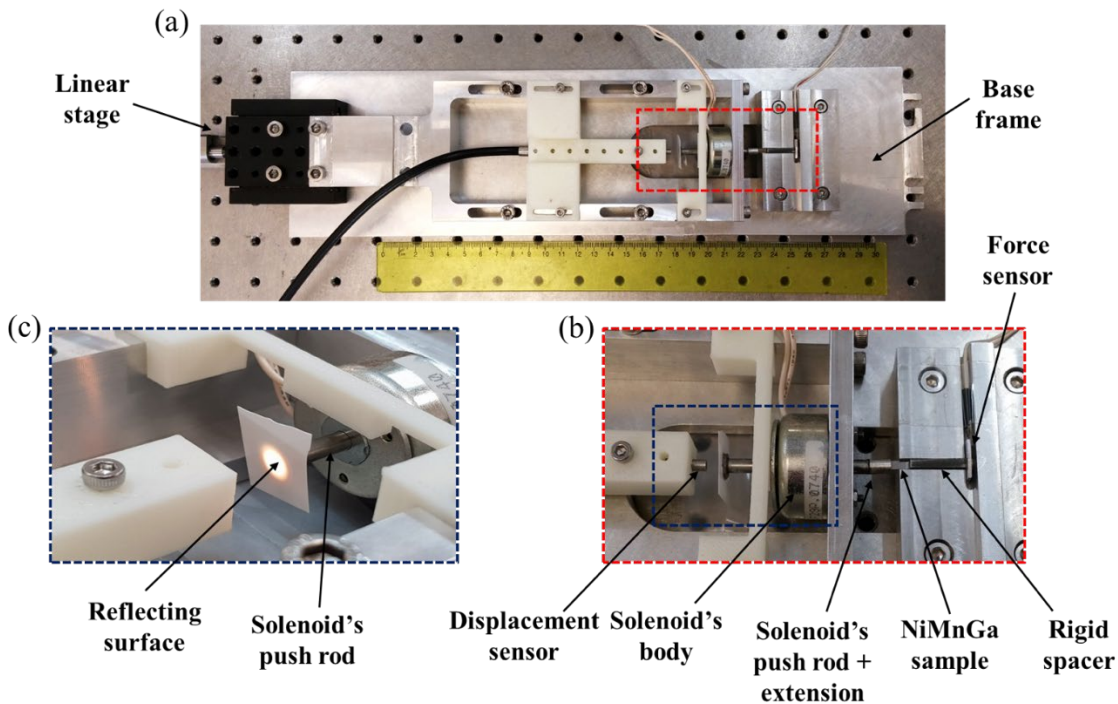


Figure 6.1 (a) Overall image of the base frame and setup for the experiments. The 30 cm ruler serves as a scale bar for the setup. (b) Zoom in on the region of interest that shows setup of sample, force sensor and optical displacement sensor. The solenoid's push rod provides mechanical load, and the attached extension eliminates its magnetic effect on the MSM element. The rigid spacer is required because of the MSM sample dimension. (c) Further zoom in on the solenoid region for detailed optical displacement sensor setup. The reflecting surface is attached to improve the optical signal.

3. Image Analysis

The high-speed camera provided grayscale images with 8-bit dynamic range. This implies that each pixel in the images is assigned with a value between 0 and 255, representative of its grayscale brightness (see scale bar in Figure 6.2). The displacement of the twin boundary along the crystal's long axis was obtained by systematically evaluating pairs of consecutive images (e.g., Figure 6.2 (a) and (b)). First, we calculated the absolute difference between two images, i.e., the brightness difference of each pixel in the two images, as seen in Figure 6.2 (c). An auxiliary parameter α was defined to

provide threshold on the image contrast after obtaining the absolute difference; if the brightness difference for a given pixel is larger than α , the twin boundary displacement is accepted and the pixel is assigned as white, otherwise it is disregarded and the pixel is assigned as black. The resulting white-black binary image of the absolute difference contrast is shown in Figure 6.2 (d). An optimal value of the threshold parameter was set to $\alpha = 50$.

In order to remove noise from the binary contrast image (Figure 6.2 (d)), an additional algorithm was applied on each column of the binary image. The algorithm groups consecutive indices of white pixels for each column and ignores those groups that consist of only one element in the column. If there is an isolated white pixel that does not share a neighbor up or down in the column, the pixel is considered as noise and is assigned as black. The resulting filtered binary image is shown in Figure 6.2 (e). The twin boundary displacement for a given column is taken as the total number of the grouped white pixels after filtering the noise. The total displacement of the twin boundary for a given filtered binary image is taken as the average of the number of grouped white pixels across non-zero columns (i.e., columns in which grouped white pixels were identified). We note that some columns might accept noise as valid twin boundary displacement, for example an isolated pair of two consecutive white pixels. However, since the average displacement across the non-zero columns is considered, most of the noise is suppressed. The above algorithm implies that the minimal detection limit for twin boundary displacement for each time step is two pixels. This limitation corresponds to detection capability of velocities larger than 0.22 m/s. For displacements larger than two pixels, a

resolution better than one pixel is obtained due to the averaging over all columns. Based on the obtained data, we evaluate the velocity resolution to be 0.05 m/s.

A twin boundary in Ni-Mn-Ga lies approximately on $\{110\}$ planes and is thus inclined at nearly 45° with respect to the $\{100\}$ planes of the parent austenite phase, which, in our case, are the surface planes of the crystal. Thus, the magnitude of the displacement of the twin boundary observed on the surface is larger by a factor of $\sqrt{2}$ relative to the normal displacement of the twin boundary (see Ref. [20]). Thus, the “true” displacement of the twin boundary (i.e., perpendicular to the boundary plane) is taken as the value measured on the surface multiplied by a factor of $1/\sqrt{2}$.

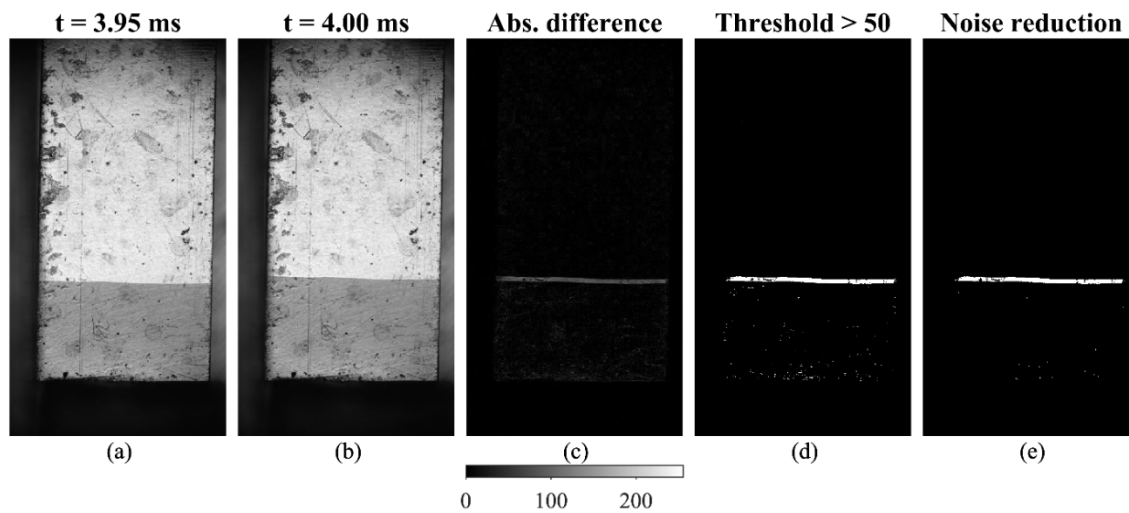


Figure 6.2 Calculating twin boundary displacement from microscope images. (a), (b) A typical pair of consecutive images, showing an individual twin boundary propagating along the sample. (c) The absolute grayscale difference between images (b) and (a). (d) A binary image map obtained from image (c) by setting a threshold value $\alpha = 50$ on the absolute difference. (e) Filtered binary image after noise reduction. The twin boundary displacement is calculated by averaging the number of white pixels in the filtered image (see text for details). The intensity scale bar displays the 256 greyscale levels in images (a), (b), (c).

4. Results

Typical profiles of the force, sample's displacement, and twin boundary displacement as a function of time are shown in Figure 6.3 (a)–(c). The displacement of the sample reaches a maximal value of 0.33 mm after about 12 ms. This value is in accordance with the 6% twinning strain corresponding to $c/a = 0.94$ (c and a are the lattice parameters of the unit cell) and indicates that the entire crystal has completely twinned during 12 ms, which corresponds to an average actuation frequency of about 40 Hz. At the same time, the maximal value of twin boundary displacement recorded by the high speed camera is smaller than 2.5 mm and is equivalent to only 3% strain. This implies that additional twin boundaries, that were not visible in the microscopy images, contributed to the total strain. This point will be elaborated further in this section.

The time derivative of the displacement data (shown in Figure 6.3 (b), (c)) represent the velocities of the sample and of the twin boundary. These data are shown in Figure 6.4 (a) alongside the force signal. Due to the lower sampling rate of the twin boundary displacement relative to the sample's displacement, the resulting twin boundary velocity data is noisier than the sample's velocity data. The twin boundary velocity changes between zero and about 1 m/s, thus covering the entire range that is relevant for practical applications and allows quantifying the full twinning kinetics.

The data displayed in Figure 6.3 (a)–(c) allowed calculating two independent dynamic stress-strain curves, which are presented in Figure 6.4 (b). The first curve (blue in Figure 6.4 (b)) is obtained from the measured displacement of the sample, d_{sample} (Figure 6.3(b)), and the strain is calculated as:

$$\varepsilon_{sample} = d_{sample} / L \quad (2)$$

where $L = 5.3$ mm is the sample length. The second curve (green in Figure 6.4 (b)) is obtained from the measured twin boundary displacement, d_{TB} (Figure 6.3 (c)), and the strain is calculated according to:

$$\varepsilon_{TB} = d_{TB} (1 - c/a) / L \quad (3)$$

Here, we assume that only the single visible twin boundary (whose position is displayed in Figure 6.3 (c)) contributes to the total strain, and thus multiply its displacement by $(1 - c/a)$ (the longitudinal component of the twinning strain). The nearly perfect overlap between the two curves at strains smaller than 0.01 (equivalent to the first 4 milliseconds of the experiment) indicates that this assumption is valid within this time period. For both stress-strain curves shown in (e), the stress is obtained by dividing the measured force by the initial cross-section area of the Ni-Mn-Ga sample.

The shape of the stress-strain curve and the values of the stress shown in Figure 6.4 (b) are significantly different than common slow-rate stress-strain curves due to the high loading rate. In particular, in a typical slow-rate stress-strain curve, the initial sharp increase in stress is associated with a dominant elastic response with negligible motion of twin boundaries [6, 24]. In the dynamic stress-strain curve in Figure 6.4 (b), the initial increase of the stress describes a "pseudo-elastic" response that involves a prominent twinning reorientation, as validated by the microscopy images.

Numbered markings that represent several important points in time are displayed on the different plots in Figure 6.3 and Figure 6.4. In the following, we discuss these points with respect to the characteristics of the experimental setup and the kinetics of twinning in the tested sample.

Point (0) marks a time of about 0.2 ms after the solenoid was activated. During this period, the force sensor shows a small increase in its reading from the preload value. This increase can be associated with the rise time of the magnetic field in the solenoid and the resulting magnetization of the push rod. No displacements were recorded during this short time and thus it does not appear in Figure 6.3 (b) and (c).

Around point (1), which corresponds to $t=1.6$ ms, the displacement sensor and the optical images start detecting motion of the sample and the twin boundary, respectively, while the force shows an initial increase above the value recorded at point (0). The higher spatial and temporal resolutions of the optical sensor relative to the camera images lead to a faster and continuous response of the sample's displacement relative to that of the twin boundary. In accordance, the velocities of the sample and the twin boundary display non-zero values around this point in time.

According to the specifications of the solenoid, its initial response time due to inertia associated with the mass of the push rod is 1-2 ms. This value is in accordance with the observed "dead-time" of about 1.6 ms. Since no motion is detected at times smaller than the point (1), the stress-strain curves during this time also show zero strain.

While point (1) marks the beginning of motion, after an additional 1 ms there is a sharp increase in the velocities of the sample and the twin boundary (marked as point (2)), which takes place during a relatively small increase in the force. The variations of the measured quantities suggest a change in the mechanism of the twin boundary motion. The value of the force around which the transition takes place is approximately 1 N, which corresponds to a stress of 0.45 MPa or a driving force of 30 kJ/m³ (under mechanical loading, the driving force for twin boundary motion is directly related to the

uniaxial stress according to $g = \sigma \varepsilon$, where $\varepsilon = 1 - c/a$ is the twinning strain). The velocity of the twin boundary around this transition point is about 0.25 m/s. This value is in agreement with the one reported earlier for the transition from slower (thermally activated motion) to faster (a-thermal) motion [6, 20].

Approximately 1 ms past point (2), i.e., at $t = 3.7$ ms, another transition is detected and is marked as (3). At this point, the velocity of the twin boundary starts decreasing, while that of the sample keeps increasing together with the force. This behavior can be explained by considering the start of motion of additional twin boundaries in the sample, which are not visible in the optical images. For example, there may be an additional twin that nucleated at the bottom surface of the crystal, opposite to the surface that is observed by the microscope. Recalling that twin boundaries in Ni-Mn-Ga are inclined by 45° with respect to $\{100\}$ planes, the additional twin can expand to a width of 1 mm (at the bottom surface) before penetrating to the top surface and be observed by the microscope.

On the stress-strain curves (Figure 6.4 (b)), point (3) marks the start of a deviation of the curve calculated based on the twin boundary displacement from the curve calculated from the sample displacement. As a result, the twin boundary curve exhibits smaller strains for similar stress values. This also supports our assumption that at this time additional twin boundary/boundaries start propagating in the sample and their motion also contributes to the overall macroscopic strain.

The last marked point (4) occurs at about $t = 4.3$ ms and marks a sudden and sharp decrease in the measured force from its peak value. This sudden drop in the force probably occurs because during this short time-segment the velocity of the solenoid's

push rod is slightly smaller than the contraction velocity of the sample. Yet, the force does not drop to zero, indicating that contact between the push rod and the sample is maintained during the entire time period. After an additional few tenths of a millisecond the force stabilizes, which implies that the velocities of the sample and the solenoid are equal again. The transient difference between the velocities of the push rod and the sample occurs probably due to the inertia of the push rod, which does not allow it to accelerate as fast as the sample's velocity changes.

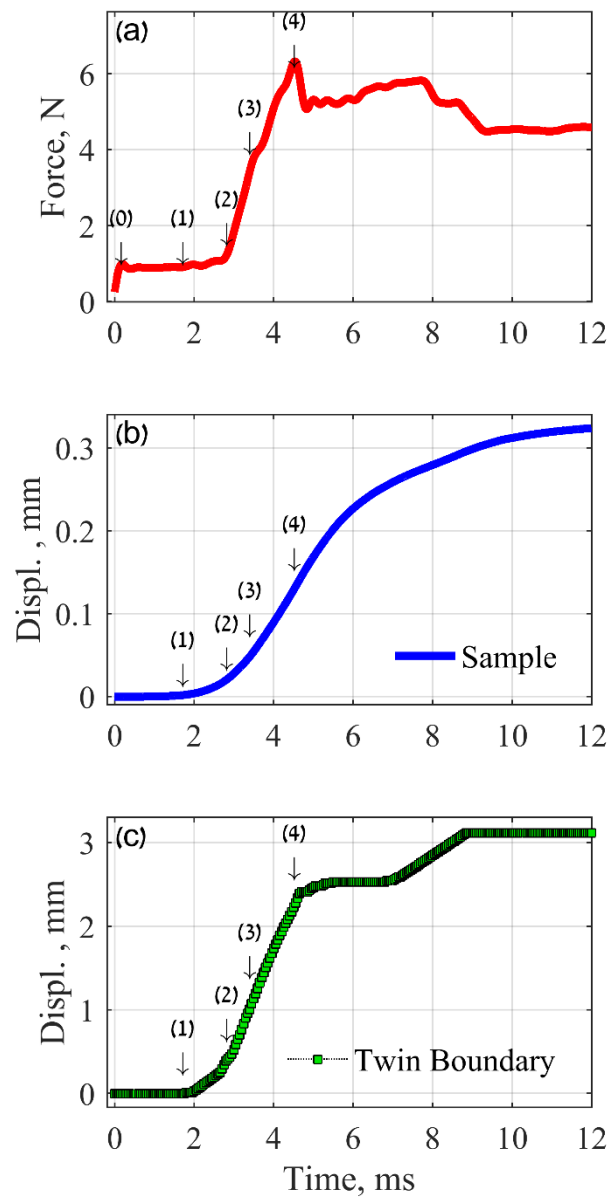


Figure 6.3 Measured profiles of the force (a), sample displacement (b), and twin boundary displacement (c), taken from a pulsed loading test on the sample shown in Figure 6.2. The numbered labels mark the same time points on all charts (see text for details).

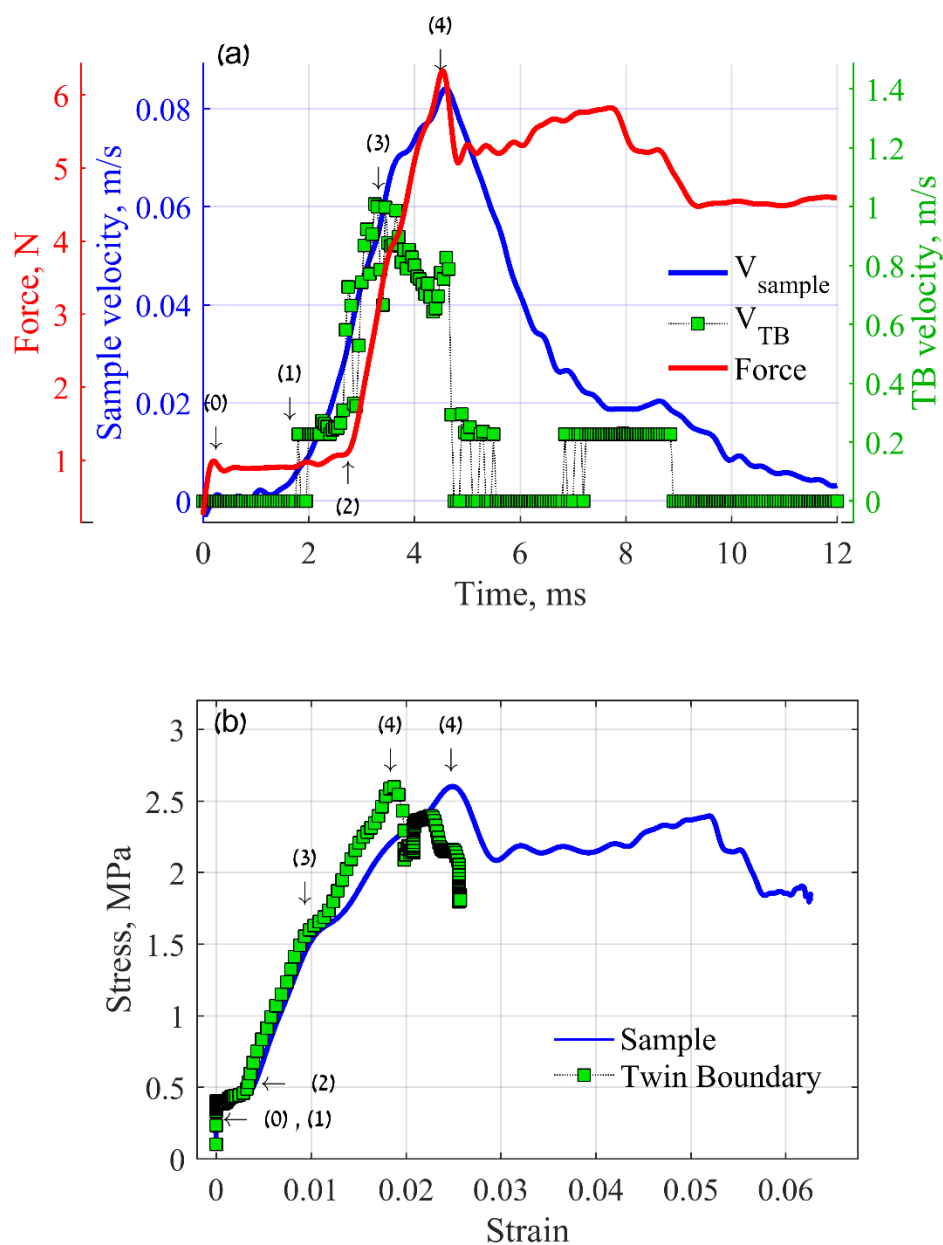


Figure 6.4 (a) Calculated velocities of the sample (blue) and the twin boundary (green), overlaid on the measured force profile (red). (b) Stress-strain curves obtained from the two displacement-force measurements. The numbered labels mark the same time points shown in Figure 6.3.

5. Discussion

The results presented in the previous section demonstrate the capabilities of the proposed experimental setup to measure and evaluate the mechanical response associated with twin boundary motion in an MSM crystal subjected to a millisecond-scale load pulse. In the following, we use the measured data to evaluate and quantify the kinetics of the process. In particular, we extract the kinetic relations for the motion of twin boundaries for two different twin types. Kinetic relations are obtained independently from the measured sample displacement and the twin boundary displacement.

Figure 6.5 presents kinetic analysis for two different experiments on the same crystal. The visible twin boundaries in each case (Figure 6.5 (a), (d)) have different macroscopic orientations with respect to the top surface plane of the sample (former $\{100\}$ plane of the austenite phase). In Figure 6.5 (a), the projection of the twin boundary on the surface plane is generally parallel to the sample's directions, while in Figure 6.5 (d), the projection is oriented at about 7 degrees with respect to the surface plane.

The stress-strain curves obtained for the two experiments (Figure 6.5 (b), (e)) show similar trends: an initial rise of the stress takes place at strain levels of up to about 0.02, followed by stabilization of the stress at a value of about 2.5 MPa during the remaining 0.04 strain range. The sharp stress drop at a strain of about 0.02 in both cases is a result of the experimental setup, as discussed in the previous section, and does not necessarily reflect the intrinsic behavior of the tested material. We note that there are slow-rate loading tests that also display a stress drop due to nucleation and initiation of twin boundary motion. In our experiments, twin boundary motion occurred already

before the stress drop and we did not observe nucleation of new twins during the force drop event.

The dynamics associated with the motion of twin boundaries are best characterized by the kinetic relation, which correlates the velocity of the process to the force that drives it, as presented in Figure 6.5 (c), (f). Note that the kinetic relation figures are based only on data recorded up to the stress peak in Figure 6.5 (b), (e), i.e., when the velocity of the push rod follows the contraction rate of the sample. Figure 6.5 (c) and (f) present two types of kinetic relations. The first is a “macroscopic” kinetic relation that correlates between the contraction velocity of the sample and the applied force (blue line). The second is a "local" kinetic relation that was tracked using the optical images (green marks) and describes the dynamics of the visualized individual twin boundary. The error bars/regime in the velocity values of the twin boundary represent the measurement uncertainty that is dictated by the finite resolution of the optical camera, the filtering algorithm and the frame rate, and is evaluated as ± 0.5 m/s. We note that the scattering of the velocity data is larger than the measurement error (for similar values of the force), and thus indicates variations in the mobility of a twin boundary at different locations along the crystal. This phenomenon was also observed and reported in previous studies employing the pulsed magnetic field method [16, 19, 20].

The vertical velocity axes of the kinetic relations in Figure 6.5 (c), (f) are scaled by a factor of $1 - c/a$, which is the value of the twinning strain. In the case that a single twin boundary propagates along the sample, the two velocities must obey the kinematic relation $v_{TB} = v_{sample} (1 - c/a)$. Indeed, the "macroscopic" (sample) and "local" (twin boundary) kinetic relations obtained during each single experiment show very good

agreement with the above relation during the first few milliseconds of the experiment, when only a single twin boundary propagated in the sample. Once the velocity of the imaged twin boundary decreases, the two relations deviate from each other: the sample's velocity keeps increasing with the force, while that of the imaged twin boundary decreases (see for example at forces larger than 4 N in Figure 6.5 (c)). This behavior results when multiple twin boundaries start propagating in the sample, as discussed in the previous section.

The shape of the kinetic relation of the overall sample and that of the twin boundary show a transition from slow to fast motion, which takes place at a force of about 1 N as indicated by an arrow. This value is equivalent to a transition driving force of about $g_o = 30 \text{ kJ/m}^3$, which is comparable, but lower, than the values reported for the two twin types using the pulsed magnetic field method [20, 28, 30]. Moreover, the good correlation between the kinetic relation obtained from the twin boundary displacement and that obtained from the sample's displacement imply that the latter can serve as a good indication for the dynamic response of the tested crystal, and in particular for the identification of the transition force g_o , which is an important material property. From an engineering perspective, the sample's kinetic relation provides a macroscopic description of the sample's dynamic response. Thus, we conclude that the simple experimental setup presented in this work, even without the addition of an optical microscope and a high-speed camera, can serve as an efficient and convenient method for complete dynamic characterization of Ni-Mn-Ga crystals, and particularly for determining the transition driving force g_o .

The differences between the stress strain curves and between the kinetic relations obtained from the two experiments are minor (compare Figure 6.5(b) to Figure 6.5 (e) and Figure 6.5(c) to Figure 6.5 (f)). This implies that the two twin boundaries shown in Figure 6.5 (a) and Figure 6.5 (d) have similar dynamic behavior. At the same time, the differences in the orientations of the two twins on the observed surface (which are influenced also by the accuracy at which the sample was cut relative to the $\{100\}$ planes of the austenite phase), may suggest that the two boundaries are of different types. In order to rigorously identify the exact characteristics of a twin boundary and correlate them to the measured dynamic response, the following procedure can be followed: (1) create a twin boundary in the tested sample. (2) perform a detailed crystallographic analysis of the twin type with electron or x-ray diffraction methods (e.g., EBSD or XRD). (3) do a mechanical pulse test using the experimental system described in this work. We note that step (2) in the above procedure is beyond the scope of the current work, and thus was not pursued here.

Recent crystallographic studies of twin boundaries in Ni-Mn-Ga using EBSD and XRD have shown that mixed regions of type II and I can coexist along a single macro twin boundary (see Refs. [31–33]), i.e., the same twin boundary can be of type I in certain regions of the sample and of type II in other regions. This complex microstructure is feasible through different arrangements of "micro" twins (typically referred to as modulation twins) across a "macro" twin boundary [31, 32]. With such XRD and EBSD characterization methods, researchers can identify the type of twins, but are restricted to a small local region, typically not larger than few tens of micrometers. At the same time, optical microscopy images (similar to those in Figure 6.5 (a) and (d)) can capture an

entire millimeter-scale macro twin boundary but can only provide the average angle that the projection of the twin boundary forms on the observed surface (see also Refs. [12, 20, 32, 34]). However, when the macro twin boundary is composed of complex arrangements of modulation twins, this average angle is not always a precise indication of the type of the macro twin boundary and at the millimeter-scale most twin boundaries may be composed of a combination of the two types, as explained in Ref. [32]. Our results (Figure 6.5) may represent such a scenario, and in particular indicate that the average inclination angle cannot predict its dynamic behavior. This emphasizes the importance in performing dynamic loading tests, as described in this work, which can characterize the actual kinetic response of a given twin boundary.

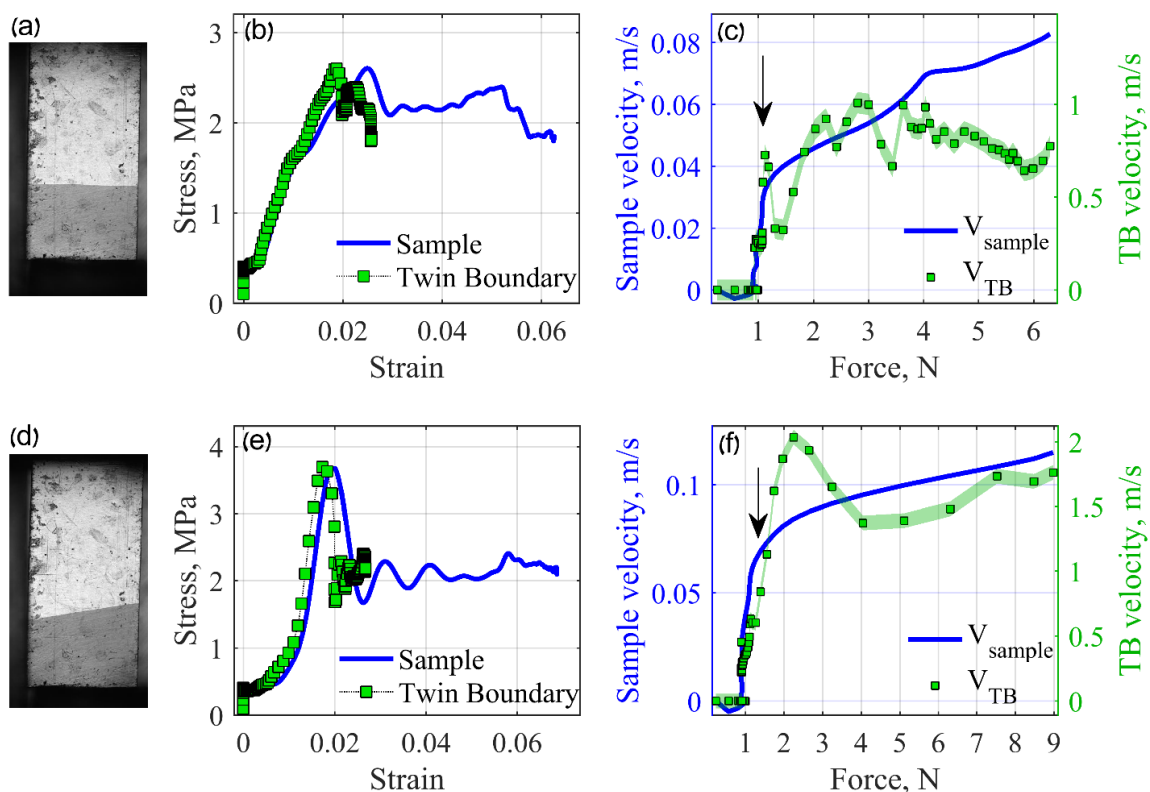


Figure 6.5 Dynamic behavior of Ni-Mn-Ga single crystal obtained from two different experiments conducted on the same sample. Experiment 1: (a), (b), (c). Experiment 2: (d), (e), (f). The visible twin boundary in each experiment is shown in (a) and (d). Stress-strain curves ((b), (e)) are calculated independently for the sample and for the twin boundary from the entire measured data. Kinetic relations ((c), (f)) are calculated independently for the sample and for the twin boundary, and include data recorded up to the stress peak in the stress-strain curves. The shaded area in light green represents the estimated measurement error in twin boundary velocity.

6. Summary

A simple experimental setup is presented that allows both macroscopic and microscopic characterization of the dynamic response of an MSM crystal. Dynamic uniaxial loading using a commercial solenoid leads to twinning reorientation in the tested sample, which is monitored via force and displacement measurements. The collected data reveals the overall kinetics of the sample, i.e., the basic relation between the sample's deformation rate and the force that acts on it. This relation is vital for characterizing the

quality of the crystal and for simulating its dynamic response as a magneto-mechanical actuator. In particular, the experimental conditions are tuned such that the velocity of the sample spans the relevant range for actuation, and allows detecting the transition force from slow thermally activated response to athermal fast response. Complementary high speed imaging allowed microscopic evaluation of the motion of individual twin boundaries within the sample, and for the correlation of this twin boundary motion with the macroscopic response of the crystal.

Acknowledgement

This research was supported by the United States - Israel Binational Science Foundation (BSF), grant No. 2016662, and by the National Science Foundation through Grant No. NSF-DMR-1710640.

References

- [1] K. Ullakko, J.K. Huang, C. Kantner, R.C. O’Handley, and V.V. Kokorin, *Appl. Phys. Lett.* 69, 1966 (1996).
- [2] P. Müllner, V.A. Chernenko, and G. Kostorz, *J. Appl. Phys.* 95, 1531 (2004).
- [3] M. Kohl, M. Gueltig, V. Pinneker, R. Yin, F. Wendler, and B. Krevet, *Micromachines* 5, 1135 (2014).
- [4] M. Chmielus, X.X. Zhang, C. Witherspoon, D.C. Dunand, and P. Mullner, *Nat Mater* 8, 863 (2009).
- [5] E. Faran and D. Shilo, *Exp. Tech.* 40, 1005 (2016).
- [6] E. Faran and D. Shilo, *Appl. Phys. Lett.* 100, 151901 (2012).
- [7] E., Faran and D., Shilo, *Smart Mater. Struct.* 25, 095020 (2016).
- [8] V.A. Chernenko, V.A. L’vov, P. Müllner, G. Kostorz, and T. Takagi, *Phys. Rev. B* 69, 134410 (2004).
- [9] I. Aaltio, O. Söderberg, Y. Ge, and S.-P. Hannula, *Scr. Mater.* 62, 9 (2009).

- [10] L. Straka, N. Lanska, K. Ullakko, and A. Sozinov, *Appl. Phys. Lett.* 96, 131903 (2010).
- [11] R.I. Barabash, C. Kirchlechner, O. Robach, O. Ulrich, J.-S. Micha, A. Sozinov, and O.M. Barabash, *Appl. Phys. Lett.* 103, 021909 (2013).
- [12] L. Straka, O. Heczko, H. Seiner, N. Lanska, J. Drahokoupil, A. Soroka, S. Fähler, H. Hänninen, and A. Sozinov, *Acta Mater.* 59, 7450 (2011).
- [13] A. Sozinov, N. Lanska, A. Soroka, and L. Straka, *Appl. Phys. Lett.* 99, 124103 (2011).
- [14] D. Kellis, A. Smith, K. Ullakko, and P. Müllner, *J. Cryst. Growth* 359, 64 (2012).
- [15] O. Heczko, J. Kopeček, L. Straka, and H. Seiner, *Mater. Res. Bull.* 48, 5105 (2013).
- [16] E. Faran and D. Shilo, *Mater. Sci. Technol.* 30, 1545 (2014).
- [17] Y. Ge, O. Heczko, O. Söderberg, and S.-P. Hannula, *Scr. Mater.* 54, 2155 (2006).
- [18] A. Pramanick, X.-L. Wang, A.D. Stoica, C. Yu, Y. Ren, S. Tang, and Z. Gai, *Phys Rev Lett* 112, 217205 (2014).
- [19] E. Faran and D. Shilo, *J. Mech. Phys. Solids* 59, 975 (2011).
- [20] E. Faran and D. Shilo, *J. Mech. Phys. Solids* 61, 726 (2013).
- [21] E. Faran, L. Riccardi, and D. Shilo, *Shape Mem. Superelasticity* (2017).
- [22] A. Saren, D. Musiienko, A.R. Smith, and K. Ullakko, *Scr. Mater.* 113, 154 (2016).
- [23] A. Saren, T. Nicholls, J. Tellinen, and K. Ullakko, *Scr. Mater.* 123, 9 (2016).
- [24] N. Zreihan, E. Faran, and D. Shilo, *Scr. Mater.* 144, 44 (2018).
- [25] Z. Li, Y. Zhang, C. Esling, X. Zhao, and L. Zuo, *Acta Mater.* 59, 3390 (2011).
- [26] L. Straka, O. Heczko, and H. Hänninen, *Acta Mater.* 56, 5492 (2008).
- [27] R. Chulist, E. Pagounis, A. Böhm, C.G. Oertel, and W. Skrotzki, *Scr. Mater.* 67, 364 (2012).

- [28] N. Zreihan, A. Krimer, D. Avisar, E. Pagounis, D. Shilo, and E. Faran, *Funct. Mater. Lett.* 12, 1850102 (2019).
- [29] E. Faran, I. Benichou, S. Givli, and D. Shilo, *J. Appl. Phys.* 118, 244104 (2015).
- [30] N. Zreihan, E. Faran, and D. Shilo, *Appl. Phys. Lett.* 107, 041605 (2015).
- [31] R. Chulist, L. Straka, N. Lanska, A. Soroka, A. Sozinov, and W. Skrotzki, *Acta Mater.* 61, 1913 (2013).
- [32] O. Heczko, L. Straka, and H. Seiner, *Acta Mater.* 61, 622 (2013).
- [33] H. Seiner, R. Chulist, W. Maziarz, A. Sozinov, O. Heczko, and L. Straka, *Scr. Mater.* 162, 497 (2019).
- [34] L. Straka, A. Soroka, H. Seiner, H. Hänninen, and A. Sozinov, *Scr. Mater.* 67, 25 (2012).

CHAPTER SEVEN: TWIN BOUNDARY STRUCTURE AND MOBILITY

Doron Shilo¹,

Eilon Faran¹,

Bibek J. Karki²,

Peter Müllner²

¹ Technion - Israel Institute of Technology, Haifa 3200003, Israel

² Micron School of Materials Science and Engineering, Boise State University,

Boise, ID, 83725, USA

Published as an Invited Feature Article in Acta Materialia: D. Shilo, E. Faran, B.J.

Karki, P. Mullner, Twin boundary structure and mobility, Acta Materialia 220 (2021)

117316

Abstract

Twinning is an important mechanism of deformation in various crystalline materials, and in particular in shape memory alloys, where it is inherent to the shape memory and super-elasticity effects. This paper presents a generalized methodological approach for analyzing and modeling twin boundary dynamics with particular relevance for shape memory alloys. This approach combines the topological model description of the interface structure at the atomistic/lattice scale with analytical analysis of energy barriers and mechanisms of motion that provide macro-scale kinetic laws for the twin boundary motion. We emphasize the main differences between the topological structures of different types of twin interfaces and their implications for the mobilities of the different twin types. In particular, we elaborate on the relaxed topological structure of type II twin boundaries that contains a coherently faceted structure, where the facets are rational planes that accommodate misfit strain. Then, we clarify the lattice barriers' role in determining the different regimes of the kinetics of twin boundary motion. Further, we develop models leading to analytical expressions for the activation energies of various nucleation processes that dictate the overall kinetics of twin boundary motion and identify the rate-limiting process for the different twin types. In the case of compound and type I twins, the analysis leads to an explicit expression for the magnitude of the twinning stress, revealing a strong dependency on the shear modulus and the twinning shear, which is in excellent quantitative agreement with experimental values reported for BaTiO₃, Ni-Ti, Cu-Al-Ni, and 10M and NM Ni-Mn-Ga. Moreover, our analysis explains the different temperature dependencies of the twinning stress exhibited by the different twin types, and in particular the very low temperature sensitivity of type II twins.

1. Introduction

Twinning is an essential mode of plastic deformation in a variety of solid materials, such as hexagonal close-packed (HCP) metals (e.g., Mg and Ti) [1] as well as nano-crystalline and nano-structures of face-centered cubic (FCC) metals (e.g., Cu and Ni) [2–4]. Besides, twinning reorientation in ferroelectric materials and shape memory alloys (SMA) facilitates significant straining [5], thus providing the fundamental mechanisms for transformation between electric/magnetic/thermal energy and mechanical energy, which are used in a variety of advanced actuation, sensing, and energy harvesting applications [6–9].

Given the importance of twinning to the functionality of advanced materials, an understanding of interrelations between the often-complex twin boundary (TB) structure of different twin types and their mobility is required. Further, the knowledge of the relations between twin boundary mobility and fundamental material properties, such as the twinning shear strain and the shear modulus, is of substantial importance. Such knowledge can be acquired through the development of general yet simple microstructure-based models that can be applied to different material systems (see, e.g., Refs. [10, 11]). This approach should be validated by its power to explain twinning behavior based on fundamental material properties such as lattice parameters, twinning elements, and elastic constants, and on experimental evidence that has been reported in recent years.

In the classical description of twinning, twins are related by a simple shear. The classical model predicts the twinning mode of a given crystal lattice by identifying the twinning elements: the twinning invariant planes \mathbf{K}_1 , \mathbf{K}_2 , the twinning directions $\boldsymbol{\eta}_1$, $\boldsymbol{\eta}_2$,

and the twinning shear strain s [1, 12–14]. Following this description, twins are classified into three types: type I, type II and compound. In type I twins, \mathbf{K}_1 and $\boldsymbol{\eta}_2$ are rational, while \mathbf{K}_2 and $\boldsymbol{\eta}_1$ are irrational. In type II twins \mathbf{K}_1 and $\boldsymbol{\eta}_2$ irrational while \mathbf{K}_2 and $\boldsymbol{\eta}_1$ are rational. In compound twins, all four twinning elements are rational. In tetragonal martensite (e.g., BaTiO₃ [15], non-modulated Ni-Mn-Ga [16]) only compound twins exist, while all three twin types can exist in lower symmetry structures, such as monoclinic (e.g., NiTi [17], 10M Ni-Mn-Ga [18]) and rhombohedral and hexagonal (e.g., Cu-Al-Ni [19], Ti-Al [20]) martensite.

Experiments indicate that the dynamics of type II twins are fundamentally different from those of type I twins. Type II twins display smaller twinning stress values than type I, as reported for several material systems, e.g., Ni-Mn-Ga, Ni-Mn-Sn, and Cu-Al-Ni [18, 19, 21]. For these materials, the room temperature twinning stress of type II twins is smaller than that of the conjugate type I twins by at least a factor of 5 [18, 22, 23]. Previous studies by several research groups, focusing mainly on the Ni-Mn-Ga system, have attempted to explain these differences based on the complex twinned microstructure occurring at various length scales [24–29]. Here, we analyze and explain the different mobilities of type I and II twins based on the periodicity of the lattice as a source for energy barriers and the different lattice-scale topological structures.

Moreover, the twinning stress of type II twins shows a very weak, in some cases indiscernible, temperature sensitivity (e.g., Ni-Mn-Ga, Cu-Al-Ni [30–32]). This is in contrast to the behavior of type I and compound twins, which typically display an increase in twinning stress as the temperature is decreased relative to the martensite to austenite transformation temperature [21, 32–34]. Such behavior indicates that the rate-

limiting process in the motion of type II twins is different from that in compound and type I twins. Moreover, a finite and relatively low twinning stress value of type II TBs was reported for 10M Ni-Mn-Ga at temperatures as low as 1.7 K [30]. This indicates that the mechanisms responsible for TB motion can proceed in an athermal manner even at low driving force values.

The evolution of twinning, i.e., the micro mechanisms and kinetics by which one twin expands at the expense of another through the motion of twin boundaries (TBs), is associated with the nucleation and propagation of twinning defects known as twinning disconnections (TD). A disconnection is a linear defect with both step and dislocation characters [35, 36]. Therefore, a thorough understanding of the origin and dynamics of twinning requires the knowledge and modeling of the defect structure and the corresponding physical mechanisms of motion.

The content, properties, and arrangement of TBs and TDs can be well described with the topological model (TM) [35–38]. Researchers have applied the TM to explain the formation and motion of many interfaces, including precipitate/matrix interfaces, martensite/austenite interfaces, as well as compound and type I twins [1, 38, 39]. Type II twins, which play a dominant role in twinning evolution in many SMAs, pose a challenge for the TM description because of the irrational character of their twinning plane that results in an undefined distance between consecutive twinning planes. Recently, Pond et al. introduced a TM-based description for the formation of type II twins and implemented it for several material systems (e.g. α -U_r, NiTi) [40, 41]. Following these works, possible equilibrium structures of type II twins in Ni-Mn-Ga and Ni-Ti were proposed based on

the TM [42, 43]. Sehitoglu et al. [44] used a combined atomistic-topological approach to describe an equilibrium structure of type II twins in Ni-Ti.

The TM provides a crucial bridge between TB structure and mobility, as it describes the twinned interface as an arrangement of TD defects whose nucleation and motion can be evaluated based on principles of the classical dislocation theory. Specifically, the mobility of a TD is directly related to the fundamental properties of the linear defect: the Burgers vector \mathbf{b} and the core width δ , and potentially other interfacial properties, such as the step height h . For example, small Burgers vector and large core width are expected to promote high mobility of a linear defect. A fundamental feature of any twinning system is the twinning shear strain s . The TM indicates that the magnitude of s is related to the properties of a TD according to $s = b / h$ [36]. Different materials, as well as different twinning systems within the same material, have significantly different twinning shear values [1]. In these cases, the twinning shear may strongly influence the twin boundary mobility.

In this study we analyze the impact of topological parameters on the mobility of twin boundaries. The topological parameters derive from the crystal structure and orientation. To facilitate the crystallographic representation of twinning for modulated martensite in different SMAs, the TM adopts an approximated crystallographic structure that averages out the modulation. (e.g., an effective monoclinic unit cell in 10M Ni-Mn-Ga, Refs [42, 45]). This approach is useful for defining and quantifying the topological parameters of the interface defects (e.g., \mathbf{b} , h). In addition, it allows describing the lattice barrier for TB motion (see Section 4) by a simple periodic function with periodicity on the order of a single lattice spacing of the effective unit cell. By averaging out the lattice

modulation we disregard shuffles required to establish the correct structure. In the cases discussed here, particularly for type II twins in 10M Ni-Mn-Ga, shuffles are very small (substantially below the interatomic distance) and do not include the switching of atoms. In such cases, shuffle does not contribute significantly to twin boundary mobility [1].

In order to establish general relations between the structure of the TB (as described by the TM) and its mobility, the mechanisms of motions for twins in various materials must be clarified. In this context, a mechanism of motion is a description of a sequence of several sub-processes by which the TB propagates and an identification of the rate-limiting process. This knowledge allows the formulation of kinetic relations that quantify the velocity of the interface as a function of the thermodynamic driving force. The term driving force represents the sum of all tractions that act on a twin boundary through various types of external loads (e.g., mechanical, magnetic, electrical), as further explained in Section 2. The kinetic relation is the basic input for models describing the macroscopic mechanical response of materials due to twinning.

Recently, Müllner analyzed the mechanisms of motions associated with nucleation of new TDs, focusing on the relations between the TM of type I and II boundaries and the resulting barriers for TD nucleation [11]. Faran and Shilo suggested analytical models for the kinetic relations of TB motion based on different mechanisms of motion [46, 47, 23]. These studies revealed a clear transition between slow and fast regimes of motion that takes place at driving forces much larger than the value related to the twinning stress [46–49]. The source for this transition is not yet fully explained. Specifically, it is unclear if this source is different for type I and II twin boundaries or if this transition is expected to appear in other SMA.

This paper is organized as follows: Section 3 presents several basic concepts that are essential for the analysis of TB motion in a variety of material systems, focusing on the definitions and application of the driving force and kinetic relations. Section 3 contains a basic description of the structure of a twinning interface based on the TM. In Section 4 we present the energy barriers that are imposed by the lattice and resist the motion of the TB, which leads to the classification of different regimes of the twin boundary motion. Section 5 presents an analytical formulation of the activation energies of different processes that occur during the twin boundary motion. In Section 6 we focus our analysis on TB motion in the slow rate regime and identify the rate limiting process that determines the dynamics of different twin types. Further, we obtain explicit expressions for the twinning stress for the driving force regime where thermal activation dominates the kinetic relation and for the different nucleation energies that were developed in Section 5. In Section 7 we employ the insights presented in the previous sections to explain the available results for the motion of different twin types in different materials systems. Emphasis is given to results reported on ferromagnetic SMA 10M Ni-Mn-Ga because TB motion in this system was widely investigated by several research groups with high quality single crystals.

2. Definitions and Basic Concepts

When discussing the motion of TBs, several basic concepts should be defined and clarified to allow for a general description that is valid for a variety of material systems. We start with the concept of the *thermodynamic driving force* (*driving force* in short) g , which is well known from the field of phase transformations, and represents the change in free energy due to the transformation from one state (or phase) to another [50–52]. For

the case of a TB, the *thermodynamic driving force* is the derivative of the TB energy \bar{U}_{TB} (per unit area) with respect to the propagation coordinate z normal to the TB plane:

$$\mathbf{g} = -\frac{\partial}{\partial z}(\bar{U}_{TB}) \quad (1)$$

The driving force has the dimension of energy per unit volume. Equation (1) represents a continuum (macroscopic) model, and the definition of \bar{U}_{TB} does not account for local atomistic effects such as the lattice potentials. The influence of the lattice periodicity on the TB energy is introduced in Section 4. A similar expression can be formulated for the case of a linear TD defect [53, 54].

The total energy \bar{U}_{TB} contains several contributions, which represent the strain, electric (e.g., in ferroelectric crystals), and magnetic (e.g., in ferromagnetic crystals) energies that vary due to the TB propagation:

$$\bar{U}_{TB} = U_{TB}^{mech} + U_{TB}^{elec} + U_{TB}^{mag} \quad (2)$$

The use of the *driving force* is general and allows us to decouple the thermodynamic traction applied on a moving material defect from the overall mechanical state of the macroscopic crystal. For example, Equations (1) and (2) show that a ferromagnetic crystal subjected to an external magnetic field results in a non-zero driving force for TB motion, even if there is no mechanical load. In this case, the frequent use of the term *magneto stress*, which is equivalent to the effect of the magnetic driving force (U_{TB}^{mag} in Equation (2)), is ambiguous since it is not a real mechanical stress and does not appear in the basic equations of force equilibrium over the macroscopic crystal. Furthermore, the general formulation of the *driving force* enables accounting for other effects, such as that of demagnetization energy (as in Refs. [47, 55]) or cases where the TB area is not constant.

The *kinetic relation* [51, 56] is a constitutive material law that correlates the velocity of an individual TB to the *thermodynamic driving force*. Different kinetic relations may arise for different ranges of the driving force, but all kinetic relations are determined by properties at the atomistic and mesoscopic scales. Kinetic relations serve as the basic input in models describing the overall twinning dynamics. Specifically, discrete twin boundary dynamic simulations, based on measured kinetic relations, have been demonstrated as a powerful tool for calculating the dynamic response of Ni-Mn-Ga actuators [57, 58]. Kinetic relations can be obtained experimentally by tracking the motion of individual TBs [46, 47] and can also be formulated analytically. To the latter end, one must identify the *mechanism of motion* and formulate the kinetic laws for the rate of this mechanism. Comparing experimental and analytical kinetic relations allows validating the assumptions taken during the analytical approach and extracting values of basic material properties [23, 47].

Another common term in the dynamics of twinning is the *twinning stress*, which is usually obtained from quasi-static uniaxial mechanical experiments at strain rates typically slower than 10^{-2} s^{-1} [59]. Under these conditions, the only non-zero term in Equation (2) is the mechanical energy, $U_{TB}^{mech} = -z \cdot \sigma_{TS} \cdot \varepsilon_s$. Here, σ_{TS} is the twinning stress, which is typically measured along a $\langle 100 \rangle$ longitudinal direction of a single crystal cut with faces parallel to $\{100\}$ planes of the parent cubic phase (e.g., Refs. [60, 19, 61, 21]). ε_s is the corresponding longitudinal strain (i.e., along the same direction as σ_{TS}) associated with TB motion. For example, $\varepsilon_s = 1 - c/a$ in tetragonal martensite. z is the propagation distance normal to the TB plane, to straddle a volume that is transformed due

to the TB motion. Since the twinning shear equals $s = 2\varepsilon_s$, the specific driving force g_{TS} (energy / volume, Equation (1)) associated with the twinning stress is given by:

$$g_{TS} = \frac{\sigma_{TS} s}{2} \quad (3)$$

In cases where the mechanism of motion is thermally activated, the *twinning stress* σ_{TS} depends on the temperature and the applied strain rate (or TB velocity). Therefore, in general, the *twinning stress* is not identical to a barrier for the twin boundary motion.

3. Topological Models for Twin Interfaces

While the classical description of twinning predicts the twinning mode of a given lattice (see Section 1), this model does not establish the micro mechanisms of twinning. For instance, it does not provide insight into the formation mechanism and equilibrium structure of type II twins because the invariant plane \mathbf{K}_1 is irrational in this case [1]. The topological model proposed by Pond and Hirth [36, 37, 39, 40, 62] provides a framework to extensively characterize the defect contents of interfaces, including twinning [63, 64]. The model assumes the formation and growth of terraces separated by disconnections as the mechanism of formation and growth of twins.

In compound and type I twins, the invariant plane of twinning, \mathbf{K}_1 , is rational, and thus disconnections, (\mathbf{b}, h) , are rigorously defined in the interface [37]. For example, for a type I twin, the Burgers vector, \mathbf{b} , of the disconnection is parallel/antiparallel to the shear direction, $\boldsymbol{\eta}_1$, and the step height, h , is equal to the interplanar spacing of the \mathbf{K}_1 plane. The Burgers vector quantifies the lattice displacement required for maintaining a coherent interface, and the step height quantifies the displacement of the interface accompanying the motion of the disconnection. In a relaxed condition, the lowest energy configuration of a TB is a flat \mathbf{K}_1 plane without any disconnections.

The twinning plane of type II twins is irrational, which poses intuitive (but not conceptual) difficulties in describing the topological structure of the interface. This has motivated several studies, both theoretical [40–42, 44] and experimental [65–69] in an attempt to unravel the equilibrium structure of a type II interface. These studies state that an irrational twinning plane possesses high energy, which promotes relaxation of the interface to various types of lower energy configurations. For example, experimental characterization using HRTEM images sometimes reveals a faceted structure [68, 69], while in other cases, the structure relaxes more randomly [65]. Macroscopically, the orientation of the relaxed twinning plane coincides with the irrational plane predicted by the classical theory of twinning.

A flat twinning plane that lies along an irrational crystallographic plane is highly incoherent, since the two twins only share a common lattice direction but not a plane. The incoherency results in a high interfacial energy, and thus the atomistic structure of the type II TB is likely to relax to lower energy configurations [70]. A possible relaxed interface for a type II TB is the formation of a coherently faceted structure [71, 68, 44, 42]. In this description (Figure 7.1), the TB forms facets that lie along low-index planes, separated by equally spaced steps that lie along another low-index plane. The “average” interface plane, formed by the facets and the steps, lies very close to the irrational twinning plane \mathbf{K}_1 , calculated based on the classical theory of twinning. In general, while the low-index facet planes are common to both the parent and the twin, there is some in-plane rotation of the lattices of the parent and the twin within this plane. This rotation results in a misfit of the parent and twin lattices in the facet plane. This misfit can be accommodated either by long range elastic strains, resulting in a fully-coherent interface,

or by an array of misfit screw dislocations, resulting in a coherently faceted interface. For some materials, e.g., Ni-Ti, the misfit screw dislocations coincide with the steps between facets, as demonstrated in Figure 7.1, thus forming an array of equally spaced misfit screw disconnections, characterized by a step height and a Burgers vector [44]. In other materials, such as Ni-Mn-Ga, the direction of the Burgers vector of the misfit dislocation results in steps that rotate the average plane formed by the faceted interface out of the irrational \mathbf{K}_1 plane [42]. Thus, for these materials, the description of the twin boundary as a coherently faceted structure is still an unsolved problem.

At a scale larger than the equilibrium distance between adjacent disconnections (l_0 in Figure 7.1), which is on the order of few nm (Refs. [42, 44] and values in Table 7.2), the strain field produced by the array of dislocations is equal in magnitude but opposite in sign to the strain field produced by the misfit at the faceted interfaces. Thus, the two contributions cancel each other, resulting in zero long-range strains. In materials where the coherently faceted structure is possible, the array of equally spaced disconnections represents a low-energy configuration of the type II TB, and can thus serve as an equilibrium state.

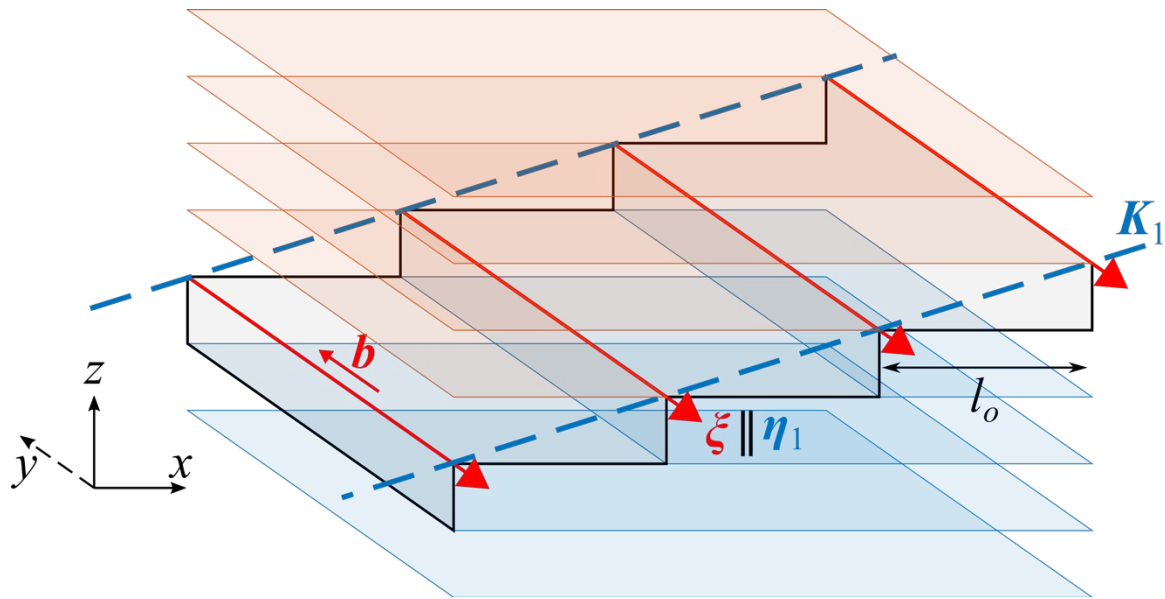


Figure 7.1 Schematic illustration of a coherently faceted type II TB, showing the low index plane facets separated by an array of screw disconnections. b is the Burgers vector of a disconnection, ξ is the disconnection line direction and is (anti) parallel to the shear direction η_1 . The disconnections are equally spaced at a distance l_o , such that the average interface plane coincides with the irrational K_1 twinning plane.

4. Lattice Barriers for Twin Boundary Motion and Classifications of Different Regimes

To define possible mechanisms of motion that lead to twin boundary propagation, we identify the energy barriers that resist each sub-process involved in the motion. Here, we present a general analysis that considers only the periodicity of the lattice as a source for energy barriers. Other, aperiodic barriers may arise due to interactions of the twin boundary with crystal defects, such as surface roughness, precipitates, dislocations, phase boundaries, and grain boundaries. The effects of these barriers depend on the specific problem and the quality of the crystal. The lattice barriers are shown in Figure 7.2 and the different sub-processes are summarized in Table 7.1. Two different barriers separate the

driving force scale into three regions. In each of these regions, different processes take place, resulting in different velocities through different kinetic relations.

Compound and type I TBs are parallel to low-index lattice planes. Such interfaces are subjected to a lattice barrier that resists their motion as a flat plane. The periodicity of this barrier is equivalent to the lattice spacing of the low-index plane, d_{TB} , and its amplitude is denoted as γ_{TB} (energy per unit area), as shown in Figure 7.2 (a). Type II twin boundaries, on the other hand, are characterized by an irrational twinning plane, which poses difficulties in realizing the role of a periodic lattice barrier that resists the propagation of the twin boundary as a flat plane. However, we note that the step height of disconnection on a type II interface has a discrete value. For Ni-Mn-Ga, the step height is of the same order of magnitude as d_{TB} [42]. Moreover, the coherent facets that constitute the coherently faceted structure lie on low-index planes (Figure 7.1 and related discussion), and are thus subjected to a periodic lattice barrier.

An additional periodic lattice barrier is associated with the motion of twinning disconnections. A disconnection line tends to lie along low-index lattice directions, even when the Burgers vector is irrational, e.g., in type I twins [42], and is thus subjected to a periodic lattice barrier that resists its glide, similarly to the Peierls barrier for the glide of ordinary dislocations. The periodicity of the Peierls barrier is the lattice spacing perpendicular to the disconnection line on the glide plane, d_D , and its amplitude is denoted as Γ_D (energy per unit length), as shown in Figure 7.2 (b).

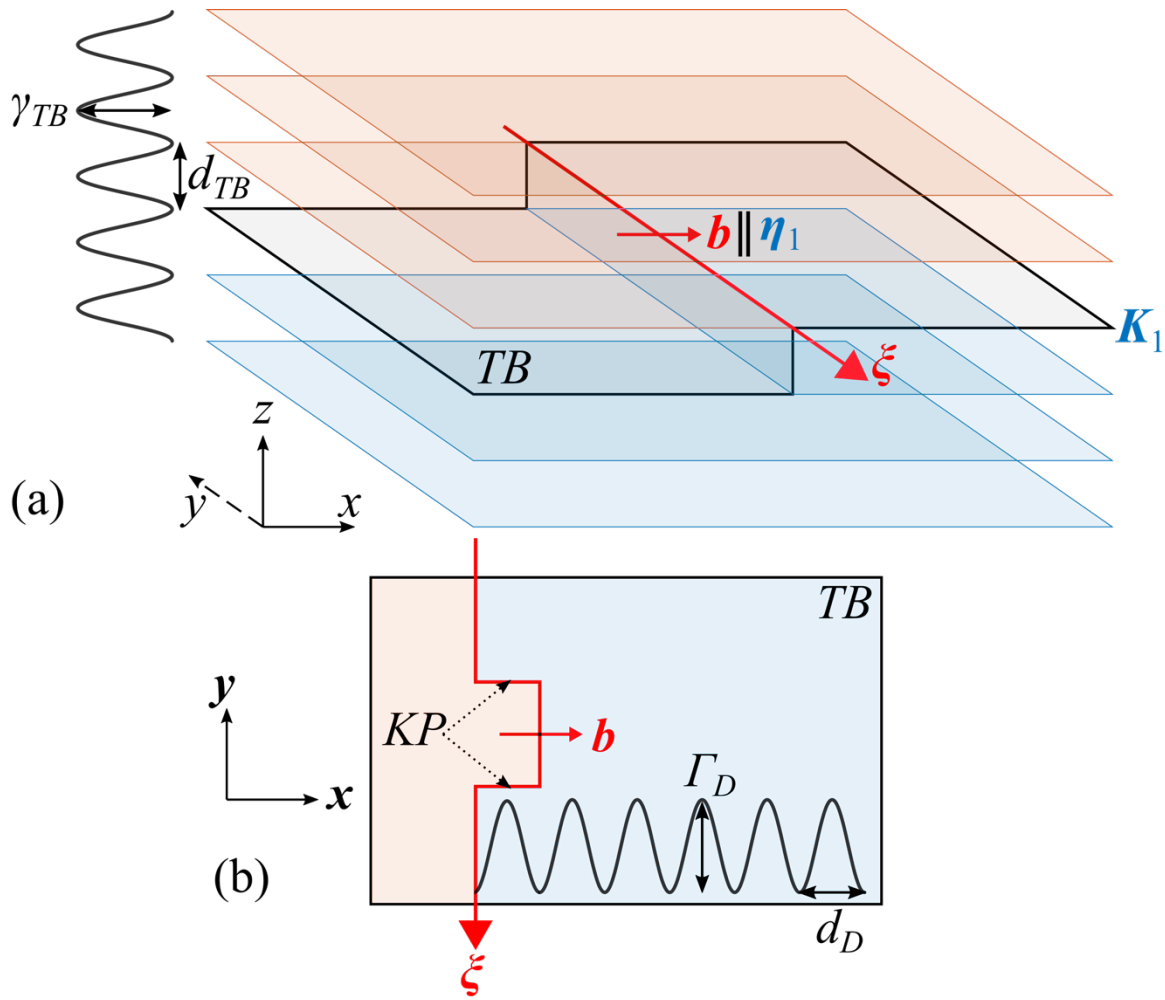
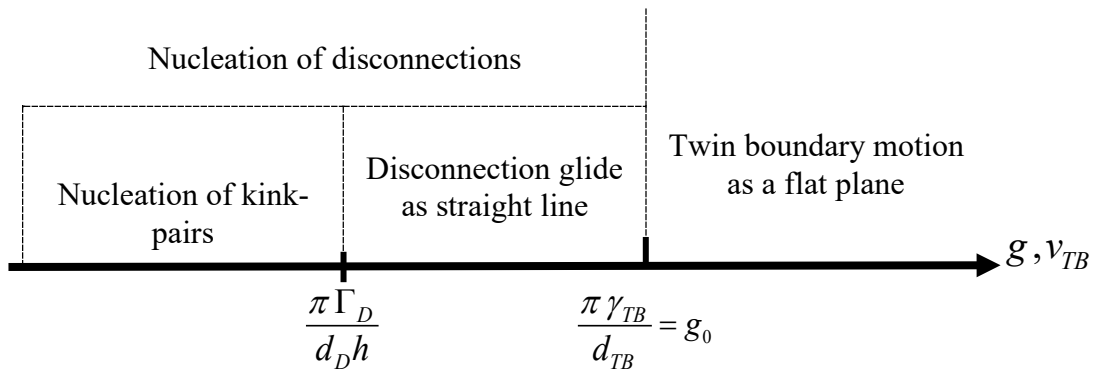


Figure 7.2 Schematic description of the different lattice barriers for TB motion. The illustrations depict a TB with a rational twinning plane K_1 , as in compound and type I twins. (a) The lattice barrier for the motion of the TB as a flat plane along z direction. The barrier is characterized by an amplitude γ_{TB} (energy/ area) and periodicity d_{TB} . The TB can also propagate via the glide of twinning disconnections on the rational twinning plane K_1 , along x direction. b , ξ are the Burgers vector and line direction of the disconnection, and η_1 is the shear direction. (b) Peierls barrier for the glide of a disconnection. The barrier is characterized by an amplitude Γ_D (energy/length) and periodicity d_D . A kink-pair (KP) mechanism allows disconnection motion at driving force values that are smaller than the Peierls barrier.

Table 7.1 Sub-processes in the various ranges of the driving force (g) and TB velocity (v_{TB}). The different ranges of the driving force are defined based on the magnitudes of the lattice barriers Γ_D , γ_{TB} .



To evaluate the effects of the lattice barriers presented in Figure 7.2 on the motion of a TB, we introduce periodic functions that depict the energy landscapes of the lattice barriers, and add them to the total energy of the system. In Figure 7.3 and Figure 7.4 we plot the energy landscapes encountered by a moving TB and a moving TD for two ranges of the external driving force with respect to the lattice barrier amplitude. This representation corresponds to cases where the driving force is the input parameter and dictates the dynamics of the TB or TD through fundamental kinetic relations (see, e.g., Refs. [47, 48]). The analysis presented below shows that the energy landscapes are qualitatively similar for a moving TB and a TD, and thus the schematic plots in Figure 7.3 and Figure 7.4 are valid to both defect types.

For an existing TB, we express the change in energy per unit area U_{TB} , as a function of the boundary position z , where z is the coordinate perpendicular to the boundary plane (Figure 7.2 (a)):

$$U_{TB}(z) = -g z + \gamma_{TB} \sin^2\left(\frac{\pi z}{d_D}\right) \quad (4)$$

The first term in Equation (4) is the work per unit area associated with the motion of the TB under the driving force g along the coordinate z (identical to the continuum quantity $\bar{U}_{TB}(z)$ in Equation (1)). The second term in Equation (4) represents the periodic lattice barrier for TB motion (Figure 7.2 (a)). Analysis of Equation (4) points to two different cases. In the driving force range $g > g_o$, where $g_o = \pi \gamma_{TB} / d_{TB}$ is the driving force associated with overcoming the lattice barrier γ_{TB} , the function $U_{TB}(z)$ decreases monotonically for all values of z (Figure 7.3). In this case, the driving force enables overcoming the lattice barrier, and the twin boundary moves as a flat plane. In this regime, the twin boundary motion is restricted only by the internal friction of the material and does not require a thermally activated process.

If $g < \pi \gamma_{TB} / d_{TB}$ the twin boundary encounters a positive energy barrier (marked as U_{TB}^{bar} in Figure 7.4) as it propagates from one potential well to the next. Therefore, motion in this range of the driving force necessitates nucleation of disconnections and their further glide. This motion type results in a slower advancement of the TB than the motion as a flat plane. For compound and type I twins, whose equilibrium topological structure does not contain disconnections, the nucleation requires overcoming an energy barrier via a thermally activated process, as discussed in Section 5.2. For type II twins, where disconnections are an inherent part of the equilibrium structure, there is a unique mechanism of athermal heterogeneous nucleation of disconnections at the surface, as we discuss in detail in Section 5.3.

A similar analysis is applicable also for the motion of a disconnection. The change in energy (per unit length) of the disconnection is given by

$$u_D(x) = -g h x + \Gamma_D \sin^2 \left(\frac{\pi x}{d_D} \right) \quad (5)$$

Here $-g h x$ is the work per unit length associated with the motion of the disconnection along a distance x under the driving force g , x is the coordinate perpendicular to the disconnection line on the twinning plane (Figure 7.2 (b)), and h is the step height of the disconnection. The second term in Equation (5) represents the periodic lattice barrier for disconnection motion (Figure 7.2 (b)).

When $g > (\pi \Gamma_D) / (d_D h)$ in Equation (5), the function $u_D(x)$ decreases monotonically for all values of x (Figure 7.3) and the disconnection can propagate as a straight line in an athermal manner and its motion is restricted only by the internal viscosity (i.e., does not require a thermally activated process). Alternatively, when $g < (\pi \Gamma_D) / (d_D h)$, the disconnection encounters a positive energy barrier, u_D^{bar} , as it propagates from one potential well to the next (Figure 7.4). Following classical dislocation theory (see, e.g., p. 242 in Ref. [72]), motion of a disconnection in this range of the driving force is possible through nucleation of kink pairs on the disconnection line and the subsequent expansion of the kinks along the disconnection line (Figure 7.2 (b)). The kink pair mechanism for the advancement of a TD is reproduced in atomistic simulations of twinning in ferroelastics (see, e.g., Ref. [73]).

The above discussion implies that under any value of the driving force there exists a mechanism of motion that can lead to the propagation of the TB, as summarized in Table 7.1. In practice, the actual movement mechanism of the TB may be indistinguishable in a specific type of experiment. For example, slow-rate mechanical tests apply a constant controlled strain rate on the sample. The stress reaches a plateau, denoted as the twinning stress, at a value at which the microscopic strain rate induced by the moving twin boundary is equal to the macroscopic strain rate. At stress levels smaller

than the twinning stress, the stress increases, but this does not mean that there is no twin boundary motion in this range.

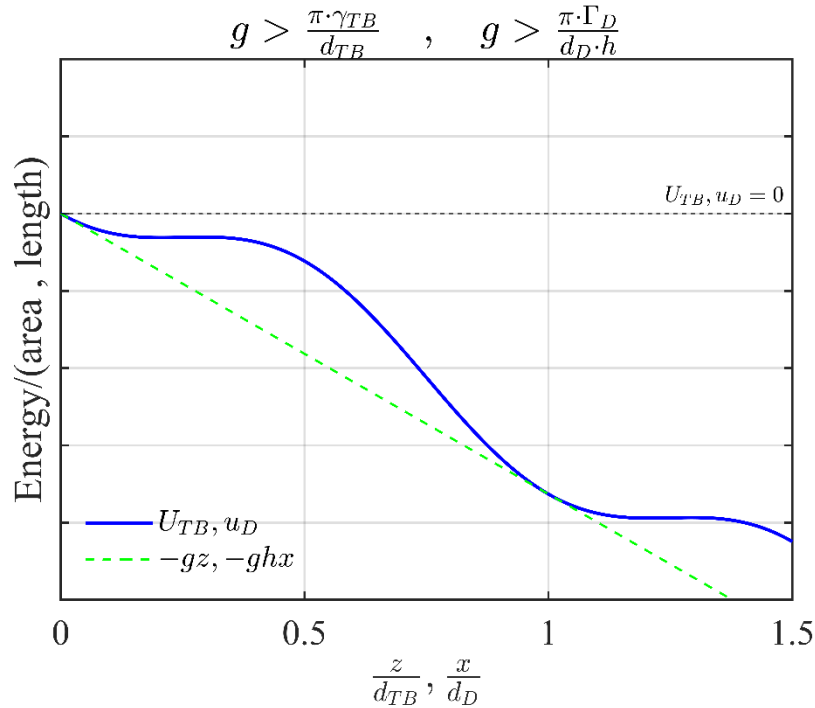


Figure 7.3 Energy profile of a twin boundary U_{TB} (energy/area, Equation (4)) or twinning disconnection u_D (energy / length, Equation (5)), for the case that the driving force g (energy/volume) is larger than the lattice barrier. The dashed green line represents the work associated with the motion of the TB ($-g z$ in Equation (4)) or the disconnection ($-g h x$ in Equation (5)). The normalized coordinates z/d_{TB} , x/d_D represent the directions normal to the TB plane and TD line, respectively (as in Figure 7.2).

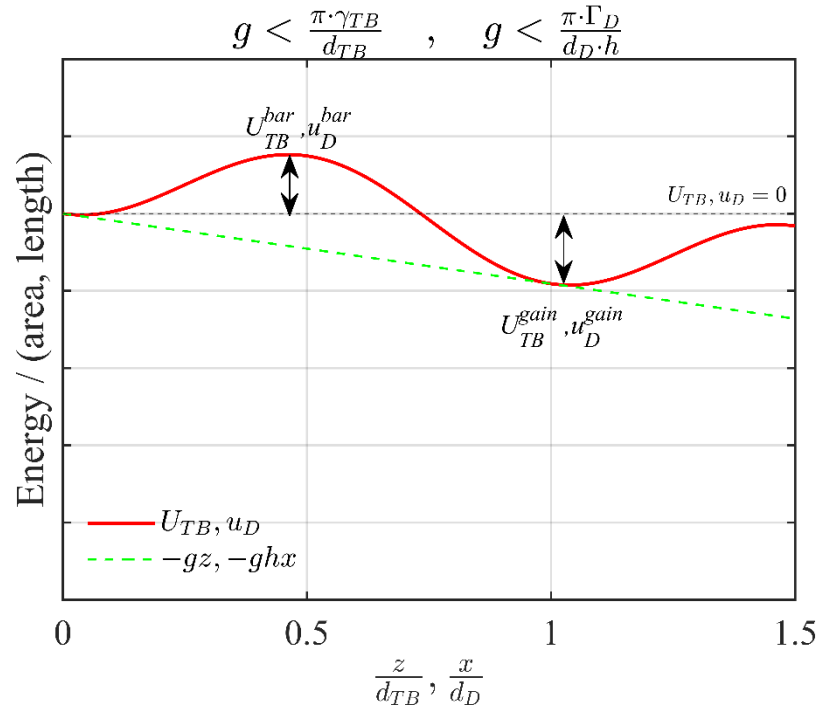


Figure 7.4 Energy profile of a twin boundary U_{TB} (energy/area, Equation (4)) or twinning disconnection u_D (energy / length, Equation (5)), for the case that the driving force g (energy/volume) is smaller than the lattice barrier. The dashed green line represents the work associated with the motion of the TB ($-g z$ in Equation (4)) or the disconnection ($-g h x$ in Equation (5)). The normalized coordinates z/d_{TB} , x/d_D represent the directions normal to the TB plane and TD line, respectively (as in Figure 7.2). The magnitude of the barrier for TB or disconnection motion associated with the lattice potential is marked as U_{TB}^{bar} and u_D^{bar} , respectively. The energy gained due to the local advancement of the TB or the disconnection is labeled as U_{TB}^{gain} and u_D^{gain} , respectively (see discussion on the different energy terms in Section 5.1 and 5.2).

5. Activation Energies for Nucleation Process

In Section 4 we identified two nucleation processes associated with different mechanisms of TB motion, namely the nucleation of disconnections and the nucleation of kink pairs on disconnections. Next, we formulate analytical expressions for the corresponding activation energies of these nucleation processes and discuss their relevance to the motion of the different type of TBs. Here, we distinguish three nucleation processes: the first analyzes the nucleation of kink-pairs on an existing

disconnection line. This mechanism is required for the glide of a disconnection and thus, it is applicable to all twin types. The second process is the homogenous nucleation of disconnection loops that is relevant mainly to compound and type I twins. The third process is the heterogenous nucleation of disconnections at the surface that is unique to the relaxed structure of type II twins.

In the following analysis, we employ isotropic elasticity for evaluating the energies of individual disconnections and disconnection arrays. This provides simple analytical expressions that can be quantified and compared between different material systems. Yet, isotropic elasticity assumes that the shear stiffness is identical in all directions, which is not the case for elastically anisotropic martensitic SMAs. In order to account for this, we associate the shear stiffness μ in the isotropic formulation with the C' elastic modulus of the austenite phase near the martensitic transformation temperature, and not with the isotropic shear modulus G (see values in Table 7.2, Table 7.3, and similar discussion in Ref. [11]).

5.1 Homogeneous Nucleation of Kink Pairs on Disconnection Lines

When the driving force is smaller than the Peierls barrier for disconnection glide (i.e., $g < (\pi \Gamma_D) / (d_D h)$), the glide of a disconnection requires the nucleation and expansion of kinks. This allows part of the disconnection to locally overcome the energy barrier u_D^{bar} , as illustrated in Figure 7.4. Based on the theory of dislocation kinks (Ref. [72], page 242), we consider the homogenous nucleation of a kink-pair on an existing disconnection line.

The activation energy for the homogenous nucleation of a kink-pair with a kink separation y is expressed by:

$$Q_{KP} = u_D^{bar} y + E_{KP}^{self}(y) \quad (6)$$

Here, u_D^{bar} is the energy per unit length required to overcome the periodic Peierls potential of the disconnection and is equal to the first maximum of the disconnection energy $u_D(x)$ (given by Equation (5)), calculated at $x = d_D / 2$ (see Figure 7.4):

$$u_D^{bar} = u_D(x = d/2) = \Gamma_D - \frac{g h d_D}{2} \quad (7)$$

$E_{KP}^{self}(y)$ in Equation (6) is the self-energy of the kink-pair and is generally given by:

$$E_{KP}^{self} = 2 e_f - \frac{e_{int}}{y} \quad (8)$$

where, e_f and e_{int} are formation and interaction energies, respectively. Under the approximation of isotropic elasticity, the two energies scale as $e_f \sim \mu b^2 d_D$ and $e_{int} \sim \mu b^2 d_D^2$ (see Ref. [72], page 244), where μ is the shear stiffness.

Both terms in Equation (6) are positive and increase as y increases. Further, after the nucleation, if y is too small, the attraction forces between the two kinks results in an annihilation of the kinks. Therefore, we must find the minimal value of y for which the nucleated kink-pair tends to grow, i.e., to increase the value of y . For this purpose, we express the energy of an existing kink-pair, for which $x = d_D$, as a function of y :

$$E_{KP}^{existing}(x = d_D) = u_D^{gain} y + E_{KP}^{self}(y) = -g h d_D y + E_{KP}^{self}(y) \quad (9)$$

Here, u_D^{gain} is the first minima of the energy of the disconnection u_D (Figure 7.4). At $x = d_D$, the periodic lattice barrier (2nd term in Equation (5)) is zero, and thus:

$$u_D^{gain}(x = d_D) = -g h d_D \quad (10)$$

The critical length of the kink pair y_c is obtained by finding the first extremum of

Equation (9), i.e., solving $\left. \frac{\partial E_{KP}^{self}}{\partial y} \right|_{x=d_D} = 0$, which provides:

$$y_c = \sqrt{\frac{e_{int}}{g h d_D}} \quad (11)$$

And thus, Equation (6) becomes:

$$Q_{KP} = \left(\Gamma_D - \frac{g h d_D}{2} \right) + \left(2e_f - \frac{e_{int}}{y} \right) \quad (12)$$

Under the conditions of thermally activated motion (i.e., $g < (\pi \Gamma_D) / (d_D h)$), both bracketed terms in Equation (12) are positive, and thus the total activation energy Q_{KP} is always positive. This implies that kink-pair nucleation is not a spontaneous process, and requires some finite activation energy. As we show in Section 7.3, in some twin types and material systems the magnitude of Q_{KP} is comparable to the thermal energy even near 0 K. Thus, a finite concentration of kinks is expected to be always present on the disconnection line even under zero driving force (see also Ref. [74]). At the same time, TB motion requires annihilation of existing kinks and nucleation of fresh kink-pairs. The rate of the later process is determined by the driving force g .

5.2 Thermally Activated Homogeneous Nucleation of Disconnection Loops

In compound and type I twins, the equilibrium structure of the twin boundary is a flat interface that coincides with a low index plane. Thus, when the driving force is lower than the barrier for twin boundary motion as a flat plane, i.e., $g < (\pi \Gamma_D) / (d_D h)$, twin boundary motion requires the nucleation of disconnections on the TB plane. We consider nucleation of disconnection loops in the bulk or nucleation of half-loops at the surface, under the application of an external driving force g . This nucleation process is consistent with the recent description of an evolving topology of type I and compound twins under non-zero loading conditions (see Ref. [75]).

The analytical approach is similar to that employed for the nucleation of kink-pairs, in Section 5.1. The activation energy for the nucleation of a disconnection loop with a radius r is expressed by:

$$Q_{DL} = U_{TB}^{bar} \pi r^2 + E_{DL}^{self}(r) \quad (13)$$

The first term on right-hand side of Equation (13), $U_{TB}^{bar} \pi r^2$, represents the energy required to move the disconnection loop across the lattice barrier perpendicular to the twinning plane under the application of an external driving force g (Figure 7.4 and also in Ref. [47]). The magnitude of the barrier (energy per unit length) is given by

$$U_{TB}^{bar} = \gamma_{TB} - g \frac{d_{TB}}{2} = d_{TB} \left(\frac{g_o}{\pi} - \frac{g}{2} \right) \quad (14)$$

where we substituted $\gamma_{TB} = d_{TB} g_o / \pi$.

The barrier U_{TB}^{bar} is positive within the relevant range of the driving force $g < (\pi \gamma_{TB}/d_{TB})$. The second term in Equation (13) $E_{DL}^{self}(r)$ represents the self-energy of the disconnection loop. The magnitude of $E_{DL}^{self}(r)$ may depend on the type of nucleation process. Heterogeneous nucleation of a disconnection loop, for example at crystal defects, may result in a negligibly small value of $E_{DL}^{self}(r)$. This in turn, may lead to a negligibly small activation energy Q_{DL} . However, given that the equilibrium structure of compound and type I twins contains no disconnections, continuous motion of the TB at a scale larger than the lattice scale requires nucleation events that occur regardless of the TB position within the crystal, i.e., not just in some few specific locations of crystal defects. Thus, we consider here the case of a homogenous nucleation, for which the activation energy given by Equation (13) is always positive and increases as r increases.

After the nucleation event, if r is too small, the attraction forces between segments of the disconnection loop will result in an annihilation of the loop. Therefore, we find the minimal value of r for which the nucleated disconnection loop tends to grow, i.e., to increase the value of r . For this purpose, we express the energy of an existing disconnection loop with radius r :

$$E_{DL}^{existing}(r) = U_{TB}^{gain} \pi r^2 + E_{DL}^{self}(r) \quad (15)$$

Equation (15) describes the energy of a loop that has already “surpassed” the activation energy Q_{DL} (expressed in Equation (13)). Thus, $U_{TB}^{gain} \equiv U_{TB}(z = d_{TB})$ represents the first minima of U_{TB} and it has a negative value (see Equation (4) and Figure 7.4 in Section 4). This distinguishes Equation (15) from Equation (13), where U_{TB}^{bar} represents the first maxima of U_{TB} , and it has a positive value. Further, the lattice potential (second term in Equation (4)) is zero at $z = d_{TB}$. Thus, Equation (15) becomes:

$$E_{DL}^{existing}(r) = -g d_{TB} \pi r^2 + E_{DL}^{self}(r) \quad (16)$$

The self-energy of the disconnection loop $E_{DL}^{self}(r)$ can be expressed using the energy per unit length of the disconnection loop, $q_D(r)$:

$$E_{DL}^{self}(r) = 2\pi r q_D(r) \quad (17)$$

Equation (16) has a maximal value at $r = r_c$. For $r < r_c$, $\partial E_{DL}^{existing} / \partial r > 0$, which means that such a loop will collapse and disappear. For $r > r_c$, $\partial E_{DL}^{existing} / \partial r < 0$, which means that such a nucleated loop will grow and increase its radius. Thus, only loops with $r > r_c$ contribute to the propagation of the twin boundary. For loops with $r \geq r_c$, the minimal value of the activation energy is obtained by substituting $r = r_c$ in Equation (13). The energy per unit length of the disconnection loop $q_D(r)$ is a slow-varying function of r that

changes as $\ln(r)$. For simplicity, Faran and Shilo [47] assumed that $q_D(r)$ can be taken as a constant. Thus, solving $\partial E_{DL}^{existing} / \partial r = 0$ for r_c under these conditions results in:

$$r_c = \frac{q_D}{g d_{TB}} \quad (18)$$

The substitution of Equation (18) in Equation (13) provides an expression for the activation energy for the nucleation of a stable disconnection loop:

$$Q_{DL} = \frac{\pi q_D^2}{g d_{TB}} \left[\frac{3}{2} + \frac{\gamma_{TB}}{g d_{TB}} \right] \approx \frac{\pi (0.5\mu b^2)^2}{g d_{TB}} \left[\frac{3}{2} + \frac{\gamma_{TB}}{g d_{TB}} \right] \quad (19)$$

In the second equality in Equation (19) we introduced a rough approximation based on isotropic elasticity for the line energy of the disconnection $q_D \approx 0.5\mu b^2$ (see page 169, Eqn. 6-51 in Ref. [72]).

The nucleation of a disconnection half-loop on the surface can be treated similarly, resulting in activation energy that is half the value expressed by Equation (19).

5.3 Athermal Heterogeneous Nucleation of Disconnections at the Surface

The topological structure of a coherently faceted type II boundary is inherently different from that of compound and type I, and contains a dense, ordered array of screw, misfit relieving disconnections (Figure 7.1 and related discussion in Section 3). The disconnection array is preserved during motion of the interface. Thus, different nucleation mechanisms of disconnections are required to account for the motion of type II twins. In this section, we discuss a mechanism that enables athermal generation of disconnections on a type II TB. We evaluate and verify our analytical formulations by inserting material parameters for two representative material systems (10M Ni-Mn-Ga and Ni-Ti, see Table 7.2), in which type II twins play a significant role and the coherently faceted structure of the TB is well established.

We propose the following mechanism for the motion of a coherently faceted type II interface (Figure 7.5). The twin boundary contains a regular disconnection array (as shown also in Figure 7.1) in which the disconnection lines are parallel to the free surfaces. The parallelism assumption is valid for example when samples are cut with all faces along $\{100\}$. This is the case essentially for all published experimental results (e.g., Refs. [18, 19, 21–23, 26, 31, 32, 46, 49, 54, 60]). Under an applied driving force, the slow-rate motion of this boundary (from top to bottom) involves two processes. One is the collective glide (from left to right in Figure 7.5) of the disconnection array that advances the twin boundary perpendicular to its plane. Here we consider conditions under which the applied driving force enables disconnection glide over the Peierls barrier. As the disconnections reach the right surface they are emitted to the surface. Thus, a second process is required to occur simultaneously to maintain the topological structure and the motion of the TB: the nucleation of disconnections on the left surface. Next, we discuss conditions under which disconnections nucleate athermally.

Due to the disconnection glide, there is a region close to the left surface that becomes depleted of disconnections. The typical thickness of this region x_o is much larger than the equilibrium spacing l_o between disconnections in the array (as we show next). Therefore, this region is subjected to misfit elastic strains (as discussed in Section 3) that are not accommodated by the disconnections array. The misfit strain builds up energy that grows with increasing x_o . The tendency to reduce the elastic energy in this region results in a restoring force that pulls the array of disconnections back towards the left side. This force is not to be confused with the image force, which is caused due to the

self-strain field of the disconnection. The tendency to reduce the elastic energy also encourages nucleation of disconnections on the left surface.

Recalling the low-energy configuration of the TB structure, presented in Section 3, we assume that the equilibrium distance l_o between disconnections is maintained during the motion of the array. This means that under an external driving force g_{TS} (that corresponds to the twinning stress) all disconnections move approximately the same distance x_o , leaving a region with a width x_o near the left surface that is depleted of disconnections Figure 7.5 (b). After a disconnection is nucleated on the left surface, Figure 7.5 (c), it moves to the right and joins the array of disconnections with equilibrium distance l_o . The array of equally spaced disconnections forms a strain field that cancels out the misfit strain across the interface, except at the depleted region. Due to the misfit-strain in the depleted region, the separation distance between the few furthestmost disconnections at the left side of the array is larger than l_o . As we show later, this does not alter the main results of our analysis, because $l_o \ll x_o \ll L$, where L is the width of the crystal.

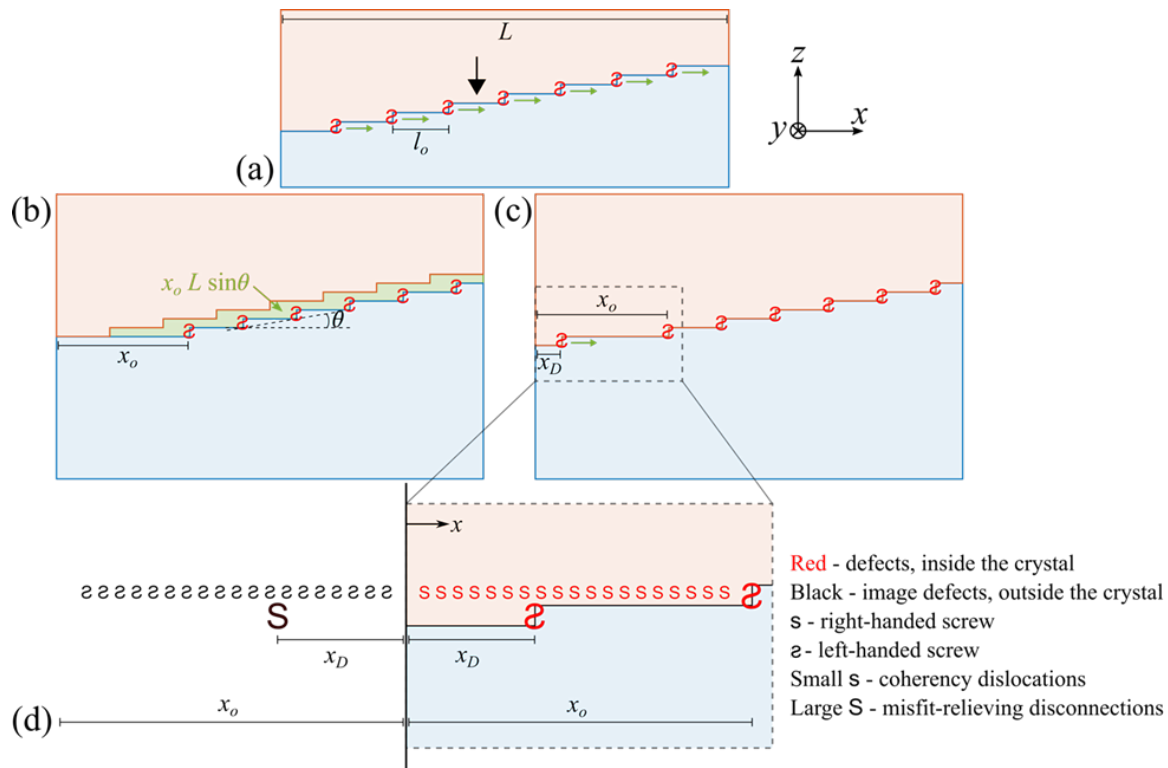


Figure 7.5 Schematic description of the equilibrium coherently faceted type II interface (inset (a)), that contains an array of left-handed screw disconnections, which are marked with an inverted ‘S’. L marks the width of the crystal. Under an applied driving force, the disconnections move to the right (green arrows), transforming material from the top variant to the bottom (the green area in inset (b)), leading to the advancement of the TB downwards (direction marked by the vertical black arrow). The collective motion of the disconnection array creates a “depleted” region of length x_o close to the left surface (inset (b)). To maintain the coherently faceted structure, disconnections nucleate at the left surface and propagate to the right (inset (c)). The position x_D marks the location of a newly nucleated disconnection relative to the left surface. (d) A schematic illustration of the depleted region x_o close to the surface with a representation of the disconnections (large S with Burgers vector b) and coherency dislocations (small s with Burgers vector db_{mis}). Image defects maintain zero stresses on the free surface (the vertical black line).

In the following, we calculate the elastic energy due to the misfit strain. Further, we develop an expression for the equilibrium value of x_o and show that the misfit strain at the depleted region results in an additional energy term that promotes nucleation of disconnections at this surface. We develop an expression for the resulting activation energy and show that the term originated from the misfit strain may be dominant, thus

promoting athermal nucleation. Then, we develop an expression for the equilibrium value of x_o and estimate x_o for Ni-Ti and Ni-Mn-Ga. Further, we show that misfit strain at the depleted region results in an additional energy term that promotes nucleation of disconnections at this surface. We develop an expression for the resulting activation energy and show that the term originated from the misfit strain may be dominant, as is the case for Ni-Mn-Ga.

The strain field caused by the misfit shear in the region x_o is equivalent to a strain field caused by an infinite array of equally-spaced coherency screw dislocations with an infinitesimal Burgers vector $db_{mis} = \varepsilon_o dx$, such that the continuous integration of all Burgers vectors results in $\varepsilon_o x_o$ [64, 65]. The concept of coherency dislocations at an interface was introduced by Olson and Cohen (see, e.g., Refs. [77, 78]), and was successfully applied by Speck *et al.* in modeling coherency strain at film/substrate interfaces of ferroelastic materials [79, 80]. To maintain a zero stress near the left surface, we consider an equivalent array of image dislocations with a Burgers vector of the same size as the coherency dislocations but an opposite direction. The elastic energy associated with the coherency dislocations, per unit length perpendicular to the plane shown in Figure 7.5, can be expressed as [79–81]:

$$E_{elastic}^{coh. disl.} = \frac{\mu (\varepsilon_o x_o)^2}{4\pi} \ln \left(\frac{4L}{x_o} \right) \cong C \mu (\varepsilon_o x_o)^2 \quad (20)$$

where L is typically on the order of 1 mm and C is a constant on the order of unity.

The work associated with the motion of the TB under the driving force g_{TS} , per unit length perpendicular to the plane shown in Figure 7.5, is given by

$$W_{TB} L \cong -g_{TS} L x_o \sin \theta \quad (21)$$

Here, $x_o L \sin\theta$ is the area (in the $x - z$ plane) subjected to twinning reorientation due to the propagation of all disconnections in the array by a distance x_o , where θ is the angle between the TB and the rational twinning plane (Figure 7.5 (b)).

To calculate the equilibrium value of x_o , we minimize the overall energy (per unit length perpendicular to the viewing plane of Figure 7.5) that includes the elastic energy in the depleted region, given by Equation (20), and the work expressed in Equation (21), i.e.,

$$\frac{\partial [C\mu(\varepsilon_o x_o)^2 - g_{TS} L x_o \sin\theta]}{\partial x_o} = 0 \quad (22)$$

This results in:

$$x_o^{eq} = \frac{g_{TS} L \sin\theta}{2C\mu\varepsilon_o^2} \quad (23)$$

A substitution of material parameters listed in Table 7.2 and $C = 1$, $L = 1$ mm in Equation (23) provides $x_o^{eq} \cong 3 \mu\text{m}$ for Ni-Mn-Ga and $x_o^{eq} \cong 35 \mu\text{m}$ for Ni-Ti. These values satisfy the model assumption, $l_o \ll x_o \ll L$, as x_o is larger than l_o by few orders of magnitude and smaller than L by few orders of magnitude.

Next, we consider the lastly nucleated disconnection with a Burgers vector \mathbf{b} , located at a distance $x_D < x_o$ from the left surface, as illustrated in Figure 7.5 (d). This disconnection is subjected to several interaction forces as it travels along x . The resultant force per unit length perpendicular to the plane shown in Figure 7.5, is given by:

$$F = \frac{\mu b}{2\pi} \left[\int_{-x_o}^0 \frac{\varepsilon_o}{x_D - x} dx - \int_0^{x_o} \frac{\varepsilon_o}{x_D - x} dx \right] - \frac{\mu b^2}{2\pi 2x_D} + F_{PK} - F_{Peierls} \quad (24)$$

The first two terms in Equation (24) represent the sum of interaction forces between the left-handed screw disconnection \mathbf{b} located at x_D and the array of coherency dislocations $db_{mis} = \varepsilon_o dx$ located at $0 < x < x_o$. The image forces are accounted for by considering an

equivalent array of image coherency dislocations $db_{mis} = -\varepsilon_o dx$ at $-x_o < x < 0$, as shown in Figure 7.5 (d). The term $\frac{\mu b^2}{2\pi 2x_D}$ in Equation (24) is the image force of the disconnection **b**. F_{PK} is the Peach-Koehler force under the driving force g_{TS} , and $F_{Peierls}$ represents the resisting Peierls force acting on the moving disconnection by the lattice.

Our analysis considers conditions under which the driving force is sufficient to propagate the other disconnections along the TB. This means that the Peach-Koehler force is equal to, or greater than, the resisting Peierls force. Because we analyze a case where the resultant force on the lastly nucleated disconnection is always positive, we assume that $F_{PK} = F_{Peierls}$. Interaction forces due to the other disconnections in the array along the TB (not visible in Figure 7.5 (d)) are not included in Equation (24) because, as stated earlier, at length scales larger than l_o their strain field is canceled by the strain field of the misfit at the interface in their vicinity.

Solving the integrals and adding the disconnection's image force term in Equation (24) results:

$$F = \frac{\mu b \varepsilon_o}{2\pi} \left(\ln \left[\left(\frac{x_o}{x_D} \right)^2 - 1 \right] - \frac{b}{2\varepsilon_o x_D} \right) \quad (25)$$

At the nucleation event $x_D \ll x_o$. In this region, the natural logarithmic term in Equation (25) is a slowly varying positive function, while the last term in Equation (25) is negative and its magnitude increases rapidly as x_D decreases. The lower limit for x_D is taken as a single lattice spacing a , below which elasticity theory fails and the interaction forces described by Equations (24) and (25) remain nearly constant. Taking $x_D = a$, and inserting the values in Table 7.2, we obtain $\ln \left[\left(\frac{x_o}{x_D} \right)^2 - 1 \right] \cong 20$ for both Ni-Mn-Ga and Ni-Ti (the

slow varying logarithmic term “alleviates” the one order of magnitude difference in x_o).

In addition, $\frac{b}{2\varepsilon_o a} \leq 3.5$ for both materials, resulting in:

$$F \cong (20 - 3.5) \frac{\mu b \varepsilon_o}{2\pi} = 8.25 \frac{\mu b \varepsilon_o}{\pi} \quad (26)$$

This indicates that in the range relevant for the nucleation event, $x_D \ll x_o$ the force F is always positive and pushes the disconnection towards the right side. Consequently, the self-energy E_D^{self} of the disconnection that nucleates at the surface (i.e., at $x_D \cong a$) is negative and is given by:

$$E_D^{self} = Y \int_0^{x_D} -F dx_D = -Y a 8.25 \frac{\mu b \varepsilon_o}{\pi} \quad (27)$$

where Y is the disconnection length in the direction perpendicular to the plane shown in Figure 7.5.

Next, we use this result to evaluate the activation energy for the heterogenous nucleation process. In Section 5.2 (Equation (13)) we obtained a general expression for the activation energy for nucleation of a disconnection loop, Q_{DL} . Similarly, the activation energy for nucleation of a linear disconnection, Q_D , is given by:

$$Q_D = U_{TB}^{bar} A + E_D^{self} \quad (28)$$

Here $A \cong Y a$ is the area of the TB that has been reoriented by the formation of the disconnection at $x_D \cong a$, and U_{TB}^{bar} is the energy barrier imposed by the lattice potential, as expressed in Equation (14).

Substituting Equation (14) (for U_{TB}^{bar}) and Equation (27) (for E_D^{self}) into Equation (28) provides

$$Q_D = Y a d_{TB} \left(\frac{g_o}{\pi} - \frac{g}{2} - 8.25 \frac{\mu b \varepsilon_o}{\pi} \right) \quad (29)$$

Recalling that $b/h = s$, and that the periodicity of the lattice potential approximately equals the disconnection step height (i.e., $d_{TB} \approx h$), we obtain the following expression for the activation energy for the nucleation of a disconnection at the surface.

$$Q_D = Y a h \left(\frac{g_o}{\pi} - \frac{g}{2} - 8.25 \frac{\mu s \varepsilon_o}{\pi} \right) \quad (30)$$

In cases where $8.25 \mu \varepsilon_o s > g_o$, Q_D in Equation (30) is negative for any value of the applied driving force g , indicating that this nucleation process can occur athermally. This condition is determined only by material properties and can be evaluated based on the values listed in Table 7.2. For 10M Ni-Mn-Ga, $8.25 \mu \varepsilon_o s \cong 20 \cdot 10^6 \text{ J/m}^3$, and is larger than $g_o \cong 85 \cdot 10^3 \text{ J/m}^3$ by several orders of magnitude (see Ref. [47]). For Ni-Ti, $8.25 \mu \varepsilon_o s \cong 500 \cdot 10^6 \text{ J/m}^3$, indicating that this nucleation process can occur athermally if $\gamma_{TB} < 30 \text{ mJ/m}^2$ (recall that $g_o = \pi \gamma_{TB} / d_{TB}$). Such a value of γ_{TB} is comparable to atomistic calculations reported by Sehitoglu *et al.* [70].

We now re-evaluate the model assumption that the equilibrium distance l_o between disconnections is maintained during the motion of the array, such that all disconnections move approximately the same distance x_o , leaving a region with a thickness x_o depleted of disconnections. To hold this assumption, the lastly nucleated disconnection has to be subjected to a positive force (Equation (25)), until it meets the other disconnections in the array. The force is indeed positive for all values of x_D smaller than $x_o / \sqrt{2}$. For larger values of x_D , Equation (25) predicts that the net force on the disconnection becomes negative. However, when the disconnection reaches a value of x_D that is on the order of x_o , it can be regarded as being part of the disconnection array that composes the TB. This is in accordance with our previous comment, stating that the leftmost disconnections in the array are spread apart a distance that is larger than the

equilibrium value l_o . This relaxation has a minor effect on the elastic energy estimated by Equation (20) and hence on the estimated value of x_o^{eq} provided by Equation (23).

Further, the exact value of x_o has a minor effect on the evaluation of the force F (using Equation (25)) in the range, $x_D \ll x_o$, relevant for the nucleation event. We disregard these effects in the current treatment.

Table 7.2 Typical material parameters for type II twins in 10M Ni-Mn-Ga and Ni-Ti.

	10M Ni-Mn-Ga	NiTi
μ (GPa) *	~ 2 [11, 84]	~ 5 [85, 86]
ε_o	0.0092 [42]	0.049 [44]
s	0.127 [42]	0.280 [44]
θ	4.12° [42]	10.11° [44]
l_o (nm)	≈ 6 [42]	≈ 4 [44]
a (nm)	≈ 0.6 [18]	≈ 0.4 [87]
$ b $ (nm)	0.023 [42]	0.071 [44]
g_{TS} (J/m ³)	$1.3 \cdot 10^4$ [88]	$\sim 3 \cdot 10^6$ [70] **
x_o^{eq} (μm)	~ 3 [Equation (23)]	~ 35 [Equation (23)]

* Value of shear stiffness μ in the isotropic elasticity formulation is related to the elastic constant C' .

** Value is estimated based on the twinning stress $\sigma_{TS} \cong 20$ MPa [71, 89]

Finally, because the model relies on nucleation at the surface, we evaluate the case of sub-mm size samples, e.g., micropillars, where surface to volume ratio is much larger compared to ordinary mm-size crystals. In particular, the relation $l_o \ll x_o \ll L$ (see Equation (23)) remains valid even for values of L that are on the order of a few tens of

microns (typical to micropillars). Thus, the increase in twinning stress observed in some 10M Ni-Mn-Ga micropillars can be associated with the presence of defects that hinder TB motion, and result from the unique fabrication process of the pillar [82, 83]. In case the crystal size is further decreased, such that our model assumptions are no longer valid, we expect the twinning stress to increase, because the proposed mechanism of athermal disconnection nucleation may not be relevant in such scales.

6. Kinetic relations for TB Motion, Rate-Limiting Processes and Twinning Stress

In this section, we formulate relations between the different activation energies developed in Section 5 and the measured quantities that represent the mobility of the different types of TBs, and in particular the twinning stress. This analysis relies on the kinetic relation, which provides an analytical expression for the velocity of a TB as a function of the driving force, and is dictated by the rate limiting process of the overall TB motion. We focus on TB motion in the low driving force range, and discuss separately the situations of compound and type I twins (Section 6.2, which is based on the analysis in Sections 5.1 and 5.2) and type II twins (Section 6.3, which is based on Section 5.3).

6.1 Kinetic Relations

To study the kinetic relations, the twin boundary velocity v_{TB} has to be measured under different values of the driving force. This is in contrast to measuring the twinning stress, which occurs at a constant value, g_{TS} , of the driving force. Kinetic measurements were performed mainly on the 10M Ni-Mn-Ga material system, using μs -scale pulsed magnetic field experiments, as reported by Faran and Shilo [46, 47] and by Saren et al [48, 89]. Recently, fast TB motion in 10M Ni-Mn-Ga was also studied by short ms -scale force pulses [90–92].

Faran and Shilo [46, 47] measured the kinetic relations in a systematic manner by applying magnetic pulses with controlled values of the driving force and tracking the motion of a discrete twin boundary. They captured the kinetic relations for twin boundary motion in 10M Ni-Mn-Ga over wide ranges of driving force and TB velocity. For both type I and II twins, they found a clear transition between two types of kinetic relations, as is explained herein.

For the thermally activated regime of TB motion (i.e. at low driving force), an exponential type kinetic relation for the twin boundary velocity v_{TB} can be assigned:

$$v_{TB}(g) = v_o \exp\left(\frac{-Q(g)}{n k T}\right) \quad (31)$$

In Equation (31) v_o is a temperature-independent pre-exponent term, $Q(g)$ is the activation energy of the rate limiting process, which is a function of the driving force g , and n is a parameter that represents the dimension of the problem (following the analysis of Avrami in Refs. [93, 94]). For example, for the nucleation of a two-dimensional disconnection loop, $n = 3$, while for nucleation of a linear kink $n = 2$.

In slow rate experiments, where a constant deformation rate is applied, the average velocity of an individual TB $v_{TB}^{(TS)}$ (i.e., the velocity associated with the measured twinning stress property) is determined by the number of moving twin boundaries in the sample and the applied strain-rate (e.g., Ref. [88]). Therefore, the set value of the velocity $v_{TB}^{(TS)}$ in Equation (31) determines the twinning stress σ_{TS} or the related value of the driving force, $g_{TS} = \sigma_{TS} s/2$ (Equation (3)), at which TB motion occurs, via:

$$Q(g_{TS}) = n k T \ln\left(\frac{v_o}{v_{TB}^{(TS)}}\right) \quad (32)$$

As we show in the next sections, for type I twins, the activation energy corresponds to Q_{DL} (see Section 6.2) while for type II it corresponds to Q_{KP} (see Section 6.3).

In the study by Faran and Shilo on 10M Ni-Mn-Ga [46, 47], it was found that above some transition value of the driving force g_T , the kinetic relation had the form

$$v_{TB} \propto \sqrt{g^2 - g_T^2} \quad (33)$$

indicating a process that is resisted by viscous forces. Similar types of viscous-controlled kinetic relations were suggested for data measured in other material systems such as Cu-Al-Ni [95] and gadolinium molybdate [96].

Faran and Shilo [46, 47] suggested that the transition at g_T is attributed to overcoming the lattice barrier for the motion of the TB as a flat plane, γ_{TB} (as shown in Table 7.1), resulting in athermal motion of the TB. According to that interpretation, the transition driving force is directly related to the lattice barrier via

$$g_T = g_o = \frac{\pi \gamma_{TB}}{d_{TB}} \quad (34)$$

For type I twins in 10M Ni-Mn-Ga, the transition driving force was $g_o = 105 \text{ kJ/m}^3$ [47], relating to a stress of approximately 1.75 MPa, i.e., about twice the twinning stress for this type of twin [23]. For type II twins, the transition driving force was $g_o = 85 \text{ kJ/m}^3$ [47] related to a stress of approximately 1.4 MPa, i.e., ten times the twinning stress for this twin type [23].

6.2 Motion of Compound and Type I Twins in the Low Driving Force Range

The rate limiting process for the motion of compound and type I twins in the slow velocity range is either the nucleation of kink pairs or nucleation of disconnection loops. The two processes are characterized by their activation energies Q_{KP} and Q_{DL} , given by Equation (12) in Section 5.1 and Equation (19) in Section 5.2, respectively.

In order to evaluate which energy dominates, we consider the ratio between the two activation energies at a driving force equivalent to the twinning stress, i.e., at $g_{TS} = \sigma_{TS} s/2$. Specifically, we use an under-estimation of Q_{DL} (by neglecting the positive γ_{TB} term in Equation (19)) and consider only the dominant term $2e_f$ in the expression for Q_{KP} (Equation (12)). This results in:

$$\frac{Q_{DL}}{Q_{KP}} \geq \frac{3}{2} \frac{\pi (0.5 \mu b^2)^2}{g_{TS} d_{TB}} \left(\frac{1}{2e_f} \right) \quad (35)$$

Using an isotropic approximation for the formation energy of a kink $2e_f \approx \mu b^2 d_D$ (see Section 5.1), and substituting $g_{TS} = \sigma_{TS} s/2$, $b = h s$ and $h \approx d_D \approx d_{TB}$, we obtain

$$\frac{Q_{DL}}{Q_{KP}} \geq s \frac{\mu}{\sigma_{TS}} \quad (36)$$

The ratio μ / σ_{TS} is typically several orders of magnitude larger than unity for all material systems and the value of s is typically on the order of 0.1 (see, e.g., values in Table 7.2, Table 7.3). Thus, we can conclude that for the lower driving force range, the activation energy Q_{DL} is much larger than Q_{KP} .

The above discussion implies that in the thermally activated regimes, the nucleation of disconnection loops is the rate-limiting step in the overall motion of the TB for compound and type I twins. Even if the driving force does not allow overcoming the Peierls barrier for disconnection glide, i.e., $g < (\pi \Gamma_D) / (d_D h)$, the thermally activated disconnection glide is still a faster process than the thermally activated disconnection nucleation, because $Q_{DL} \gg Q_{KP}$. Thus, inserting Q_{DL} (Equation (19)) as the activation energy in the kinetic relation for compound and type I twins (Equation (32)) results in:

$$Q_{DL}(g_{TS}) \approx \frac{\pi \mu^2 s^3 d_{TB}^3}{2 \sigma_{TS}} \left[\frac{3}{2} + \frac{2 \gamma_{TB}}{\sigma_{TS} s d_{TB}} \right] = 3 k T \ln \left(\frac{v_0}{v_{(TS)}} \right) \quad (37)$$

Here we used the relations $g_{TS} = \sigma_{TS} s/2$ and $b = h s \approx d_{TB} s$.

Typically, the value of $v_{TB}^{(TS)}$ is smaller than v_o by many orders of magnitude. Therefore, a change of $v_{TB}^{(TS)}$ by an order of magnitude results in a minor change of $\ln(v_o/v_{TB}^{(TS)})$, which is often undetectable due to the inherent stress fluctuations and insufficient repeatability that are common in such experiments. For example, based on intermediate-rate experiments performed on 10M Ni-Mn-Ga single crystals, Faran and Shilo extracted the value $v_o = 6.6$ m/s for type I boundary [47]. A typical twin boundary velocity in a slow rate experiment is $v_{TB}^{(TS)} = 10^{-5}$ m/s [97]. For these values, a change of $v_{TB}^{(TS)}$ by an order of magnitude results in a change of Q_{DL} by 17%, which is comparable to the variations of the approximately plateau stress during the experiment. Thus, the estimation of the term $\ln(v_o/v_{TB}^{(TS)}) \approx 13.4$ can be assumed to be valid in most SMAs. Inserting this approximation in Equation (37) results in:

$$\frac{\pi \mu^2 s^3 d_{TB}^3}{2 \sigma_{TS}} \left[\frac{3}{2} + \frac{2 \gamma_{TB}}{\sigma_{TS} s d_{TB}} \right] = 40 k T \quad (38)$$

Equation (38) allows estimating the magnitude of the twinning stress σ_{TS} , and its temperature dependence, provided that the material properties μ , s , d_{TB} , γ_{TB} are known. We note that a measured value for γ_{TB} is available only for 10M Ni-Mn-Ga.

6.3 Motion of Type II Twins in the Low Driving Force Range

In Section 5.3 we presented a mechanism of motion for type II TBs, which results from the topological structure of this twin type. Our analyses identified that heterogeneous nucleation of disconnections at the surface is essential for TB motion, and an expression for the activation energy for such a nucleation process was formulated in Equation (30). Further, we showed that for certain materials, such as Ni-Mn-Ga, the expression for the activation energy obtains negative values for any value of the applied

driving force, implying that nucleation of disconnections occurs athermally. In these materials the twinning stress of type II TBs is related solely to the glide of disconnections. This is in contrast to the case of compound and type I TBs, for which disconnection nucleation is the rate limiting step that determines the twinning stress (Section 6.1).

Similar to the motion of ordinary dislocations, disconnection glide proceeds through the nucleation and expansion of kink-pairs, where nucleation is typically the rate limiting step. Consequently, for a type II TB, the thermally activated kinetic relation (Equation (31)) is dictated by the activation energy for the nucleation of kink-pairs (Q_{KP} in Equation (12)). The combination of these two expressions, and by substituting $g = g_{TS}$, results in:

$$Q_{KP}(g_{TS}) \approx \left(\Gamma_D - \frac{g_{TS} h d_D}{2} \right) y_c + \left(2e_f - \frac{e_{int}}{y_c} \right) = 2 k T \ln \left(\frac{v_o}{v_{(TS)}} \right) \quad (39)$$

An estimation for the amplitude of the disconnection's Peierls barrier Γ_D can be obtained from the condition $g > (\pi \Gamma_D) / (d_D h)$ that defines the driving force range of athermal disconnection glide, i.e., the driving force required to overcome the Peierls barrier Γ_D at $T = 0$ K. Thus, we can write

$$\Gamma_D \leq g_{TS}(T = 0 \text{ K}) d_D h / \pi \quad (40)$$

By inserting the expression for Γ_D (Equation (40)) and y_c (Equation (11) in Section 5.1) into Equation (30) and rearranging, we obtain:

$$\left(\frac{g_{TS}(T = 0 \text{ K})}{\pi g_{TS}(T)} - \frac{3}{2} \right) \sqrt{g_{TS}(T) e_{int} h d_D + 2e_f} = 2 k T \ln \left(\frac{v_o}{v_{(TS)}} \right) \quad (41)$$

Here, $g_{TS}(T)$ represents the driving force associated with the twinning stress at a temperature $T > 0$ K. Equation (41) may have various solutions for $g_{TS}(T)$, depending on

the ratio between $2 k T \ln(v_o/v_{TB}^{(TS)})$ and $2e_f$. In Section 7.3 we discuss experimental data measured for 10M Ni-Mn-Ga in light of this analysis.

7. Comparison of Model Predictions to Experimental Results

The identification of the different nucleation processes required for TB motion and their associated activation energies (Section 5), as well as the identification of the rate limiting processes for different twin types (Section 6) allows us to quantitatively evaluate our predictions and compare them to experimental results for TB motion. Because the analysis presented in this paper considers only the lattice barrier as the source for the twinning stress, comparison to experiments is meaningful primarily for data measured on high quality single crystals, where the effects of other barriers is negligible. For example, grown Ni-Ti single crystals typically include nanoscale Titanium carbides and Ni-rich precipitates, which strongly influence the mobility of the TB's (see, e.g., [17]). Thus, twinning stress values measured in such cases are expected to be higher than our predictions.

In the following sections we discuss results from slow-rate deformation experiments with strain rates below about 10^{-2} s^{-1} , which have been studied extensively for various shape memory alloys. These low strain rates correspond to the small driving force regime. The primary measured parameter that characterizes TB motion within this regime of motion is the twinning stress (defined in Section 2). Available experimental values for the twinning stress raise several questions, which we address in the following sections by employing the equations developed in Section 6.

In Section 7.1 we explain why the twinning stress at room temperature of type II twins is much smaller than that of type I twins in the same material. In Section 7.2 we

employ Equation (38) to predict the values of the twinning stress of compound and type I twins in different materials, and compare our predictions to experimental data. In addition, we reason the measured temperature dependence of the twinning stress (available mainly for 10M Ni-Mn-Ga). In Section 7.3, we reason the unique temperature insensitivity of type II twinning stress, as demonstrated by very low values measured for 10M Ni-Mn-Ga down to near zero temperatures.

7.1 Differences in Twinning Stress between Twin Types

Available experimental data reveals a large difference between the measured twinning stress of conjugate type I and type II twins in the same alloy, the latter being significantly smaller. This is the case, for example, in 10M Ni-Mn-Ga, where differences as high as one order of magnitude are commonly reported between the twinning stress of conjugate type I and type II twins [18]. Similar relations were reported for conjugate type I and type II twins in Cu-Al-Ni [19, 31] and in Ni-Ti [17, 98, 99].

The term conjugate twins implies that the classical twinning elements of both twins, i.e., twinning planes $\mathbf{K}_1, \mathbf{K}_2$, twinning directions $\boldsymbol{\eta}_1, \boldsymbol{\eta}_2$, and twinning shear s , obey $\mathbf{K}_1^{II} = \mathbf{K}_2^I, \mathbf{K}_2^{II} = \mathbf{K}_1^I, \boldsymbol{\eta}_1^{II} = \boldsymbol{\eta}_2^I, \boldsymbol{\eta}_2^{II} = \boldsymbol{\eta}_1^I$, and $s^I = s^{II}$. Thus, the twinning shears of both types are identical. Moreover, variations in lattice parameters that directly affect the magnitude of the twinning shear, as well as the value of the shear stiffness are identical in the two twin types. The TM shows that the magnitudes of the Burgers vector and the step height of a disconnection in “conjugate” type I and type II twins, are nearly equal (e.g., the calculations performed for 10M Ni-Mn-Ga in [42]). Thus, by discussing differences in the twinning stress between “conjugate” twins in the same alloy we separate the effect of the topological structure of the TB that dictates the rate limiting mechanism of motion,

from the impact of material properties (e.g., shear stiffness twinning shear and lattice spacing), which are discussed in Section 7.2.

The different topological structures of type I and type II twins (Section 3) lead to different rate limiting mechanisms during TB motion (Sections 5 and 6). On the one hand, the motion of type I TB is determined by the rate of homogenous nucleation of disconnection loops on the low index boundary plane, with an activation energy Q_{DL} . On the other hand, the motion of a coherently faceted type II TB is determined by the rate at which disconnections glide on the same low index planes. For type II TBs, disconnection glide is dictated by the nucleation rate of kink-pairs, with an activation energy Q_{KP} . As we showed in Section 6.2, $Q_{DL} \gg Q_{KP}$ for a given material system. Thus, the activation energy for type II TB motion (which is Q_{KP}) is much smaller than the activation energy for type I TB motion (which is Q_{DL}). This implies that the twinning stress of a type II twins is much lower than that of type I and the temperature dependence is much weaker, in agreement with experiemmtal observations.

7.2 Twinning Stress of Compound and Type I Twins

The twinning stress of compound and type I twins in a given material can be approximated based on Eq. (38), provided that the properties $\mu, s, d_{TB}, \gamma_{TB}$ are known.

We first analyze the situation in which the term containing γ_{TB} in Eq. (38) is much smaller than $3/2$, and can thus be neglected (which is the case for 10M Ni-Mn-Ga). This results in a simplified expression for the twinning stress:

$$\sigma_{TS} \cong \frac{3\pi}{160kT} d_{TB}^3 \mu^2 s^3 = \beta \mu^2 s^3 \quad (42)$$

The value of the lattice spacing for twinning d_{TB} is similar for different SMA, and can be taken as $d_{TB} = 0.2$ nm for all materials. Under these conditions, Equation (42) predicts a

linear relation between the twinning stress σ_{TS} and the product $\mu^2 s^3$, with a proportionality factor $\beta = (3\pi) / (160 k T) d_{TB}^3$. This relation, for the twinning stress at the room temperature, is plotted as the solid black line in Figure 7.6 using logarithm scaling of the variables. In this representation, the straight-line has a slope of 1 and it intercepts the vertical axis at β .

Experimental data for different materials is also plotted in Figure 7.6, using the same logarithm scaling. The values of μ and s used for plotting the data for each twinning system and material were reported in the literature and are given in Table 7.3. The dashed line in Figure 7.6 presents the relation express in Equation (42) with a proportionality factor $\beta' = 0.64 \beta$ that best fits the experimental data. The relatively small difference between β and β' can be attributed to the estimations we took in Equation (37), e.g., the value of 13.4 assigned to the term $\ln(v_o/v_{TB}^{(TS)})$, or the factor 0.5 in the isotropic approximation $q_D \approx 0.5 \mu b^2$.

The good fit to a linear dependence of the measured twinning stress with the product $\mu^2 s^3$ (dashed line in Figure 7.6, R -squared larger than 0.99) strengthens the validity of our analysis. In addition, it implies that our assumption $2\gamma_{TB}/(\sigma_{TS} s d_{TB}) \leq 3/2$ is valid in most materials. Recalling that $g_{TS} = \sigma_{TS} s/2$ (Equation (3)) and $g_o = \pi \gamma_{TB} / d_{TB}$ (Equation (34)), the relation $2\gamma_{TB}/(\sigma_{TS} s d_{TB}) \leq 3/2$ implies that $g_o \leq 5 g_{TS}$. This means that for most materials² a transition from thermal activated motion to fast athermal

² Equation (42) does not apply to materials for which the nucleation of disconnection loops is not the rate limiting mechanism. For example, for face-centered cubic (austenitic, twin-induced plasticity, TWIP) steel $\mu^2 s^3$ is in the order of 104 GPa² and Equation (42) predicts a twinning stress about three orders of magnitude higher than actual values. In these materials, substantial deformation by slip precedes the onset of twinning. Twin nucleation results from dislocation reactions at sites of high dislocation density and strong stress concentrations. The stress concentrations result from dislocation pileups of dozens or hundreds of dislocations. Accordingly, dislocation reactions resulting in partial (twinning) dislocations and

TB motion is expected to occur at stress values equal or smaller than 5 times the twinning stress. Measured values of g_o and g_{TS} in 10M Ni-Mn-Ga comply with this condition (see discussion in Section 6.1).

In a rough approximation, at which the temperature effect on the shear modulus and twinning stress is ignored, Equation (42) predicts that the temperature variation of twinning stress of compound and type I twins follows an inverse $1/T$ relation. Data reported in Ref. [32] for a type I twin in 10M Ni-Mn-Ga revealed a linear increase in the twinning stress as the temperature decreases (Figure 7.7). Data measured over a wider range of at least 100 degrees in 10M Ni-Mn-Ga [30, 34, 100] showed a variation that can be interpreted as $\sigma_{TS} \propto 1/T$ (Figure 7.7). A similar dependence was recently reported for compound twins in Ni-Mn-Ga-Co-Cu [101] and type I twins in 4M Ni-Mn-Sn alloy [21]. These observations rely on measurements taken over a relatively narrow temperature range of about 40 degrees.

The calculated temperature dependence according to Equation (42), with μ and s taken as their room temperature values, for type I twin in 10M Ni-Mn-Ga is plotted in Figure 7.7 (blue dashed line), showing a weaker dependence on temperature compared to the measured data. We can reason this difference by considering the effects of the temperature on product $\mu^2 s^3$. Both the shear stiffness (again we refer to μ as the elastic constant C') [102–104], and the twinning strain [105] increase as the temperature is decreased, and thus amplify the $1/T$ dependence in Equation (42). In addition, for materials in which $2\gamma_{TB}/(\sigma_{TS} s d_{TB})$ is comparable to $3/2$, the dependence of γ_{TB} on the

disconnections occur at stresses several orders of magnitude below the stress predicted by Equation (42) [101].

temperature (as was reported in Ref. [106]) also contributes to the temperature effect on the twinning stress.

Table 7.3 Material properties and measured data used for plotting (in Figure 7.6) the room temperature twinning stress of type I and compound twins in several materials.

	10M Ni-Mn-Ga	NM Ni-Mn-Ga	Cu-Al-Ni	Cu-Al- Ni	BaTiO ₃	NiTi
Twin type	Type I	Compound	Compound	Type I	Compound	Compound
μ (GPa)	2 [11, 84]	2 [11, 84]	9.14 [31]	9.14 [31]	50 [107]	5 [85, 86]
s	0.127 [42]	0.36 [108]	0.074 [31, 109]	0.26 [31]	0.0109 [6]	0.2385 [44]
σ_{TS} (MPa) (exp.)	0.8 [18]	11 [110, 111]	2 [19]	> 100 [31]	0.25 [6]	25 [17]

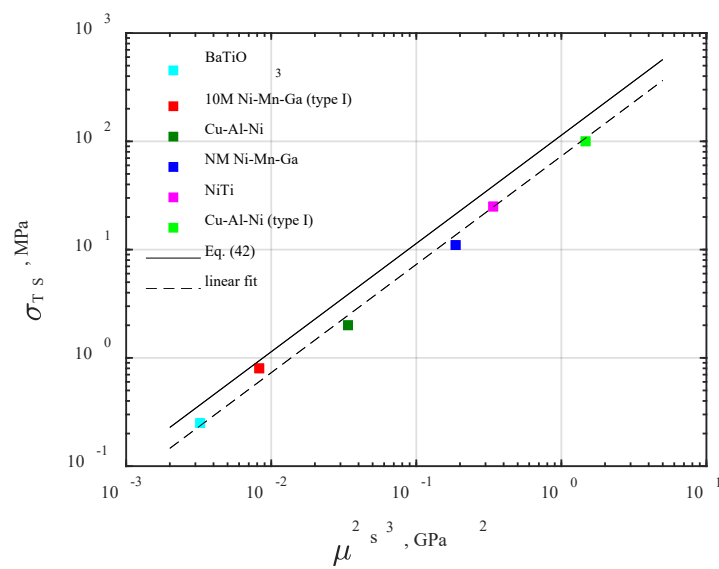


Figure 7.6 Twining stress at room temperature versus the product $\mu^2 s^3$ for compound and type I twins in several SMA systems, presented on logarithm scales. Data for different alloys were taken from Table 7.3. The dashed grey line is a linear fit to the experimental data, exhibiting $R^2 > 0.99$. The solid black line represents the calculated relation given by Equation (42).

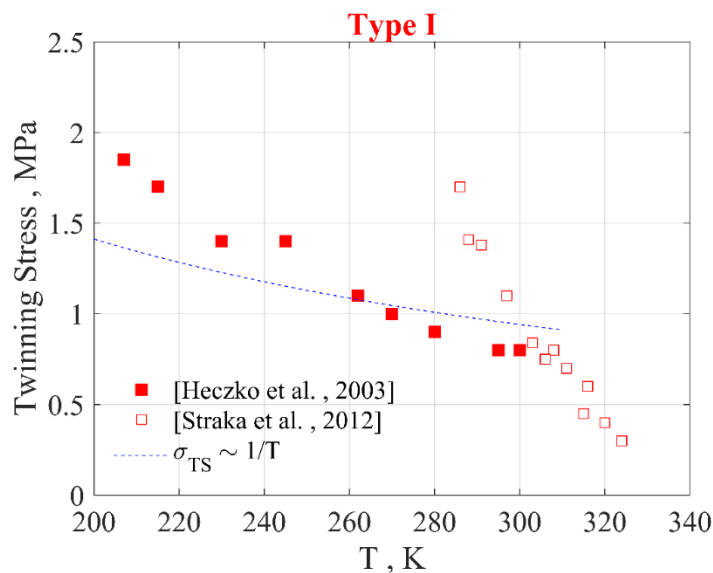


Figure 7.7 Temperature variation of the twinning stress of type I twin in 10M Ni-Mn-Ga. Experimental data is taken from Refs. [32, 34]. The dashed blue line represents the $1/T$ dependence obtained from Equation (42), using the room temperature values of μ and s listed in Table 7.3.

7.3 Twinning Stress of Type II Twins

Information on the twinning stress of type II TBs is available mainly for Cu-Al-Ni and 10M Ni-Mn-Ga, the latter being extensive and measured on high quality single crystals over a large temperature range. In the following, we discuss data obtained for 10M Ni-Mn-Ga, which reveals two interesting behaviors: (1) an extremely small twinning stress of approximately 0.25 MPa at 1.7 K and (2) a modest temperature sensitivity of the twinning stress over a range of 300 K (see Figure 7.8).

In Section 6.3, we obtained an expression for the temperature dependence of the driving force associated with the twinning stress (Equation (41)). We assumed that the type II TB motion follows an exponential type kinetic relation (Equation (31)), which is dictated by the activation energy for the nucleation of kink-pairs Q_{KP} (Equation (12)). This approach is valid in case the activation energy Q_{KP} is smaller than the thermal energy, and resulted in:

$$\left(\frac{g_{TS}(T=0 \text{ K})}{\pi g_{TS}(T)} - \frac{3}{2} \right) \sqrt{g_{TS}(T) e_{int} h d_D + 2e_f} = 2 k T \ln \left(\frac{v_o}{v_{TB}^{(TS)}} \right) \quad (43)$$

The data presented in Figure 7.8 indicates that for 10M Ni-Mn-Ga, $(g_{TS}(T=0 \text{ K})) / (\pi g_{TS}(T)) < 3/2$ over the temperature range $0 < T \leq 300 \text{ K}$. Thus, if Equation (43) is valid then $2e_f$ should be larger than $2kT \ln(v_o/v_{TB}^{(TS)})$, for any temperature up to $T \cong 300 \text{ K}$. Recalling that $2e_f \cong \mu b^2 d_D \cong \mu s^2 d_D^3$ (the first equality follows page 244, Eqn. 8-47 in Ref. [72], and the second equality is obtained by taking $b = h s \approx d_D s$) and plugging typical material parameters for type II twins in 10M Ni-Mn-Ga (Table 7.2), yields $2e_f \cong 2.5 \cdot 10^{-22} \text{ J}$. Thus, already for temperatures as low as $T = 10 \text{ K}$, the term $2e_f$ (which determines the magnitude of the activation energy) is smaller than the thermal energy term, $2kT_{(T=10 \text{ K})} \ln(v_o/v_{TB}^{(TS)}) \approx 30kT_{(T=10 \text{ K})} \cong 4 \cdot 10^{-21} \text{ J}$. This implies that for 10M Ni-

Mn-Ga, the description of the nucleation-controlled kinetics of type II TB motion by an exponential relation (Equation (31), which leads to the formulation of Equation (43)) is not valid. Moreover, because the activation energy for nucleation of kink pairs is comparable to the thermal energy even at very low temperatures, thermally activated disconnection glide, which is weakly dependent on temperature and proceeds at very low stress, is possible down to very low temperatures. This agrees with the experimental data in Figure 7.8.

In other materials, the magnitude of $2e_f$ is larger than the value for 10M Ni-Mn-Ga (e.g., in Cu-Al-Ni it is ~ 20 times larger). However, there is no experimental data on the value of $\sigma_{TS}(T = 0 \text{ K})$ in other materials, and it may be much larger than the value at room temperature, such that $(g_{TS}(T = 0 \text{ K})) / (\pi \cdot g_{TS}(T)) > 3/2$, and $2e_f \gg kT$ over a wide temperature range. Under these conditions the analysis leading to Equation (43) is valid. In such cases, the twinning stress of type II TB is also expected to be larger than the extremely low values measured for 10M Ni-Mn-Ga.

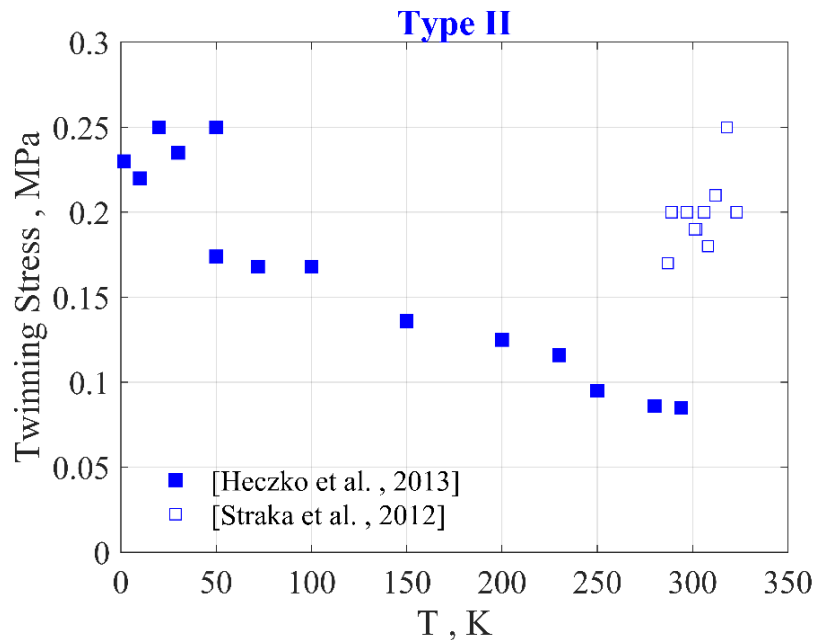


Figure 7.8 Temperature variation of the twinning stress of type II twins in 10M Ni-Mn-Ga. Experimental data is taken from Refs. [30, 32]. The temperature dependence is substantially weaker than that of the conjugate type I twins (Figure 7.7).

8. Summary

This paper combines the TM descriptions for the equilibrium structures of TB in SMA with an analysis of energy barriers and mechanisms of motion. This unified approach provides a general analysis of TB motion and explains experimental findings on TB motion in different SMA systems, in particular in the slow rate regime of TB motion. We identify the topological, structural aspects that control the rate limiting mechanisms of motion of different twin types, and deduce quantitative predictions for the magnitude and temperature dependency of the twinning stress of different twin types.

The slow rate motion of TB is controlled by different rate-limiting processes, which are dictated by the equilibrium topological structure of the TB interface. For type II twins, we discuss the case of a coherently faceted interface, which contains an ordered

array of equally spaced twinning disconnections. We show that for this low-energy relaxed structure, the nucleation of new disconnections at the crystal's surface, which is essential for maintaining the lateral propagation of the TB, can proceed athermally, even at very low temperatures. This explains the lower twinning stress of type II twin relative to its value in the conjugate type I twin, as reported for various materials. In addition, it accounts for the extremely low twinning stress value of type II TB in 10M Ni-Mn-Ga measured at temperatures close to absolute zero.

In compound and type I twins, the equilibrium boundary structure does not contain disconnections. Thus, the rate-limiting step for the motion of the entire TB is the thermally activated nucleation of disconnection loops, resulting in an exponential type kinetic relation. We formulate an expression for the activation energy for nucleation of disconnection loops, and use it to obtain an analytical prediction for the magnitude of the twinning stress. We show that the main material properties that control the twinning stress are the shear modulus μ and the twinning shear s , and obtain a dependence that follows $\sigma_{TS} \propto \mu^2 s^3$. This dependence is in excellent agreement with reported twinning stress in several materials, e.g., Ni-Mn-Ga, Cu-Al-Ni, Ni-Ti and BaTiO₃.

Acknowledgement

This research was supported by the United States - Israel Binational Science Foundation (BSF), grant No. 2016662, and by the National Science Foundation NSF-DMR, grant No. 1710640.

References

- [1] J.W. Christian, S. Mahajan, Deformation twinning, Progress in Materials Science. 39 (1995) 1–157. [https://doi.org/10.1016/0079-6425\(94\)00007-7](https://doi.org/10.1016/0079-6425(94)00007-7).

- [2] M.A. Meyers, A. Mishra, D.J. Benson, Mechanical properties of nanocrystalline materials, *Progress in Materials Science*. 51 (2006) 427–556.
<https://doi.org/10.1016/j.pmatsci.2005.08.003>.
- [3] Y.T. Zhu, X.Z. Liao, X.L. Wu, Deformation twinning in nanocrystalline materials, *Progress in Materials Science*. 57 (2012) 1–62.
<https://doi.org/10.1016/j.pmatsci.2011.05.001>.
- [4] R.J. Asaro, P. Krysl, B. Kad, Deformation mechanism transitions in nanoscale fcc metals, *Philosophical Magazine Letters*. 83 (2003) 733–743.
<https://doi.org/10.1080/09500830310001614540>.
- [5] K. Bhattacharya, *Microstructure of Martensite: Why it Forms and how it Gives Rise to the Shape-memory Effect*, OUP Oxford, 2003.
<http://books.google.co.il/books?id=gas0P67KijcC>.
- [6] E. Burcu, G. Ravichandran, K. Bhattacharya, Large electrostrictive actuation of barium titanate single crystals, *Journal of the Mechanics and Physics of Solids*. 52 (2004) 823–846. <https://doi.org/10.1016/j.jmps.2003.08.001>.
- [7] M. Kohl, B. Krevet, S.R. Yeduru, Y. Ezer, A. Sozinov, A novel foil actuator using the magnetic shape memory effect, *Smart Materials and Structures*. 20 (2011) 094009.
- [8] I. Suorsa, E. Pagounis, K. Ullakko, Position dependent inductance based on magnetic shape memory materials, *Sensors and Actuators A: Physical*. 121 (2005) 136–141. <https://doi.org/10.1016/j.sna.2005.01.001>.
- [9] I. Karaman, B. Basaran, H.E. Karaca, A.I. Karsilayan, Y.I. Chumlyakov, Energy harvesting using martensite variant reorientation mechanism in a NiMnGa magnetic shape memory alloy, *Applied Physics Letters*. 90 (2007).
<http://dx.doi.org/10.1063/1.2721143>.
- [10] E. Bronstein, E. Faran, D. Shilo, Analysis of austenite-martensite phase boundary and twinned microstructure in shape memory alloys: The role of twinning disconnections, *Acta Materialia*. 164 (2019) 520–529.
<https://doi.org/10.1016/j.actamat.2018.11.003>.

- [11] P. Müllner, Twinning stress of type I and type II deformation twins, *Acta Materialia*. 176 (2019) 211–219. <https://doi.org/10.1016/j.actamat.2019.07.004>.
- [12] B.A. Bilby, A.G. Crocker, A.H. Cottrell, The theory of the crystallography of deformation twinning, *Proceedings of the Royal Society of London. Series A. Mathematical and Physical Sciences*. 288 (1965) 240–255. <https://doi.org/10.1098/rspa.1965.0216>.
- [13] M. Bevis, A.G. Crocker, L. Rosenhead, Twinning shears in lattices, *Proceedings of the Royal Society of London. Series A. Mathematical and Physical Sciences*. 304 (1968) 123–134. <https://doi.org/10.1098/rspa.1968.0077>.
- [14] M. Bevis, A.G. Crocker, L. Rosenhead, Twinning modes in lattices, *Proceedings of the Royal Society of London. A. Mathematical and Physical Sciences*. 313 (1969) 509–529. <https://doi.org/10.1098/rspa.1969.0208>.
- [15] Z. Li, C.M. Foster, X. -H. Dai, X. -Z. Xu, S. -K. Chan, D.J. Lam, Piezoelectrically-induced switching of 90° domains in tetragonal BaTiO₃ and PbTiO₃ investigated by micro-Raman spectroscopy, *Journal of Applied Physics*. 71 (1992) 4481–4486. <https://doi.org/10.1063/1.350792>.
- [16] B. Muntifering, L. Kovarik, N.D. Browning, R.C. Pond, W.B. Knowlton, P. Müllner, Stress-assisted removal of conjugation boundaries in non-modulated Ni–Mn–Ga by coordinated secondary twinning, *J Mater Sci*. 51 (2016) 457–466. <https://doi.org/10.1007/s10853-015-9236-1>.
- [17] H. Sehitoglu, I. Karaman, R. Anderson, X. Zhang, K. Gall, H.J. Maier, Y. Chumlyakov, Compressive response of NiTi single crystals, *Acta Materialia*. 48 (2000) 3311–3326. [https://doi.org/10.1016/S1359-6454\(00\)00153-1](https://doi.org/10.1016/S1359-6454(00)00153-1).
- [18] L. Straka, O. Heczko, H. Seiner, N. Lanska, J. Drahokoupil, A. Soroka, S. Fähler, H. Hänninen, A. Sozinov, Highly mobile twinned interface in 10 M modulated Ni–Mn–Ga martensite: Analysis beyond the tetragonal approximation of lattice, *Acta Materialia*. 59 (2011) 7450–7463. <https://doi.org/10.1016/j.actamat.2011.09.020>.

- [19] V. Novák, P. Šittner, S. Ignacová, T. Černoš, Transformation behavior of prism shaped shape memory alloy single crystals, *Materials Science and Engineering: A*. 438–440 (2006) 755–762. <https://doi.org/10.1016/j.msea.2006.02.192>.
- [20] K. Kishida, Y. Takahama, H. Inui, Deformation twinning in single crystals of a D019 compound with an off-stoichiometric composition (Ti–36.5at.%Al), *Acta Materialia*. 52 (2004) 4941–4952. <https://doi.org/10.1016/j.actamat.2004.06.051>.
- [21] P. Czaja, R. Chulist, K. Nalepka, T. Tokarski, Y.I. Chumlyakov, W. Maziarz, Temperature dependence of twinning stress in Ni_{49.5}Mn_{38.4}Sn_{12.2} single crystal, *Journal of Applied Physics*. 126 (2019) 145107. <https://doi.org/10.1063/1.5097372>.
- [22] A. Sozinov, N. Lanska, A. Soroka, L. Straka, Highly mobile type II twin boundary in Ni-Mn-Ga five-layered martensite, *Applied Physics Letters*. 99 (2011) 124103–3.
- [23] E. Faran, D. Shilo, Dynamics of twin boundaries in ferromagnetic shape memory alloys, *Materials Science and Technology*. 30 (2014) 1545–1558. <https://doi.org/10.1179/1743284714Y.0000000570>.
- [24] O. Heczko, J. Kopeček, L. Straka, H. Seiner, Differently mobile twin boundaries and magnetic shape memory effect in 10M martensite of Ni–Mn–Ga, *Materials Research Bulletin*. 48 (2013) 5105–5109. <https://doi.org/10.1016/j.materresbull.2013.04.034>.
- [25] H. Seiner, L. Straka, O. Heczko, A microstructural model of motion of macro-twin interfaces in Ni–Mn–Ga 10 M martensite, *Journal of the Mechanics and Physics of Solids*. 64 (2014) 198–211. <https://doi.org/10.1016/j.jmps.2013.11.004>.
- [26] O. Heczko, L. Straka, H. Seiner, Different microstructures of mobile twin boundaries in 10 M modulated Ni–Mn–Ga martensite, *Acta Materialia*. 61 (2013) 622–631. <https://doi.org/10.1016/j.actamat.2012.10.007>.
- [27] L. Straka, N. Lanska, K. Ullakko, A. Sozinov, Twin microstructure dependent mechanical response in Ni–Mn–Ga single crystals, *Applied Physics Letters*. 96 (2010) 131903.

- [28] S. Kaufmann, R. Niemann, T. Thersleff, U.K. Röbber, O. Heczko, J. Buschbeck, B. Holzapfel, L. Schultz, S. Fähler, Modulated martensite: why it forms and why it deforms easily, *New J. Phys.* 13 (2011) 053029. <https://doi.org/10.1088/1367-2630/13/5/053029>.
- [29] L. Straka, J. Drahokoupil, O. Pacherová, K. Fabiánová, V. Kopecký, H. Seiner, H. Hänninen, O. Heczko, The relation between lattice parameters and very low twinning stress in Ni₅₀Mn₂₅Ga₂₅ magnetic shape memory alloys, *Smart Mater. Struct.* 25 (2015) 025001. <https://doi.org/10.1088/0964-1726/25/2/025001>.
- [30] O. Heczko, V. Kopecký, A. Sozinov, L. Straka, Magnetic shape memory effect at 1.7 K, *Applied Physics Letters*. 103 (2013) 072405. <https://doi.org/10.1063/1.4817941>.
- [31] M. Vronka, H. Seiner, O. Heczko, Temperature dependence of twinning stress – Analogy between Cu–Ni–Al and Ni–Mn–Ga shape memory single crystals, *Philosophical Magazine*. 97 (2017) 1479–1497. <https://doi.org/10.1080/14786435.2017.1303577>.
- [32] L. Straka, A. Soroka, H. Seiner, H. Hänninen, A. Sozinov, Temperature dependence of twinning stress of Type I and Type II twins in 10M modulated Ni–Mn–Ga martensite, *Scripta Materialia*. 67 (2012) 25–28. <https://doi.org/10.1016/j.scriptamat.2012.03.012>.
- [33] A. Soroka, A. Sozinov, N. Lanska, M. Rameš, L. Straka, K. Ullakko, Composition and temperature dependence of twinning stress in non-modulated martensite of Ni–Mn–Ga–Co–Cu magnetic shape memory alloys, *Scripta Materialia*. 144 (2018) 52–55. <https://doi.org/10.1016/j.scriptamat.2017.09.046>.
- [34] O. Heczko, L. Straka, Temperature dependence and temperature limits of magnetic shape memory effect, *Journal of Applied Physics*. 94 (2003) 7139–7143. <https://doi.org/10.1063/1.1626800>.

- [35] J.P. Hirth, Dislocations, steps and disconnections at interfaces, *Journal of Physics and Chemistry of Solids*. 55 (1994) 985–989. [http://dx.doi.org/10.1016/0022-3697\(94\)90118-X](http://dx.doi.org/10.1016/0022-3697(94)90118-X).
- [36] J.P. Hirth, R.C. Pond, Steps, dislocations and disconnections as interface defects relating to structure and phase transformations, *Acta Materialia*. 44 (1996) 4749–4763. [https://doi.org/10.1016/S1359-6454\(96\)00132-2](https://doi.org/10.1016/S1359-6454(96)00132-2).
- [37] R.C. Pond, J.P. Hirth, Defects at Surfaces and Interfaces, in: H. EHRENREICH, D. TURNBULL (Eds.), Academic Press, 1994: pp. 287–365. <http://www.sciencedirect.com/science/article/pii/S0081194708606414>.
- [38] R.C. Pond, X. Ma, Y.W. Chai, J.P. Hirth, Chapter 74 Topological Modelling of Martensitic Transformations, in: F.R.N. Nabarro, J.P. Hirth (Eds.), Elsevier, 2007: pp. 225–261. [https://doi.org/10.1016/S1572-4859\(07\)80006-4](https://doi.org/10.1016/S1572-4859(07)80006-4).
- [39] R.C. Pond, S. Celotto, Special interfaces: military transformations, *International Materials Reviews*. 48 (2003) 225–245. <https://doi.org/10.1179/095066003225010245>.
- [40] R.C. Pond, J.P. Hirth, Topological model of type II deformation twinning, *Acta Materialia*. 151 (2018) 229–242. <https://doi.org/10.1016/j.actamat.2018.03.014>.
- [41] R.C. Pond, J.P. Hirth, K.M. Knowles, Topological model of type II deformation twinning in NiTi martensite, *Philosophical Magazine*. 99 (2019) 1619–1632. <https://doi.org/10.1080/14786435.2019.1587185>.
- [42] B. Karki, P. Müllner, R. Pond, Topological model of type II deformation twinning in 10M Ni-Mn-Ga, *Acta Materialia*. 201 (2020) 604–616. <https://doi.org/10.1016/j.actamat.2020.10.020>.
- [43] J.P. Hirth, J. Wang, Extension of the classical theory for types I and II twinning, *Journal of Materials Research*. (2021). <https://doi.org/10.1557/s43578-020-00003-6>.
- [44] A.S.K. Mohammed, H. Sehitoglu, Modeling the interface structure of type II twin boundary in B19' NiTi from an atomistic and topological standpoint, *Acta Materialia*. 183 (2020) 93–109. <https://doi.org/10.1016/j.actamat.2019.10.048>.

- [45] H. Seiner, Two-dimensional laminates in monoclinic-II modulated martensites, *International Journal of Solids and Structures*. 221 (2021) 92–102.
<https://doi.org/10.1016/j.ijsolstr.2020.04.016>.
- [46] E. Faran, D. Shilo, The kinetic relation for twin wall motion in NiMnGa, *Journal of the Mechanics and Physics of Solids*. 59 (2011) 975–987.
<https://doi.org/10.1016/j.jmps.2011.02.009>.
- [47] E. Faran, D. Shilo, The kinetic relation for twin wall motion in NiMnGa—part 2, *Journal of the Mechanics and Physics of Solids*. 61 (2013) 726–741.
<https://doi.org/10.1016/j.jmps.2012.11.004>.
- [48] A. Saren, D. Musiienko, A.R. Smith, K. Ullakko, Pulsed magnetic field-induced single twin boundary motion in Ni–Mn–Ga 5M martensite: A laser vibrometry characterization, *Scripta Materialia*. 113 (2016) 154–157.
<http://dx.doi.org/10.1016/j.scriptamat.2015.10.020>.
- [49] A. Saren, T. Nicholls, J. Tellinen, K. Ullakko, Direct observation of fast-moving twin boundaries in magnetic shape memory alloy Ni–Mn–Ga 5 M martensite, *Scripta Materialia*. 123 (2016) 9–12.
<http://dx.doi.org/10.1016/j.scriptamat.2016.04.004>.
- [50] R. Abeyaratne, J.K. Knowles, On the driving traction acting on a surface of strain discontinuity in a continuum, *Journal of the Mechanics and Physics of Solids*. 38 (1990) 345–360. [https://doi.org/10.1016/0022-5096\(90\)90003-M](https://doi.org/10.1016/0022-5096(90)90003-M).
- [51] R. Abeyaratne, J.K. Knowles, *Evolution of Phase Transitions: A Continuum Theory*, Cambridge University Press, 2006.
<http://books.google.co.il/books?id=GFh4N8rWfS0C>.
- [52] D.A. Porter, K.E. Easterling, *Phase Transformations in Metals and Alloys*, Third Edition (Revised Reprint), Taylor & Francis, 1992.
<https://books.google.co.il/books?id=eYR5Re5tZisC>.

- [53] P. Müllner, K. Ullakko, The Force of a Magnetic/Electric Field on a Twinning Dislocation, *Physica Status Solidi (b)*. 208 (1998) R1–R2.
[https://doi.org/10.1002/\(SICI\)1521-3951\(199807\)208:1<R1::AID-PSSB99991>3.0.CO;2-4](https://doi.org/10.1002/(SICI)1521-3951(199807)208:1<R1::AID-PSSB99991>3.0.CO;2-4).
- [54] P. Müllner, V.A. Chernenko, M. Wollgarten, G. Kostorz, Large cyclic deformation of a Ni-Mn-Ga shape memory alloy induced by magnetic fields, *Journal of Applied Physics*. 92 (2002) 6708–6713.
<https://doi.org/10.1063/1.1513875>.
- [55] E. Faran, I. Benichou, S. Givli, D. Shilo, The effects of magnetic and mechanical microstructures on the twinning stress in Ni-Mn-Ga, *Journal of Applied Physics*. 118 (2015) 244104. <https://doi.org/10.1063/1.4939179>.
- [56] L. Truskinovsky, A. Vainchtein, Kinetics of Martensitic Phase Transitions: Lattice model, *SIAM Journal on Applied Mathematics*. 66 (2005) 533–553.
<https://doi.org/10.1137/040616942>.
- [57] J.D. Clayton, A continuum description of nonlinear elasticity, slip and twinning, with application to sapphire, *Proceedings of the Royal Society A: Mathematical, Physical and Engineering Science*. 465 (2009) 307–334.
<https://doi.org/10.1098/rspa.2008.0281>.
- [58] S.R. Kalidindi, Incorporation of deformation twinning in crystal plasticity models, *Journal of the Mechanics and Physics of Solids*. 46 (1998) 267–290.
[https://doi.org/10.1016/S0022-5096\(97\)00051-3](https://doi.org/10.1016/S0022-5096(97)00051-3).
- [59] E. Faran, D. Shilo, Ferromagnetic Shape Memory Alloys—Challenges, Applications, and Experimental Characterization, *Experimental Techniques*. 40 (2016) 1005–1031. <https://doi.org/10.1007/s40799-016-0098-5>.
- [60] P. Müllner, V.A. Chernenko, G. Kostorz, Stress-induced twin rearrangement resulting in change of magnetization in a Ni–Mn–Ga ferromagnetic martensite, *Scripta Materialia*. 49 (2003) 129–133. [https://doi.org/10.1016/S1359-6462\(03\)00219-7](https://doi.org/10.1016/S1359-6462(03)00219-7).

- [61] A. Sozinov, N. Lanska, A. Soroka, W. Zou, 12% magnetic field-induced strain in Ni-Mn-Ga-based non-modulated martensite, *Applied Physics Letters*. 102 (2013). <https://doi.org/10.1063/1.4775677>.
- [62] J.M. Howe, R.C. Pond, J.P. Hirth, The role of disconnections in phase transformations, *Prog Mater Sci*. 54 (2009) 47–47. <https://doi.org/10.1016/j.pmatsci.2009.04.001>.
- [63] R.C. Pond, B. Muntifering, P. Müllner, Deformation twinning in Ni₂MnGa, *Acta Materialia*. 60 (2012) 3976–3984. <https://doi.org/10.1016/j.actamat.2012.03.045>.
- [64] R.C. Pond, J.P. Hirth, A. Serra, D.J. Bacon, Atomic displacements accompanying deformation twinning: shears and shuffles, *Materials Research Letters*. 4 (2016) 185–190. <https://doi.org/10.1080/21663831.2016.1165298>.
- [65] M. Nishida, K. Yamauchi, I. Itai, H. Ohgi, A. Chiba, High resolution electron microscopy studies of twin boundary structures in B19' martensite in the Ti-Ni shape memory alloy, *Acta Metallurgica et Materialia*. 43 (1995) 1229–1234. [https://doi.org/10.1016/0956-7151\(94\)00328-F](https://doi.org/10.1016/0956-7151(94)00328-F).
- [66] Y. Liu, Z.L. Xie, Twinning and detwinning of $\langle 0\ 1\ 1 \rangle$ type II twin in shape memory alloy, *Acta Materialia*. 51 (2003) 5529–5543. [https://doi.org/10.1016/S1359-6454\(03\)00417-8](https://doi.org/10.1016/S1359-6454(03)00417-8).
- [67] Z.L. Xie *, Y. Liu, HRTEM study of $\langle 011 \rangle$ type II twin in NiTi shape memory alloy, *Philosophical Magazine*. 84 (2004) 3497–3507. <https://doi.org/10.1080/14786430412331283596>.
- [68] Y. Liu, Z.L. Xie, The Rational Nature of Type II Twin in NiTi Shape Memory Alloy, *Journal of Intelligent Material Systems and Structures*. 17 (2006) 1083–1090. <https://doi.org/10.1177/1045389X06064887>.
- [69] H. Yan, C. Zhang, Y. Zhang, X. Wang, C. Esling, X. Zhao, L. Zuo, Crystallographic insights into Ni-Co-Mn-In metamagnetic shape memory alloys, *Journal of Applied Crystallography*. 49 (2016) 1585–1592. <https://doi.org/10.1107/S1600576716012140>.

- [70] J. Wang, H. Sehitoglu, Twinning stress in shape memory alloys: Theory and experiments, *Acta Materialia*. 61 (2013) 6790–6801.
<https://doi.org/10.1016/j.actamat.2013.07.053>.
- [71] K.M. Knowles, A high-resolution electron microscope study of nickel-titanium martensite, *Philosophical Magazine A*. 45 (1982) 357–370.
<https://doi.org/10.1080/01418618208236176>.
- [72] J.P. Hirth, J. Lothe, *Theory of Dislocations*, 2nd Edition (Reprint Edition 1992), Krieger Publishing Company, 1982.
<http://books.google.co.il/books?id=LFZGAAAAYAAJ>.
- [73] X. Ding, T. Lookman, Z. Zhao, A. Saxena, J. Sun, E.K.H. Salje, Dynamically strained ferroelastics: Statistical behavior in elastic and plastic regimes, *Physical Review B*. 87 (3) 094109.
- [74] M. Boleininger, M. Gallauer, S.L. Dudarev, T.D. Swinburne, D.R. Mason, D. Perez, Statistical mechanics of kinks on a gliding screw dislocation, *Phys. Rev. Research*. 2 (2020) 043254. <https://doi.org/10.1103/PhysRevResearch.2.043254>.
- [75] A.S.K. Mohammed, H. Sehitoglu, Strain-sensitive topological evolution of twin interfaces, *Acta Materialia*. 208 (2021) 116716.
<https://doi.org/10.1016/j.actamat.2021.116716>.
- [76] J.P. Hirth, R.W. Armstrong, Straight and curved disclinations and dislocation equivalents, *Philosophical Magazine*. 0 (2020) 1–13.
<https://doi.org/10.1080/14786435.2020.1809730>.
- [77] G.B. Olson, M. Cohen, Interphase-boundary dislocations and the concept of coherency, *Acta Metallurgica*. 27 (1979) 1907–1918.
[https://doi.org/10.1016/0001-6160\(79\)90081-6](https://doi.org/10.1016/0001-6160(79)90081-6).
- [78] A.P. Sutton, R.W. Balluffi, *Interfaces in crystalline materials*, Clarendon Press, 1995. <https://books.google.co.il/books?id=oKLvAAAAMAAJ>.

- [79] A.E. Romanov, W. Pompe, J.S. Speck, Theory of microstructure and mechanics of the ...a₁/a₂/a₁/a₂... domain pattern in epitaxial ferroelectric and ferroelastic films, *Journal of Applied Physics*. 79 (1996) 4037–4049.
<https://doi.org/10.1063/1.361866>.
- [80] N. Farag, M. Bobeth, W. Pompe, A.E. Romanov, J.S. Speck, Modeling of twinning in epitaxial (001)-oriented La_{0.67}Sr_{0.33}MnO₃ thin films, *Journal of Applied Physics*. 97 (2005) 113516. <https://doi.org/10.1063/1.1914950>.
- [81] H.H. Johnson, Strain Energy of Screw Dislocation Arrays, *Journal of Applied Physics*. 37 (1966) 1763–1766. <https://doi.org/10.1063/1.1708598>.
- [82] M. Reinhold, D. Kiener, W.B. Knowlton, G. Dehm, P. Müllner, Deformation twinning in Ni–Mn–Ga micropillars with 10M martensite, *Journal of Applied Physics*. 106 (2009) 053906. <https://doi.org/10.1063/1.3211327>.
- [83] D. Musiienko, A. Saren, L. Straka, M. Vronka, J. Kopeček, O. Heczko, A. Sozinov, K. Ullakko, Ultrafast actuation of Ni-Mn-Ga micropillars by pulsed magnetic field, *Scripta Materialia*. 162 (2019) 482–485.
<https://doi.org/10.1016/j.scriptamat.2018.12.009>.
- [84] L. Dai, J. Cullen, M. Wuttig, Intermartensitic transformation in a NiMnGa alloy, *Journal of Applied Physics*. 95 (2004) 6957–6959.
<http://dx.doi.org/10.1063/1.1687203>.
- [85] J. Wang, H. Sehitoglu, Martensite modulus dilemma in monoclinic NiTi-theory and experiments, *International Journal of Plasticity*. 61 (2014) 17–31.
<https://doi.org/10.1016/j.ijplas.2014.05.005>.
- [86] P. Šesták, M. Černý, J. Pokluda, Elastic Constants of Austenitic and Martensitic Phases of NiTi Shape Memory Alloy, in: T. Brezina, R. Jablonski (Eds.), *Recent Advances in Mechatronics*, Springer Berlin Heidelberg, Berlin, Heidelberg, 2010: pp. 1–6. https://doi.org/10.1007/978-3-642-05022-0_1.
- [87] G. Ren, H. Sehitoglu, Interatomic potential for the NiTi alloy and its application, *Computational Materials Science*. 123 (2016) 19–25.
<https://doi.org/10.1016/j.commatsci.2016.06.012>.

- [88] E. Faran, D. Shilo, Implications of twinning kinetics on the frequency response in NiMnGa actuators, *Applied Physics Letters*. 100 (2012) 151901–4.
- [89] A. Saren, K. Ullakko, Dynamic twinning stress and viscous-like damping of twin boundary motion in magnetic shape memory alloy Ni-Mn-Ga, *Scripta Materialia*. 139 (2017) 126–129. <https://doi.org/10.1016/j.scriptamat.2017.06.010>.
- [90] B. Karki, Y. Behar, I. Harel, E. Caplan, A. Sabbag, D. Shilo, P. Mullner, E. Faran, A simple method to characterize high rate twin boundary kinetics in Ni-Mn-Ga, *Review of Scientific Instruments*. 90 (2019) 105107. <https://doi.org/10.1063/1.5109934>.
- [91] A. Mizrahi, U. Heller, E. Faran, D. Shilo, Under-microscope Mechanical Pulse System for Studying Deformation Processes at High Strain Rates, *Experimental Mechanics*. 60 (2020) 191–204. <https://doi.org/10.1007/s11340-019-00555-7>.
- [92] A. Mizrahi, D. Shilo, E. Faran, Variability of Twin Boundary Velocities in 10M Ni–Mn–Ga Measured Under μ s-Scale Force Pulses, *Shap. Mem. Superelasticity*. (2020). <https://doi.org/10.1007/s40830-020-00264-4>.
- [93] M. Avrami, Kinetics of Phase Change. I General Theory, *The Journal of Chemical Physics*. 7 (1939) 1103–1112. <https://doi.org/10.1063/1.1750380>.
- [94] M. Avrami, Kinetics of Phase Change. II Transformation-Time Relations for Random Distribution of Nuclei, *The Journal of Chemical Physics*. 8 (1940) 212–224. <https://doi.org/10.1063/1.1750631>.
- [95] R. Abeyaratne, C. Chu, R.D. James, Kinetics of materials with wiggly energies: Theory and application to the evolution of twinning microstructures in a Cu-Al-Ni shape memory alloy, *Philosophical Magazine A*. 73 (1996) 457–497. <https://doi.org/10.1080/01418619608244394>.
- [96] R.B. Flippen, Domain wall dynamics in ferroelectric/ferroelastic molybdates, *Journal of Applied Physics*. 46 (1975) 1068–1071. <https://doi.org/10.1063/1.322212>.

- [97] N. Zreihan, E. Faran, D. Shilo, The effect of loading rate on characteristics of type II twin boundary motion in Ni-Mn-Ga, *Scripta Materialia*. 144 (2018) 44–47. <https://doi.org/10.1016/j.scriptamat.2017.09.045>.
- [98] T. Ezaz, H. Sehitoglu, Type II detwinning in NiTi, *Appl. Phys. Lett.* 98 (2011) 141906. <https://doi.org/10.1063/1.3574775>.
- [99] H. Sehitoglu, J. Jun, X. Zhang, I. Karaman, Y. Chumlyakov, H.J. Maier, K. Gall, Shape memory and pseudoelastic behavior of 51.5%Ni–Ti single crystals in solutionized and overaged state, *Acta Materialia*. 49 (2001) 3609–3620. [https://doi.org/10.1016/S1359-6454\(01\)00216-6](https://doi.org/10.1016/S1359-6454(01)00216-6).
- [100] L. Straka, A. Sozinov, J. Drahokoupil, V. Kopecký, H. Hänninen, O. Heczko, Effect of intermartensite transformation on twinning stress in Ni-Mn-Ga 10 M martensite, *Journal of Applied Physics*. 114 (2013) 063504. <https://doi.org/10.1063/1.4817717>.
- [101] A. Sozinov, A. Soroka, N. Lanska, M. Rameš, L. Straka, K. Ullakko, Temperature dependence of twinning and magnetic stresses in Ni₄₆Mn₂₄Ga₂₂Co₄Cu₄ alloy with giant 12% magnetic field-induced strain, *Scripta Materialia*. 131 (2017) 33–36. <https://doi.org/10.1016/j.scriptamat.2016.12.032>.
- [102] T.E. Stenger, J. Trivisonno, Ultrasonic study of the two-step martensitic phase transformation in Ni_{2}MnGa , *Phys. Rev. B*. 57 (1998) 2735–2739. <https://doi.org/10.1103/PhysRevB.57.2735>.
- [103] M. Stipcich, L. Mañosa, A. Planes, M. Morin, J. Zarestky, T. Lograsso, C. Stassis, Elastic constants of $\text{Ni}\text{-Mn-Ga}$ magnetic shape memory alloys, *Phys. Rev. B*. 70 (2004) 054115. <https://doi.org/10.1103/PhysRevB.70.054115>.
- [104] Q. Hu, C.-M. Li, R. Yang, S. Kulkova, D.I. Bazhanov, B. Johansson, L. Vitos, Site occupancy, magnetic moments, and elastic constants of off-stoichiometric Ni₂MnGa from first-principles calculations, (2009). <https://doi.org/10.1103/PHYSREVB.79.144112>.

- [105] N. Glavatska, G. Mogylny, I. Glavatskiy, V. Gavriljuk, Temperature stability of martensite and magnetic field induced strain in Ni–Mn–Ga, *Scripta Materialia*. 46 (2002) 605–610.
- [106] N. Zreihan, E. Faran, D. Shilo, The effects of temperature on the lattice barrier for twin wall motion, *Applied Physics Letters*. 107 (2015) 041605.
<https://doi.org/10.1063/1.4927660>.
- [107] Z. Li, The elastic and electromechanical properties of tetragonal BaTiO₃ single crystals, (n.d.) 7.
- [108] N. Lanska, O. Söderberg, A. Sozinov, Y. Ge, K. Ullakko, V.K. Lindroos, Composition and temperature dependence of the crystal structure of Ni–Mn–Ga alloys, *Journal of Applied Physics*. 95 (2004) 8074–8078.
<https://doi.org/10.1063/1.1748860>.
- [109] N. Otani, Y. Funatsu, S. Ichinose, S. Miyazaki, K. Otsuka, Orientation dependence of the deformation modes in a γ' martensite single crystal in CuAlNi alloy, *Scripta Metallurgica*. 17 (1983) 745–750. [https://doi.org/10.1016/0036-9748\(83\)90486-6](https://doi.org/10.1016/0036-9748(83)90486-6).
- [110] O. Söderberg, L. Straka, V. Novák, O. Heczko, S.-P. Hannula, V.K. Lindroos, Tensile/compressive behaviour of non-layered tetragonal Ni_{52.8}Mn_{25.7}Ga_{21.5} alloy, *Materials Science and Engineering: A*. 386 (2004) 27–33.
<https://doi.org/10.1016/j.msea.2004.07.045>.
- [111] B. Reinholz, S. Brinckmann, A. Hartmaier, B. Muntiferling, W.B. Knowlton, P. Müllner, Influence of the twin microstructure on the mechanical properties in magnetic shape memory alloys, *Acta Materialia*. 108 (2016) 197–206.
<http://dx.doi.org/10.1016/j.actamat.2016.02.007>.

CHAPTER EIGHT: SUMMARY OF WORK AND CONTRIBUTIONS

8.1 Summary of Work

This dissertation aims to clarify the high mobility and low yield stress of type II TBs in shape memory alloys. Our primary objective is a structural characterization of TBs in SMAs because the structure and properties of materials are inherently related, and one directly affects the other. We extensively characterize the structure of TBs and their junctions using the CM of twinning and the TM of extended defects. After establishing the structure of various defects, we analyze the energy barriers for the motion of TBs and establish an analytical kinetic relation.

The formation and the equilibrium structure of type II TBs has posed a problem for the scientific community. In 2019, Pond, Hirth, and coworkers proposed to describe the formation mechanism of type II twins with the TM of extended defects, consistent with the CM of twinning [44, 45]. We implement the TM to establish the equilibrium defect structure of type I and type II twins in NMG alloys. Furthermore, we also identify the characteristic features of defects that lead to the growth of twins and the movement of TBs. Among the insights we gain from the structural characterization of defects are (i) that type II TBs may form a coherently faceted structure and (ii) that in NMG such a coherent faceting is not possible. This result implies that type II TBs do not encounter a periodic potential for their motion, unlike type I and coherently faceted type II TBs. Furthermore, the tilt-boundary of type II twins can kink to reduce the interfacial energy, leading to more effortless motion and, thus, high mobility of TB in NMG.

One of the characteristic features of type II TBs is that a serrated interfacial structure arises in its vicinity, as shown by Seiner et al. [65]. We study the properties of the serrated interface and identify a chain of quadruple junction lines (QJLs) responsible for such a structure. Implementing the principle of symmetry compensation and the CM of twinning, we identify the arrangement of TBs around QJLs. We identify NC twins in NMG, a rarely reported defect in other materials; the CM recognizes NC twins. However, no instances of such interfaces have been known until recently. The analysis of QJLs shows that two $(1r0)_m$ NC TBs and two $(110)_m$ compound TBs terminate at the junction. These QJLs have no long-range rotational displacement field, as identified by performing sequential products of OR across the TB. QJLs formed by the TBs mentioned above are always defect-free, independent of the lattice parameters of the crystal.

The probability that four TBs meet at a line to form a QJL without external driving force is reasonably low. Triple junction lines (TJLs), on the other hand, form when two TBs meet and are a much likelier defect arrangement. In NMG, TJLs carry a rotational displacement field, and disclinations accommodate the rotational misfit at the junction. TJLs accommodate three variants and given that there are four variants in the present case, four different TJLs are feasible, each with a unique disclination strength: $\omega_1, -\omega_1, \omega_2, -\omega_2$, where $\omega_1 = 0.18^\circ$ and $\omega_2 = 0.36^\circ$ in NMG. The TBs that meet at a line to form TJLs are each a unique twin mode: we have $(110)_m$ and $(1r0)_m$ TBs, as in QJLs, and the third TB that meets at a line is either $(100)_m$ or $(010)_m$. The two different disclination magnitudes, ω_1 and ω_2 , are a function of whether $(100)_m$ or $(010)_m$ TB meets at the TJL.

Disclinations are high-energy line defects whose stress field diverges.

Nonetheless, four unique disclinations forming a series of TJLs screen each other's stress field and form a stable configuration. We estimate the strain energy of the TJLs with a disclination quadrupole approximation. The quadrupole arrangement screens the long-range stresses of the disclinations but not entirely the short-range displacement field. The net strain energy scales as the function of the separation distance of defects [66–69]. Thus, as the defects approach larger length scales (i.e. for coarser twins), two TJLs may coalesce to form a QJL and reduce the system's overall energy. QJLs formed this way will retain the overall misorientation as before the coalescence.

At the sub-micron scale, Seiner et al. [65] reported regions with three variants accommodated by twinning: two variants interrelated by $(110)_m$ twinning abuts a $(100)_m$ or $(010)_m$ boundary separating a homogeneous region. This boundary is composed of a chain of TJLs, each located along a line where TBs meet. Its defect structure is equivalent to a series of disclination dipoles. A chain of TJLs carrying an array of disclination dipoles corresponds to a wall of edge dislocations, equivalent to a tilt-wall. The rotational field of the tilt-wall is partitioned across the interface, and the total misorientation depends on whether the interface is constrained or unconstrained. The total rotation of the interface depends only on the density of $(110)_m$ twin microstructure. The strain energy is a function of three variables: the density of TJLs, the magnitude of disclination, and the arm length of the dipoles. The dependence of strain energy on the separation distance of defects (dipole arm length) helps explain why these TJLs are only observed at the sub-micron length scale.

While the formation mechanism of QJLs and TJLs has not been established, the energetics study of QJLs and TJLs suggests a QJL may form by the union of two TJLs. QJLs accommodate all four variants and are defect-free. TJLs have rotational misfits and require a system of disclination quadrupole to accommodate four variants. The energy of this system is a logarithmic function of the distance between TJLs. Consequently, the QJLs we observe in the millimeter-scale range may have been formed by the union of TJLs, as it vanishes the energy of disclination quadrupole system. However, the influence of type II twins is still unclear for the occurrence of a chain of QJLs in its vicinity. Topological modeling of defect-junction formation mechanism and in-situ TEM and HRTEM experiments tracking the formation of junctions will help understand this characteristic feature of type II twins.

Another aspect of twinning is the rate at which the TB propagates. Here we set up the kinetic relation, i.e., we establish TB velocity as a function of the total driving force. Knowledge of the kinetic relation allows prediction of the dynamic behavior of SMAs under various kinds of loading. In 2014, Faran and Shilo reported experimental kinetic relations in NMG over a wide range of driving forces [24]. They demonstrated for type I and type II twins the existence of transitional stress (not the same as twinning stress), beyond which the TB velocity increases rapidly, signifying a change in the TB motion mechanism.

The transition driving force, denoted g_o , and equivalent to transitional stress is a vital parameter to attain high-speed actuation and other dynamic behaviors. One of our goals is to find a non-destructive simple method to measure this transition stress for each unique SMA sample. With an in-house built solenoid-based loading system that produces

a high-impact pulsed mechanical load, we concurrently measure the load and sample displacement and also recorded TB motion using a high-frame-rate camera. We clean the data and plot two figures: TB velocity vs. driving force and sample displacement velocity vs. driving force. Our analysis demonstrates that the trend in these two plots are similar, and one can predict the transition stress by following only the sample displacement velocity vs. driving force plot. Our work shows that one can identify the transition driving force, g_o , for each unique sample by performing a simple non-destructive pulsed loading test by tracking the sample displacement and load [70].

Faran and Shilo's analytical kinetic relation (2014) does not distinguish between type I and type II TBs [25]. Furthermore, the model does not predict why type II TBs are mobile near absolute zero temperature, i.e., follow athermal kinetics, but type I TBs are not. Consequently, we extend the model to incorporate the structural differences between type I and type II twins with the goal to elucidate the mechanism of TB motion and its temperature dependence. We show that the 2014 kinetic relation is consistent with compound and type I TBs based on their interface structure. In 2021, we further validate the model by correctly predicting the twinning stress (at room temperature) as a logarithmic function of $\mu^2 s^3$, where μ is the shear modulus, and s is the twinning shear [71]. The rate-limiting process for the twinning stress (equivalent to g_{TS}) is the nucleation rate of the disconnection loop. The transition driving force, g_o , is attributed to overcoming the lattice barrier for the motion of the TB as a flat plane.

For type II TBs, our structural characterization of the irrational interface [71, 72] provides a basis for characterizing its kinetic relations. We show the feasibility of irrational type II TBs to relax into a coherently faceted interface, for example, in NiTi.

Such structures have a rational terrace plane and a periodic array of disconnections acting as ledges to compensate for the misfit strain. In a relaxed state, the spacing of the disconnections array is such that the average habit plane is almost parallel to the irrational interface, \mathbf{K}_1 , as predicted by the CM of twinning. Analysis of potential barriers based on the structure of a coherently faceted interface informs that the disconnections nucleate athermally to compensate for the misfit strain as the disconnections array that is already present moves synchronously. Thus, the rate-limiting process for the twinning stress, g_{TS} , is the nucleation rate of kink pairs in disconnections; expansion of kink pairs requires less energy than their nucleation. The activation energy for the nucleation of kink-pairs is significantly smaller than that of the disconnection loop; the thermal energy of about 4 Kelvin is still enough for kink-pairs expansion and TB motion, as observed experimentally for type II twins. The transition stress, g_0 , for type II TBs is associated with overcoming the barrier for the glide of disconnections as a straight line.

Our work establishes the defect structure of junctions and TBs in shape memory alloys, especially NMG alloys. Structural characterization of the interface predicts the low twinning stress associated with type II twins and the high mobility of type II TBs, which is practically insensitive to temperature. We establish the kinetic relation of TBs for compound, type I, and coherently faceted type II twins.

8.2 Outstanding Questions

While extensive work has been done to establish the structure and kinetics of TBs, especially in NMG alloys, new research questions emerge. Such questions include the list given here.

1. Pond and Hirth suggested that the formation of type I and conjugate type II twins is a competitive process; type II TBs form if the disconnections formed in the conjugate type I TBs are not mobile. In NMG, non-conjugate type I and type II appear simultaneously. How does the modulated structure of NMG affect such behavior?
2. Armstrong et al. [73, 74] showed that a densely twinned microstructure homogeneously distributes the stress field and improves the reproducibility and fatigue life of NMG devices under dynamic loading. Single crystals with one or few TBs, on the other hand, have stochastic twin evolution that quickly deteriorates the performance of NMG devices. How does the interaction of disconnections in densely twinned material affect the TB dynamics and improve the performance of MSMA samples?
3. While we have characterized the defect structure of QJLs and TJLs, their origin and formation mechanism are not understood. In particular, it is not evident that four TBs meet in one line. What is the formation mechanism of QJLs, and why do QJLs form in the presence of type II twins only?
4. We establish the rate-limiting mechanism and kinetic-relation of coherently faceted type II TBs. However, we show that NMG cannot relax into a coherently faceted structure and does not follow the kinetics established for the terrace-ledges interface. What is the kinetic relation of irrational type II TBs? Are these interfaces more mobile than coherently faceted type II TBs?

8.3 Future Work

In this section, we suggest some studies, which may provide answers to questions raised in Section 8.2.

1. Since we neglected the modulation present in NMG, the actual atomic positions vary systematically from those assumed in this work. The shuffling accompanying the disconnections for mirror symmetry-related type I twins in the topological analysis may provide information about why the disconnections pile up in one case but not the other, i.e., explain why non-conjugate type I and type II twins form in NMG.
2. In dense twin microstructures, each disconnection interacts with many other disconnections. Computational simulations, specifically dislocation dynamics simulations, may provide information on how the twin density impacts the response of the material to external stimuli such as a mechanical load or a magnetic field.
3. The current analysis of QJLs and TJLs does not cover the formation mechanism of these defects. Topological analysis of defect interactions leading to the formation of QJLs and TJLs will help with the understanding of the formation mechanisms of these junctions and NC twins. Furthermore, the theory can be validated by capturing the formation mechanism using in-situ TEM and SEM experiments.
4. We show that type II TBs form a coherently faceted structure in NiTi but not in NMG, which are inherently irrational. While experimental kinetic relations of NMG are established [24, 28, 48, 64, 70], such work has not

been done with NiTi. Experiments to establish kinetic relations for NiTi will help clarify the origin of the different properties of coherently faceted and inherently irrational type II TBs.

REFERENCES

- [1] X. Wang, B. Xu, Z. Yue, Phase transformation behavior of pseudoelastic NiTi shape memory alloys under large strain, *Journal of Alloys and Compounds*. 463 (2008) 417–422. <https://doi.org/10.1016/j.jallcom.2007.09.029>.
- [2] J.V. Humbeeck, Shape Memory Alloys: A Material and a Technology, *ADVANCED ENGINEERING MATERIALS*. (2001) 14.
- [3] J.J. Zhu, N.G. Liang, K.M. Liew, W.M. Huang, Energy Conversion in Shape Memory Alloy Heat Engine Part I: Theory, *Journal of Intelligent Material Systems and Structures*. 12 (2001) 127–132. <https://doi.org/10.1106/AMFV-FPQQ-RNBK-EE50>.
- [4] A.R. Smith, J. Tellinen, K. Ullakko, Rapid actuation and response of Ni–Mn–Ga to magnetic-field-induced stress, *Acta Materialia*. 80 (2014) 373–379. <https://doi.org/10.1016/j.actamat.2014.06.054>.
- [5] I. Aaltio, K.P. Mohanchandra, O. Heczko, M. Lahelin, Y. Ge, G.P. Carman, O. Söderberg, B. Löfgren, J. Seppälä, S.-P. Hannula, Temperature dependence of mechanical damping in Ni–Mn–Ga austenite and non-modulated martensite, *Scripta Materialia*. 59 (2008) 550–553. <https://doi.org/10.1016/j.scriptamat.2008.05.005>.
- [6] S. Barker, E. Rhoads, P. Lindquist, M. Vreugdenhil, P. Müllner, Magnetic Shape Memory Micropump for Submicroliter Intracranial Drug Delivery in Rats, *Journal of Medical Devices*. 10 (2016) 041009. <https://doi.org/10.1115/1.4034576>.

- [7] S.A. Wilson, R.P.J. Jourdain, Q. Zhang, R.A. Dorey, C.R. Bowen, M. Willander, Q.U. Wahab, M. Willander, S.M. Al-Hilli, O. Nur, E. Quandt, C. Johansson, E. Pagounis, M. Kohl, J. Matovic, B. Samel, W. Van Der Wijngaart, E.W.H. Jager, D. Carlsson, Z. Djinovic, M. Wegener, C. Moldovan, R. Iosub, E. Abad, M. Wendlandt, C. Rusu, K. Persson, New materials for micro-scale sensors and actuators, *Materials Science and Engineering: R: Reports*. 56 (2007) 1–129. <https://doi.org/10.1016/j.mser.2007.03.001>.
- [8] K. Ullakko, L. Wendell, A. Smith, P. Müllner, G. Hampikian, A magnetic shape memory micropump: contact-free, and compatible with PCR and human DNA profiling, *Smart Mater. Struct.* 21 (2012) 115020. <https://doi.org/10.1088/0964-1726/21/11/115020>.
- [9] P. Lindquist, T. Hobza, C. Patrick, P. Müllner, Efficiency of Energy Harvesting in Ni–Mn–Ga Shape Memory Alloys, *Shape Memory and Superelasticity*. 4 (2018) 93–101. <https://doi.org/10.1007/s40830-018-0158-z>.
- [10] I. Suorsa, E. Pagounis, K. Ullakko, Magnetic shape memory actuator performance, *Journal of Magnetism and Magnetic Materials*. 272–276 (2004) 2029–2030. <https://doi.org/10.1016/j.jmmm.2003.12.1026>.
- [11] D.C. Lagoudas, ed., *Shape Memory Alloys: Modeling and Engineering Applications*, Springer US, 2008. <https://doi.org/10.1007/978-0-387-47685-8>.
- [12] K. Bhattacharya, Theory of Martensitic Microstructure and the Shape-Memory Effect, in: *Microstructure of Martensite, 2004*: p. 87.
- [13] R.C. Pond, X. Ma, J.P. Hirth, A Dislocation Model of Parent-Martensite Interfaces, in: G.B. Olson, D.S. Lieberman, A. Saxena (Eds.), *ICOMAT*, John Wiley & Sons, Inc., Hoboken, NJ, USA, 2013: pp. 107–114. <https://doi.org/10.1002/9781118803592.ch14>.
- [14] F.C. Frank, A note on twinning in alpha-uranium, *Acta Metallurgica*. 1 (1953) 71–74. [https://doi.org/10.1016/0001-6160\(53\)90010-8](https://doi.org/10.1016/0001-6160(53)90010-8).
- [15] M.A. Jaswon, D.B. Dove, The crystallography of deformation twinning, *Acta Cryst.* 13 (1960) 232–240. <https://doi.org/10.1107/S0365110X60000534>.

- [16] B.A. Bilby, A.G. Crocker, The theory of the crystallography of deformation twinning, *Proc. R. Soc. Lond. A.* 288 (1965) 240–255.
<https://doi.org/10.1098/rspa.1965.0216>.
- [17] M. Bevis, A.G. Crocker, Twinning modes in lattices, *Proceedings of the Royal Society A: Mathematical, Physical and Engineering Sciences.* 313 (1969) 21.
<https://doi.org/10.1098/rspa.1969.0208>.
- [18] J.W. Christian, S. Mahajan, Deformation twinning, *Progress in Materials Science.* 39 (1995) 1–157. [https://doi.org/10.1016/0079-6425\(94\)00007-7](https://doi.org/10.1016/0079-6425(94)00007-7).
- [19] M. Bevis, A.G. Crocker, Twinning shears in lattices, *Proc. R. Soc. Lond. A.* 304 (1968) 123–134. <https://doi.org/10.1098/rspa.1968.0077>.
- [20] J.P. Hirth, R.C. Pond, Steps, dislocations and disconnections as interface defects relating to structure and phase transformations, *Acta Materialia.* 44 (1996) 4749–4763. [https://doi.org/10.1016/S1359-6454\(96\)00132-2](https://doi.org/10.1016/S1359-6454(96)00132-2).
- [21] R.C. Pond, J.P. Hirth, Defects at Surfaces and Interfaces, in: *Solid State Physics*, Elsevier, 1994: pp. 287–365. [https://doi.org/10.1016/S0081-1947\(08\)60641-4](https://doi.org/10.1016/S0081-1947(08)60641-4).
- [22] R.C. Pond, S. Celotto, Special interfaces: military transformations, *International Materials Reviews.* 48 (2003) 225–245.
<https://doi.org/10.1179/095066003225010245>.
- [23] O. Heczko, Magnetic shape memory effect and highly mobile twin boundaries, *Materials Science and Technology.* 30 (2014) 1559–1578.
<https://doi.org/10.1179/1743284714Y.0000000599>.
- [24] E. Faran, D. Shilo, The kinetic relation for twin wall motion in Ni-Mn-Ga, *Journal of the Mechanics and Physics of Solids.* 59 (2011) 975–987.
<https://doi.org/10.1016/j.jmps.2011.02.009>.
- [25] E. Faran, D. Shilo, Ferromagnetic shape memory alloys—challenges, applications, and experimental characterization, *Exp Tech.* 40 (2016) 1005–1031.
<https://doi.org/10.1007/s40799-016-0098-5>.

- [26] A. Sozinov, N. Lanska, A. Soroka, L. Straka, Highly mobile type II twin boundary in Ni-Mn-Ga five-layered martensite, *Appl. Phys. Lett.* 99 (2011) 124103. <https://doi.org/10.1063/1.3640489>.
- [27] E. Faran, D. Shilo, The kinetic relation for twin wall motion in Ni-Mn-Ga—part 2, *Journal of the Mechanics and Physics of Solids.* 61 (2013) 726–741. <https://doi.org/10.1016/j.jmps.2012.11.004>.
- [28] E. Faran, D. Shilo, Dynamics of twin boundaries in ferromagnetic shape memory alloys, *Materials Science and Technology.* 30 (2014) 1545–1558. <https://doi.org/10.1179/1743284714Y.0000000570>.
- [29] N. Zreihan, E. Faran, D. Shilo, The effect of loading rate on characteristics of type II twin boundary motion in Ni-Mn-Ga, *Scripta Materialia.* 144 (2018) 44–47. <https://doi.org/10.1016/j.scriptamat.2017.09.045>.
- [30] L. Straka, A. Soroka, H. Seiner, H. Hänninen, A. Sozinov, Temperature dependence of twinning stress of type I and type II twins in 10M modulated Ni–Mn–Ga martensite, *Scripta Materialia.* 67 (2012) 25–28. <https://doi.org/10.1016/j.scriptamat.2012.03.012>.
- [31] A. Armstrong, F. Nilsén, M. Rameš, R.H. Colman, P. Veřtát, T. Kmječ, L. Straka, P. Müllner, O. Heczko, Systematic Trends of Transformation Temperatures and Crystal Structure of Ni–Mn–Ga–Fe–Cu Alloys, *Shap. Mem. Superelasticity.* 6 (2020) 97–106. <https://doi.org/10.1007/s40830-020-00273-3>.
- [32] V.A. L'vov, A. Kosogor, Temperature-dependent magnetostriction as the key factor for martensite reorientation in magnetic field, *J. Phys. D: Appl. Phys.* 49 (2016) 355005. <https://doi.org/10.1088/0022-3727/49/35/355005>.
- [33] O. Heczko, V. Kopecký, A. Sozinov, L. Straka, Magnetic shape memory effect at 1.7 K, *Appl. Phys. Lett.* 103 (2013) 072405. <https://doi.org/10.1063/1.4817941>.
- [34] M. Nishida, K. Yamauchi, I. Itai, H. Ohgi, A. Chiba, High resolution electron microscopy studies of twin boundary structures in B19' martensite in the Ti-Ni shape memory alloy, *Acta Metallurgica et Materialia.* 43 (1995) 1229–1234. [https://doi.org/10.1016/0956-7151\(94\)00328-f](https://doi.org/10.1016/0956-7151(94)00328-f).

- [35] M. Nishida, T. Hara, M. Matsuda, S. Ii, Crystallography and morphology of various interfaces in Ti–Ni, Ti–Pd and Ni–Mn–Ga shape memory alloys, *Materials Science and Engineering: A*. 481–482 (2008) 18–27.
<https://doi.org/10.1016/j.msea.2007.01.179>.
- [36] M. Matsuda, Y. Yasumoto, K. Hashimoto, T. Hara, M. Nishida, Transmission electron microscopy of twins in 10M martensite in Ni–Mn–Ga ferromagnetic shape memory alloy, *Mater. Trans.* 53 (2012) 902–906.
<https://doi.org/10.2320/matertrans.M2012002>.
- [37] T. Onda, Y. Bando, T. Ohba, K. Otsuka, Electron Microscopy Study of Twins in Martensite in a Ti–50.0 at%Ni Alloy, *Materials Transactions, JIM*. 33 (1992) 354–359. <https://doi.org/10.2320/matertrans1989.33.354>.
- [38] K.M. Knowles, A high-resolution electron microscope study of nickel-titanium martensite, *Philosophical Magazine A*. 45 (1982) 357–370.
<https://doi.org/10.1080/01418618208236176>.
- [39] Y. Liu, Z.L. Xie, The rational nature of type II twin in Ni–Ti shape memory alloy, *Journal of Intelligent Material Systems and Structures*. 17 (2006) 1083–1090.
<https://doi.org/10.1177/1045389X06064887>.
- [40] Y. Liu, Z.L. Xie, Twinning and detwinning of <011> type II twin in shape memory alloy, *Acta Materialia*. 51 (2003) 5529–5543.
[https://doi.org/10.1016/S1359-6454\(03\)00417-8](https://doi.org/10.1016/S1359-6454(03)00417-8).
- [41] H. Yan, C. Zhang, Y. Zhang, X. Wang, C. Esling, X. Zhao, L. Zuo, Crystallographic insights into Ni–Co–Mn–In metamagnetic shape memory alloys, *J Appl Crystallogr.* 49 (2016) 1585–1592.
<https://doi.org/10.1107/S1600576716012140>.
- [42] A.S.K. Mohammed, H. Sehitoglu, Modeling the interface structure of type II twin boundary in B19' Ni–Ti from an atomistic and topological standpoint, *Acta Materialia*. 183 (2020) 93–109. <https://doi.org/10.1016/j.actamat.2019.10.048>.

- [43] R.C. Pond, D.J. Bacon, A. Serra, A.P. Sutton, The crystallography and atomic structure of line defects in twin boundaries in hexagonal-close-packed metals, *MTA*. 22 (1991) 1185–1196. <https://doi.org/10.1007/BF02660650>.
- [44] R.C. Pond, J.P. Hirth, Topological model of type II deformation twinning, *Acta Materialia*. 151 (2018) 229–242. <https://doi.org/10.1016/j.actamat.2018.03.014>.
- [45] R.C. Pond, J.P. Hirth, K.M. Knowles, Topological model of type II deformation twinning in Ni-Ti martensite, *Philosophical Magazine*. 99 (2019) 1619–1632. <https://doi.org/10.1080/14786435.2019.1587185>.
- [46] C. Velmurugan, V. Senthilkumar, S. Dinesh, D. Arulkirubakaran, Review on phase transformation behavior of NiTi shape memory alloys, *Materials Today: Proceedings*. 5 (2018) 14597–14606. <https://doi.org/10.1016/j.matpr.2018.03.051>.
- [47] A.V. Shubnikov, V.A. Koptsik, *Symmetry in Science and Art*, Springer US, 1974. <https://www.springer.com/gp/book/9781468420692> (accessed June 9, 2020).
- [48] A. Saren, Twin boundary dynamics in magnetic shape memory alloy Ni-Mn-Ga five-layered modulated martensite, (2018) 127.
- [49] R.C. Pond, Line defects in interfaces, in: *Dislocations in Solids*, Elsevier Science Publishers, Amsterdam, 1988: pp. 1–66.
- [50] R.C. Pond, B. Muntifering, P. Müllner, Deformation twinning in Ni₂MnGa, *Acta Materialia*. 60 (2012) 3976–3984. <https://doi.org/10.1016/j.actamat.2012.03.045>.
- [51] P. Müllner, A.E. Romanov, Internal Twinning in Deformation Twinning, *Acta Materialia*. 48 (2000) 15.
- [52] B. Muntifering, R.C. Pond, L. Kovarik, N.D. Browning, P. Müllner, Intra-variant substructure in Ni–Mn–Ga martensite: conjugation boundaries, *Acta Materialia*. 71 (2014) 255–263. <https://doi.org/10.1016/j.actamat.2014.03.018>.
- [53] T. Braisaz, P. Ruterana, G. Nouet, R.C. Pond, Investigation of {10 1 2} twins in Zn using high-resolution electron microscopy: Interfacial defects and interactions, *Philosophical Magazine A*. 75 (1997) 1075–1095. <https://doi.org/10.1080/01418619708214012>.

- [54] P. Müllner, G. Kostorz, Microstructure of magnetic shape-memory alloys: between magnetoelasticity and magnetoplasticity, *MSF*. 583 (2008) 43–65. <https://doi.org/10.4028/www.scientific.net/MSF.583.43>.
- [55] R.C. Pond, On the characterisation of interfacial defects using high resolution electron microscopy, *Interface Sci.* 2 (1995). <https://doi.org/10.1007/BF00222621>.
- [56] H.A. Khater, A. Serra, R.C. Pond, Atomic shearing and shuffling accompanying the motion of twinning disconnections in Zirconium, *Philosophical Magazine*. 93 (2013) 1279–1298. <https://doi.org/10.1080/14786435.2013.769071>.
- [57] J. Wang, S.K. Yadav, J.P. Hirth, C.N. Tomé, I.J. Beyerlein, Pure-Shuffle Nucleation of Deformation Twins in Hexagonal-Close-Packed Metals, *Materials Research Letters*. 1 (2013) 126–132. <https://doi.org/10.1080/21663831.2013.792019>.
- [58] R.C. Pond, J.P. Hirth, A. Serra, D.J. Bacon, Atomic displacements accompanying deformation twinning: shears and shuffles, *Materials Research Letters*. 4 (2016) 185–190. <https://doi.org/10.1080/21663831.2016.1165298>.
- [59] E. Faran, D. Shilo, Twin motion faster than the speed of sound, *Phys. Rev. Lett.* 104 (2010) 155501. <https://doi.org/10.1103/PhysRevLett.104.155501>.
- [60] E. Faran, D. Shilo, Multi-Scale Dynamics of Twinning in SMA, *Shap. Mem. Superelasticity*. 1 (2015) 180–190. <https://doi.org/10.1007/s40830-015-0012-5>.
- [61] R. Abeyaratne, S. Vedantam, A lattice-based model of the kinetics of twin boundary motion, *Journal of the Mechanics and Physics of Solids*. 51 (2003) 1675–1700. [https://doi.org/10.1016/s0022-5096\(03\)00069-3](https://doi.org/10.1016/s0022-5096(03)00069-3).
- [62] L. Truskinovsky, A. Vainchtein, Kinetics of Martensitic Phase Transitions: Lattice model, *SIAM Journal on Applied Mathematics*. 66 (2005) 533–553. <https://doi.org/10.1137/040616942>.
- [63] R.C. Miller, G. Weinreich, Mechanism for the Sidewise Motion of 180° Domain Walls in Barium Titanate, *Phys. Rev.* 117 (1960) 1460–1466. <https://doi.org/10.1103/PhysRev.117.1460>.

- [64] N. Zreihan, A. Krimer, D. Avisar, E. Pagounis, D. Shilo, E. Faran, Microstructure evolution and kinetic laws for the motion of multiple twin boundaries in Ni–Mn–Ga, *Funct. Mater. Lett.* 12 (2019) 1850102.
<https://doi.org/10.1142/S1793604718501023>.
- [65] H. Seiner, R. Chulist, W. Maziarz, A. Sozinov, O. Heczko, L. Straka, Non-conventional twins in five-layer modulated Ni-Mn-Ga martensite, *Scripta Materialia*. 162 (2019) 497–502. <https://doi.org/10.1016/j.scriptamat.2018.12.020>.
- [66] P. Müllner, W.-M. Kuschke, Disclinations due to grain boundary relaxation in fine-grained materials and thin films, *Scripta Materialia*. 36 (1997) 1451–1455.
[https://doi.org/10.1016/S1359-6462\(97\)00042-0](https://doi.org/10.1016/S1359-6462(97)00042-0).
- [67] A.E. Romanov, Screened disclinations in solids, *Materials Science and Engineering: A*. 164 (1993) 58–68.
- [68] A.E. Romanov, A.L. Kolesnikova, Application of disclination concept to solid structures, *Progress in Materials Science*. 54 (2009) 740–769.
<https://doi.org/10.1016/j.pmatsci.2009.03.002>.
- [69] A.E. Romanov, V.I. Vladimirov, Disclinations in Crystalline Solids, *Dislocations in Solids*. 9 (1992). <https://ci.nii.ac.jp/naid/10029464238/> (accessed October 8, 2021).
- [70] B.J. Karki, Y. Behar, I. Harel, E. Caplan, A. Sabbag, D. Shilo, P. Mullner, E. Faran, A simple method to characterize high rate twin boundary kinetics in Ni-Mn-Ga, *Review of Scientific Instruments*. 90 (2019) 105107.
<https://doi.org/10.1063/1.5109934>.
- [71] D. Shilo, E. Faran, B. Karki, P. Müllner, Twin boundary structure and mobility, *Acta Materialia*. (2021) 117316. <https://doi.org/10.1016/j.actamat.2021.117316>.
- [72] B. Karki, P. Müllner, R. Pond, Topological model of type II deformation twinning in 10M Ni-Mn-Ga, *Acta Materialia*. 201 (2020) 604–616.
<https://doi.org/10.1016/j.actamat.2020.10.020>.

- [73] H. Zhang, A. Armstrong, P. Müllner, Effects of surface modifications on the fatigue life of unconstrained Ni-Mn-Ga single crystals in a rotating magnetic field, *Acta Materialia*. 155 (2018) 175–186.
<https://doi.org/10.1016/j.actamat.2018.05.070>.
- [74] A. Armstrong, B. Karki, A. Smith, P. Müllner, Traveling surface undulation on a Ni–Mn–Ga single crystal element, *Smart Mater. Struct.* (2021) 14.